

Advances in Meteorology

Meteorological Impacts on Landform Changes

Guest Editors: Hongming He, Zhongping Lai, and Steffen Mischke





Meteorological Impacts on Landform Changes

Advances in Meteorology

Meteorological Impacts on Landform Changes

Guest Editors: Hongming He, Zhongping Lai,
and Steffen Mischke



Copyright © 2016 Hindawi Publishing Corporation. All rights reserved.

This is a special issue published in "Advances in Meteorology." All articles are open access articles distributed under the Creative Commons Attribution License, which permits unrestricted use, distribution, and reproduction in any medium, provided the original work is properly cited.

Editorial Board

- José Antonio Adame, Spain
Cesar Azorin-Molina, Spain
Guillermo Baigorria, USA
Marina Baldi, Italy
Abderrahim Bentamy, France
Massimo A. Bollasina, UK
Stefania Bonafoni, Italy
Isabella Bordi, Italy
Alex Cannon, Canada
Claudio Carbone, Italy
Dominique Carrer, France
Charles Chemel, UK
Annalisa Cherchi, Italy
James Cleverly, Australia
Jill S. M. Coleman, USA
Gabriele Curci, Italy
Mladjen Ćurić, Serbia
Maher A. Dayeh, USA
Klaus Dethloff, Germany
Panuganti C. S. Devara, India
Julio Diaz, Spain
Arona Diedhiou, France
Stefano Dietrich, Italy
Eugenio Domínguez Vilches, Spain
Antonio Donateo, Italy
Igor Esau, Norway
Stefano Federico, Italy
Enrico Ferrero, Italy
Rossella Ferretti, Italy
Roberto Fraile, Spain
Charmaine Franklin, Australia
Jan Friesen, Germany
- Maria Ángeles García, Spain
Herminia García Mozo, Spain
Eduardo García-Ortega, Spain
Luis Gimeno, Spain
Jorge E. Gonzalez, USA
Ismail Gultepe, Canada
Rafiq Hamdi, Belgium
Adel Hanna, USA
Hiroyuki Hashiguchi, Japan
Tareq Hussein, Jordan
Bradley G. Illston, USA
Ivar S A Isaksen, Norway
Yasunobu Iwasaka, Japan
Pedro Jiménez-Guerrero, Spain
Kuruvilla John, USA
Charles Jones, USA
Hann-Ming H. Juang, USA
George Kallos, Greece
Harry D. Kambezidis, Greece
Nir Y. Krakauer, USA
Simon O. Krichak, Israel
Hisayuki Kubota, Japan
Haim Kutiel, Israel
Richard Leaitch, Canada
Monique Leclerc, USA
Ilan Levy, Israel
Gwo-Fong Lin, Taiwan
Anthony R. Lupo, USA
Paolo Madonia, Italy
Andreas Matzarakis, Germany
Samantha Melani, Italy
Nicholas Meskhidze, USA
- Christophe Messenger, France
Mario M. Miglietta, Italy
Takashi Mochizuki, Japan
Goro Mouri, Japan
Brian R. Nelson, USA
Efthymios I. Nikolopoulos, USA
Sandip Pal, USA
Giulia Panegrossi, Italy
Giulia Pavese, Italy
Kyaw T. Paw, USA
Olivier P. Prat, USA
Sara C. Pryor, USA
Philippe Ricaud, France
Tomeu Rigo, Spain
Filomena Romano, Italy
Jose Antonio Ruiz-Arias, Spain
Haydee Salmun, USA
Pedro Salvador, Spain
Arturo Sanchez-Lorenzo, Spain
Andres Schmidt, USA
Shraddhanand Shukla, USA
Fiona Smith, UK
Francisco J. Tapiador, Spain
Yoshihiro Tomikawa, Japan
Tomoo Ushio, Japan
Rogier Van Der Velde, Netherlands
Sergio M. Vicente-Serrano, Spain
Francesco Viola, Italy
Alastair Williams, Australia
Olga Zolina, France

Contents

Meteorological Impacts on Landform Changes

Hongming He, Zhongping Lai, and Steffen Mischke

Volume 2016, Article ID 8048174, 3 pages

The Effects of Climate and Anthropogenic Activity on Hydrologic Features in Yanhe River

Yang Cheng, Hongming He, Nannan Cheng, and Wenming He

Volume 2016, Article ID 5297158, 11 pages

Coupling Analysis of Hydrometeorology and Erosive Landforms Evolution in Loess Plateau, China

N. N. Cheng, H. M. He, Y. J. Lu, and S. Y. Yang

Volume 2016, Article ID 9732864, 11 pages

Numerical Simulation of the Topographical Change in Korea Mountain Area by Intense Rainfall and Consequential Debris Flow

Byong-Hee Jun

Volume 2016, Article ID 9363675, 11 pages

Spatial Variability and Periodicity of Precipitation in the Middle Reaches of the Yellow River, China

Yi He, Xingmin Mu, Peng Gao, Guangju Zhao, Fei Wang, Wenyi Sun, and Yuqing Zhang

Volume 2016, Article ID 9451614, 9 pages

1600 AD Huaynaputina Eruption (Peru), Abrupt Cooling, and Epidemics in China and Korea

Jie Fei, David D. Zhang, and Harry F. Lee

Volume 2016, Article ID 3217038, 12 pages

Holocene Vegetation Succession and Response to Climate Change on the South Bank of the Heilongjiang-Amur River, Mohe County, Northeast China

Chao Zhao, Xiaoqiang Li, Xinying Zhou, Keliang Zhao, and Qing Yang

Volume 2016, Article ID 2450697, 11 pages

Determination of the Effect of Water Depth and Flow Velocity on the Quality of an In-Stream Habitat in Terms of Climate Change

V. Macura, Z. Štefunková, and A. Škrinár

Volume 2016, Article ID 4560378, 17 pages

Numerical Modeling of Topography-Modulated Dust Aerosol Distribution and Its Influence on the Onset of East Asian Summer Monsoon

Hui Sun and Xiaodong Liu

Volume 2016, Article ID 6951942, 15 pages

Universal Power Law for Relationship between Rainfall Kinetic Energy and Rainfall Intensity

Seung Sook Shin, Sang Deog Park, and Byoung Koo Choi

Volume 2016, Article ID 2494681, 11 pages

NDVI Variation and Its Responses to Climate Change on the Northern Loess Plateau of China from 1998 to 2012

Tingting Ning, Wenzhao Liu, Wen Lin, and Xiaoqiang Song

Volume 2015, Article ID 725427, 10 pages

Contribution of River Mouth Reach to Sediment Load of the Yangtze River

C. Wang, S. B. Dai, L. S. Ran, L. Jiang, and W. T. Li

Volume 2015, Article ID 415058, 9 pages

Millennial-Scale Asian Monsoon Influenced Longjie Lake Evolution during Marine Isotope Stage 3, Upper Stream of Changjiang (Yangtze) River, China

Chaozhu Li, Jianli Fu, Liang Yi, Xin Zhou, Shubing Wang, and Fuchu Jiang

Volume 2015, Article ID 592894, 10 pages

Impacts of Climate Change and Human Activities on Runoff and Sediment Load of the Xiliugou Basin in the Upper Yellow River

Haifang Yao, Changxing Shi, Wenwei Shao, Jianbin Bai, and Hui Yang

Volume 2015, Article ID 481713, 12 pages

Editorial

Meteorological Impacts on Landform Changes

Hongming He,¹ Zhongping Lai,² and Steffen Mischke³

¹*Institute of Soil and Water Conservation, Northwest Agriculture and Forestry University and Chinese Academy of Sciences and Ministry of Water Resources, No. 26 Xinong Road, Yangling, Shaanxi 712100, China*

²*School of Earth Sciences, China Geosciences University (Wuhan), No. 388 Lumo Road, Hongshan, Wuhan, Hubei 430074, China*

³*Faculty of Earth Sciences, University of Iceland, Sturlugata 7, 101 Reykjavík, Iceland*

Correspondence should be addressed to Hongming He; hongming.he@yahoo.com

Received 29 October 2015; Accepted 29 October 2015

Copyright © 2016 Hongming He et al. This is an open access article distributed under the Creative Commons Attribution License, which permits unrestricted use, distribution, and reproduction in any medium, provided the original work is properly cited.

1. Introduction

Surface landforms are influenced by various forces, such as natural processes and human activities, over long-term periods of time. Landform is the primary issue that we need to understand while addressing global change and the impact of anthropogenic activities on the environment and the past processes. Landform evolution is an important aspect of Earth Sciences and involves complicated interaction among different physical processes and environmental factors, such as topography, underlying rock types and structures, tectonics, climate, vegetation, and human activities, all occurring over a wide range of spatial and temporal scales. Different landform patterns are derived from tectonic movements and erosion and accumulation in specific meteorological settings. The exogenic meteorological forces control the hydrological conditions, the regional vegetation and fauna, and the mode and efficiency of weathering processes. Preserved and changing landforms recorded and registered the meteorological conditions in the past and at present, and future topographical conditions can be simulated for changing meteorological parameters. The investigation of meteorological impacts on the landform can improve the understanding of characteristics and processes of landform evolution and provide scientific support for the protection of the environment, for the maintenance of functioning rivers in sustainable landscape settings. We invited investigations to contribute original research articles as well as review articles that explored this issue from new aspects and used new methodologies.

2. Climate Change

J. Fei et al. discussed the hypothesis that geological events dramatically affected the weather and environment in China and the Korean Peninsula in historical times. The results of their study suggest that widespread epidemics occurred in the summer and autumn of 1601 AD in China and Korea and they suppose that the Huaynaputina eruption possesses a major burden of responsibility for these concurrent epidemic outbreaks. Then, C. Li et al. take a closer into the characteristics of marine isotope stage 3 (MIS 3) and lake records of upper stream of Yangtze River in Millennial-scale Asian monsoon and the authors suggest that signals of the Dansgaard-Oeschger (DO) events were possibly transmitted to the lake evolution by Asian monsoon.

C. Zhao et al. reconstruct a vegetation succession history, explore vegetation succession responses to climate change (especially during the Holocene Megathermal), and provide evidence for the evaluation of the possible effects of future climate change. The result of their work suggests that vegetation experienced five successions from cold temperature mixed coniferous and broadleaved forest, to forest-steppe, steppe-woodland, steppe, and finally meadow-woodland in Holocene. And the Holocene warm period in NE China (7800–7300 cal yr B.P.) could have resulted in strengthening of precipitation in northernmost NE China and encouraged the development of broadleaved forests. T. Ning et al. analyzed temporal and spatial normalized difference vegetation index (NDVI) changes on the northern Loess Plateau and their correlation with climatic factors from 1998 to 2012. As

a result, they detected positive effects of human activities, including the “Grain for Green” program and successful environmental treatments at coal mining bases, in addition to other factors that improved the vegetation state.

V. Macura et al. focus on determination of the effect of water depth and flow velocity on the quality of an instream habitat in terms of climate change using Instream Flow Incremental Methodology (IFIM). They investigated an optimum ratio of the weights of the flow velocity and water depth for an assessment of the quality of an instream habitat. Furthermore, H. Yao et al. examine the reductions of the runoff and sediment load of the upper Yellow River and separated the effects of climate change and human activities. Their results show that human activities are the major drivers of the runoff and sediment load variations in the Xiliugou basin, while climate change also contributed to the observed reductions.

3. Soil Erosion

N. N. Cheng et al. investigate the impacts of hydrometeorological changes on the evolution of erosive landforms in the Loess Plateau in the past 60 years (1950–2010). The result of their study shows that erosive landforms were largely shaped by hydrometeorological characteristics in comparison with other contributors. It shows that there is strong positive relationship between precipitation and erosion. In addition, C. Wang et al. investigated the sediment budget of the river mouth reach of the Yangtze River. The results demonstrate that the river mouth reach acted as a sink but not as a source due to impoundment measures, which exacerbates the decrease of sediment discharge into the sea. The authors also discuss that uncertainties exist in examination of the sediment processes due to insufficient datasets as well as deficiencies in the methodologies used to calculate changes in river channels.

S. S. Shin et al. propose a new equation of power law based on the rainfall power theory under the ideal assumption that drop-size is uniformly distributed in constant rainfall intensity. In addition, they evaluated rainfall energy through comparing between existing empirical equations and equation of rainfall power. This result supports the conclusion that the rainfall energy equations can be more useful in the development of soil erosion models due to significant increase in sediment yield by increasing transport capacity of surface runoff in the high rainfall intensity. Moreover, H. Yao et al. also suggest that different influences rates of rainfall (climate change, human activities) change to the deviations of runoff and sediment load could be produced by using different categories of annual precipitation. Thus, researchers need to pay attention to the effects of rainfall intensity to avoid overestimating or underestimating the contributions of rainfall changes to the variations of runoff and sediment load. Moreover, a further inspection on the changes flow frequency distribution and the water-sediment indicated that the implementation of soil and water conservation measures should be the main reason for the phenomenon.

H. Sun et al. conducted a set of sensitivity experiments under conditions of low and high orography in the northern

Tibetan Plateau (TP) using a regional climate model with and without the dust module to further discuss the dust distribution and the impacts of dust effects in TP and East Asia. As the condition of the northern TP uplift to present altitude, the effect of dust delays the East Asia summer monsoon onset in the southern and northern monsoon regions and greatly suppresses precipitation in East Asia compared with results in the low terrain experiments.

4. Hydrometeorology

Y. He et al. investigate temporal and spatial variation characteristics of precipitation of flood season. The results show that precipitation is affected by the large-scale circulation patterns. Thus, they show the current trends of precipitation increase in the Yangtze River catchment will likely continue in the future. B. Jun identifies the morphological changes associated with the soil erosion flow and determines the affected area and total volume of debris flow. He revealed both the area affected by the flow and the spatial distribution of sediments with reasonable accuracy for most of the study area, and considerate for technicians dealing with the protection of the mountain area from intense rainfall. Y. Cheng studied the analysis of the effects of precipitation and anthropogenic activity on hydrologic features in Yanhe during 1961 to 2008 in support for regional water management and evaluation of soil and water conservation practices. He shows not only that the monthly distribution of precipitation and runoff and sediment discharge is extremely uneven in the river basin, but also that the precipitation decreased in most seasons except in winter with particularly decreasing precipitation in fall.

Finally, the presented papers cover various fields of research (climate change, soil erosion, hydrometeorology, etc.) impressively highlighting the versatility of the model in general and specifically in the field of landform evolution such as the Riverine HABitat SIMulation (RHABSIM) model which determines the quality of an aquatic habitat based on the preferences of fish for a wider range of discharges; Community Land Model version4 (CLM4) which investigates response of stream flow to land use cover change and climate change; Soil and Water Assessment Tool (SWAT) and Geographic Information System (GIS), and so forth. Moreover, most of the presented studies focus on adverse effects of climate change and anthropogenic activities like Yangtze River, Loess Plateau, and so forth. The individual articles highlight the need of further improvements and developments.

Acknowledgments

We acknowledge with gratitude the research grants kindly provided by the Hundred-Talent Project of the Chinese Academy of Sciences (Dr. H. M. He, 2011009), the Innovation Frontier Project of Institute of Soil and Water Conservation of the Chinese Academy of Sciences (10502), Key Research Program of the Chinese Academy of Sciences (Grant no. KZZD-EW-04), Strategic Priority Research Program of the Chinese Academy of Sciences (Grant no. XDB03020300), the State Key Laboratory of Soil Erosion and Dryland Farming on

the Loess Plateau (10501-192), and the State Key Laboratory of Soil Erosion and Dryland Farming on the Loess Plateau (K318009902-1402).

*Hongming He
Zhongping Lai
Steffen Mischke*

Research Article

The Effects of Climate and Anthropogenic Activity on Hydrologic Features in Yanhe River

Yang Cheng,¹ Hongming He,² Nannan Cheng,^{2,3} and Wenming He⁴

¹Department of Civil and Environmental Engineering, Syracuse University, Syracuse, NY 13210, USA

²State Key Laboratory of Soil Erosion and Dryland Farming on Loess Plateau, Northwest of Agriculture & Forestry University and Institute of Soil and Water Conservation, Chinese Academy of Sciences & Ministry of Water Resources, Yangling, Shaanxi 712100, China

³Graduate University, Chinese Academy of Sciences, Beijing 712100, China

⁴School of Chemistry and Environment, Jiaying University, Guangdong, China

Correspondence should be addressed to Hongming He; hongming.he@yahoo.com

Received 30 April 2015; Revised 2 August 2015; Accepted 6 August 2015

Academic Editor: Olga Zolina

Copyright © 2016 Yang Cheng et al. This is an open access article distributed under the Creative Commons Attribution License, which permits unrestricted use, distribution, and reproduction in any medium, provided the original work is properly cited.

This paper aims to analyze the effects of precipitation and anthropogenic activity on hydrologic features in Yanhe River so as to provide support for regional water management and evaluation of water and soil conservation measures. Thiessen Polygon was created to calculate mean values of watershed, and Mann-Kendall statistic test and Sen's slop estimator test were adapted to analyze variation trend and interaction between precipitation, runoff, and sediment discharge. When 1961~1970 was set as reference period (ignoring human effects), the double mass curve quantified the effects of precipitation and anthropogenic activity on runoff and sediment discharge in Yanhe River during 1961~2008. The result showed that the monthly distribution of precipitation, runoff, and sediment discharge was extremely uneven. 78.1% of precipitation, 64.1% of runoff, and 98.6% of sediment discharge occurred in the flood season. Precipitation, runoff, and sediment discharge performed significant downward trends during 1961~2008. Therein, anthropogenic factors contributed 66.7% and 51.1% to sediment discharge reduction during 1971~1994 and 1995~2008, respectively. They contributed 103.8% and 82.9% to runoff reduction during these two periods, respectively.

1. Introduction

Precipitation variation and anthropogenic activities are major effects on hydrology and soil erosion. Global warming accelerates regional water cycle, changes precipitation intensity and frequency, and therefore affects hydrologic process [1]. The responses of basin hydrology to climate are different over the world. Goode et al. [2] expected sediment yields to increase in response to changing climate in northern Rocky Mountains, USA. Mouri et al. [3] estimated that suspended sediment yield would increase from 8% to 24% per year for the MRI-GCM in response to future climate changing. However, Liu et al. [4] found that precipitation in most weather stations of China have significant reducing trend, and Wang et al. [5] showed that decrease of precipitation induced temporal and spatial decrease of streamflow. Meanwhile, anthropogenic activities for transformation of underlying

surface such as land use change, water conservancy construction, and water and soil conservation measures have both significant effects on water cycle and runoff process. Moreover, human activities have altered the spatial-temporal distribution of water resources [6–8]. Hence, water balance becomes an urgent problem in Loess Plateau under both effects of precipitation variation and human activities. Currently, there are several methods such as watershed comparison, hydrologic modeling, and analysis of time series to quantify hydrologic effects caused by environmental change. Therein, analysis of time series has widespread use in evaluation of environment effect due to its simple use and operability [9]. Through researching streamflow of the mainstream of Yellow River during 1956–2000, Liu and Zhang [10] concluded that effect of precipitation on runoff reduction of upper reaches of the Yellow River accounted for 75%, whereas human activities accounted for 25%; however, precipitation accounted for 43%

and human activities accounted for 57% in middle reaches of the Yellow River. Li [9] found that precipitation and human activities contribute 24% and 76%, respectively, to runoff reduction in Hei He watershed (secondary tributary) during 1972 to 2000. These researches show that runoff has various responses to precipitation and anthropogenic activities by different spatial scales. The considerable attention has been paid to studying the impacts of climate variations and human-induced factors on water resources within a watershed scale [11–17].

Loess Plateau is a region of severest water and soil loss in China. YanHe River is first tributary of Yellow River and it has typical landform of hilly-gully in north part of Loess Plateau. Variation of runoff and sediment discharge to some extent represents the trend of runoff and sediment discharge of the middle reaches of Yellow River because heavy erosion occurred in Yanhe watershed. Climate change impacts on hydrogeomorphological processes are dominated by short and severe rainstorms which accelerated erosion [18]. He et al. [19] also indicated that concurrent flooding in multiple tributary rivers accounted for 67.5% of the total flooding in the middle Yellow River. Numerous studies indicated that the sediment load in many large rivers has been reduced significantly by human activities such as construction of dams, water divisions, and other water stores [20–23]. In the middle of 1980s, sediments of hilly-gully region of Loess Plateau have been significantly decreased due to vegetation practices and engineering measures [24]. Particularly, sediments reduced 81.8% after 2000 compared to past 60 years in the middle reaches of Yellow River [25].

The government had conducted a series of soil and conservation measures in Yanhe River since 1960s. Major measures included vegetation planting, silt dam and reservoir built, and terraced field construction. Moreover, government implemented massive projects of Grain for Green which returned farmland to forest or grassland after 1997. Many researches for effects of water and sediment by management measures concluded that the benefits of these measures significantly appeared around 1971 [14, 26] and the project of Grain for Green in the late 20th century had significantly reduced runoff and sediment discharge [27–29]. Combined with previous studies in small scale watershed such as land use/cover change and meteorological events, it is helpful to quantify the effects of anthropogenic and meteorological factors on runoff and sediment discharge in Yanhe River. The study will support not only water and soil conservation but also sustainable water resource use of Yanhe River.

2. Study Area

Yanhe River is the first-grade tributary flowing of Yellow River and stems from the south of Bai Yu Mountain. It has overall length of 284.4 km and the total area of 7591 km². The river flows through northwest to southeast via Zhi Dan, An Sai, Yan An, and Yan Chang counties. The watershed (36°21′–37°19′N, 108°38′–110°29′E) has several tributaries such as Xi Chuan, Pan Long Chuan, and Nan Chuan, and the average watercourse gradient, average slope,

and average elevation are 3.29‰, 17°, and 1218 m, respectively [30] (this reference is Chinese version with English abstract).

The watershed is located in temperate continental semi-arid monsoon area. The weather is arid, windy, and varying in temperature in spring. In summer, the weather is tepid but has intensive runoff. Compared to the weather of winter which is cold and dry and lasts longer, it is rainy with rapid temperature decreasing in autumn. Interannual precipitation has significant change, and annual mean precipitation is around 500 mm. Particularly, 60% of annual precipitation is coming from July to September and most of it is rainstorm. Average wind speed in watershed is between 1.3 and 3 m/s [30]. Southeaster dominated in summer and northwester prevails in winter. Strong gale of cold wave occurs during spring and winter and is accompanied with rapid temperature change. Average temperature in watershed is 9.4°C and increasing from northwest to southeast. Interannual temperature has substantial change that average daily difference of temperature reaches almost 13°C. Vegetation is distributed in the order of forest, forest steppe, and grass from southeast to northwest [31]. Main soil type is loessal soil; the others are red clay and Heilu soil. Loessal soil is predominately cultivated soil because it is fertile and holding more than 85% area in the watershed [31]. Silt is major constitution of pore-size distribution in loessal soil so that its persistence for erosion is poor and it is easy to disperse and carry. Loessal soils are widespread on the sloping fields. Red soil contains higher content of clay but it is less fertile, is hard for tillage, and has lower permeability. Red soils are widespread on the bottom of trench or slop.

3. Material and Methods

3.1. Data Source. The precipitation data used in the paper come from county-level station of China, including Yan An, An Sai, Zhi Dan, and Yan Chang weather stations and Gan Guyi during 1961 to 2008 (Figure 1). Time series of data processing are defined as flood season (June to September), spring (March to May), summer (June to August), fall (September to November), and winter (December to February). In this study, climate, hydrological, and sediment datasets are used to investigate effects of climate and anthropogenic activity on hydrologic features in Yanhe River in the past 60 years. These include climatic, hydrologic, and topographic datasets (Figure 1). The meteorological datasets of 4 observation stations, which include daily, monthly, and annual precipitation during 1961–2008, were used to illustrate climate change situations in Yanhe River. These datasets were provided by National Meteorological Information Center (NMIC), China Meteorological Administration (CMA). The hydrological datasets of gauge station were used to carry out hydrometeorological analysis and soil erosion as well. These datasets include daily stream-flow and sediment discharge from 1961 to 2008. These datasets were provided by Ecological Environment Database of the Loess Plateau, Chinese Academy of Sciences and Ministry of Water Resources (CAS&MWR). Topographic parameters, such as gully density, slope, aspect, relief, and river network, were extracted

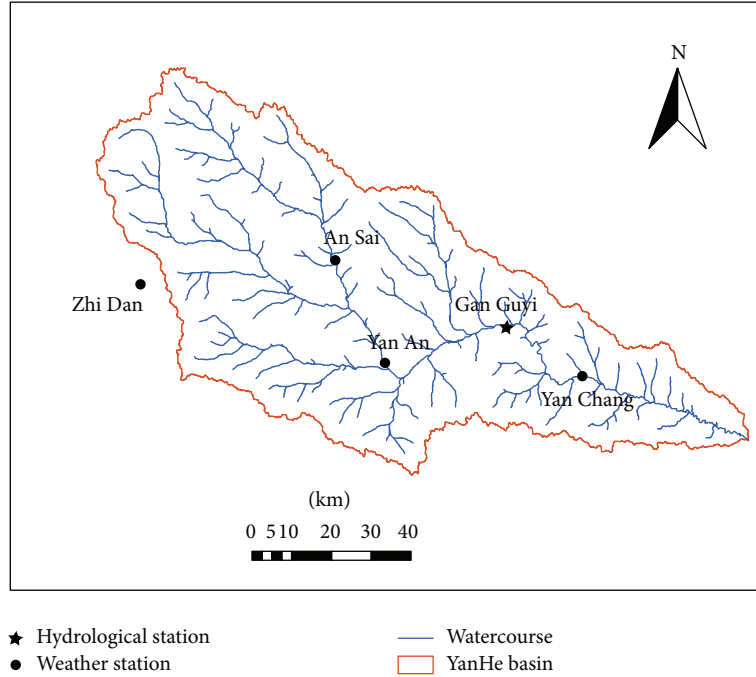


FIGURE 1: Geographic location of the Yanhe River and its meteorological and hydrological stations.

from 30 meters resolution DEM which was downloaded from International Scientific & Technical Data Mirror Site, Computer Network Information Center of Chinese Academy of Sciences.

3.2. Methods. Analysis of precipitation and runoff was based on four observed stations (Figure 1). When it comes to the whole river basin situation, the total runoff and sediment correspond to the total precipitation of the Yanhe River, while in correlation analysis of precipitation, runoff, and sediments at subbasin scales, specific observation datasets were used. Using dataset of a specific gauge station or an average of the whole river basin depends on specific task in data analysis. While the precipitation was never uniformly falling over the entire area of the subbasin but varies in intensity and duration from place to place, Thiessen Polygon method was more suitable than arithmetic mean method, which assigned at each weather station in proportion to the watershed area that is the closest to that station, so as to attain mean rainfall by calculating weighted average. For missing data of precipitation in An Sai weather station in 1962, 1968, and 1969, we interpolated the missing historic precipitation data by using the nearest weather station (Zhao An) which has less than 15 km away from An Sai station. Therefore, effective precipitation data of 48 years in each weather station were ensured.

Mann-Kendall statistical method [32] is applied for trend analysis. In the 2-sided trend test, for given significant α , if $|Z|$ is smaller than $Z_{1-\alpha/2}$, null hypothesis is accepted. If $|Z|$ is greater than $Z_{1-\alpha/2}$, null hypothesis is not accepted; in other words, time series data has significant trend of growth or decrease. The trend would be increased when Z becomes positive and vice versa. The values of 1.28, 1.64, and 2.32 represent confidence of 90%, 95%, and 99%, respectively.

When Mann-Kendall is used for detecting changing point, test statistic is different with Z ; define statistic through

$$S_k = \sum_{i=1}^k \sum_{j=1}^i \alpha_{ij} \quad (k = 2, 3, 4, \dots, n), \quad (1)$$

where

$$\alpha_{ij} = \begin{cases} 1, & x_i > x_j \\ 0, & x_i \leq x_j \end{cases} \quad 1 \leq j \leq i. \quad (2)$$

Then,

$$UF_k = \frac{|S_k - E(S_k)|}{\sqrt{\text{Var}(S_k)}} \quad (k = 1, 2, \dots, n), \quad (3)$$

where

$$E(S_k) = \frac{k(k-1)}{4}; \quad (4)$$

$$\text{Var}(S_k) = \frac{k(k+1)(2k+5)}{72}.$$

UF_i is standard normal distribution. For given confidence α , if $|UF_i| > U_{\alpha/2}$, the sequence has significant trend. To calculate UB_k using the above equation, inverse time sequence, and make $UB_k = -UF_k$ ($k = n, n-1, \dots, 2$) and $UB_1 = 0$, if the curve of UF_k and UB_k has intersection and the point of intersection is located within the critical lines, the corresponding time of intersection point is the time for abrupt change.

Sen [33] developed the nonparametric procedure to estimate the slope of trend in the sample of N pairs of data:

$$Q_i = \frac{x_j - x_k}{j - k} \quad (i = 1, \dots, N), \quad (5)$$

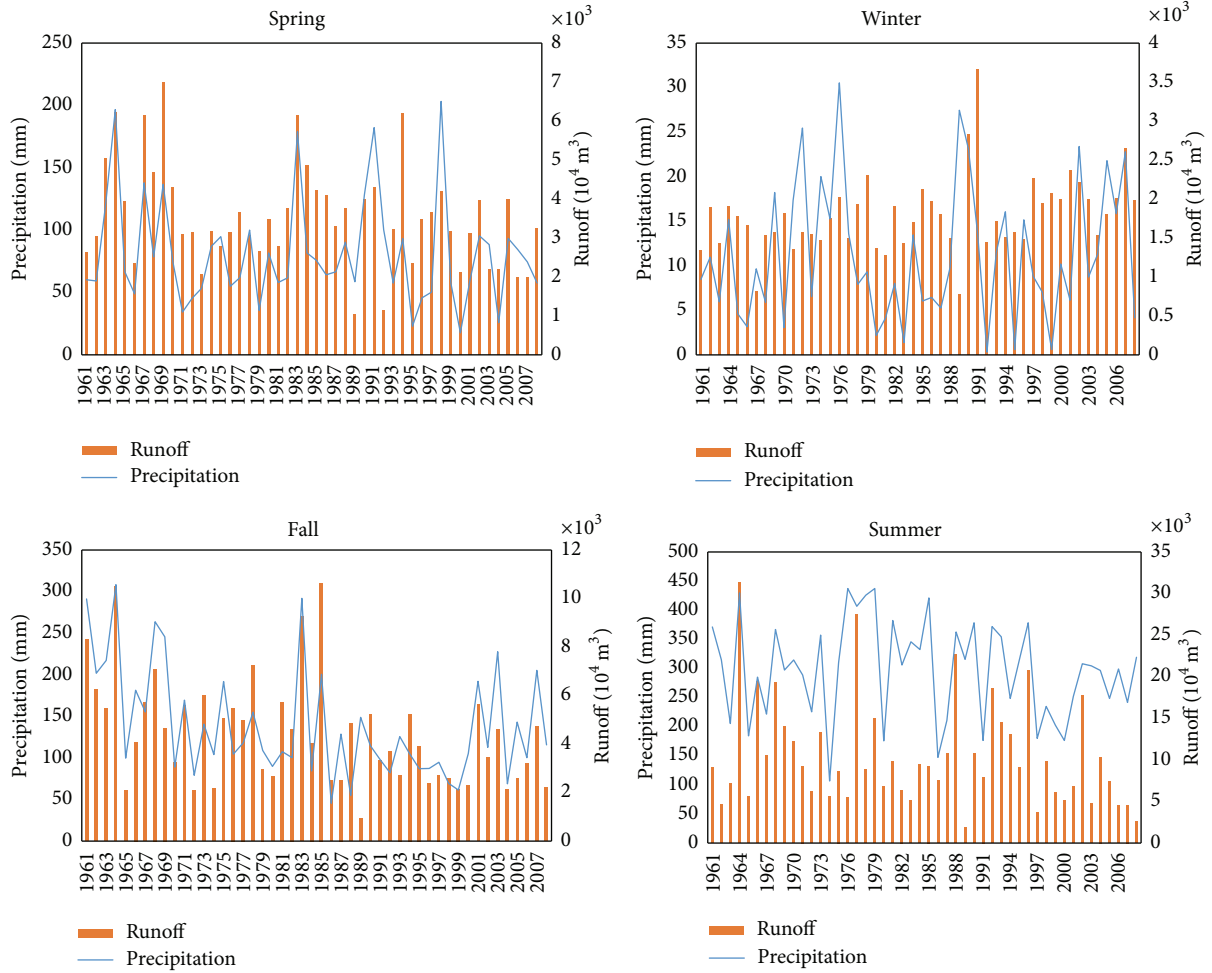


FIGURE 2: Seasonal distribution of runoff and precipitation in the Yanhe River.

where x_j and x_k are the values at times j and k ($j > k$), respectively. The N values of Q_i are ranked from smallest to largest and the median value of Q_i is slope of this datum [34]. Q_{med} is computed as

$$Q_{\text{med}} = \begin{cases} Q_{(n+1)/2}, & \text{if } n \text{ is odd,} \\ \frac{Q_{n/2} + Q_{(n+2)/2}}{2}, & \text{if } n \text{ is even.} \end{cases} \quad (6)$$

Q_{med} does not contain zero and its values indicate the steepness of trend.

The double mass curve is a method to test consistency and variation between two parameters. The double mass curve is a relation line of two variables in the same period drawn in rectangular coordinate system. It is used to test consistency of meteorological elements, interpolate missing values, or data rectification [35, 36].

4. Result and Discussion

4.1. Changing Pattern of Precipitation, Runoff, and Sediment Discharge in Yanhe River from 1961 to 2008. The seasonal distribution of precipitation and runoff in Yanhe River is

extraordinarily uneven (Figure 2). The most of precipitation and runoff occurred in the summer and fall and accounted for 82.5% and 73.8% of annual amount, respectively (Table 1). The precipitation and runoff in summer accounted for 56.2% and 51.7%, and variable coefficients are 0.28 and 0.61, respectively. The precipitation and runoff in fall accounted for 26.3% and 21.1, respectively, and variable coefficients of them are 0.48 and 0.51. Compared with the proportion of precipitation and runoff in summer and fall, however, the proportion of precipitation in other seasons is lower but variable coefficients are higher, and the variable coefficients of runoff in winter and spring are lower which means the runoff of Yanhe River in winter and spring is relatively stable and less affected by precipitation. Base flow from upstream is major contribution to runoff of Yanhe River. In other words, the precipitation is major recharge source of runoff in Yanhe River in summer and fall.

Results of applying trend analysis by Mann-Kendall and Sen's slope estimator statistical tests for seasonal precipitation and runoff over period of 1961–2008 are presented in Table 2. As shown, the precipitation of spring, summer, and fall performed subtly increasing trend in seasonal time scale. Thereinto, the decreasing trend in fall was detected at 95%

TABLE 1: The characteristics of precipitation and runoff at the outlet (river mouth) in Yanhe River.

		Annual	Spring	Summer	Fall	Winter
Precipitation	Maximum (mm)	954	204.6	440	308.7	30.8
	Minimum (mm)	264.6	177	107.3	45.6	0.3
	Average (mm)	531.5	81.8	299.1	139.4	11.3
	Percentage (%)	—	15.4	56.2	26.3	2.1
	Variable coefficient	0.26	0.52	0.28	0.48	0.68
Runoff	Maximum (10^4 m^3)	50206.4	7040.3	31520.2	10650.6	3692
	Minimum (10^4 m^3)	4609.1	1036.3	1859	926.3	787.4
	Average (10^4 m^3)	20291	3566.5	10500.4	4283	1808.5
	Percentage (%)	—	17.6	51.7	21.1	8.9
	Variable coefficient	0.39	0.37	0.61	0.52	0.27

TABLE 2: The results of Mann-Kendall and Sen's slope for precipitation, runoff, and sediment discharge.

	Test	Trend				
		Annual	Spring	Summer	Fall	Winter
Precipitation	Z_s	-2.40	-0.46	-1.08	-2.46	0.46
	Q_{med}	-2.65	-0.12	-1.06	-1.71	0.03
Runoff	Z_s	-2.37	-1.63	-1.80	-3.05	2.85
	Q_{med}	-173.03	-23.33	-87.53	-62.95	10.68
Sediment discharge	Z_s	-2.39	—	—	—	—
	Q_{med}	-57.24	—	—	—	—

confidence level. The precipitation in winter infinitesimal increased 0.03 mm per year. The runoff from Gan Guyi hydrological station showed that the trends were downward except in winter, the runoff in winter significantly increased (2.85), and there was 0.11 million cubic meters increased per year. However, the runoff in spring, summer, and fall had negative trends in about 0.23, 0.87, and 0.62 million m^3 per year decrease, respectively. Thereinto, runoff in summer had negative trend (-1.8) at 95% confidence level, and the runoff in fall had negative trends (-3.05) at 99% confidence level. The reason why runoff in these two seasons (summer and fall) had downward trends was probably because of two aspects: the decreasing of precipitation in these two seasons and the other might be related to human activity such as land cover change and the surged demand of water caused by popularity growth.

The trends of annual precipitation and runoff change were shown in Figure 3. Generally, the variation of precipitation corresponds to runoff changes. The precipitation had decreased between the late 1960s and middle of 1970s. During late 1970s and middle of 1980s, the precipitation had dramatic fluctuation. Its variation became gentle after 1990s. The trend line of precipitation in Figure 3 showed that annual average precipitation was decreasing and annual average decline factor is -3.1 mm/a . In Sen's slope estimator statistic test, the trend of precipitation was detected at rate of -2.65 mm/a . Through nonparametric Mann-Kendall test, M-K rank correlation coefficient of precipitation (-2.40) has 99% confidence which showed that precipitation has significantly reduced trend along with time sequence. The trend of runoff decreased as well and annual average reduction is 1.97 million m^3 . M-K test (-2.37) indicated the decreasing

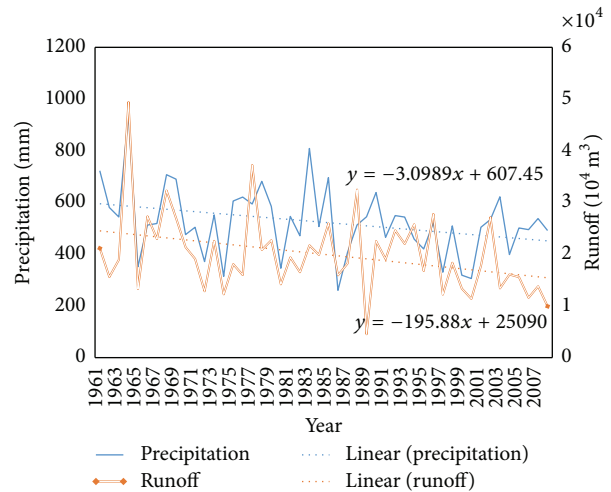


FIGURE 3: Annual precipitation and runoff in the Yanhe River during 1961–2008.

trend is significant within 99% confidence and annual runoff trend in Sen's slope estimator statistic test detected that it was reducing at the rate of 1.73 million m^3 per year.

Figure 4 performed the interannual monthly average variable characters of precipitation, runoff, and sediment discharge. The amount of precipitation was basically concentrated on flood season which accounted for 71.8% of a year. Most of sediment discharge also occurred in flood season which accounted for 98.6%. The distribution of monthly runoff performed the similar distribution of sediment discharge that there was 64.1% runoff occurring in flood season.

TABLE 3: Cumulative area and ratios of human measures in Yanhe River [37].

Year	Terrace		Siltling dam		Afforestation		Grass planting		Total area	
	Area (Km ²)	Ratio	Area (Km ²)	Total ratio						
1959	4.13	8	4.62	9	41.33	82	0.33	1	50.41	0.7
1969	47.2	21	15.83	7	161.27	71	3.73	2	228.03	3
1979	97.53	23	28.73	7	286.93	67	17.47	4	430.66	5.7
1989	174.33	15	37.8	3	840.73	70	145.2	12	1198.06	15.8
1996	275.6	16	41.67	2	1100.2	66	259.87	15	1677.34	22.1
2000	219.6	14	38.1	3	1637.5	67	180.4	16	2577.4	34
2005	285.5	9	49.5	5	2128.8	68	243.5	18	3350.6	44.1

Ratio indicates the ratio of the area in each period and total measured area. Total ratio indicates the ratio of the total measured area and total area of watershed.

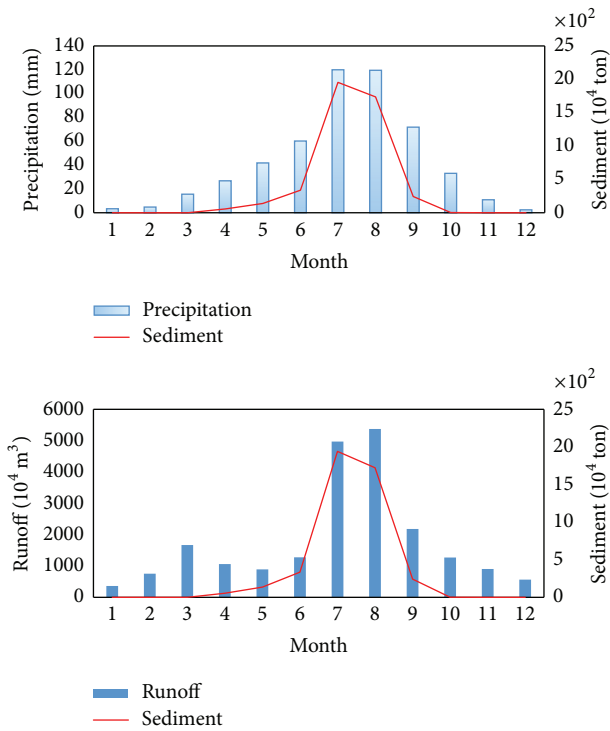


FIGURE 4: The monthly distribution of precipitation, runoff, and sediment discharge in the Yanhe River from 1961 to 2008.

There was a peak of runoff in March which was different with sediment discharge because snow melting in spring causes the rise of runoff. Another phenomenon in Figure 4 was shown that the month of maximum runoff that occurred was not in accord with the time of maximum sediment discharge that occurred. It could be explained that early intensive runoff and precipitation in July had eroded erosive soil particles on watercourse and slope and scoured them out of the outlet. Although the precipitation or runoff was larger than that in later month, the rest of erodible particles were smaller than those eroded in early time so that average sediment discharge in August had reduced. The trends of annual sediment discharge were shown in Figure 5. Sen's slope estimator test performed downward trend and sediment discharge reduced at rate of 57.24 t/a. In M-K statistic test, the trend of

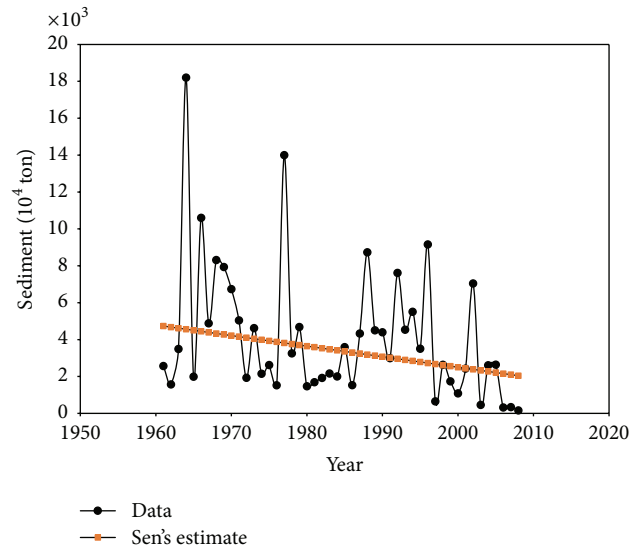


FIGURE 5: The annual sediment discharge at the Gan Guyi station from 1961 to 2008.

sediment discharge had significant reduction (-2.37) within 99% confidence level.

4.2. The Determination of Reference Period and Changing Periodicity. The reference period is defined as the fact that hydrological features and underlying surface in this period are under "nature" background (ignoring human intervention). As mentioned above, the measures of water and soil conservation in Yanhe River had been conducted since 1960s and benefits of these measures appeared around 1971 [14, 26]. Before 1959, the treated area was only 0.7% (Table 3). During 1959–1969, 3% of total area of watershed had been treated which means the effects of humans on underlying surface were negligible. The abrupt changes of runoff and sediment discharge by Mann-Kendall test were shown in Figures 6 and 7. The trend of both runoff and sediment discharge increased before 1971. However, it was going down after 1971. This trend is in accord with the previous results that benefits had appeared around 1971. Therefore, it is reasonable to define reference period during 1961–1970.

The period during 1971–1994 is the period that increased anthropogenic intervention over Yanhe River. During this

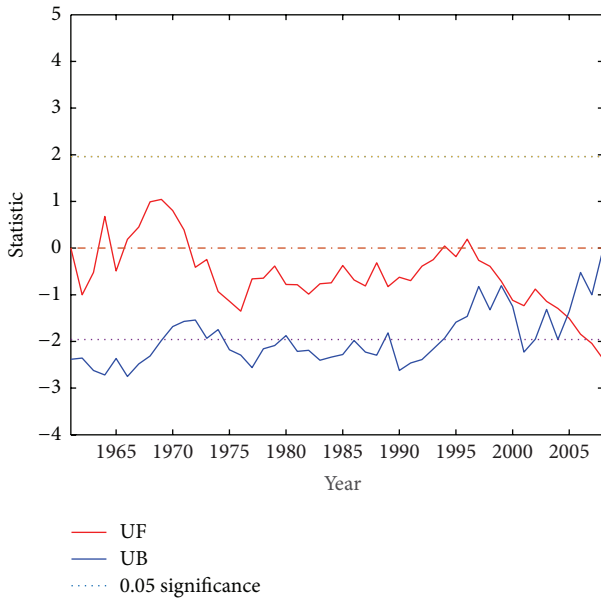


FIGURE 6: Mann-Kendall abrupt change point detection of the runoff.

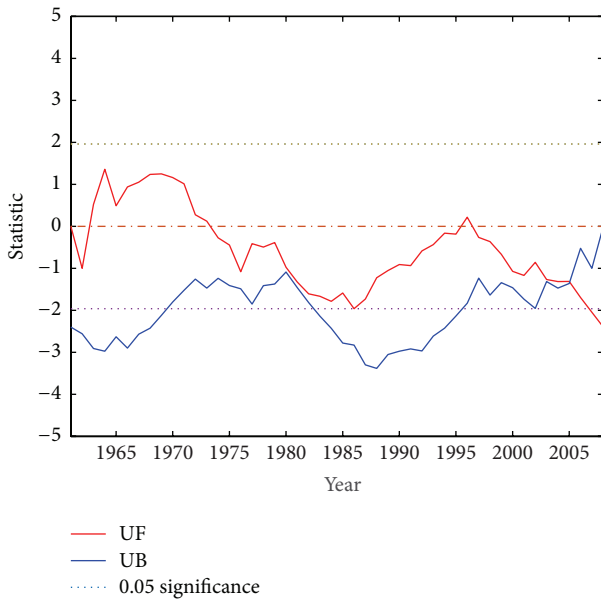


FIGURE 7: Mann-Kendall abrupt change point detection of the sediment discharge.

period, the UF of runoff and sediment discharge decreased until late 1980s and then increased. Continual water and soil conservation measures are the reason that the trend of runoff and sediment discharge decreased. There was 12.8% of Yanhe River watershed that had been treated (Table 3) during 1969–1989 and 6.3% of watershed treatment had been completed during 1990–1996. Although there was 6.3% increment treated, the trend of runoff and sediment discharge still upsurges in last 6 years of the period. In Figure 3, the annual precipitation during 1990–1996 increased. There were

several reasons that might lead to this. One might be that water conservancy facilities such as terrace and silting dams gradually lose their function because of intensive rainfall or being out of repair. Another one could be the implement of Contracted Farmland policy during 1980s. This policy encouraged farmers in cultivating steep slope, deforesting for farmland, and mining.

There were two events that occurred during 1994–2008. One is the project of soil and water conservation in Yanhe River loaned by The World Bank (1994–2001). Another is Grain for Green project proposed by Chinese State Council in late 1990s. During 1994–2008, the runoff and sediment discharge had dramatically decreased (Figures 6 and 7). Kang et al. [38] quantified the benefits of the project of soil and water conservation in Loess Plateau and indicated that there was 549.7 km² area replaced by vegetation. Xie et al. [39] indicated that the area of farmland decreased from 3083.56 km² to 2191.86 km², and the area of forest and grass increased from 4549.78 km² to 5439.97 km² during 1997–2000. The third period during 1994–2008 is the period in which intensive anthropogenic activities were implemented in Yanhe River. The runoff and sediment discharge have their abrupt change points during this period. The abrupt change point of runoff occurred at 2005 and the abrupt change points of sediment discharge occurred at 2003 and 2005. These abrupt change points indicated that the benefits of the projects of water and soil conservation had significantly appeared around 2005.

4.3. *The Effects of Climate and Anthropogenic Activities on Hydrologic Features.* Runoff and sediment discharge changes were both affected by climate change and human activities. To better understand dominant factor in variation of runoff and sediment, and effects of human activities on runoff and sediment, it is necessary to quantify the effects of precipitation and human factor on runoff and sediment. The double mass curves of runoff-precipitation and sediment discharge-precipitation in different period were shown in Figures 8 and 9. The double mass curve of runoff-precipitation in reference period showed the high correlation between runoff and precipitation. The curve should be a straight line in other periods if there were no effects of precipitation and human activity. However, the curve in other periods was not totally consistent with reference period. Therefore, it is necessary to quantify the contribution of either precipitation or anthropogenic effects to runoff and sediment discharge variation. Predicted values in period of 1971–1994 and 1995–2008 could be obtained by using linear regression formula of reference period which represent values under stationary underlying surface. Through the comparison of observed values and predicted values, the quantification of effects of climate and human on hydrologic features was summarized in Table 4. Actual annual average values of runoff during 1971–1994 reduced by 48 million m³ compared to reference period. The effects of precipitation accounted for 33.3% and human activities accounted for 66.7%. Actual annual average values of runoff reduced by 90 million m³ during 1995–2008 compared to reference period. The effects of precipitation

TABLE 4: The effects of precipitation and human factors on hydrological features in Yanhe River.

	Period	Observed value	Predicted value	Annual actual reduction		Effects of precipitation		Effects of human activity	
				Reduction	Percentage	Reduction	Percentage	Reduction	Percentage
Runoff/ 10^8 m^3	1961~1970	2.53	2.53						
	1971~1994	2.05	2.37	0.48	19	0.16	33.3	0.32	66.7
	1995~2008	1.63	2.09	0.9	35.6	0.44	48.9	0.46	51.1
Sediment discharge/ 10^8 t	1961~1970	0.66	0.66						
	1971~1994	0.4	0.67	0.26	0.394	-0.01	-3.8	0.27	103.8
	1995~2008	0.25	0.59	0.41	0.621	0.07	17.1	0.34	82.9

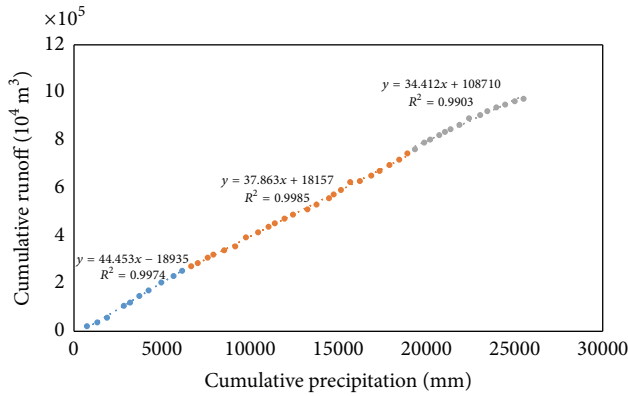


FIGURE 8: The double mass curve of the precipitation-runoff in Yanhe River.

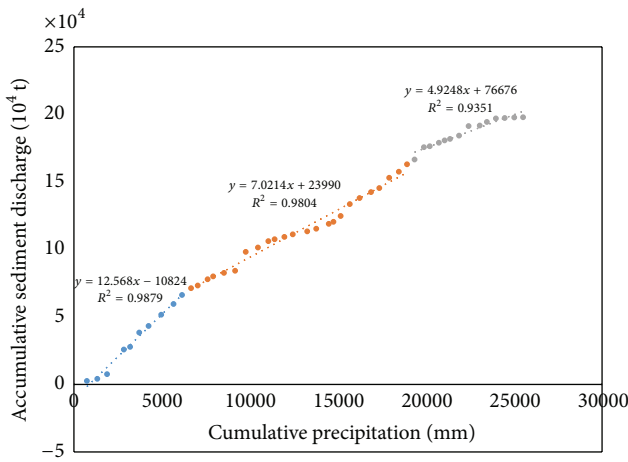


FIGURE 9: The double mass curve of the precipitation-sediment in Yanhe River.

accounted for 48.9% and human activities accounted for 51.1%. For variation of sediment discharge, human activity is a major factor of reduction. The main reason might be the engineered transformation on underlying surface such as Grain for Green project. During 1971–1994, human activities had contributed 103.8% to sediment reduction. They also contributed 82.9% during 1995–2008.

Since Grain for Green projects were conducted after 1998 that improved ability of soil and water storage for grass and forest, the contribution of anthropogenic factors to runoff reduction has reduced. However, excessive demand of increasing population and development of economy for water resource would be a challenge for runoff decline. Facility agriculture and fruit industry become major agricultural production models which acquire more water resource than traditional agriculture. In addition, runoff reduction would aggravate degeneration of natural vegetation and expansion of desertification. Therefore, quantification of effects of human factors on runoff would help improve water resource management for maintaining hydroecological positive cycle. The results of quantification for effects of human activities on

sediment discharge indicate that water and soil conservation measures have achieved significant benefits.

5. Conclusion

The monthly distribution of precipitation, runoff, and sediment discharge was extremely uneven. 78.1% of precipitation, 64.1% of runoff, and 98.6% of sediment discharge occurred in the flood season. Precipitation, runoff, and sediment discharge performed downward trends during 1961–2008. The Mann-Kendall and Sen’s slope estimator test showed that precipitation had decreased trend in seasonal distribution except winter; particularly, precipitation in fall had significantly decreased. Runoff during 1961–2008 performed significantly downward trends in summer and fall and upward trend in winter. Based on previous studies and major anthropogenic events, the periods were divided into three parts. 1961–1970 was set as reference period which was considered that underlying surface of watershed kept relatively stationary. The effects of precipitation and anthropogenic factors during 1971–1994 and 1995–2008 were quantified through comparing with reference period. Thereinto, anthropogenic factors contributed 66.7% and 51.1% to sediment discharge reduction during 1971–1994 and 1995–2008, respectively. They contributed 103.8% and 82.9% to runoff reduction during these two periods, respectively. The abrupt change points of runoff and sediment discharge appeared around 2005. This indicates that benefits of Grain for Green projects were significantly achieved.

The selection of reference period is important since it would affect the results in quantification of other factors. Therefore, combination with previous studies in Yanhe River would improve the accuracy for reference period selection. In addition, effects on hydrologic features are complicated. Other meteorological elements such as temperature in this paper were not considered which might impact the accuracy of evaluating effects of meteorological and human activity on the hydrologic elements. Coupling more related factors in studying climate hydrology and anthropogenic effects at watershed scale is further goal in the research.

Conflict of Interests

The authors declare that there is no conflict of interests regarding the publication of this paper.

Acknowledgment

The authors acknowledge with gratitude the research grants kindly provided by the Hundred-talent Project of the Chinese Academy of Sciences (20110009, Dr. Hongming He), the Key Research Program of Chinese Academy of Sciences (KZZD-EW-04), Innovation Frontier Project of Institute of Soil and Water Conservation of the Chinese Academy of Sciences, and State Key Laboratory of Soil Erosion and Dryland Farming on the Loess Plateau (10501-192).

References

- [1] IPCC, *Climate Change 2007: Synthesis Report. Contribution of Working Groups I, II and III to the Fourth Assessment Report of the Intergovernmental Panel on Climate Change*, Cambridge University Press, Cambridge, UK, 2007.
- [2] J. R. Goode, C. H. Luce, and J. M. Buffington, "Enhanced sediment delivery in a changing climate in semi-arid mountain basins: implications for water resource management and aquatic habitat in the northern Rocky Mountains," *Geomorphology*, vol. 139-140, pp. 1-15, 2012.
- [3] G. Mouri, V. Golosov, S. Chalov et al., "Assessment of potential suspended sediment yield in Japan in the 21st century with reference to the general circulation model climate change scenarios," *Global and Planetary Change*, vol. 102, pp. 1-9, 2013.
- [4] Q. Liu, Z. Yang, and B. Cui, "Spatial and temporal variability of annual precipitation during 1961-2006 in Yellow River Basin, China," *Journal of Hydrology*, vol. 361, no. 3-4, pp. 330-338, 2008.
- [5] H. Wang, Z. Yang, Y. Saito, J. P. Liu, and X. Sun, "Interannual and seasonal variation of the Huanghe (Yellow River) water discharge over the past 50 years: connections to impacts from ENSO events and dams," *Global and Planetary Change*, vol. 50, no. 3-4, pp. 212-225, 2006.
- [6] T. Jiang, T. Fischer, and X. X. Lu, "Larger Asian rivers: climate change, river flow, and watershed management," *Quaternary International*, vol. 226, no. 1, pp. 1-3, 2010.
- [7] P. C. D. Milly, K. A. Dunne, and A. V. Vecchia, "Global pattern of trends in streamflow and water availability in a changing climate," *Nature*, vol. 438, no. 7066, pp. 347-350, 2005.
- [8] Y. Wang, Y. J. Ding, B. S. Ye, F. J. Liu, J. Wang, and J. Wang, "Contributions of climate and human activities to changes in runoff of the Yellow and Yangtze rivers from 1950 to 2008," *Science China Earth Sciences*, vol. 56, no. 8, pp. 1398-1412, 2013.
- [9] Z. Li, W. Z. Liu, F. L. Deng et al., "Effects of climate change and human activities on runoff in loess region," *Journal of Ecology*, vol. 30, no. 9, pp. 2379-2386, 2010 (Chinese).
- [10] C. M. Liu and X. C. Zhang, "Genetic analysis of decreasing water flow in mainstream of the Yellow River," *Journal of Geography*, vol. 59, no. 3, pp. 323-330, 2004 (Chinese).
- [11] Y. Zhang, D. Guan, C. Jin, A. Wang, J. Wu, and F. Yuan, "Analysis of impacts of climate variability and human activity on streamflow for a river basin in northeast China," *Journal of Hydrology*, vol. 410, no. 3-4, pp. 239-247, 2011.
- [12] Z. Ma, S. Kang, L. Zhang, L. Tong, and X. Su, "Analysis of impacts of climate variability and human activity on streamflow for a river basin in arid region of northwest China," *Journal of Hydrology*, vol. 352, no. 3-4, pp. 239-249, 2008.
- [13] P. C. D. Milly, J. Betancourt, M. Falkenmark et al., "Climate change—stationarity is dead: whither water management?" *Science*, vol. 319, no. 5863, pp. 573-574, 2008.
- [14] X. Mu, C. Basang, Z. Lu, P. Gao, F. Wang, and X. Zhang, "Impact of soil conservation measures on runoff and sediment in Hekou-Longmen region of the Yellow River," *Journal of Sediment Research*, no. 2, pp. 36-41, 2007 (Chinese).
- [15] X. Mu, L. Zhang, T. R. McVicar, B. Chille, and P. Gau, "Analysis of the impact of conservation measures on stream flow regime in catchments of the Loess Plateau, China," *Hydrological Processes*, vol. 21, no. 16, pp. 2124-2134, 2007.
- [16] H. Tao, M. Gemmer, Y. G. Bai, B. D. Su, and W. Y. Mao, "Trends of streamflow in the Tarim River Basin during the past 50 years: human impact or climate change?" *Journal of Hydrology*, vol. 400, no. 1-2, pp. 1-9, 2011.
- [17] J. Q. Zhai, B. D. Su, V. Krysanova, T. Vetter, C. Gao, and T. Jiang, "Spatial variation and trends in PDSI and SPI indices and their relation to streamflow in ten large regions of China," *Journal of Climate*, vol. 23, no. 3, pp. 649-663, 2010.
- [18] H. He, J. Zhou, M. R. Peart, J. Chen, and Q. Zhang, "Sensitivity of hydrogeomorphological hazards in the Qinling Mountains, China," *Quaternary International*, vol. 282, pp. 37-47, 2012.
- [19] H. He, J. Zhou, Q. Yu, Y. Q. Tian, and R. F. Chen, "Flood frequency and routing processes at a confluence of the middle Yellow River in China," *River Research and Applications*, vol. 23, no. 4, pp. 407-427, 2007.
- [20] J. P. M. Syvitski, C. J. Vörösmarty, A. J. Kettner, and P. Green, "Impact of humans on the flux of terrestrial sediment to the global coastal ocean," *Science*, vol. 308, no. 5720, pp. 376-380, 2005.
- [21] X. L. Yue, X. M. Mu, G. J. Zhao, H. B. Shao, and P. Gao, "Dynamic changes of sediment load in the middle reaches of the Yellow River basin, China and implications for eco-restoration," *Ecological Engineering*, vol. 73, pp. 64-72, 2014.
- [22] G. J. Zhao, P. Tian, X. M. Mu, J. Y. Jiao, F. Wang, and P. Gao, "Quantifying the impact of climate variability and human activities on streamflow in the middle reaches of the Yellow River basin, China," *Journal of Hydrology*, vol. 519, pp. 387-398, 2014.
- [23] G. M. Kondolf, Y. Gao, G. W. Annandale et al., "Sustainable sediment management in reservoirs and regulated rivers: Experiences from five continents," *Earth's Future*, vol. 2, no. 5, pp. 256-280, 2014.
- [24] Q. Yan, T. Lei, C. Yuan et al., "Effects of watershed management practices on the relationships among rainfall, runoff, and sediment delivery in the hilly-gully region of the Loess Plateau in China," *Geomorphology*, vol. 228, pp. 735-745, 2015.
- [25] Yellow River Conservancy Commission of MWR, *Yellow River Sediment Bulletin*, China WaterPower Press, Beijing, China, 2008 (Chinese).
- [26] P. Gao, X. Zhang, X. Mu, F. Wang, R. Li, and X. Zhang, "Trend and change-point analyses of streamflow and sediment discharge in the Yellow River during 1950-2005," *Hydrological Sciences Journal*, vol. 55, no. 2, pp. 275-285, 2010 (Chinese).
- [27] H. Xie, R. Lee, Q. Yang et al., "Effect of returning farmland to forest (pasture) and changes of precipitation on soil erosion in the Yanhe Basin," *Scientia Agricultura Sinica*, no. 2, pp. 569-576, 2009.
- [28] Z. Lian, P. Liu, C. Chen et al., "Effects of sediment reduction by restoration on the loess plateau," *Bulletin of Soil and Water Conservation*, vol. 1, pp. 10-13, 2008 (Chinese).
- [29] X. He, Y. Gao, and Z. Zhu, "The simulation of spontaneous restoration of vegetation spatial pattern in the Yanhe River Catchment," in *Proceedings of the 4th International Yellow River Forum on Ecological Civilization and River Ethics*, vol. 2, pp. 148-155, Zhengzhou, China, 2010.
- [30] L. Qiu, *Evaluation of Impacts of the Climatic Variable Changes and Human Activity on the Runoff and Sediment in the Yanhe Watershed*, Northwest A & F University, Yangling, China, 2012.
- [31] Z. Zhou, *The Coupling Analysis of Landscape Pattern and Hydrological Process in Yanhe Watershed*, Shaanxi Normal University, Xi'an, China, 2014.
- [32] H. B. Mann, "Nonparametric tests against trend," *Econometrica*, vol. 13, no. 3, pp. 245-259, 1945.

- [33] P. K. Sen, "Estimates of the regression coefficient based on Kendall's tau," *Journal of the American Statistical Association*, vol. 63, no. 324, pp. 1379–1389, 1968.
- [34] D. A. Burns, J. Klaus, and M. R. McHale, "Recent climate trends and implications for water resources in the Catskill Mountain region, New York, USA," *Journal of Hydrology*, vol. 336, no. 1-2, pp. 155–170, 2007.
- [35] X. Mu, X. Zhang, P. Gao et al., "Theory of double mass curves and its applications in hydrology and meteorology," *Journal of China Hydrology*, vol. 30, no. 4, pp. 47–51, 2010 (Chinese).
- [36] X. M. Mu, X. Q. Zhang, P. Gao, and F. Wang, "Theory of double mass curves and its applications in hydrology and meteorology," *Journal of China Hydrology*, vol. 30, no. 4, pp. 47–51, 2010 (Chinese).
- [37] C. Lee, H. Wang, F. Yu et al., "Impact of soil and water conservation on runoff and sediment in Yanhe River Basin," *Science of Soil and Water Conservation*, no. 1, pp. 1–8, 2011 (Chinese).
- [38] L. Kang, Y. Wei, Y. Wang, and W. Yao, "Preliminary opinions on ecological benefits of eco-environment construction of soil and water conservation on Loess Plateau," *Chinese Journal of Eco-Agriculture*, vol. 12, no. 4, pp. 198–200, 2004 (Chinese).
- [39] H. Xie, R. Li, Q. Yang, J. Li, and W. Liang, "Effect of returning farmland to forest (pasture) and changes of precipitation on soil erosion in the yanhe basin," *Journal of Scientia Agricultura Sinica*, vol. 42, no. 2, pp. 569–579, 2009 (Chinese).

Research Article

Coupling Analysis of Hydrometeorology and Erosive Landforms Evolution in Loess Plateau, China

N. N. Cheng,^{1,2} H. M. He,^{1,3} Y. J. Lu,³ and S. Y. Yang⁴

¹State Key Laboratory of Soil Erosion and Dryland Farming on the Loess Plateau, Institute of Soil and Water Conservation, CAS and MWR, Yangling, Shaanxi 712100, China

²University of Chinese Academy of Sciences, Beijing 100049, China

³Institute of Soil and Water Conservation, Northwest A&F University, Yangling, Shaanxi 712100, China

⁴Department of Forestry, Mississippi State University, Starkville, MS 39759, USA

Correspondence should be addressed to H. M. He; hongming.he@yahoo.com

Received 30 April 2015; Accepted 14 July 2015

Academic Editor: Pedro Salvador

Copyright © 2016 N. N. Cheng et al. This is an open access article distributed under the Creative Commons Attribution License, which permits unrestricted use, distribution, and reproduction in any medium, provided the original work is properly cited.

The purpose of this study is to investigate hydrometeorology changing patterns impacts on erosive landforms evolution in Loess Plateau in the past 60 years (1950–2010). We firstly describe hydrometeorology changing patterns (rainfall-runoff-soil erosion response) at different time scales (daily, monthly, and yearly) in perspective of river basins and then further investigate hydrometeorology impacts on erosive landform through combined analysis of statistical quantification and proposed conceptual model of rainfall-runoff-soil erosion landform. Through the above investigations, the following findings are achieved. Firstly, it shows that annual runoff and sediment discharges decreased obviously although precipitation remained at the same level in the past 50 years (1960–2010). Discharges of annual runoff and sediment decreased by 30%–80% and 60%–90%, respectively. Secondly, contributors of soil erosion are determined by integrated factors such as precipitation, river network, and topography characteristics of river basins. The strong soil erosion area existed in the middle hilly-gully region, while the high precipitation was in southern mountains. Thirdly, erosion landform development was largely shaped by hydrometeorology characteristics in comparison with other contributors. It shows that there is strong positive relationship between precipitation and erosion.

1. Introduction

Soil erosion has been one of the most triggering environmental issues for decades for its destructive effects [1–7]. Soil erosion deteriorates natural environment and socioeconomic properties as well, such as soil quality, agricultural production, ecosystem stability, and Loess of socioeconomic properties [8–10]. Soil erosion, which is classified into different categories (water, wind, glacier, gravity, and human erosions), is caused by contributors such as climate (e.g., rainfall), topography (slope, river network), vegetation and land use cover, and human activities. Soil erosion patterns changed with the changes of these contributors. For example, Mediterranean environments in Spain have become more prone to soil erosion [11], Alpine areas have a high risk for soil erosion associated with the extreme climatic and topographic conditions, and sediments of Mississippi River, Nile River,

and Mekong River also changed significantly during the last several decades [12–16] because of climate change and human activities [17–19]. Sediment yield is primarily controlled by plan curvature and highest-order channel length, followed by hypsometric integral, rainfall, basin relief, and so forth. In Loess Plateau, watershed shape parameters and relief parameters are the major factors that affect sediment yield [20]. With construction of dams and reservoirs, watershed longitudinal linkages are weakened which caused decrease of sediment yield, while natural vegetation clearance and mining activity reduce resistance of land surface and enhance the effectiveness of flow on sediments, thus increasing sediment yield [21, 22]. In Loess Plateau, precipitation decrease is the main reason for reduction of sediment transport, and their spatiotemporal patterns are consistent in the last several decades. Contribution rate of human activities is 61%–93%

to decrease of sediment discharge in 10 tributaries of Yellow River's middle reach [23].

Various approaches were developed to investigate soil erosion and its related issues, including field observation, laboratory test, quantitative analysis, and model simulation [13, 24]. Field observations provide the first hand data for soil erosion investigations [21, 25]. Mathematical statistics mainly focus on the trend analysis, test of observed streamflow, and precipitation, which include parametric and nonparametric tests. Nonparametric tests are generally used to quantify hydrological parameters; for example, Mann-Kendall Test has been widely used for trend analysis [26–30]. Geographic statistics is mainly used for spatial distribution analysis of observed data. However, the statistical methods cannot reveal the physical process and relations of hydrological parameters and explain the reasons of change. As a result, mathematical and hydrological models have been widely used. Hydrological models are commonly applied to effectively and efficiently analyze changes of hydrological parameters and their response to climate change, human activities, and landform evolution. Soil and Water Assessment Tool (SWAT) model, Distributed Biosphere-Hydrological (DBH) model, and Community Land Model (CLM4) version 4 were often used to investigate response of streamflow to LUCC, climate change, and human activities [31]. The Universal Soil Loss Equation [32] and its successors, the Revised Universal Soil Loss Equation (RUSLE), are by far the most often used models for soil erosion predictions. USLE and WEPP were used to study fluctuations of soil erosion on the influence of rainfall, vegetation coverage, conservation measures, and land use [33–36].

Loess Plateau has been experiencing severe soil erosion for decades influenced by climatic change, hydrology change, and human activities [37–40]. Previous investigations show that rainfall density played an important role in soil erosion process compared to other features in Loess Plateau [41, 42]. Land use is critical in controlling soil erosion in this area [43, 44], and it was reported that soil erosion decreased dramatically with the increase of vegetation cover during the past decades in Loess Plateau. Soil erosion intensity, process, and mechanism are influenced by topographic factors such as slope, water velocity, amount of penetration, and runoff amount in Loess Plateau [20, 45–49]. Soil erosion closely related to the sediment transportation in the middle Yellow River. Changes of sediment in the mainstreams of the middle Yellow River reflected the changes of soil erosion in Loess Plateau [50]. These investigations provide abundant background knowledge in soil erosion in Loess Plateau. However, these studies mainly focus on spatiotemporal characteristics of soil erosion and climate change at large scales and rainfall and erosion process at watershed scale. Interaction between hydrometeorology and erosive landform evolution in Loess Plateau remains unclear. Coupling response of soil erosion and landform evolution has not been quantitatively analyzed in detail, especially in Loess Plateau. Therefore, it is necessary to carry out coupling analysis and quantitative investigation of hydrometeorology and erosive landform evolution in Loess Plateau. The purpose of this study is to investigate hydrometeorology changing patterns impacts on erosive landforms

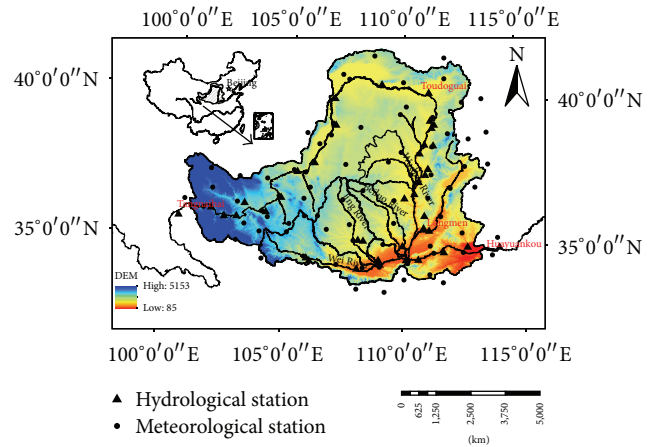


FIGURE 1: Sketch map and DEM of the study area (Loess Plateau) (triangle, hydrological gauged stations; rectangle, meteorological station).

evolution in Loess Plateau in the past 60 years (1950–2010) through combined analysis of statistical quantification and proposed conceptual model of rainfall-runoff-soil erosion landform. We firstly describe hydrometeorology changing patterns (rainfall-runoff-soil erosion response) at different time scales (hourly, daily, monthly, and yearly) from the perspective of river basins and then analyze hydrometeorology and erosive landforms evolution.

2. Study Area

The Loess Plateau (100°54' to 114°33'E and 33°43' to 41°16'N) which covers 624,000 km² with over 60% subjected to soil and water losses is mainly located in the middle reaches of the Yellow River (3943 km) (Figure 1). The average annual precipitation on the Loess Plateau ranges from 250 mm to 600 mm, which gradually increases from northwest to southeast. Precipitation of rainy season (from June to September) accounts for 60–70% of the total of the year. Heavy rain in form of rainstorms occurs frequently in rainy season which causes flood and severe soil erosion. Strong erosion forms specific geomorphologic features with many gullies and fragmented landforms in Loess Plateau. Tableland (Yuan), ridges (Liang), and hills (Mao) are typical erosion landforms of Loess Plateau. Gully erosion accounts for more than 80% of the soil erosion in this area. Gully density and segmentation of the ground are as high as 8 km/km², and segmentation of the ground is about 43.7% in some area. The average erosion modulus reaches 5000–10000 t·km⁻²·a⁻¹, sometimes even reaching to 20000–30000 t·km⁻²·a⁻¹, and it decreased to 2205.4 t·km⁻²·a⁻¹ in He-Long region in 2011 [51]. The sediment discharge of He-Long section of Yellow River was about 3.1 × 10⁸ t during 1980–2010 and 1.6 × 10⁸ t during 2000–2010 [51]. Vegetation destruction was one of the key contributors to soil erosion in Loess Plateau for decades because of improper human activities (such as cultivation, deforestation, and development of economy). However, it improved a lot after implementation of Grain-for-Green

Project in 1990s with increase of grassland cover (30.5% of the total) and forest (12.0% of the total) in Loess Plateau. What is more, the vegetation improved after a large number of ecological engineering projects such as check dams, terraces, and reforestation were implemented.

3. Materials and Methodology

3.1. Data Sources and Materials. In this study, precipitation and hydrology datasets were obtained from the hydrological and meteorological stations of Loess Plateau (Figure 1), and topographic datasets were extracted from digital elevation model (DEM). All these datasets are used to investigate hydrometeorology changing patterns impact on erosive landforms evolution in Loess Plateau in the past 60 years. The meteorological datasets of 76 observation stations, which include daily, monthly, and annual precipitation during 1960–2011, were used to illustrate situations of climate change and human activities in Loess Plateau. Precipitation datasets are further trimmed and classified as erosive precipitation and rainstorms in terms of rainfall intensity. For example, an erosive precipitation is defined when daily precipitation is equal or larger than 12 mm/d [52], while it is defined as rainstorm if daily precipitation is equal or larger than 50 mm/d. These datasets were provided by National Meteorological Information Center (NMIC), China Meteorological Administration (CMA). The hydrological datasets of 41 gauge stations were used to carry out hydrometeorological analysis and soil erosion as well. These datasets include daily streamflow and sediment discharge from 1960 to 2011. Among these 41 gauges stations, 5 stations are located in the mainstream of the middle Yellow River, including Tangnaihui, Toudaoguai, Longmen, Tongguan, and Huayuankou, which will be emphasized in this study. These datasets were provided by Ecological Environment Database of Loess Plateau, Chinese Academy of Sciences and Ministry of Water Resources (CAS&MWR). Topographic parameters, such as gully density, slope, relief amplitude (RDLS), and river network, were extracted from 30-meter resolution DEM which was downloaded from International Scientific and Technical Data Mirror Site, Computer Network Information Center of Chinese Academy of Sciences.

3.2. Analysis of Hydrometeorological Spatiotemporal Distribution. Hydrometeorological spatiotemporal distribution patterns were analyzed by using Mann-Kendall Test (Mann, 1945; Kendall, 1975), Geographic Information System approaches, for example, Inverse Distance Weighted (IDW) [53]. Mann-Kendall Test is applied for detecting changing points in hydroclimatic time series. Meanwhile, temporal characteristics and relationships of precipitation, runoff and sediment in Loess Plateau, and the middle Yellow River basin were also described by Mann-Kendall Test. Changing patterns of climatic and hydrologic spatial distributions were illustrated by spatial interpolation technique, the Inverse Distanced Weighted (IDW). Topographic parameters were further analyzed after extraction from DEM, such as gully density, slope, aspect, relief, and river network, which were

extracted from 30-meter resolution DEM. In comparison, soil erosion landforms in different river basins were characterized through these topographic parameters.

3.3. Erosive Landform Evolution Index for Soil Erosion and Landform Evolution. To quantify soil erosion contributors to landform evolution, we proposed an Erosive Landform Evolution Index (ELEI) for description of soil erosion and landform evolution in Loess Plateau. Considering the complexity of landforms and contributors to soil erosion, those parameters of gully density, relief amplitude (RDLS), and hilly slope are chosen to quantify landform changes, and precipitation, runoff, and sediment are defined as primary parameters of soil erosion. Landform evolution change (Ev_{landform}) is function of gully length (L_g), relief amplitude (A_r), and hilly slope (S_h). Soil erosion intensity (Er_{landform}) is function of precipitation (P), runoff (R), and sediment transportation (S). Erosive Landform Evolution Index (ELEI) is function of landform evolution change (Ev_{landform}) and soil erosion intensity (Er_{landform}). By using the principal components analysis (PCA), we can select comprehensive factors for landform evolution change (Ev_{landform}) and soil erosion intensity (Er_{landform}) from parameters of Erosive Landform Evolution Index (ELEI) and climate factors and establish functions for landform evolution change (Ev_{landform}) and soil erosion intensity (Er_{landform}). Meanwhile, we can also build the function between Ev_{landform} and Er_{landform} by using linear regression analysis:

$$\begin{aligned} Ev_{\text{landform}} &= F(L_{\text{gully}}, A_{\text{relief}}, S_{\text{hilly}}), \\ Er_{\text{landform}} &= G(P, R, S), \\ ELEI &= H(F, G). \end{aligned} \quad (1)$$

According to referenced geomorphological mapping taxonomy, it defines RDLS as flat (0–20 m), small (20–75 m), middle (75–300 m), mountain (300–600 m), and high mountain (>600 m). On the basis of characteristics of DEM in Loess Plateau, the slope can be defined as 5 grades (<3°, 3~7°, 7~15°, 15~25°, and >25°). In this study, we calculated percentages of different RDLS and slope.

4. Results

4.1. Changing Patterns of Rainfall-Runoff-Soil Erosion Process in the Loess Plateau (1950–2010). Changes of precipitation, runoff, and sediment displayed different patterns during the past 60 years (1950–2010). Although annual precipitation had no obvious change, average annual runoff has decreased by 30%–80%, and sediment discharge has decreased by 60%–90% in 2000s in comparison with those in 1960s. Figure 2 displays distribution of annual rainfall, rainfall erosivity (rainfall erosivity is the kinetic energy of raindrop's impact and the rate of associated runoff, $\text{MJ}\cdot\text{mm}\cdot\text{ha}^{-1}\cdot\text{h}^{-1}\cdot\text{yr}^{-1}$), and specific soil yield (SSY refers to sediment export per unit area, $\text{Mg}\cdot\text{km}^{-2}\cdot\text{y}^{-1}$) from 1960 to 2010. It shows that only four stations in the west and north part indicate increasing trend (0–1.7 $\text{mm}\cdot\text{y}^{-1}$), and all the other stations present downward

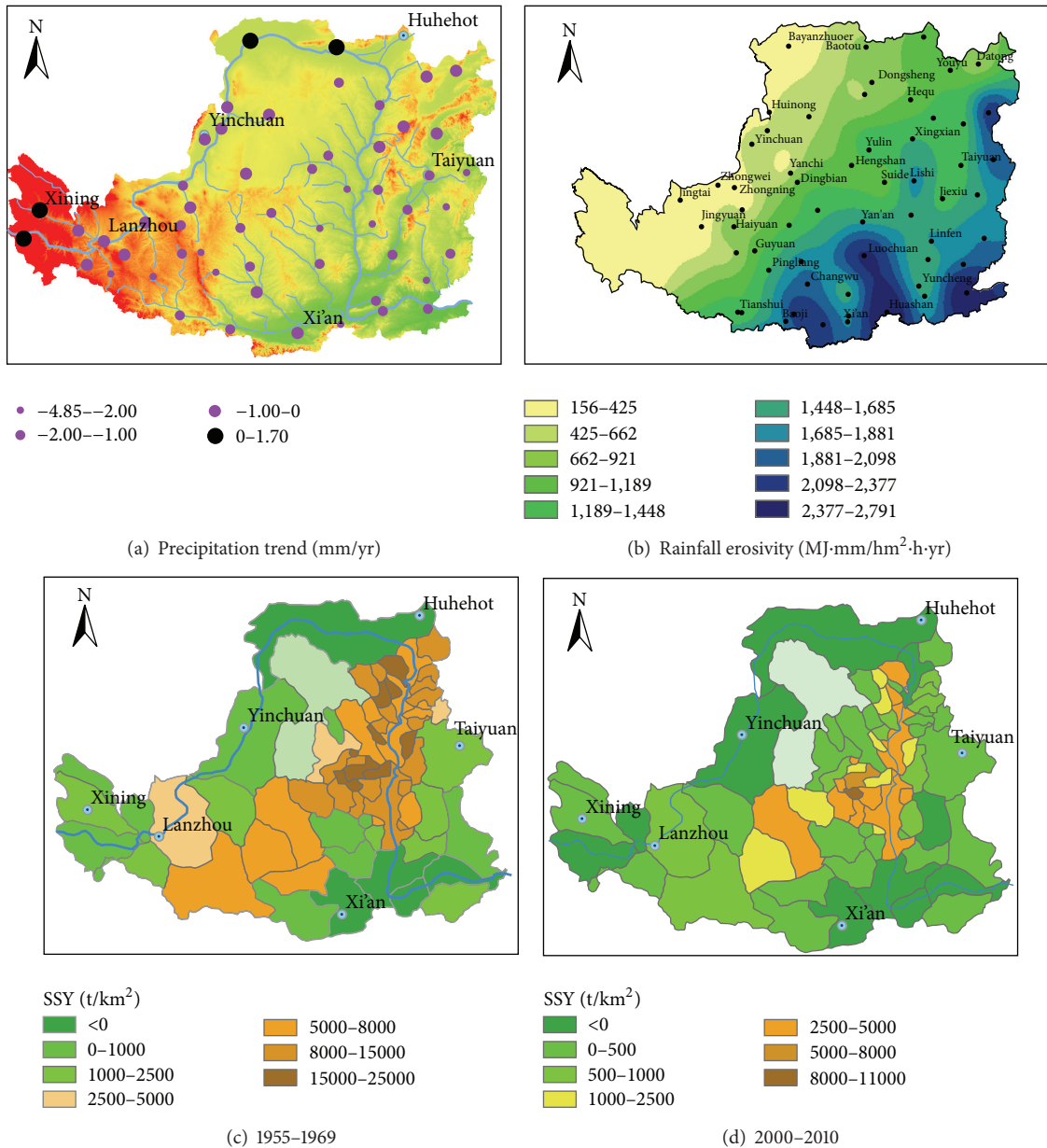


FIGURE 2: Distribution of precipitation, rainfall erosivity, and specific soil yield (SSY) in Loess Plateau (modified after [37]). ((a) Precipitation trend distribution map, (b) rainfall erosivity distribution map, (c) specific soil yield distribution map (1955-1969), and (d) specific soil yield distribution map (2000-2009)).

trend ranging from -4.85 mm to -0.02 mm, particularly near Lanzhou and Yinchuan cities as well as the northeast of Loess plateau [37]. Further, through the Mann-Kendall Test, the change points of annual precipitation usually occur in late 1980s, and annual precipitation increased slightly after change points (Figure 3). Annual runoff of all hydrological stations decreased at 99% confidence interval during the past 50 years, and the significant change often began after 1980s ($p = 0.01$) through the Man-Kendall Test. Spatial distribution of average annual Specific Sediment Yield on Loess Plateau within the two periods. During the period from 1955 to 1969, the most severe soil erosion regions with SSY higher than

$8,000 \text{ Mg}\cdot\text{km}^{-2}\cdot\text{y}^{-1}$ lie in the section between Toudaoguai and Longmen stations (Figure 1), which is also called “the Coarse Sandy Hilly Catchments” [19]. This region covers an area of $7.86 \times 10^4 \text{ km}^2$, accounting for only 14.8% of the whole Yellow River basin but producing nearly 80% of the coarse sediment to the Yellow River [37]. Obviously, heavy rain causes increase in runoff and the tendencies of them are consistent, but the impact of precipitation is postponed because of runoff and flood process. In Loess Plateau, more than 50% of annual precipitation and runoff concentrate during the rainy season (June, July, August, and September), and soil erosion is mainly caused by heavy rainfall (Figure 4).

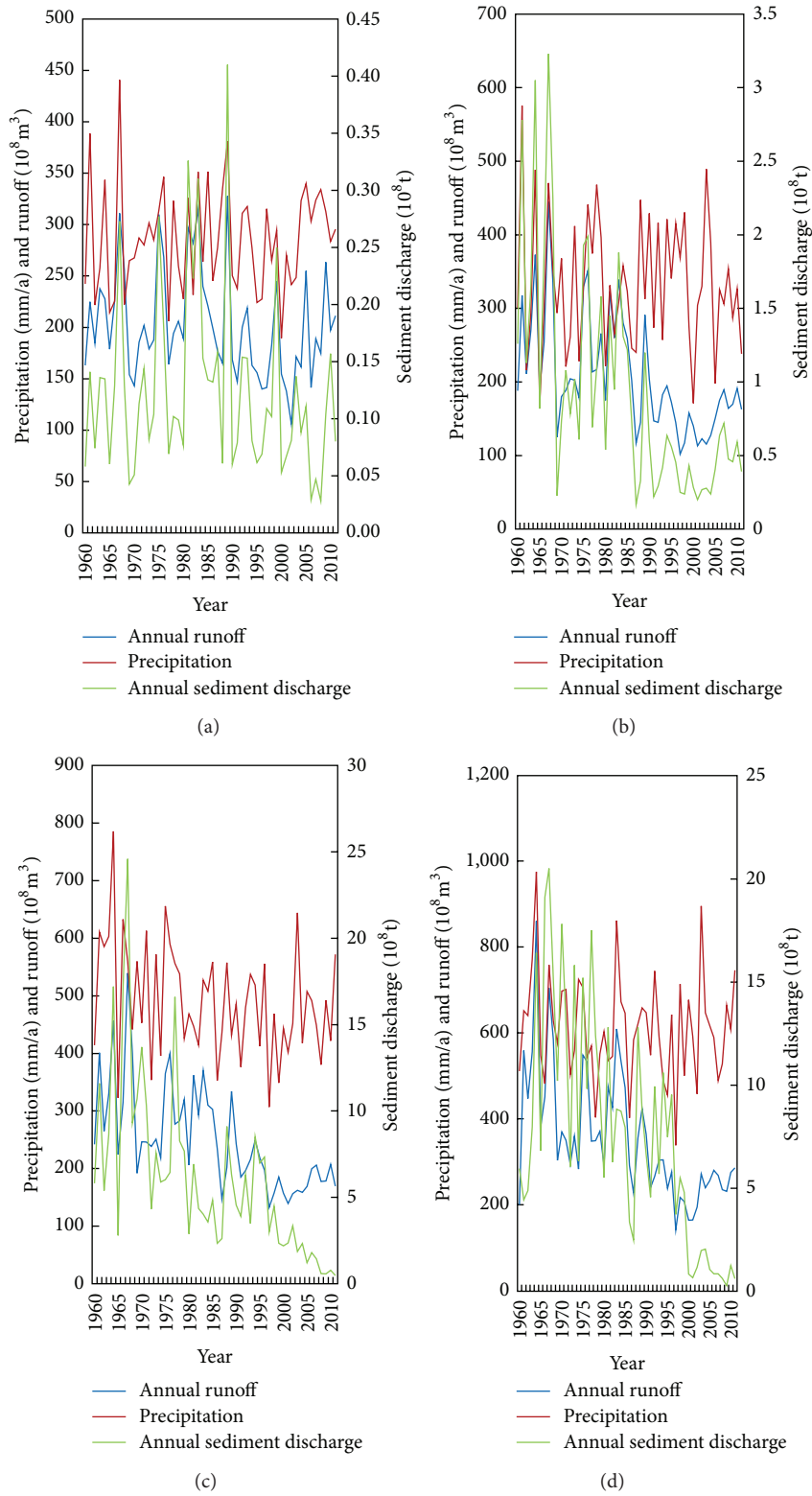


FIGURE 3: Changes of annual precipitation, runoff, and sediment discharge during the past 50 years (1960–2010) ((a) Tangnaihai, (b) Toudaoguai, (c) Longmen, and (d) Huayuankou).

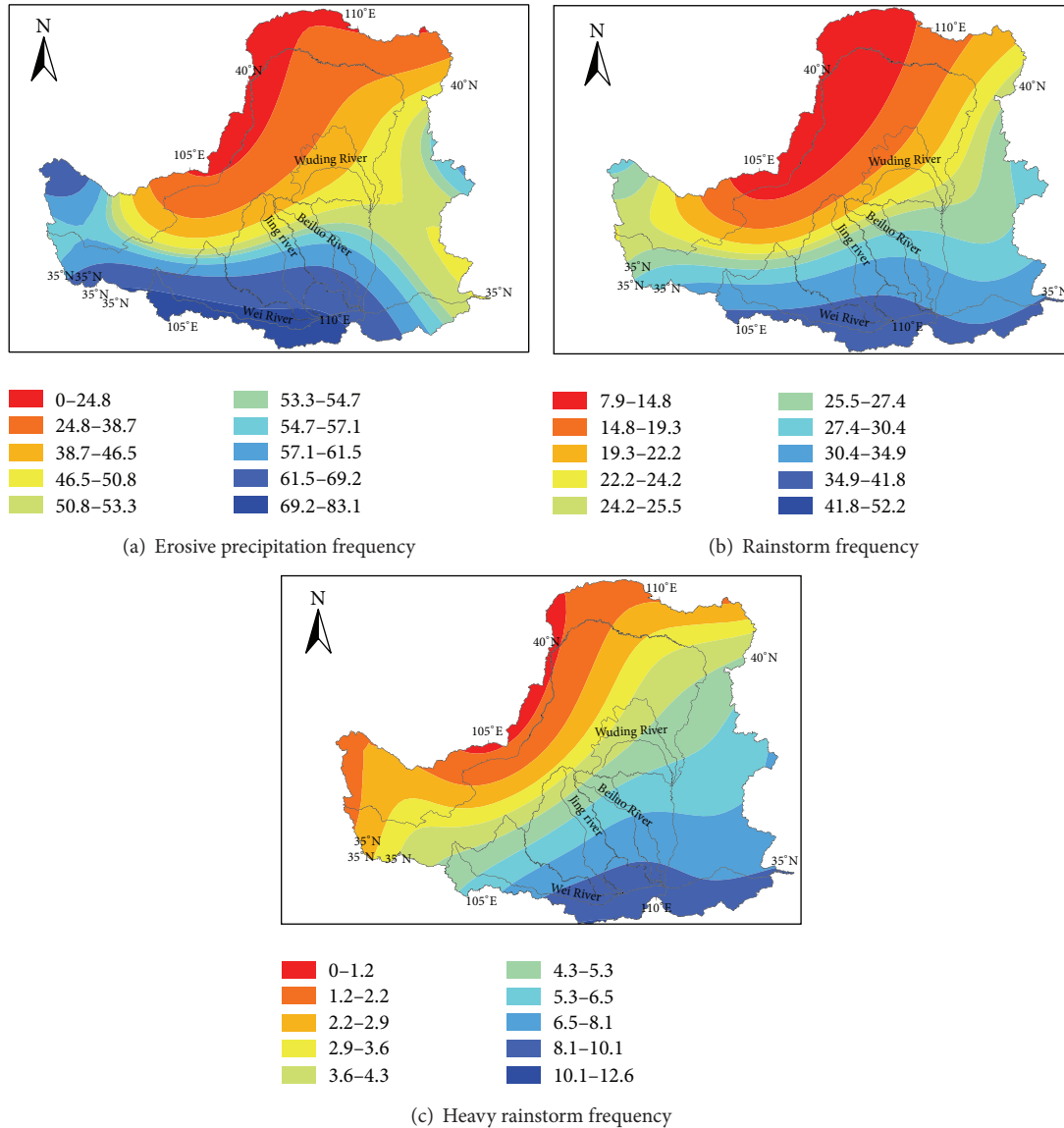


FIGURE 4: Frequency of different rainfall types ((a) erosive precipitation, (b) rainstorm, and (c) heavy rainstorm).

It is obvious that there were time lags between rainfall and runoff, runoff, and sediment transportation in the observed stations. For example, precipitation peak was on the 18th day at Tangnaihai station in 1967, the nearest runoff began to increase on the 22nd day, and the runoff peak was on the 35th day; in 1976, the peaks of runoff were about 4–8 days late compared to that of precipitation.

Differences between precipitation and runoff and sediment increased from upstream to downstream in the mainstream of upper and middle Yellow River, although precipitations fluctuated at around a certain level. And sediment decreased much more than runoff. Higher precipitation of these cities (Tangnaihai, Toudaoguai, Longmen, Tongguan, and Huayuankou) which locate from the upper of Yellow River to lower of it corresponded to higher runoff and sediment from 1960 to 2010. Correlation between precipitation and runoff is positive ($r = 0.565$, $p < 0.01$), and it is

much more obvious during 1960 and 1990. In 1960s and 1970s, change of runoff was mainly caused by fluctuation of rainfall. With development of society and increase of human activities, factors influencing runoff increased, and the coupling relationship between rainfall and runoff has become more complex. Moreover, annual runoff increases from upstream to downstream as well as annual precipitation.

Although annual precipitation fluctuates during the study period, annual runoff sediment discharge decreased obviously. However, runoff peaks correspond with rainfall events, especially for rainstorm (daily rainfall is larger than 50 mm/d). Sediment discharge does not display well correlations with precipitation; as a result, sediment discharge (soil erosion) is mainly influenced by vegetation, land cover, and human activities. The relationship of rainstorm and runoff can correspond well. In July of 1977 at Pingliang, there was a rainstorm which lasted for 19 hours and covered 33200 km².

TABLE 1: Parameters configuration of Erosive Landform Evolution Index (ELEI).

Parameters of Erosive Landform Evolution Index	Weihe River	Jinghe River	Beiluo River	Wudinghe River
Gully				
Gully density (km/km ²)	0.13	0.15	0.15	0.13
Runoff (10 ⁸ m ³)	64.62	16.01	8.16	10.86
Sediment discharge (10 ⁸ t)	2.94	2.08	0.68	0.92
RDLS				
0–20	0.44%	0.23%	0.61%	1.67%
20–75	5.81%	1.01%	3.96%	37.30%
75–300	29.82%	52.36%	58.94%	53.12%
300–600	42.31%	44.49%	36.45%	7.85%
600–max	21.62%	1.91%	0.04%	0.06%
Runoff (10 ⁸ m ³)	64.62	16.01	8.16	10.86
Sediment discharge (10 ⁸ t)	2.942	2.083	0.682	0.916
Slope (°)				
0~5	24.32%	16.69%	19.12%	57.46%
6~15	38.14%	40.77%	41.05%	27.89%
16~25	23.98%	32.75%	29.54%	11.94%
26~35	9.56%	6.24%	8.85%	2.31%
36~40	2.20%	2.92%	0.88%	0.22%
41~45	1.08%	0.30%	0.31%	0.09%
46~max	0.73%	0.34%	0.24%	0.09%
Runoff (10 ⁸ m ³)	64.62	8.16	16.01	10.86
Sediment discharge (10 ⁸ t)	2.942	0.682	2.083	0.916
ELEI				
Gully length (km)	9334.05	3501	5865.51	4414.58
RDLS (km ² , 20–600 m)	48825.22	26755.75	44496.04	29713.77
Slope (km ² , 0–25°)	54150.01	24294.27	40790.31	29417.45

Its rainfall was 255 mm, and the maximum peak flow was 5220 m³/s. In August of 1984 at Zhengning, there was a rainstorm which lasted for 6 hours and covered 423 km², and the maximum peak flow was 586 m³/s. In May of 1985 at Zhenyuan, the rainstorm lasted for 2.5 hours and covered 480 km² with 359 mm precipitation, the maximum peak flow of which was 1260 m³/s. In July of 1996 at Qingyang, the rainstorm lasted for 19.5 hours and covered 33150 km² with 257.2 mm precipitation, and the maximum peak flow was 4680 m³/s.

Frequency of low intensity rainfall was higher than that of high intensity rainfall, and frequency of the same intensity rainfall is higher in downstream than that of upstream. The average annual precipitation increases from northwest to southeast, and the minimum annual precipitation (46.80 mm/a) is in Linhe, Inner Mongolia, and the maximum annual precipitation (1262.3 mm/a) is in Huashan, Shaanxi. Overall, high rainfall (more than 720 mm/a) region mainly concentrates in south of Shaanxi province, and the low rainfall (less than 250 mm/a) is in Inner Mongolia, Ningxia province, and northwest of Gansu province. The tendency of average decade precipitation is consistent with that of average annual precipitation which increases from northwest (138 mm) to southeast (819 mm). In the typical reach of the Yellow River, sediment discharge and annual runoff of specific stations which are

close to downstream are larger than others. It indicates that (a) the downward trend of sediment discharge in upstream catchment is more significant than that in downstream basins for the same grade tributaries and (b) the trend of annual runoff in downstream catchment is more significant than that in upstream basin. The trend of sediment discharge is similar to that of runoff which increases from upstream to downstream.

4.2. Coupling Analysis of Soil Erosion and Landforms Evolution in the Loess Plateau. Tectonic movements in Quaternary formed the basic topography in Loess Plateau. Based on the above analysis of rainfall, runoff, and sediment transport, we can observe that peaks of runoff and sediment discharge are consistent with rainfall peak with time lags, and time lags of runoff and sediment discharge became longer in downstream than that in upstream for a normal distribution rainfall.

As indicated in methodology section, the higher values of Erosive Landform Evolution Index (ELEI) represent late stage of landform erosion. Table 1 displays parameters configuration of Erosive Landform Evolution Index (ELEI). By using the PCA method, we can easily get a comprehensive factor to stand for the three landform factors (gully length, RDLS, and slope). Before the PCA process, we standardized the data of three landform factors because of the difference of

TABLE 2: The proportion of covariance and first principal values of landform and climatic factors.

(a)							
PRIN number	Eigenvalue	Difference	Proportion	Cumulative			
Landform factors							
1	2.9524	2.9051	0.9841	0.9841			
2	0.0473	0.0470	0.0158	0.9999			
3	0.0003		0.0001	1.0000			
Climatic factors							
1	2.7813	2.6352	0.9271	0.9271			
2	0.1461	0.0734	0.0487	0.9758			
3	0.0726		0.0242	1.0000			
(b)							
Basins	Weihe River	Wudnghe River	Beiluoh River	Jinghe River	Fenhe River	Qinhe River	Yanhe River
Landform factors	2.7176	0.1526	-0.3206	1.3861	0.1233	-1.9096	-2.1495
Climatic factors	3.3354	-0.3999	-0.4694	0.9867	-0.7555	-1.3332	-1.3640

TABLE 3: The estimation parameters of the regression modeling.

Variable	Parameter estimate	Standard error	<i>t</i> value	<i>p</i> value
Comprehensive factor of erosive landform				
Intercept	0	0.270	0	1.00
E_e	0.953	0.004	150.87	<0.003

the units. The results of PCA (Table 2) show that the proportion of first principal is 98.41% which has significant correlation with the three landform factors. So we choose the first principal components as the comprehensive factor of erosion landform; higher PRIN values mean higher development of the erosion landform. Furthermore, with the PCA results we build (2) between the first PRIN and landform factors. The equation indicates that the three landform factors have positive correlation with the comprehensive landform factor:

$$Y_e = 0.576X_1 + 0.575X_2 + 0.582X_3, \quad (p < 0.05). \quad (2)$$

In the equation, the Y_e is the comprehensive factor of erosion landform, X_1 is the standardized value of gully length, X_2 is the standardized value of waviness, and X_3 is the standardized value of slope.

On the other hand, we also applied the same PCA process of calculation of the comprehensive factor of erosion landform, to calculate the comprehensive effect of erosion landform. By using the data of effects of erosion landform (Table 2), we obtain the comprehensive effect of erosion landform based on these erosion landform effects (runoff, sediment, and rainfall volume). The results (Table 2) indicate that the proportion of first principal is 92.71%, which means the first principal can explain all the erosion landform effects very well. Therefore, we select the first principal component as the comprehensive effect of erosion landform, and higher principal scores mean more influence on the erosion

landform. The equation of comprehensive effect of erosion landform is as follows:

$$E_e = 0.570Z_1 + 0.578Z_2 + 0.584Z_3, \quad (p < 0.05), \quad (3)$$

where the E_e is the comprehensive effect of erosion landform, Z_1 is the standardized value of runoff, Z_2 is the standardized value of sediment, and Z_3 is the standardized value of rainfall volume.

Finally, by using regression analysis, we can figure out the relationship between the comprehensive factor and comprehensive effect of erosion landform. Via the first principal scores of both comprehensive indexes (Table 2) in seven basins, we can calculate the relationship between these two indexes. The results (Table 3) show that the erosion landform comprehensive factor has the significant correlation ($p < 0.003$) with comprehensive effect of erosion landform, and the intercept of the model is not significant with erosion landform comprehensive factor ($p > 0.05$). Therefore we remove the intercept from the model.

Moreover, through the regression analysis we also obtain (4) between the erosion landform comprehensive factor and comprehensive effect. Meanwhile from the equation, we can also indicate that the erosion landform comprehensive factor has positive relationship with the effects of erosion landform. Therefore, the development level of erosion landform will increase as the effects values increase:

$$Y_e = 0.953E_e, \quad (p < 0.003). \quad (4)$$

In this equation, the Y_e is the comprehensive factor of erosion landform and the E_e is the comprehensive effect of erosion landform.

5. Conclusion

The aim of this study was to identify coupling relationship of soil erosion and landforms evolution under the background of climate change and human activities. Through mathematical statistics, regression analysis, and PCA method, it was found that the main effects of erosion landform are rainfall volume, runoff, and sediment in Chinese Loess Plateau. The results of PCA indicate that the erosion landform comprehensive factor is composed of the three landform factors, which are gully length, RDLS, and slope. It also shows that there is a significant positive relationship between erosion landform comprehensive factor and landform factors, and this means that these three factors can stand for erosion landform. Therefore, they can be used as evaluation factors of erosion landform. The results of multiregression analysis indicate that annual rainfall volume, runoff, and sediment are the main effects of erosion landform, and they drive the changes of landform in the Loess Plateau. Furthermore, both landform factors and erosion landform effects should be standardized before using them to build up the correlation model because standardization can reduce the influence of unequal units of these factors, which is a very important part in this modeling. Meanwhile, the regression results also show that there is also a significant positive linear relationship between the erosion landform comprehensive factor and its effects. As a result, the development level of erosion landform will increase as its effects' values increase. Thus, this study provides useful information on impacts of erosion landforms evolution and can be used to guide soil and water conservation and investigate landforms evolution.

Conflict of Interests

The authors declare that there is no conflict of interests regarding the publication of this paper.

Acknowledgments

The authors acknowledge with gratitude the research grants kindly provided by the Hundred-Talent Project of the Chinese Academy of Sciences (20110009, Dr. H. M. He), the Key Research Program of Chinese Academy of Sciences (KZZD-EW-04), Innovation Frontier Project of Institute of Soil and Water Conservation of the Chinese Academy of Sciences, State Key Laboratory of Soil Erosion, and Dryland Farming on the Loess Plateau (10501-192). They acknowledge with gratitude the help of Dr. Zhao Guangju (Institute of Soil and Water Conservation of the Chinese Academy of Sciences & Ministry of Water Resources) for supporting them with datasets to perfect their research.

References

- [1] B. Fu, "Soil erosion and its control in the Loess Plateau of China," *Soil Use & Management*, vol. 5, no. 2, pp. 76–82, 1989.
- [2] S. Kang, L. Zhang, X. Song et al., "Runoff and sediment loss responses to rainfall and land use in two agricultural catchments on the Loess Plateau of China," *Hydrological Processes*, vol. 15, no. 6, pp. 977–988, 2001.
- [3] J. L. M. P. De Lima, V. P. Singh, and M. I. P. de Lima, "The influence of storm movement on water erosion: storm direction and velocity effects," *Catena*, vol. 52, no. 1, pp. 39–56, 2003.
- [4] P. Davison, M. G. Hutchins, S. G. Anthony, M. Betson, C. Johnson, and E. I. Lord, "The relationship between potentially erosive storm energy and daily rainfall quantity in England and Wales," *Science of the Total Environment*, vol. 344, no. 1–3, pp. 15–25, 2005.
- [5] L. Chen, Z. Huang, J. Gong, B. Fu, and Y. Huang, "The effect of land cover/vegetation on soil water dynamic in the hilly area of the loess plateau, China," *Catena*, vol. 70, no. 2, pp. 200–208, 2007.
- [6] J. Casali, R. Gastesi, J. Álvarez-Mozos et al., "Runoff, erosion, and water quality of agricultural watersheds in central Navarre (Spain)," *Agricultural Water Management*, vol. 95, no. 10, pp. 1111–1128, 2008.
- [7] W. Wei, L. Chen, B. Fu, and J. Chen, "Water erosion response to rainfall and land use in different drought-level years in a loess hilly area of China," *Catena*, vol. 81, no. 1, pp. 24–31, 2010.
- [8] A. Gafur, J. R. Jensen, O. K. Borggaard, and L. Petersen, "Runoff and losses of soil and nutrients from small watersheds under shifting cultivation (Jhum) in the Chittagong Hill Tracts of Bangladesh," *Journal of Hydrology*, vol. 274, no. 1–4, pp. 30–46, 2003.
- [9] M. J. Singer and A. I. Shainberg, "Mineral soil surface crusts and wind and water erosion," *Earth Surface Processes and Landforms*, vol. 29, no. 9, pp. 1065–1075, 2004.
- [10] B. M. Ulén and T. Kalisky, "Water erosion and phosphorus problems in an agricultural catchment—need for natural research for implementation of the EU Water Framework Directive," *Environmental Science and Policy*, vol. 8, no. 5, pp. 477–484, 2005.
- [11] J. M. García-Ruiz, "The effects of land uses on soil erosion in Spain: a review," *Catena*, vol. 81, no. 1, pp. 1–11, 2010.
- [12] J. A. Nittrouer, J. Shaw, M. P. Lamb, and D. Mohrig, "Spatial and temporal trends for water-flow velocity and bed-material sediment transport in the lower Mississippi River," *Bulletin of the Geological Society of America*, vol. 124, no. 3–4, pp. 400–414, 2012.
- [13] J.-P. Bravard, M. Goichot, and H. Tronchère, "An assessment of sediment-transport processes in the Lower Mekong River based on deposit grain sizes, the CM technique and flow-energy data," *Geomorphology*, vol. 207, pp. 174–189, 2014.
- [14] C. L. Blanchet, R. Tjallingii, M. Frank et al., "High- and low-latitude forcing of the Nile River regime during the Holocene inferred from laminated sediments of the Nile deep-sea fan," *Earth and Planetary Science Letters*, vol. 364, pp. 98–110, 2013.
- [15] J.-J. Wang, X. X. Lu, and M. Kumm, "Sediment load estimates and variations in the Lower Mekong River," *River Research and Applications*, vol. 27, no. 1, pp. 33–46, 2011.
- [16] Y. S. A. Ali, A. Crosato, Y. A. Mohamed, S. H. Abdalla, and N. G. Wright, "Sediment balances in the Blue Nile River Basin," *International Journal of Sediment Research*, vol. 29, no. 3, pp. 316–328, 2014.
- [17] X. X. Lu and R. Y. Siew, "Water discharge and sediment flux changes over the past decades in the Lower Mekong River: possible impacts of the Chinese dams," *Hydrology and Earth System Sciences*, vol. 10, no. 2, pp. 181–195, 2006.

- [18] D. Conway, "The climate and hydrology of the Upper Blue Nile river," *The Geographical Journal*, vol. 166, no. 1, pp. 49–62, 2000.
- [19] Y.-K. Zhang and K. E. Schilling, "Increasing streamflow and baseflow in Mississippi River since the 1940s: effect of land use change," *Journal of Hydrology*, vol. 324, no. 1–4, pp. 412–422, 2006.
- [20] H. Y. Zhang, Z. H. Shi, N. F. Fang, and M. H. Guo, "Linking watershed geomorphic characteristics to sediment yield: evidence from the Loess Plateau of China," *Geomorphology*, vol. 234, pp. 19–27, 2015.
- [21] C. S. Renschler and J. Harbor, "Soil erosion assessment tools from point to regional scales—the role of geomorphologists in land management research and implementation," *Geomorphology*, vol. 47, no. 2–4, pp. 189–209, 2002.
- [22] A. Gobin, G. Govers, R. Jones et al., "Assessment and reporting on soil erosion," Tech. Rep., European Environment Agency, Copenhagen, Denmark, 2003.
- [23] Z.-B. Xin, J.-X. Xu, and X.-X. Yu, "Temporal and spatial variability of sediment yield on the Loess Plateau in the past 50 years," *Acta Ecologica Sinica*, vol. 29, no. 3, pp. 1129–1139, 2009.
- [24] R. Mukundan, S. M. Pradhanang, E. M. Schneiderman et al., "Suspended sediment source areas and future climate impact on soil erosion and sediment yield in a New York City water supply watershed, USA," *Geomorphology*, vol. 183, pp. 110–119, 2013.
- [25] B. Pradhan, A. Chaudhari, J. Adinarayana, and M. F. Buchroithner, "Soil erosion assessment and its correlation with landslide events using remote sensing data and GIS: a case study at Penang Island, Malaysia," *Environmental Monitoring and Assessment*, vol. 184, no. 2, pp. 715–727, 2012.
- [26] H. B. Mann, "Nonparametric tests against trend," *Econometrica*, vol. 13, pp. 245–259, 1945.
- [27] M. G. Kendall, *Rank Correlation Methods*, Griffin, London, UK, 4th edition, 1948.
- [28] G. Bing, *Land-atmosphere coupling simulation and analysis of streamflow changes in the Yangtze River Basin [Ph.D. thesis]*, Tsinghua University, Beijing, China, 2012.
- [29] F. Fathian, Z. Dehghan, M. H. Bazrkar, and S. Eslamian, "Trends in hydrologic and climatic variables affected by four variations of Mann-Kendall approach in Urmia Lake basin, Iran," *Hydrological Sciences Journal*, 2014.
- [30] I. Ahmad, D. Tang, T. Wang, M. Wang, and B. Wagan, "Precipitation trends over time using Mann-Kendall and spearman's rho tests in swat river basin, Pakistan," *Advances in Meteorology*, vol. 2015, Article ID 431860, 15 pages, 2015.
- [31] H. Hu, G. Wang, Z. Li et al., "Study on response of runoff of Weihe river to LUCC and climate changes," *Yellow River*, vol. 30, no. 7, pp. 25–26, 2008.
- [32] W. H. Wischmeier and D. D. Smith, *Predicting Rainfall Erosion Losses—A Guide to Conservation Planning*, Science and Education Administration, 1978.
- [33] E. Tunc, T. Iserloh, and Ş. Gülmez, "Soil erosion mapping by application of RUSLE and GIS-technology in the Turkish province Gaziantep/Southeastern Anatolia," *Journal of GIS Trends*, vol. 4, no. 1, pp. 1–10, 2014.
- [34] B. Jiang, *GIS-Based Time Series Study of Soil Erosion Risk Using the Revised Universal Soil Loss Equation (Rusle) Model in a Micro-Catchment on Mount Elgon, Uganda*, Student Thesis Series INES, 2013.
- [35] T. Chen, R.-Q. Niu, P.-X. Li, L.-P. Zhang, and B. Du, "Regional soil erosion risk mapping using RUSLE, GIS, and remote sensing: a case study in Miyun Watershed, North China," *Environmental Earth Sciences*, vol. 63, no. 3, pp. 533–541, 2011.
- [36] B. J. Fu, W. W. Zhao, L. D. Chen et al., "Assessment of soil erosion at large watershed scale using RUSLE and GIS: a case study in the Loess Plateau of China," *Land Degradation & Development*, vol. 16, no. 1, pp. 73–85, 2005.
- [37] G. Zhao, X. Mu, Z. Wen, F. Wang, and P. Gao, "Soil erosion, conservation, and eco-environment changes in the loess plateau of China," *Land Degradation & Development*, vol. 24, no. 5, pp. 499–510, 2013.
- [38] Y. Liu, B. Fu, Y. Lü, Z. Wang, and G. Gao, "Hydrological responses and soil erosion potential of abandoned cropland in the Loess Plateau, China," *Geomorphology*, vol. 138, no. 1, pp. 404–414, 2012.
- [39] L. Wang, Z. H. Shi, J. Wang, N. F. Fang, G. L. Wu, and H. Y. Zhang, "Rainfall kinetic energy controlling erosion processes and sediment sorting on steep hillslopes: a case study of clay loam soil from the Loess Plateau, China," *Journal of Hydrology*, vol. 512, pp. 168–176, 2014.
- [40] W. Sun, Q. Shao, and J. Liu, "Soil erosion and its response to the changes of precipitation and vegetation cover on the Loess Plateau," *Journal of Geographical Sciences*, vol. 23, no. 6, pp. 1091–1106, 2013.
- [41] I. D. Moore and J. P. Wilson, "Length-slope factors for the revised universal soil loss equation: simplified method of estimation," *Journal of Soil & Water Conservation*, vol. 47, no. 5, pp. 423–428, 1992.
- [42] K. Van Oost, W. Van Muysen, G. Govers, J. Deckers, and T. A. Quine, "From water to tillage erosion dominated landform evolution," *Geomorphology*, vol. 72, no. 1–4, pp. 193–203, 2005.
- [43] Z. Zhou and Z. Ren, "Correlation between land use and soil erosion intensities based on GIS: taking Loess Plateau in North Shaanxi Province as an example," *Chinese Journal of Ecology*, vol. 25, no. 6, pp. 629–634, 2006.
- [44] S. Wang, G. Wang, and Z. Chen, "Relationship between land use and soil erosion in Yellow River Basin," *Journal of Natural Disasters*, vol. 1, article 004, 2005.
- [45] A. H. Abu Salim, "Geomorphological analysis of the morphometric characteristics that determine the volume of sediment yield of Wadi Al-Arja, South Jordan," *Journal of Geographical Sciences*, vol. 24, no. 3, pp. 457–474, 2014.
- [46] J. B. Zhao, J. Du, and C. C. Huang, "Study on erosion periods in Loess Plateau," *Journal of Desert Research*, vol. 22, no. 3, pp. 257–261, 2002.
- [47] P. Gao, X. Zhang, X. Mu, F. Wang, R. Li, and X. Zhang, "Trend and change-point analyses of streamflow and sediment discharge in the Yellow River during 1950–2005," *Hydrological Sciences Journal*, vol. 55, no. 2, pp. 275–285, 2010.
- [48] H. He, J. Zhou, M. R. Peart, J. Chen, and Q. Zhang, "Sensitivity of hydrogeomorphological hazards in the Qinling Mountains, China," *Quaternary International*, vol. 282, no. 1, pp. 37–47, 2012.
- [49] H. He, J. Zhou, Q. Yu, Y. Q. Tian, and R. F. Chen, "Flood frequency and routing processes at a confluence of the middle Yellow River in China," *River Research & Applications*, vol. 23, no. 4, pp. 407–427, 2007.
- [50] H. He, Q. Yu, J. Zhou, Y. Q. Tian, and R. F. Chen, "Modelling complex flood flow evolution in the middle Yellow River basin, China," *Journal of Hydrology*, vol. 353, no. 1, pp. 76–92, 2008.
- [51] J. X. Liu, Z. G. Li, X. P. Zhang, R. Li, X. Liu, and H. Zhang, "Responses of vegetation cover to the Grain for Green Program and their driving forces in the He-Long region of the middle reaches of the Yellow River," *Journal of Arid Land*, vol. 5, no. 4, pp. 511–520, 2013.

- [52] Y. Xie, B.-Y. Liu, and W.-B. Zhang, "Study on standard of erosive rainfall" *Journal of Soil and Water Conservation*, vol. 14, no. 4, pp. 6-11, 2000.
- [53] K. Chang, *Introduction to Geographic Information Systems*, McGraw-Hill Higher Education, Boston, Mass, USA, 2006.

Research Article

Numerical Simulation of the Topographical Change in Korea Mountain Area by Intense Rainfall and Consequential Debris Flow

Byong-Hee Jun

Department of Disaster Prevention & Safety Engineering, Kangwon National University, Samcheok 245-905, Republic of Korea

Correspondence should be addressed to Byong-Hee Jun; bhjun@kangwon.ac.kr

Received 20 April 2015; Revised 16 July 2015; Accepted 12 August 2015

Academic Editor: Zhongping Lai

Copyright © 2016 Byong-Hee Jun. This is an open access article distributed under the Creative Commons Attribution License, which permits unrestricted use, distribution, and reproduction in any medium, provided the original work is properly cited.

The objectives of this study are to simulate the topographical changes associated with rainfall and the consequential debris flow using terrestrial LiDAR (Light Detection And Ranging). Three rainfall events between July 9 and July 14, 2009, triggered a number of debris flows at Jecheon County in Korea. Rain fell at a rate of 64 mm/h, producing 400 mm of total accumulation during this period. Tank simulation model for SWI (Soil Water Index) estimated the water stored beneath the ground and debris flow occurrence in study area. For the LiDAR (Light Detection and Ranging) survey, the terrestrial laser scanning system RIEGL LMS-Z390i consists of an accurate and fast 3D scanner, associated RTK GPS system. The DEM derived from LiDAR enabled the debris flow to be mapped and analyzed in great detail. The estimated affected area and erosion/deposition volumes by debris flow were compared with two-dimensional numerical simulation. The simulation results were sufficiently in good agreement with the debris flow track, and a success rate of over 90% was achieved with a simulation time of 300 s. A comparison of the simulated and surveyed results based on deposition volume yields a success rate of over 97% with 350 s of simulation time.

1. Introduction

Since the debris flows generally transport huge volumes of sediments in mountain torrents, it is important to understand the characteristics of erosion, transportation, and deposition of debris flows, especially mountainous areas. In a previous study, the peak discharge of the water and sediment mixture was reported to be an order of magnitude greater, and the density of the mixture can be two times greater than the density of water [1]. Moreover, the debris flow discharges are much higher than clean water discharges; thus, the hydrodynamic forces are increased [2]. Climatic factors are an important subject for a better understanding of hydrological response of landslide activity and are essential for developing landslide/debris flow warning systems. Intense rainstorms may directly trigger shallow landslides (<3 m deep), and an upper threshold for landslide initiation with rainfall intensity and rainfall duration was defined. The Indian Ocean monsoon produces seasonal precipitation in Korea [3], which causes landslides and debris flows. Recently, these events have

resulted in notably higher damage [4]. In both Korea and all around Northeast Asia, the sediments in debris flows often cause catastrophic damage in local communities [5].

Many researchers have proposed mathematical models of debris flow. A number of these models employ empirical formulas concerning run-out and deposition [6–9]. Other models focus on the physical and dynamic aspects of debris flows [10–14]. In recent studies, incorporating numerical simulations with GIS (Geographic Information System) enabled the evaluation of debris flow risk through the integrated simulation of triggering, propagation, and deposition [15, 16]. Takahashi [10] used Bagnold's dilatant fluid hypothesis and proposed that the erosion/deposition rate is a function of sediment concentration and controlled by the excess concentration over the equilibrium concentration. These models incorporate the rheological properties, such as friction parameters, as input data, and back calculation is usually required for estimating these rheological properties.

The observation of topographic changes with high-resolution imaging can help validate debris flow simulations.

LiDAR (Light Detection and Ranging) is a remote sensing technology that collects three-dimensional point clouds of the surface. LiDAR data has already been used for studying landslide morphology and distribution [17–19], local relief [20, 21], channel bed morphology [22, 23], and headwater channel network analysis [24, 25], as well as for the hill slope-to-valley transition [26]. LiDAR data also enables the calculation of surface characteristics [27] and the extraction of geometry and identification of failure [28]. Various researchers have investigated the effect of DEM (Digital Elevation Model) resolution on landscape representation [29–31]. These data were combined with landslide observations and landslide models [32]. The benefits of laser scanning are the ability to quickly generate data of an object surface, easy leveling process, and fewer human errors [33].

This study presents results from quantification of the volume and pattern of debris flow deposits using DEMs generated from GPS (Global Positioning System) measurement through the LiDAR survey. The objectives of this study are to identify the morphological changes associated with the debris flow and to determine the affected area and total volume of debris flow using high-resolution terrestrial LiDAR. The estimated results of the affected area and erosion/deposition volumes by debris flow were compared with the numerical simulation results.

2. Methods

2.1. Study Area. Due to an intensive rainfall from 9 to 14 July 2009 in Jecheon County, a large number of debris flows occurred around the mountainous area. The study examined one of these debris flow occurrences areas in Jecheon County, which is located at 37°07'N latitude and 128°04'E longitude. Figure 1 shows the location and morphology of study area and also shows channelized debris flow. The damage from these debris flows was large; they destroyed 2 houses on the apex and 6 houses at the alluvial fan and damaged several vinyl greenhouses and all of the fields around the channels. The morphologies of the basin and channel in this study are listed in Table 1. The area of catchment is approximately 1.22 km², rising from 275 m to 680 m, with water flowing NW.

Figure 2 shows an aerial photograph of the study area and a terrestrial photograph of areas with erosion or deposition. The white circles (A), (B), and (C) represent the area of the subsequent photograph. The rectangular transparent gray zone represents the LiDAR scanning area for this study, which is also applied to the mathematical simulation.

Figure 3 shows the rainfall events at Baekun weather station near the study area from 7 to 16 July 2009. In Jecheon County, six weather stations were operated, and, among them, the Baekun weather station was closest to the study area. The rainfall data indicates that high intensive and sequential rainfall occurred between July 9 and July 14, totaling 455.5 mm. Rainfall intensity increased on July 14 to the maximum rainfall intensity of 64 mm/h and 201 mm/d at Baekun weather station and debris flow occurred at 21:00 on July 14.

High water content is necessary for soil saturation, and it was reported that most debris flows occurred during or after

TABLE 1: Topographic parameters in study area.

Parameters (unit)	Value
Basin area (km ²)	1.22
Basin maximum elevation (m, a.s.l.)	680
Basin minimum elevation (m, a.s.l.)	275
Basin mean elevation (m, a.s.l.)	464
Basin mean slope (degree)	22.0
Channel length (m)	2,030
Channel slope (degree)	7.8
Debris flow area slope (degree)	11.9

heavy and sustained rainfalls [34]. Antecedent moisture also plays an important role in the saturation of soils, and it rises with groundwater level and soil moisture [35, 36]. The SWI (Soil Water Index) has been used as a variable in landslide and debris flow warning systems [37]. SWI estimates the water stored beneath the ground and landslide disaster occurrence by comparing current and past SWI values. Tank simulation models for SWI evaluation are semiphysical models that generalize the geometrical, spatial, and material conditions. Due to the simplicity, a tank model can be used for long time periods and GIS applications [38]. This model also shows how long it takes for rain to become groundwater. We verified the SWI in this study area and investigated the applicability of a tank model. In this study, SWI was defined to be the total storage thickness of the three tanks.

Figure 4 shows the part of temporal variation from 1 to 31 July 2009 in the study area. Three major rainfall events occurred within six days and the sequence of debris flow events in the study area started on 14 July 2009 during the third rainfall peak, which had a maximum rainfall intensity of 64 mm/h and 201 mm/d. The temporal variations of SWI represent the possibility of prediction tools for landslide occurrence. The antecedent rainfall seemed to have a strong effect on triggering debris flows in this study area.

2.2. LiDAR Scanning. For the LiDAR survey, the terrestrial laser scanning system RIEGL LMS-Z390i consists of a highly accurate and fast 3D scanner using TOF (time of flight) method, associated RTK GPS system, and high-resolution digital camera. The TOF method calculates the time taken by the light pulse and finds x , y , and z coordinates and the distance from the source to the object. TOF scanner used in this study has the ability to measure 11,000 points every second. The point cloud contains information including x , y , and z coordinates.

The LiDAR provides high-resolution DEMs that provide better land surface representation. In debris flow studies, LiDAR is often used in conjunction with other datasets such as DEMs derived from photogrammetry to compare with LiDAR topography. To gather and compare the digital information available for the study area, we used ArcGIS tools, which enabled volume calculations.

2.3. Numerical Model. A mathematical model is applied to simulate the debris flow in study area. The fundamental theory of the numerical model is based on mass and

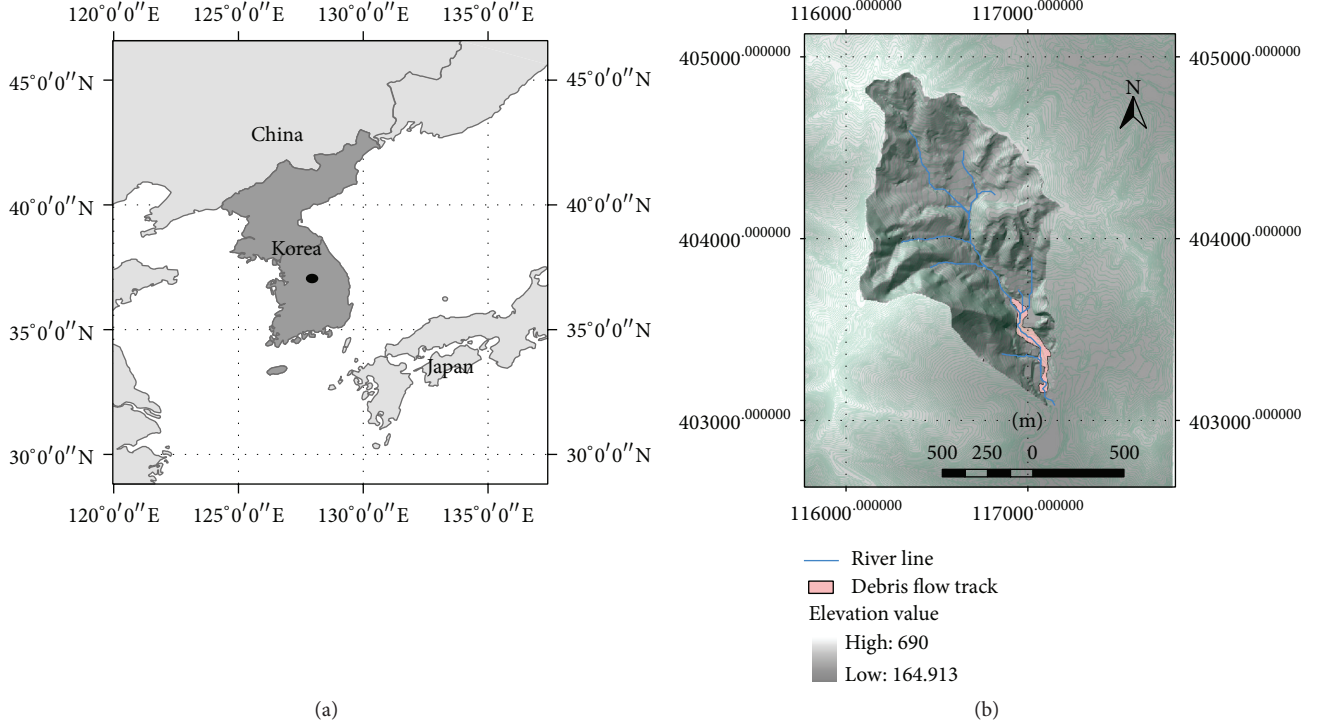


FIGURE 1: The location of study area (a) and debris flow occurring in basin (b).

momentum conservation with a shallow-water assumption and storm-induced debris flow often moves as a continuous fluid until stoppage [39]. To estimate the debris flow, this study adopted Takahashi model [10], which treats a debris flow as a steady fully developed laminar flow and assumes that the flow is dilatant fluid and governed by Navier-Stokes and continuity equations. The model fluid is considered a solid-liquid mixture of sediments and interstitial fluid. Assuming that the solids and the interstitial fluid move downstream with the same velocity, the flow of the mixture is described using a two-dimensional depth averaged model with a 2D momentum equation and two mass balance equations for the mixture and the sediments. Differential equations are integrated with an upwind explicit finite-difference scheme. By introducing shear stresses at the flow surface, the depth-wise averaged two-dimensional momentum equations of debris flow for x (down valley) and y (lateral) directions are described as follows:

$$\begin{aligned} & \frac{\partial M}{\partial t} + \beta \frac{\partial (uM)}{\partial x} + \beta \frac{\partial (vM)}{\partial y} \\ & = gh \sin \theta_{bx0} - gh \cos \theta_{bx0} \frac{\partial (z_b + h)}{\partial x} - \frac{\tau_{bx}}{\rho_T}, \\ & \frac{\partial N}{\partial t} + \beta \frac{\partial (uN)}{\partial x} + \beta \frac{\partial (vN)}{\partial y} \\ & = gh \sin \theta_{by0} - gh \cos \theta_{by0} \frac{\partial (z_b + h)}{\partial y} - \frac{\tau_{by}}{\rho_T}, \end{aligned} \quad (1)$$

where $M (=uh)$ and $N (=vh)$ are the flow discharge per unit width in x and y directions, t is time, u and v are the velocity components in x and y directions, β is momentum correction factor equal to 1.25 for a stony debris flow, g is gravitational acceleration, h is flow depth, θ_{bx0} and θ_{by0} are x and y components of the slope of the original bed surface, z_b is erosion or deposition thickness of the bed measured from the original bed surface elevation, τ_{bx} and τ_{by} are the bottom shear stresses in x and y directions, and ρ_T is the mixture density.

The continuity equation of the total volume is

$$\frac{\partial h}{\partial t} + \frac{\partial M}{\partial x} + \frac{\partial N}{\partial y} = i_b, \quad (2)$$

where i_b is the erosion (≥ 0) or deposition (< 0) velocity.

The continuity equation of the coarse particle fraction that is sustained in the flow by the action of particle encounters is

$$\frac{\partial (Ch)}{\partial t} + \frac{\partial (CM)}{\partial x} + \frac{\partial (CN)}{\partial y} = i_b C_*, \quad (3)$$

where C is the volumetric sediment concentration in the flow and C_* is the volumetric sediment concentration in the original bed. The erosion or deposition thickness to calculate the bed surface elevation is given by

$$\frac{\partial z_b}{\partial t} + i_b = 0. \quad (4)$$

The change of the debris flow density can be modeled through the mass balance of both phases (solid and liquid) and the

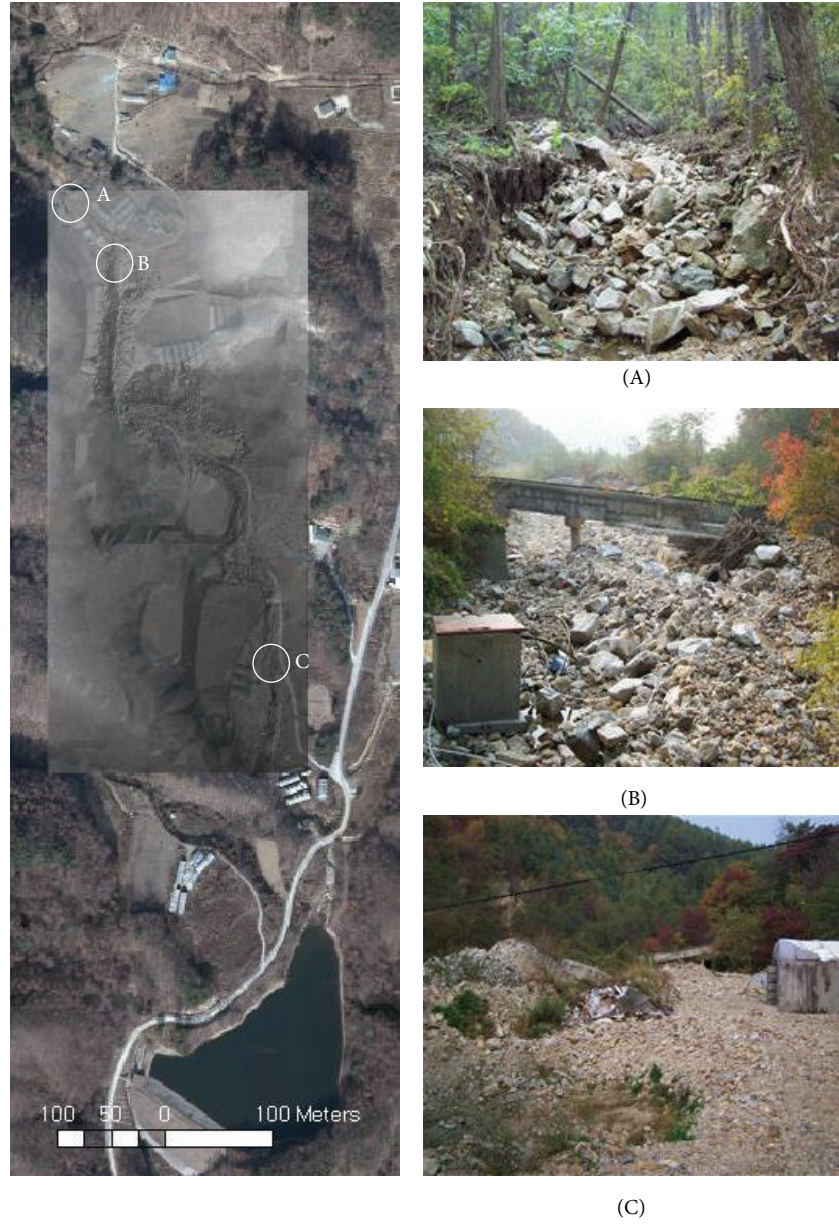


FIGURE 2: The aerial photograph in study area and terrestrial photograph showing flooding area.

definition of the erosion/deposition rate as a function of the sediments concentration. The debris flow can be numerically simulated by two-dimensional governing equations composed of the momentum conservation equation for the mixture of solid and liquid, the mass conservation equations for the liquid phase and solid phase, respectively, and the equation for bed height change. Since the resistance term involves the momentum conservation equations, the different constitutive equations for fully developed stony debris flow and immature debris flow and turbulent flow should be contained in the momentum conservation equation. The bottom resistance for a two-dimensional flow is described as follows.

For a fully developed stony debris flow ($C > 0.4C_*$),

$$\begin{aligned}\tau_{bx} &= \frac{u}{\sqrt{u^2 + v^2}} \tau_{yx} + \rho f_b u \sqrt{u^2 + v^2}, \\ \tau_{by} &= \frac{v}{\sqrt{u^2 + v^2}} \tau_{yy} + \rho f_b v \sqrt{u^2 + v^2},\end{aligned}\tag{5}$$

in which τ_{yx} and τ_{yy} are the yield stresses in x and y directions, which can be expressed using constitutive equations of Takahashi et al. [40].

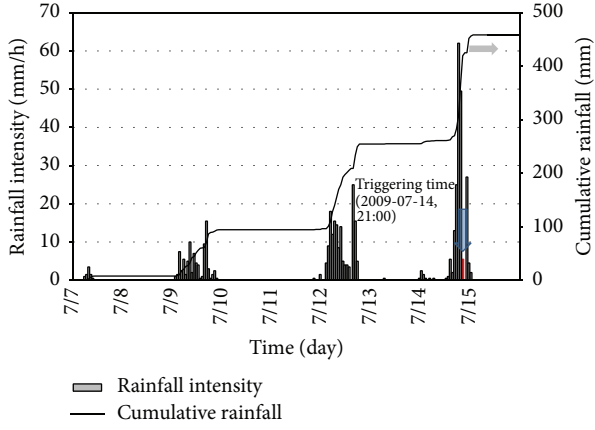


FIGURE 3: Rainfall at Baekun weather station on 7-16 July 2009.

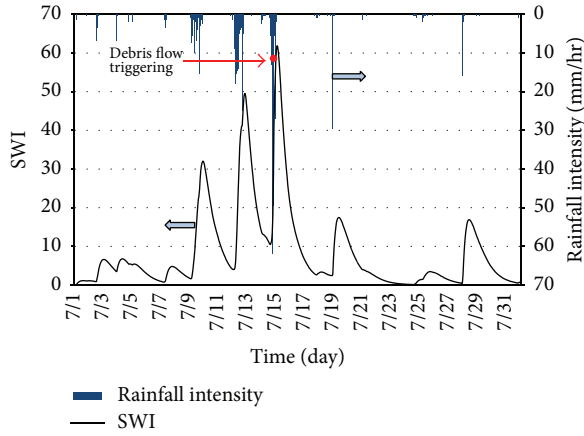


FIGURE 4: Temporal variation in Soil Water Index from 1 to 31 July 2009 in Jecheon area.

For an immature debris flow ($0.02 \leq C \leq 0.4C_*$),

$$\tau_{bx} = \frac{\rho_T}{0.49} \left(\frac{d_m}{h} \right)^2 u \sqrt{u^2 + v^2},$$

$$\tau_{by} = \frac{\rho_T}{0.49} \left(\frac{d_m}{h} \right)^2 v \sqrt{u^2 + v^2}.$$
(6)

For a turbulent flow ($C < 0.02$),

$$\tau_{bx} = \frac{\rho g n^2 u \sqrt{u^2 + v^2}}{h^{1/3}},$$

$$\tau_{by} = \frac{\rho g n^2 v \sqrt{u^2 + v^2}}{h^{1/3}}.$$
(7)

Since the volume of debris flow traveling downstream will increase with the bed erosion or decrease with deposition, the erosion and deposition velocity equations should be contained in the mass conservation equations. The erosion and deposition velocity equations for two-dimensional debris flow model are given by Takahashi et al. [40].

TABLE 2: Summary of values used in simulations.

Parameters (unit)	Value
Solid density (kg/m^3)	2.65
Fluid density (kg/m^3)	1
Volumetric sediment concentration in bed	0.65
Mean diameter of sediment particle (m)	0.03
Gravity acceleration (m/s^2)	9.8
Erosion coefficient	0.0007
Deposition coefficient	0.05
Tangent of internal friction angle of sediment	0.7
Manning coefficient	0.04
Time interval (s)	0.02
Mesh size (m)	5

Erosion velocity equation is

$$i_b = \delta_e \frac{C_\infty - C}{C_* - C_\infty} \frac{\sqrt{u^2 + v^2} h}{d_m}, \quad (8)$$

where δ_e is erosion coefficient and C_∞ is the equilibrium concentration.

Deposition velocity equation for a fully developed stony debris flow is

$$i_b = \delta_d \left(1 - \frac{\sqrt{u^2 + v^2}}{pU_e} \right) \frac{C_\infty - C}{C_*} \sqrt{u^2 + v^2}, \quad (9)$$

where δ_d is deposition coefficient, p ($=2/3$) is numerical constant, and U_e is the equilibrium velocity at which neither erosion nor deposition takes place as follows:

$$U_e = \frac{2}{5d_m} \left[\frac{g \sin \theta_e}{a_i \sin \alpha_i} \left\{ C + (1 - C) \frac{\rho_m}{\sigma} \right\} \right]^{1/2} \cdot \left\{ \left(\frac{C_*}{C} \right)^{1/3} - 1 \right\} h^{3/2}, \quad (10)$$

where θ_e is channel slope in which sediment concentration is in equilibrium, which can be obtained as follows:

$$\tan \theta_e = \frac{C(\sigma - \rho_m) \tan \phi}{C(\sigma - \rho_m) + \rho_m}. \quad (11)$$

For the cases of an immature debris flow and a turbulent flow, the respective deposition equation is expressed as

$$i_b = \delta_d \frac{C_\infty - C}{C_*} \sqrt{u^2 + v^2}. \quad (12)$$

The input values and unit of the parameters for simulations are listed in Table 2.

Taking into consideration a previous study by Salciarini et al. [41], the soil depth was assumed to be 3 m, based on the results from terrestrial LiDAR survey. A simulation time interval of 0.01 s was used for the simulation of debris flow.

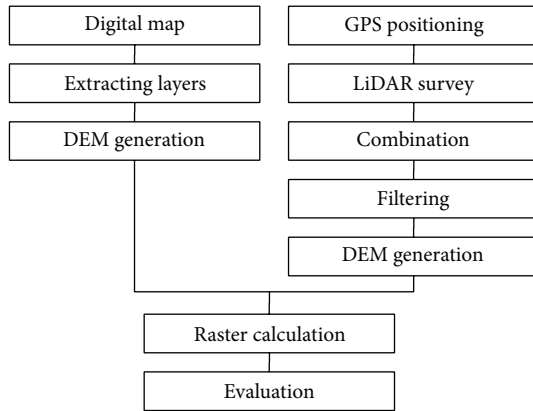


FIGURE 5: Main LiDAR processing steps in this study.

3. Result and Discussion

3.1. LiDAR Scanning. Figure 5 shows the DEM manipulation and the main LiDAR processing steps in a flow chart. For the DEM generation before the debris flow, we used a digital map that was provided by Korea Geography Information Institute because there was no available LiDAR data around study area. The digital map with 1:5000 scale was constructed in 2007, and the DEM before the occurrence was generated with the grid cell of $5\text{ m} \times 5\text{ m}$ spatial resolution.

The first step in LiDAR survey involves the RTK GPS (Global Position System) receiver setup. The LiDAR survey produces quantification of the volume and pattern of debris flow deposits using DEM generated from GPS and LiDAR data [42]. Synchronization of GPS and LiDAR was obtained using the starting point as a reference for the survey processes. The GPS and LiDAR sensor were both connected to a computer for the data management and storage. The LiDAR scanning integrated the georeferenced cloud points. The study area required scanning from 21 locations to capture debris flow track geometry and these 21 locations were combined to one dataset. Due to the presence of vegetation and houses, mask and filtering was performed.

Next, a triangulated irregular network (TIN) was constructed for the point cloud. Finally, a raster DEM was generated with $5\text{ m} \times 5\text{ m}$ spatial resolution. The DEM generation was performed using the universal Kriging interpolation method. Using these two DEMs, further raster calculations were performed by ArcGIS. A number of results can be derived from the raw data, including morphology, geometry, and cross-sectional profiles.

Figure 6 shows the capture of whole cloud points combined by the RiSCAN PRO program, which is the companion software for RIGLE terrestrial 3D laser scanner system along the debris flow track. The study area consisted of 21 scanning points to capture whole debris flow track. Initial raw data consisting of more than 350,000 points required postprocessing before DEM generation. The first step in postprocessing involves the elimination of points identified as beyond the nominal ground surface. Next, the objects except the surface of the earth should be removed from the original data by

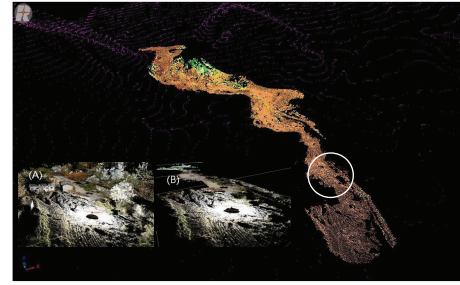


FIGURE 6: The capture of combined cloud points: original LiDAR range image subjected to debris flow (A) and cutting result of forest canopies and artificial structures (B).

filtering. The points returned from forest around the debris flow track are identified and removed using visual inspection of the 3D data. Figure 6(A) shows a magnified part (white circle) of original scanning point cloud data including some woods and artificial structures and Figure 6(B) shows the filtered point cloud data at the same area with (A).

Figure 7 shows the topographic map before (a) or after (b) debris flow. The left upper corner of the figure shows the area upstream of the debris flow track. Figure 7(b) shows the high-resolution DEM as a result of overlapping the digital map and 3D point cloud data. Figure 7(b) also shows obvious erosion scars in the upstream region and detailed topography features all over debris flow track. It is shown that the debris flow track tends to reach a configuration of dynamic equilibrium in the downstream zone, while in the upstream zone the erosion is dominant.

Through the raster calculation of results in Figure 7, we can calculate erosion and deposition. Figure 8 shows the evaluated values of erosion and deposition depth. The blue and brown areas represent erosion and deposition areas, respectively. Whereas deep erosion was shown at the upstream region, the erosion became smaller and the deposition more broad downstream. Figure 8 also represents the affected area of the debris flow track. Furthermore, the volume changes by the debris flow event could be estimated based on a comparison between the eroded or deposited surface area and its heights. Next, the total volume and area of erosion and of deposition were calculated by summing the negative and positive pixels, respectively. According to this comparison, the erosion volume was approximately $32,847\text{ m}^3$ and the deposition volume was approximately $22,889\text{ m}^3$, respectively. As a consequence, it was thought that discharged sediment volume was $9,958\text{ m}^3$. Generally, a debris volume could increase during the landslide event, as a consequence of the deposition during the landslide [18]. However, the deposition volume was estimated to be less than that of erosion. The underestimated deposition volume can be assumed to be discharge volume into the reservoir located downstream of the study area.

The debris flow volumes and discharges can be much greater than clean water due to rainfall. The density of the mixture is two times greater than that of the liquid flow. In

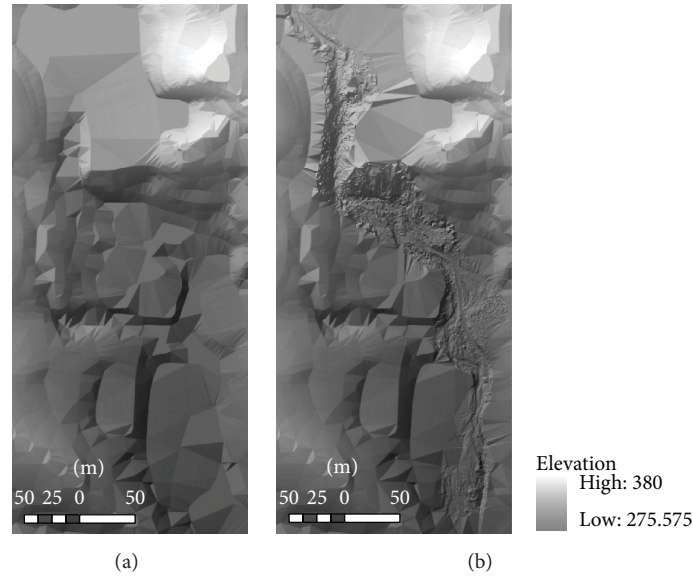


FIGURE 7: Topographic map before (a) and after (b) debris flow.

consequence, the hydrodynamic forces acting on the structure are increased. Therefore, the debris flow volumes should be considered to design hydraulic structures such as dams and bridges. With the classification of Jakob [2], the flow was rated as size class 4, which could destroy parts of village and destroy sections of infrastructure corridors and bridges.

3.2. Topographical Change Simulation. A debris flow model is used to simulate the transport and deposition of failed materials from the identified source areas. In absence of any recorded discharge amount on the upper part of triggering point, a rectangular discharge hydrograph with flow of $20 \text{ m}^3/\text{s}$ was assumed. The computational domain was discrete with 108×48 square cells with a size of 5 m. A DEM was obtained from a 1:5000 digital map and was not refined anywhere. Figure 9 shows the morphological variations evaluated between the initial condition and the temporal progression of the simulated debris flows. The solid line represents the affected area results from the LiDAR survey as shown in Figure 8.

In Takahashi model, if debris flow contains lower solid concentration than the equilibrium concentration, the bed would be eroded, and if the solid concentration is higher than the equilibrium value, solid would be deposited. This method was applied to cases of laboratory experiment [43] and various field researches [4]. Comparing with stochastic method such as random walk model deciding the flow direction by the probability proportional to the flow velocities calculated from the elevation differences between the adjacent grid points, demerit of random walk model is that the deposition proceeds with one-dimensional motion despite the complex topology [44]. This study uses horizontally two-dimensional momentum conservation and mass conservation equations representing the two-dimensional flow.

It reveals that the simulation results are sufficiently good excluding the northern part of the domain where the model

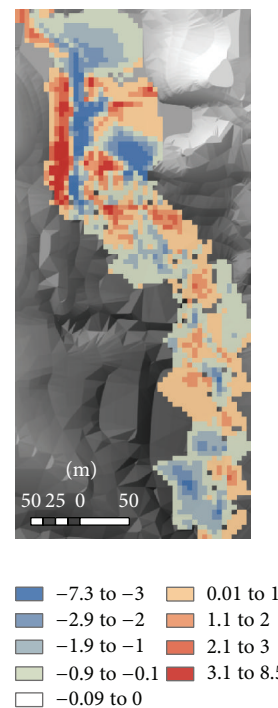


FIGURE 8: The evaluated values of erosion and deposition depth.

simulates wide spreading of the wave in the upper stream. This broad deposition did not occur in the real world event. Debris flow moves with the mean velocity of 3.5 m/s along a path with the average slope of 11.9° .

To validate the model performance, we extracted the affected area with a terrestrial LiDAR survey and compared the affected area with the results of debris flow simulation. Figure 10 shows the details of the model performance in predicting the affected areas.

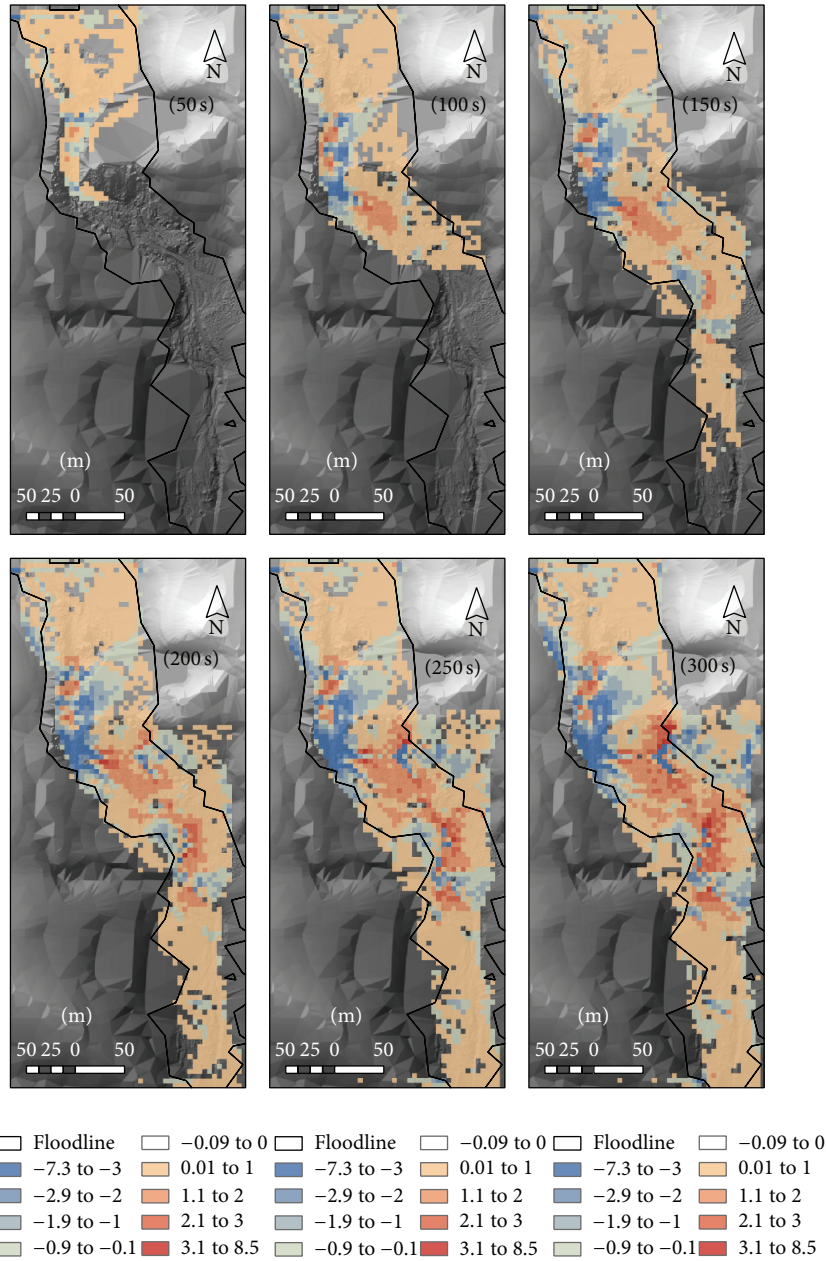


FIGURE 9: The temporal progression of the simulated debris flows.

For the evaluation of success rate, the proportions of successfully predicted affected areas (A_s) were calculated:

$$A_s = \frac{N_p}{N_t} \times 100 (\%), \quad (13)$$

where N_t is the total cell number of surveyed affected areas and N_p is the correctly simulated cell number within the affected areas. In Figure 9, the solid line represents the terrestrial LiDAR surveyed affected areas and corresponds to N_t . The differences between the solid line area and colored area by the simulation time represent the discordances with

the surveyed area and the simulated results. A high success rate over 90% was achieved with a simulation time of 300 s.

Moreover, because the terrestrial LiDAR survey results have depth information, we could validate simulated erosion/deposition volume change along within the affected area. The depth of sediment deposition before and after debris flow can be used to estimate the model performance [45]. The second validation defined the prediction accuracy by calculating the ratio of the simulated erosion/deposition volume and surveyed erosion/deposition volume, respectively.

Figure 11 shows the simulated erosion/deposition volume and the success rate. In this study, deposition volumes were lower than erosion volumes. For the success rate evaluation of

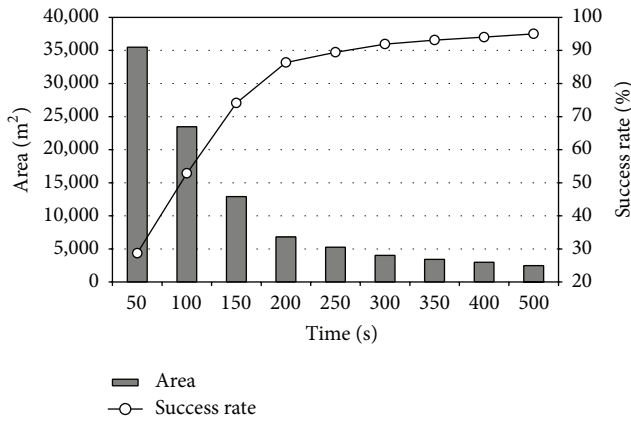


FIGURE 10: Variation of discordance area and the success rate.

the erosion/deposition volume, the proportions of predicted erosion/deposition volume and measured erosion/deposition volume by the LiDAR survey (V_s) were calculated:

$$V_s = \frac{V_{\text{simulated}}}{V_{\text{measured}}} \times 100 (\%), \quad (14)$$

where V_{measured} is the LiDAR surveyed erosion/deposition volume as shown in Figure 8 and $V_{\text{simulated}}$ is the simulated erosion/deposition volume. A comparison of the simulated and survey results, based on the deposition volume, yields a success rate of over 97% at 350 s simulation time. The erosion volume success rate reaches the highest value at 500 s simulation time. It was thought that this delayed result is probably due to the soil depth limitation in the model assumptions.

The results reproduced both the zone affected by the debris flow and the spatial distribution of sediments with reasonable accuracy for most of the domain. The model test and validation results confirm the usefulness of the model in calculating the number and size of affected areas, run-out path, and volume of run-out deposits.

These results suggest some important considerations for technicians dealing with the protection of the mountain areas from intense rainfall. This debris flow model can be applied to design and construct the hydraulic structures like dams and bridges with the consideration of hydraulic forces. The hydraulic structures have been designed referring to the peak discharge and the volume was regarded to be of minor importance. However, the numerical model can show the propagation and the stoppage of the debris flow by the hydraulic structure. The simulation and validation results confirm the usefulness of the model for creating hazard maps and reducing debris flow risk.

4. Conclusions

This study presented the tank simulation model for SWI estimating the water stored beneath the ground and debris flow occurrence using high-resolution terrestrial LiDAR at the Jecheon County in Korea. The DEM derived from the LiDAR enabled the debris flow to be mapped and analyzed

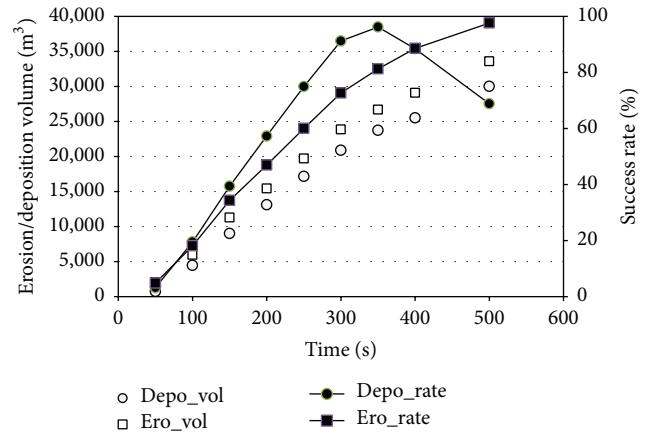


FIGURE 11: Variation of erosion/deposition volume and its success rate.

in great detail. The study area required scanning from 21 locations to capture debris flow track geometry and these 21 locations were combined to one dataset. The morphological change associated with the debris flow and the affected area and total erosion/deposition volume by debris flow were calculated. The estimated volumes of erosion and deposition are 32,847 m³ and 22,889 m³, respectively. The estimated results of affected area and erosion/deposition volume by debris flow were compared with two-dimensional numerical simulation results. We adopted Takahashi model for the friction terms, which treats a debris flow as a dilatant fluid and is governed by Navier-Stokes and continuity equations. The simulation results agreed well with the debris flow track, and a high success rate of over 90% was achieved with simulation time of 300 s. A comparison of the simulated and surveyed results based on the deposition volume yields a success rate of over 97% at 350 s simulation time. The erosion volume success rate reaches the highest value at 500 s simulation time. It was thought that this delayed result is probably due to the soil depth limitation in the model assumptions. These results revealed both the area affected by the debris flow and the spatial distribution of sediments with reasonable accuracy for most of the study area. The simulation and validation results confirm the usefulness of the model for creating hazard maps and reducing debris flow risk. These results suggest some important considerations for technicians dealing with the protection of the mountain areas from intense rainfall.

Conflict of Interests

The author declares that there is no conflict of interests regarding the publication of this paper.

Acknowledgment

This research was supported by a grant (“Development of Multi-Function Debris Flow Control Technique Considering Extreme Rainfall Event”) [MPSS-NH-2014-74] from the National Hazard Mitigation Research Group, Ministry of Public Safety and Security of Korea.

References

- [1] P. Ghilardi, L. Natale, and F. Savi, "Modeling debris flow propagation and deposition," *Physics and Chemistry of the Earth Part C: Solar, Terrestrial & Planetary Science*, vol. 26, no. 9, pp. 651–656, 2001.
- [2] M. Jakob, "A size classification for debris flows," *Engineering Geology*, vol. 79, no. 3–4, pp. 151–161, 2005.
- [3] D. Kim, S. Im, S. H. Lee, Y. Hong, and K.-S. Cha, "Predicting the rainfall-triggered landslides in a forested mountain region using TRIGRS model," *Journal of Mountain Science*, vol. 7, no. 1, pp. 83–91, 2010.
- [4] D. W. Park, N. V. Nikhil, and S. R. Lee, "Landslide and debris flow susceptibility zonation using TRIGRS for the 2011 Seoul landslide event," *Natural Hazards and Earth System Sciences*, vol. 13, no. 11, pp. 2833–2849, 2013.
- [5] T. Mizuyama, "Structural countermeasures for debris flow disasters," *International Journal of Erosion Control Engineering*, vol. 1, no. 2, pp. 38–43, 2008.
- [6] M. Berti and A. Simoni, "Prediction of debris flow inundation areas using empirical mobility relationships," *Geomorphology*, vol. 90, no. 1–2, pp. 144–161, 2007.
- [7] M. Hürlimann, D. Rickenmann, V. Medina, and A. Bateman, "Evaluation of approaches to calculate debris-flow parameters for hazard assessment," *Engineering Geology*, vol. 102, no. 3–4, pp. 152–163, 2008.
- [8] M. Portilla, G. Chevalier, and M. Hürlimann, "Description and analysis of the debris flows occurred during 2008 in the Eastern Pyrenees," *Natural Hazards and Earth System Science*, vol. 10, no. 7, pp. 1635–1645, 2010.
- [9] C. S. Magirl, P. G. Griffiths, and R. H. Webb, "Analyzing debris flows with the statistically calibrated empirical model LAHARZ in southeastern Arizona, USA," *Geomorphology*, vol. 119, no. 1–2, pp. 111–124, 2010.
- [10] T. Takahashi, *Debris Flow*, Balkema, Rotterdam, The Netherlands, 1991.
- [11] B. Hunt, "Newtonian fluid mechanics treatment of debris flows and avalanches," *Journal of Hydraulic Engineering*, vol. 120, no. 12, pp. 1350–1363, 1994.
- [12] R. M. Iverson, M. E. Reid, and R. G. LaHusen, "Debris-flow mobilization from landslides," *Annual Review of Earth and Planetary Sciences*, vol. 25, pp. 85–138, 1997.
- [13] H. M. Blijenberg, "Application of physical modelling of debris flow triggering to field conditions: limitations posed by boundary conditions," *Engineering Geology*, vol. 91, no. 1, pp. 25–33, 2007.
- [14] Z. Han, G. Chen, Y. Li et al., "Numerical simulation of debris-flow behavior incorporating a dynamic method for estimating the entrainment," *Engineering Geology*, vol. 190, pp. 52–64, 2015.
- [15] B. Q. Luna, A. Remaître, T. W. J. van Asch, J.-P. Malet, and C. J. van Westen, "Analysis of debris flow behavior with a one dimensional run-out model incorporating entrainment," *Engineering Geology*, vol. 128, pp. 63–75, 2012.
- [16] G. T. Aronica, G. Biondi, G. Brigandi, E. Cascone, S. Lanza, and G. Randazzo, "Assessment and mapping of debris-flow risk in a small catchment in eastern Sicily through integrated numerical simulations and GIS," *Physics and Chemistry of the Earth Parts A/B/C*, vol. 49, pp. 52–63, 2012.
- [17] J. McKean and J. Roering, "Objective landslide detection and surface morphology mapping using high-resolution airborne laser altimetry," *Geomorphology*, vol. 57, no. 3–4, pp. 331–351, 2004.
- [18] R.-F. Chen, K.-J. Chang, J. Angelier et al., "Topographical changes revealed by high-resolution airborne LiDAR data: the 1999 Tsaoling landslide induced by the Chi-Chi earthquake," *Engineering Geology*, vol. 88, no. 3–4, pp. 160–172, 2006.
- [19] J. Iwahashi, I. Kamiya, and H. Yamagishi, "High-resolution DEMs in the study of rainfall- and earthquake-induced landslides: use of a variable window size method in digital terrain analysis," *Geomorphology*, vol. 153–154, pp. 29–38, 2012.
- [20] G. Priestnall, J. Jaafar, and A. Duncan, "Extracting urban features from LiDAR digital surface models," *Computers, Environment and Urban Systems*, vol. 24, no. 2, pp. 65–78, 2000.
- [21] H. X. Volker, T. A. Wasklewicz, and M. A. Ellis, "A topographic fingerprint to distinguish alluvial fan formative processes," *Geomorphology*, vol. 88, no. 1–2, pp. 34–45, 2007.
- [22] M. Cavalli, P. Tarolli, L. Marchi, and G. D. Fontana, "The effectiveness of airborne LiDAR data in the recognition of channel-bed morphology," *Catena*, vol. 73, no. 3, pp. 249–260, 2008.
- [23] G. Ventura and G. Vilaro, "Emplacement mechanism of gravity flows inferred from high resolution Lidar data: the 1944 Somma-Vesuvius lava flow (Italy)," *Geomorphology*, vol. 95, no. 3–4, pp. 223–235, 2008.
- [24] S. A. White and Y. Wang, "Utilizing DEMs derived from LIDAR data to analyze morphologic change in the North Carolina coastline," *Remote Sensing of Environment*, vol. 85, no. 1, pp. 39–47, 2003.
- [25] A. Vianello, M. Cavalli, and P. Tarolli, "LiDAR-derived slopes for headwater channel network analysis," *Catena*, vol. 76, no. 2, pp. 97–106, 2009.
- [26] P. Tarolli and G. D. Fontana, "Hillslope-to-valley transition morphology: new opportunities from high resolution DTMs," *Geomorphology*, vol. 113, no. 1–2, pp. 47–56, 2009.
- [27] N. F. Glenn, D. R. Streutker, D. J. Chadwick, G. D. Thackray, and S. J. Dorsch, "Analysis of LiDAR-derived topographic information for characterizing and differentiating landslide morphology and activity," *Geomorphology*, vol. 73, no. 1–2, pp. 131–148, 2006.
- [28] S. A. Dunning, C. I. Massey, and N. J. Rosser, "Structural and geomorphological features of landslides in the Bhutan Himalaya derived from Terrestrial Laser Scanning," *Geomorphology*, vol. 103, no. 1, pp. 17–29, 2009.
- [29] W. Zhang and D. R. Montgomery, "Digital elevation model grid size, landscape representation, and hydrologic simulations," *Water Resources Research*, vol. 30, no. 4, pp. 1019–1028, 1994.
- [30] L. Claessens, G. B. M. Heuvelink, J. M. Schoorl, and A. Veldkamp, "DEM resolution effects on shallow landslide hazard and soil redistribution modelling," *Earth Surface Processes and Landforms*, vol. 30, no. 4, pp. 461–477, 2005.
- [31] P. Tarolli and D. G. Tarboton, "A new method for determination of most likely landslide initiation points and the evaluation of digital terrain model scale in terrain stability mapping," *Hydrology and Earth System Sciences*, vol. 10, no. 5, pp. 663–677, 2006.
- [32] H. Hu, T. M. Fernandez-Steege, M. Dong, and R. Azzam, "Numerical modeling of LiDAR-based geological model for landslide analysis," *Automation in Construction*, vol. 24, pp. 184–193, 2012.
- [33] J.-C. Du and H.-C. Teng, "3D laser scanning and GPS technology for landslide earthwork volume estimation," *Automation in Construction*, vol. 16, no. 5, pp. 657–663, 2007.
- [34] J.-P. Malet, D. Laigle, A. Remaître, and O. Maquaire, "Triggering conditions and mobility of debris flows associated to complex earthflows," *Geomorphology*, vol. 66, pp. 215–235, 2005.

- [35] E. J. Gabet, D. W. Burbank, J. K. Putkonen, B. A. Pratt-Sitaula, and T. Ojha, "Rainfall thresholds for landsliding in the Himalayas of Nepal," *Geomorphology*, vol. 63, no. 3-4, pp. 131-143, 2004.
- [36] R. K. Dahal and S. Hasegawa, "Representative rainfall thresholds for landslides in the Nepal Himalaya," *Geomorphology*, vol. 100, no. 3-4, pp. 429-443, 2008.
- [37] K. Sassa, H. Fukuoka, F. Wang, G. Wang, K. Okada, and H. Marui, "Landslide disasters triggered by the 2004 mid-niigata prefecture earthquake in Japan," *Annuals of Disaster Prevention Research Institute*, vol. 49, pp. 119-136, 2006.
- [38] D. Brunsten, "Some geomorphological considerations for the future development of landslide models," *Geomorphology*, vol. 30, no. 1-2, pp. 13-24, 1999.
- [39] C. Wang, T. Esaki, M. Xie, and C. Qiu, "Landslide and debris-flow hazard analysis and prediction using GIS in Minamata-Hougawachi area, Japan," *Environmental Geology*, vol. 51, no. 1, pp. 91-102, 2006.
- [40] T. Takahashi, H. Nakagawa, T. Harada, and Y. Yamashiki, "Routing debris flows with particle segregation," *Journal of Hydraulic Engineering*, vol. 118, no. 11, pp. 1490-1507, 1992.
- [41] D. Salciarini, J. W. Godt, W. Z. Savage, R. L. Baum, and P. Conversini, "Modeling landslide recurrence in Seattle, Washington, USA," *Engineering Geology*, vol. 102, no. 3-4, pp. 227-237, 2008.
- [42] S. J. Conway, A. Decaulne, M. R. Balme, J. B. Murray, and M. C. Townner, "A new approach to estimating hazard posed by debris flows in the Westfjords of Iceland," *Geomorphology*, vol. 114, no. 4, pp. 556-572, 2010.
- [43] P. Brufau, P. García-Navarro, P. Ghilardi, L. Natale, and F. Savi, "1D mathematical modelling of debris flow," *Journal of Hydraulic Research*, vol. 38, no. 6, pp. 435-446, 2000.
- [44] T. Takahashi, "A review of Japanese debris flow research," *International Journal of Erosion Control Engineering*, vol. 2, no. 1, pp. 1-14, 2009.
- [45] M.-H. Li, R.-T. Sung, J.-J. Dong, C.-T. Lee, and C.-C. Chen, "The formation and breaching of a short-lived landslide dam at Hsiaolin Village, Taiwan—part II: simulation of debris flow with landslide dam breach," *Engineering Geology*, vol. 123, no. 1-2, pp. 60-71, 2011.

Research Article

Spatial Variability and Periodicity of Precipitation in the Middle Reaches of the Yellow River, China

Yi He,¹ Xingmin Mu,^{1,2,3} Peng Gao,^{2,3} Guangju Zhao,^{2,3} Fei Wang,^{2,3}
Wenyi Sun,^{2,3} and Yuqing Zhang⁴

¹College of Water Resources and Architectural Engineering, Northwest A&F University, Yangling, Shaanxi 712100, China

²Institute of Soil and Water Conservation, Northwest A&F University, Yangling, Shaanxi 712100, China

³Institute of Soil and Water Conservation, Chinese Academy of Sciences and Ministry of Water Resources, Yangling, Shaanxi 712100, China

⁴School of Atmospheric Science, Nanjing University of Information Science & Technology, Nanjing 210044, China

Correspondence should be addressed to Xingmin Mu; xmmu@ms.iswc.ac.cn and Wenyi Sun; sunwy@ms.iswc.ac.cn

Received 30 April 2015; Revised 3 June 2015; Accepted 10 June 2015

Academic Editor: Steffen Mischke

Copyright © 2016 Yi He et al. This is an open access article distributed under the Creative Commons Attribution License, which permits unrestricted use, distribution, and reproduction in any medium, provided the original work is properly cited.

Rainfall is one of the most important reasons causing the soil erosion in the Loess Plateau. The precipitation across the most severely eroded areas in middle reaches of the Yellow River (MRYR), China, was investigated by analyzing the precipitation of flood season (P_f) and precipitation of main flood season (P_{mf}) from 26 meteorological stations during the period from 1958 to 2013. The empirical orthogonal function (EOF), ensemble empirical mode decomposition, and Hurst exponent are used to detect spatial, multiscale characteristics of periodicity and trend for precipitation. The results show that there exist quasi-3- and quasi-6-year interannual periods and quasi-11- and quasi-28-year interdecadal scale periods for P_f and P_{mf} . However, periodical features in most of the study area are not statistically noticeable. Moreover, first EOFs indicated precipitation was affected by the large-scale circulation patterns, and the spatial patterns of the second EOFs indicated an obviously north-south gradient in the MRYR, whereas the third EOFs displayed east-west patterns. Hurst exponent analysis indicates that precipitation in P_f and P_{mf} will continue the current trends in the future. These findings can provide important implications for ecological restoration and farming operations across the study region.

1. Introduction

Time series analysis of hydroclimatic observations provides direct information about hydrological changes and, therefore, plays a key role in understanding and managing water resources. Increasing knowledge is needed on large-scale variations of hydrological variables and water cycle parameters in order to assess their potential impact on water resources availability and hydrologic hazards. Precipitation is a major factor in agriculture and in recent years interest has increased in learning about precipitation variability for periods of months to years. Therefore, the spatial and temporal variability of the precipitation time series is important from both the scientific and practical point of view [1, 2].

For the last several years, a number of researches have been used to measure rainfall variability with various

approaches in many different regions in the world; for example, Barros et al. [3] showed that most of the annual precipitation trends since 1960 in the Southern South America to the east of the Andes region could be described by the first two rainfall eigenvectors of the principal component analysis (PCA). Coulibaly [4] used the wavelet and cross-wavelet to identify and describe spatial and temporal variability in Canadian seasonal precipitation and gained further insights into the dynamical relationship between the seasonal precipitation and the dominant modes of climate variability in the northern hemisphere. Feidas et al. [5] analyzed the precipitation in Greece and found that there was a link between precipitation variability in Greece and the Mediterranean pressure oscillation. Modarres and da Silva [6] analyzed the time series of annual rainfalls, number of rainy-days per year, and monthly rainfall of 20 stations by

the Mann-Kendall test to assess climate variability in the arid and semiarid regions of Iran. Liu et al. [7] investigated the spatial and temporal patterns of the precipitation trends in the Yellow River Basin, China, and showed a decreasing trend in most of stations. Li et al. [8] evaluated the variation of annual and seasonal precipitation by using the Mann-Kendall test and Hurst exponent methods in Xinjiang, China. Xue et al. [9] decomposed the autumn precipitation series by using ensemble empirical mode decomposition (EEMD) method in the Weihe River Basin and got the period characteristics of multiscales in precipitation. Yu et al. [10] investigated precipitation signals and its impact assessment on soil hydrological process by using Hilbert-Huang transform and continuous wavelet transform approaches.

The Yellow River is noted for its small water and huge sediment discharge in the world. The middle reaches of the Yellow River flow through the Loess Plateau, rainfall is one of the most important reasons causing the soil erosion in this region. The water from the middle reaches accounted for 44.3% of the Yellow River streamflow, but the sediment has accounted for 88.2% of the Yellow River sediment [11]. The annual average sediment discharge of the Yellow River was 16×10^8 t (according to the observed data from Shan County hydrological station during 1919–1960). In recent years, many studies have reported significant decrease beyond expectations in streamflow and sediment discharge in the Middle Yellow River [11–17]. The observed average annual streamflow from Toudaoguai station to Tongguan station (located in the Middle Yellow River) was 124.9×10^8 m³ during 1952–2013, while it was 68.9×10^8 m³ during 2000–2013. The 56.0×10^8 m³ decrease in streamflow accounted for 44.8% of the average annual streamflow (1952–2013) (the Ministry of Water Resources of China, 2014).

So far, most of the studies for precipitation variation were focused on analysis in yearly, while fewer studies were conducted on the periodicity of precipitation time series for identifying climate change signals in the middle reaches of the Yellow River. The periodicity of precipitation is a key factor for soil erosion, especially in the Loess Plateau. Therefore, the objectives of this study were to investigate temporal and spatial variation characteristics of precipitation of flood season precipitation (P_f) and precipitation of main flood season (P_{mf}) using monthly precipitation datasets from 1958 to 2013 and to explore the trends of P_f and P_{mf} in the future by Hurst exponent. The results may have important implications on water management and environmental phenomena, such as soil instability, erosion, and desertification.

2. Study Area and Data

2.1. Study Region. The study area is situated in the arid and subhumid Loess Plateau region in the middle reaches of the Yellow River (MRYR), between Hekouzhen (Toudaoguai) and Tongguan section, with an area of 290 000 km² between 104°–113°E and 32°–40°N, accounting for 38% of Yellow River Basin area. It encompasses parts of 159 counties, across the Ningxia Hui Autonomous Region (Ningxia), Shanxi, Inner Mongolia Autonomous Region (Inner Mongolia), and the

TABLE 1: Geographical coordinates, annual mean precipitation (P_y) for 26 meteorological stations across the middle reaches of the Yellow River.

Station (abbreviation)	Latitude (°N)	Longitude (°E)	Elevation (m)	P_y (mm)
Youyu (YY)	40.00	112.45	1345.8	421.6
Hequ (HQ)	39.38	111.15	861.5	410.4
Wuzhai (WZ)	38.92	111.82	1401.0	472.5
Xingxian (XX)	38.47	111.13	1012.6	492.9
Yulin (YL)	38.27	109.78	1157.0	406.9
Taiyuan (TY)	37.78	112.55	778.3	443.7
Hengshan (HS)	37.93	109.23	1111.0	377.6
Suide (SD)	37.50	110.22	929.7	452.7
Lishi (LS)	37.50	111.10	950.8	491.1
Jiexiu (JX)	37.03	111.92	743.9	465.5
Wuqi (WQ)	36.92	108.17	1331.4	469.0
Yan'an (YA)	36.60	109.50	958.5	542.7
Xixian (XX)	36.70	110.95	1052.7	524.5
Linfen (LF)	36.07	111.50	449.5	484.7
Huanxian (HX)	36.58	107.30	1255.6	434.2
Luochuan (LC)	35.82	109.50	1159.8	612.3
Yuncheng (YC)	35.05	111.05	365.0	528.6
Xiji (XJ)	35.97	105.72	1916.5	410.3
Pingliang (PL)	35.55	106.67	1346.6	501.3
Xifeng (XF)	35.73	107.63	1421.0	550.3
Changwu (CW)	35.20	107.80	1206.5	581.3
Tongchuan (TC)	35.08	109.07	978.9	581.6
Tianshui (TS)	34.58	105.75	1141.7	522.4
Baoji (BJ)	34.35	107.13	612.4	655.7
Wugong (WG)	34.25	108.22	447.8	602.7
Xi'an (XA)	34.30	108.93	397.5	556.7

Gansu and Shaanxi provinces. The natural environment is featured by a gradual increase in precipitation from northwest to southeast, concentrated mainly in summer, and dominated usually in the form of rainstorms. A digital elevation model (DEM) of the region is shown in Figure 1. The annual sediment transportation into the Yellow River accounts for 90% of the total sediment discharge, making the MRYR one of the most soil-eroded areas of the Loess Plateau. The area has thick (50–80 m) loess layers. The particle composition is mainly fine sand, silt (up to 50% of the total), and clay. The loess has high porosity and is prone to landslides. The soil is typical black loam soil with a loose structure that is readily degraded [18].

2.2. Data. The daily and monthly rainfall data of 26 national meteorological stations (apart from the mountain station) used in this work were extracted from the National Meteorological Information Centre (NMIC) (Table 1 and Figure 1), including daily precipitation (P_d , mm), monthly precipitation (P_m , mm), and yearly precipitation (P_y , mm) from 1958 to 2013. The dataset has been quality ensured by NMIC. We

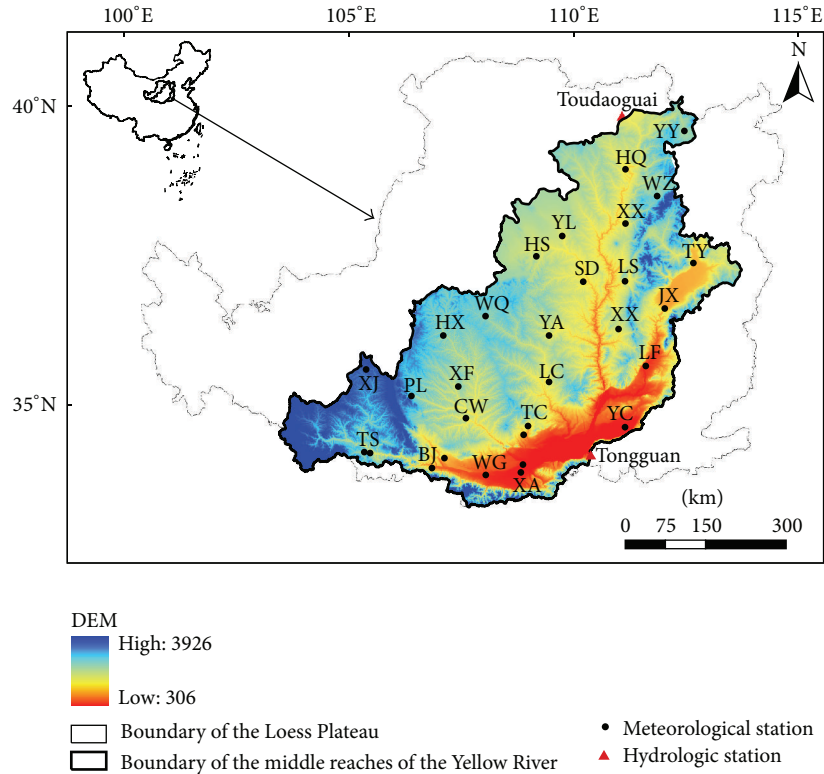


FIGURE 1: Location of the selected 26 meteorological stations on a DEM of middle reaches of the Yellow River, China.

performed further routine quality assessment and error correction procedures on the data following methods described by Peterson et al. [19]. Missing values are infrequent (during certain months in 1968 precipitation data was missing from Wuqi station, during certain months in 1969 precipitation data was missing from Lishi station, and during one month in 2013 precipitation data was missing from Baoji station). The missing data in these three stations were processed in the following ways: (1) if data were missing only for 1 day, the missing data were replaced by the average value of its neighboring days and (2) if consecutive days were missed, those were estimated by simple linear interpolation method using the data of neighboring stations ($R^2 > 0.95$) [20, 21]. Due to urbanization, data from Yaoxian station were used instead of Tongchuan station after 1999; data from Maiji station were used instead of Tianshui station after 2004; data from Fengxiang station were used instead of Baoji station after 2005; data from Jinghe station were used instead of Xi'an station after 2006. Considering the hydrogeology condition in study area, the distribution of precipitation in rainy season is the driving force for soil erosion and flood for this region, because it is well known that individual rainfall events can contribute approximately 60% to 90% of the yearly rainfall total [22]. In general, the flood season refers to June–October, and main flood season refers to July–August [17, 23], in the Loess Plateau. Consequently, this study focused only on precipitation in flood season and main flood season, which are critical agricultural months in the study area.

3. Methodology

3.1. Empirical Orthogonal Function. The empirical orthogonal function (EOF) had been used in atmospheric science since the early 1950s and EOF techniques are deeply rooted in statistics, especially in principal component analysis [24, 25]. It provides a compact description of the temporal and spatial variability of a dataset of a single variable in terms of orthogonal components or, also called, statistical “modes.” The main features of spatial variability can be outlined using EOF analysis. Essentially, the EOF reduces the data dimensionality, and the smaller set of uncorrelated variables is much easier to understand and further analyze than a larger set of correlated variables. Therefore, the EOF has become a popular tool in meteorology, geology, and geography [26–28]. More details on EOF can be found in Kim et al. [29].

3.2. Ensemble Empirical Mode Decomposition. EEMD, a fundamental part of the Hilbert-Huang transform, is an adaptive method that decomposes a time series into intrinsic mode functions (IMFs) ranging from high- to low-frequency modes, each of which represents a specific frequency range, and a long-term trend [30]. The first IMF has the highest frequency and so on. The sum of these IMFs and the long-term trend reproduces the original time series. The length of the time series determines the number of IMFs. It improves upon the empirical mode decomposition (EMD) method [31, 32], which is an adaptive data analysis method to decompose any

complicated data series into a finite and often small number of amplitude-frequency modulated oscillatory components. Based on EMD algorithm [31], EEMD method can be briefly described as follows [33]: Step 1: set the ensemble number and the amplitude of the added white noise; Step 2: add a white noise series to the targeted data with the set amplitude; Step 3: decompose the data with added white noise into IMFs; Step 4: repeat Steps 2 and 3 again and again, but with different white noise series each time; then, the final ensemble means of corresponding IMFs of the decompositions are obtained. The basics and effectiveness of this method applied to geophysical data analyses have been documented in many recent works [32–34]. For more details about EMD and EEMD, refer to Wu and Huang [33]. In this study, the ensemble number is set to 100 and the amplitude of added white noise is set to 0.2 times of standard deviation of that of the data based on suggestion by Wu and Huang [33].

3.3. Hurst Exponent Analysis. The fractal theory for time series research has been widely applied in climate change, geography, and other fields [35], used to analyze future precipitation trend in this study. The Hurst exponent, estimated by R/S analysis, is used as a measure of the long-term memory of the time series. Hurst's index (H) has a strong ability to predict future trends for a time series in relation to past trends, and it has been used to predict hydrological and climatological processes [8, 36]. H ranges between 0 and 1, where (1) $H = 0.5$ means the various essential elements are completely independent and the change is random; (2) $0.5 < H < 1$ shows that the time series has a long-term trend which is likely to continue in the future; the closer the H value to 1, the stronger the continuity; and (3) $0 < H < 0.5$ also indicates the time series has a long-term trend. However, its future tendency will be the opposite; the closer the H value to 0, the stronger the reverse tendency.

4. Results and Discussion

4.1. Annual Variability of Flood Season Precipitation and Main Flood Season Precipitation. The mean annual precipitation (P_y), precipitation of flood season (P_f), and precipitation of main flood season (P_{mf}) were 499.9 mm, 383.3 mm, and 211.0 mm in the research region, respectively (Table 2). The P_f and P_{mf} account for 76.67% and 42.21% of the annual mean precipitation, respectively. The difference between the maximum and minimum values for each variable was small. The coefficients of variation (CVs) of P_y , P_f , and P_{mf} were 0.166, 0.190, and 0.254, respectively, showing that all of their changes are stable. Both the annual average precipitation of flood season and the annual average precipitation of main flood season had no significant trends with a linear increase from 1958 to 2013 (Figure 2). Moreover, there was significant ($P < 0.01$) synchronized variation between the P_f and P_{mf} .

4.2. Spatial Patterns of the Precipitation by EOF. The EOFs of the precipitation series in flood season were calculated during 1958–2013. The significance of eigenvectors derived from EOF was tested with North's method [37]. The results showed

TABLE 2: Statistics for annual precipitation (P_y), precipitation of flood season (P_f), and precipitation of main flood season (P_{mf}) of the Middle Yellow River from 1958 to 2013.

Statistic	P_y (mm)	P_f (mm)	P_{mf} (mm)
Mean	499.9	383.3	211.0
Minimum	335.3	231.1	103.9
(Year)	(1997)	(1997)	(1991)
Maximum	758.1	549.1	345.0
(Year)	(1964)	(1964)	(1958)
Median	487.0	373.5	214.4
Standard deviation	82.9	72.8	53.6
Confidence levels (95.0%)	22.20	19.49	14.30
Coefficients of variation	0.166	0.190	0.254

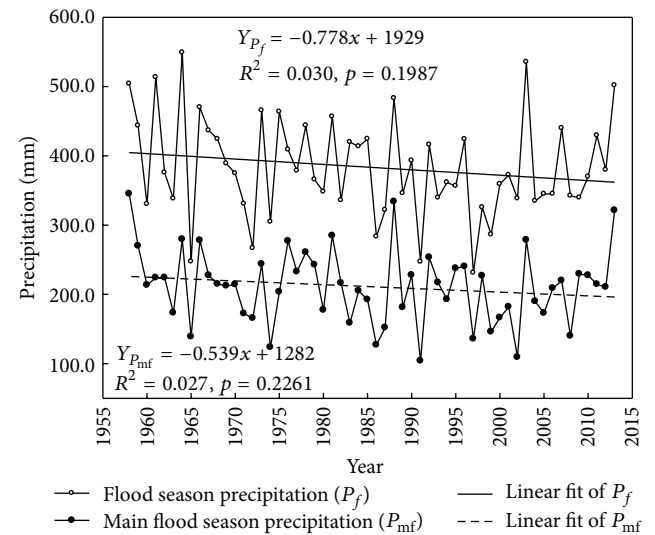


FIGURE 2: Mean annual flood season and main flood season precipitation in the middle reaches of the Yellow River during 1958–2013.

that the first three eigenvectors were valuable signals both in flood season and main flood season. The first three EOFs during the study period explained approximately 45.2%, 20.8%, and 6.0% of total variance, respectively. It is generally assumed that those EOFs, whose accumulated variance is more than 70% of the total variance, have significance in explaining the original data [28, 29]. In this study, the first three EOFs explained 72% of the total variance in flood season precipitation. Therefore, the first three EOFs were used in this study to explain the original data. The EOFs of the precipitation series in main flood season were also calculated during the study period. The first three EOFs explained 71.8% of the total variance in main flood season. Therefore, the first three EOFs of precipitation in flood season were also used in this study to explain the original data.

The first EOF values for P_f and P_{mf} were both positive (Figure 3), which indicated the precipitation was affected by the East Asian monsoon. The second EOFs for both P_f and P_{mf} indicated that precipitation had obvious north-south differences, and the zero contours for P_f and P_{mf} were

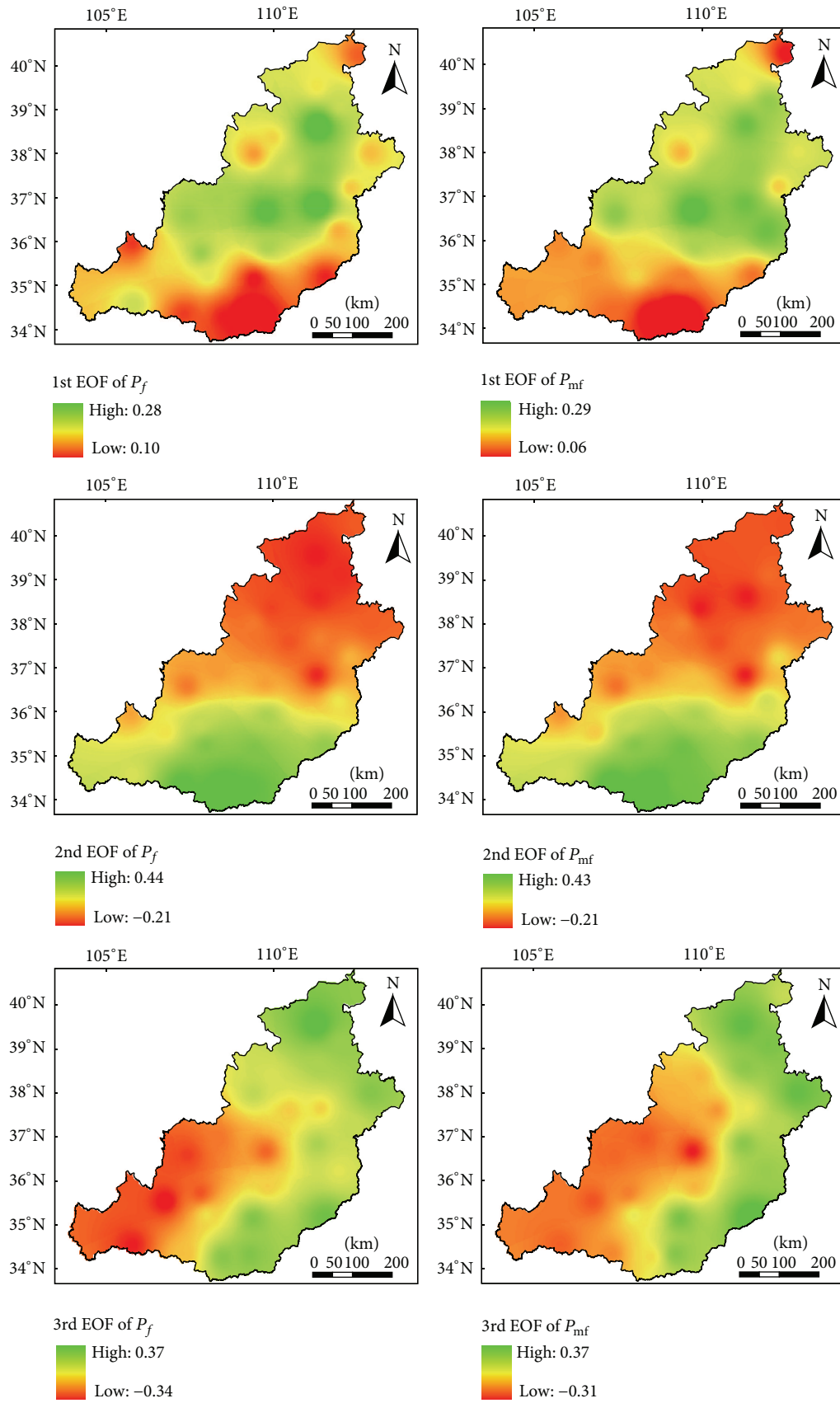


FIGURE 3: First three EOFs of the P_f and P_{mf} in MRYR.

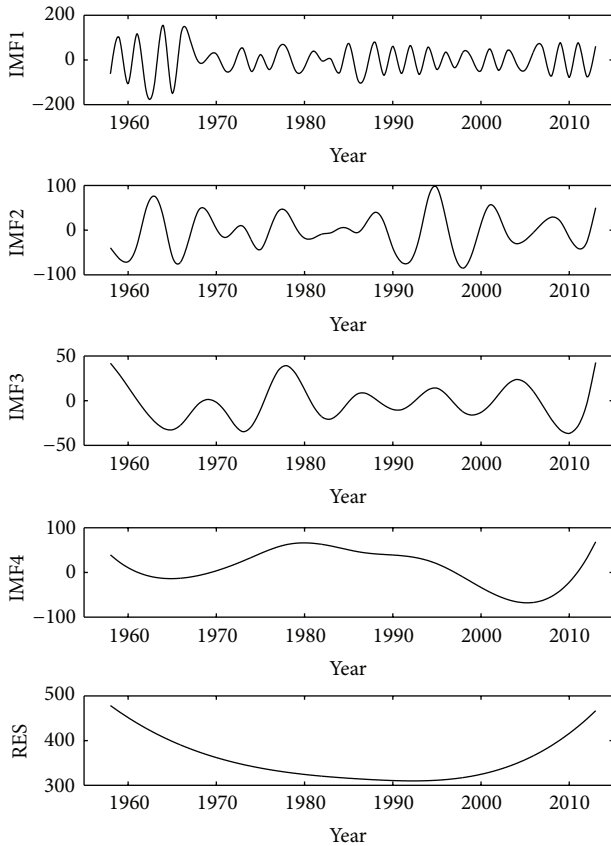


FIGURE 4: EEMD of the P_f time series from 1958 to 2013 at the Suide station.

both located in the area around Linfen, Luochuan, Xifeng, and Pingliang. It means that the trend in the precipitation variation is opposite for the northern and the southern areas of the study area, which reveals that precipitation increased in the northern area and decreased in the southern area. In the third EOFs, the zero contours for P_f and P_{mf} were both located in the area around Yulin, Suide, Luochuan, and Wugong, which indicated an approximately east-west direction.

4.3. Decomposing Annual Flood Season and Main Flood Season Rainfall Time Series Using EEMD. By employing the EEMD technique, the original annual P_f and P_{mf} time series from 26 stations are decomposed into four independent IMFs and one residue, respectively. For example, the results for the Suide station are illustrated in Figures 4 and 5. It can be observed that precipitation data are decomposed into IMFs, and we can also see that the IMFs present changing frequencies, amplitudes, and wavelengths. For all IMFs, IMF1 has the maximum amplitude, highest frequency, and shortest wavelength. The following IMF components decrease in the amplitude and frequency and increase in the wavelength. The last residue (RES) is a mode slowly varying around the long-term average.

There are few periodic variabilities of P_f in the MRYS. Both the periodicity properties of regional precipitation

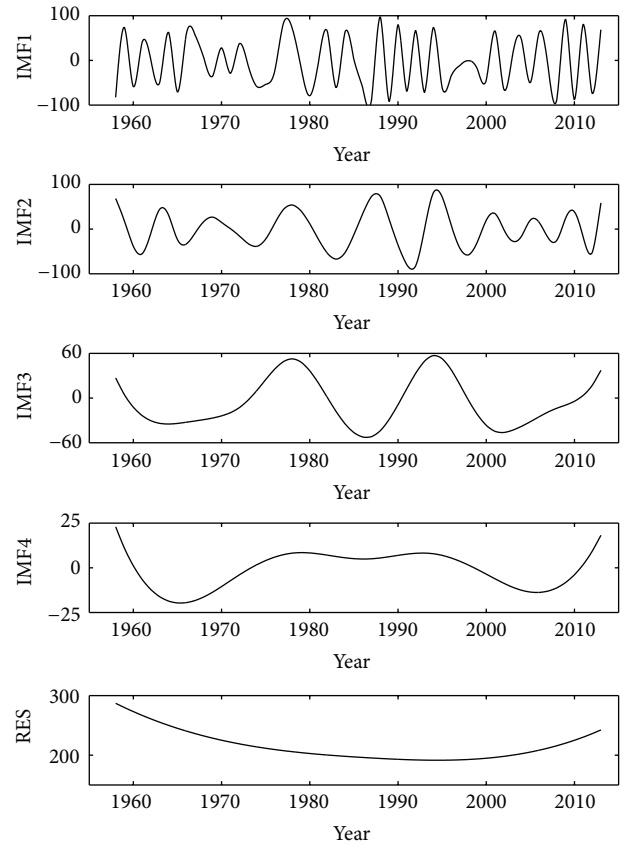


FIGURE 5: EEMD of the P_{mf} time series from 1958 to 2013 at the Suide station.

series and the periodicity properties of P_f at each station show few periodic variabilities (Table 3). The periodicity of IMF1 at each station ranges from a minimum of 2.3 to a maximum of 3.1, the periodicity of IMF2 at each station ranges from a minimum of 4.3 to a maximum of 6.2, the periodicity of IMF3 at each station ranges from a minimum of 8 to a maximum of 14, and the periodicity of IMF4 at each station ranges from a minimum of 18.6 to a maximum of 48.1. However, only the periodicity of IMF2 at Linfen station and the periodicity of IMF4 at Suide, Lishi, and Yan'an station pass the statistical significance.

The periodic variability of P_{mf} at each mode (Table 4) is similar to that in P_f . Only the periodicity of IMF1 at Hengshan station, the periodicity of IMF2 at Xifeng station, the periodicity of IMF3 at Suide and Xixian station, and the periodicity of IMF4 at Lishi, Yan'an, Yuncheng, and Baoji station pass the statistical significance. It also means that there is less periodic variability of P_{mf} in the MRYS.

Though there were few stations passing the significant test for precipitation period, the IMF2 component of Linfen station for P_f , the IMF1 component of Hengshan station, and the IMF2 component of Xifeng station for P_{mf} in Tables 3 and 4 showed that there were obvious periodic variability within 3–4 years and 6–8 years, respectively. According to multiple timescale analysis of sea surface temperature (SST) data in Niño-3 region (5°N–5°S, 150°–90°W) during 1881–2002 [38],

TABLE 3: The mean periods of various time-scale components for P_f during 1958–2013 in the MRYR obtained by the EEMD.

Station (abbreviation)	IMF1	IMF2	IMF3	IMF4
Regional precipitation (MRYR)	2.5	4.3	9.3	27.9
Youyu (YY)	2.3	5.6	11.2	21.2
Hequ (HQ)	2.7	5.6	11.2	27.9
Wuzhai (WZ)	2.8	5.6	11.2	19.2
Xingxian (XX)	2.5	5.6	11.2	24.2
Yulin (YL)	2.9	5.6	11.2	29.0
Taiyuan (TY)	2.7	5.1	9.3	21.4
Hengshan (HS)	2.8	4.7	8.0	27.3
Suide (SD)	2.5	5.6	9.3	28.1**
Lishi (LS)	2.5	5.6	11.2	46.1*
Jiexiu (JX)	2.5	4.3	9.3	27.8
Wuqi (WQ)	2.5	5.6	9.3	18.6
Yan'an (YA)	2.4	5.6	9.3	27.7*
Xixian (XX)	2.3	4.7	9.3	29.0
Linfen (LF)	2.7	5.6*	9.3	22.7
Huanxian (HX)	2.4	5.6	11.2	28.3
Luochuan (LC)	2.7	4.7	9.3	26.5
Yuncheng (YC)	2.8	5.1	11.2	30.3
Xiji (XJ)	2.9	6.2	14.0	27.9
Pingliang (PL)	2.3	4.7	9.3	18.7
Xifeng (XF)	2.8	6.2	11.2	48.1
Changwu (CW)	2.8	5.1	9.3	23.4
Tongchuan (TC)	3.1	5.6	11.2	27.0
Tianshui (TS)	2.7	4.7	11.2	28.3
Baoji (BJ)	2.7	5.1	9.3	29.5
Wugong (WG)	2.8	4.7	8.0	23.5
Xi'an (XA)	2.9	5.6	9.3	26.9

Note: * and ** represent significant trend tested at 0.1 and 0.05 significant levels, respectively.

there was also obvious periodic variability within 3–4 years and 6–8 years. Hence, the high-frequency components of annual flood season and main flood season precipitation series were consistent with SST which demonstrated that the short-term variation of annual flood season and main flood season precipitation in some area of the study area may be affected by SST. Further study will be required to explain the observed precipitation periodicities associating with the influencing climatic factors.

4.4. Future Trend of Flood Season and Main Flood Season Precipitation. The Hurst index provides statistical predictions concerning future trend. The Hurst index based on the P_f and P_{mf} time series at 26 stations from 1958 to 2013 is shown in Table 5. The H value of P_f ranges from a minimum of 0.49 to a maximum of 0.73. An H value which is greater than 0.5 refers to the persistence of the series, which indicates the same trend in the time series in the future, with a greater value for more persistence. This means that there is a long-term persistence

TABLE 4: The mean periods of various time-scale components for P_{mf} during 1958–2013 in the MRYR obtained by the EEMD.

Station (abbreviation)	IMF1	IMF2	IMF3	IMF4
Regional precipitation (MRYR)	2.8	5.6	9.3	18.8
Youyu (YY)	2.4	4.3	9.3	35.1
Hequ (HQ)	2.8	6.2	14.0	29.4
Wuzhai (WZ)	2.8	5.6	11.2	27.6
Xingxian (XX)	2.5	5.1	11.2	18.5
Yulin (YL)	2.8	5.6	11.2	32.9
Taiyuan (TY)	2.8	5.1	9.3	18.6
Hengshan (HS)	3.3*	6.2	14.0	42.5
Suide (SD)	2.8	6.2	18.7*	24.9
Lishi (LS)	2.8	5.1	11.2	39.6**
Jiexiu (JX)	2.7	5.6	9.3	27.8
Wuqi (WQ)	2.5	4.7	9.3	19.2
Yan'an (YA)	2.8	5.1	14.0	27.9*
Xixian (XX)	2.7	5.1	14.0**	47.6
Linfen (LF)	2.7	5.6	9.3	18.6
Huanxian (HX)	2.5	7.0	14.0	29.9
Luochuan (LC)	2.7	5.6	11.2	27.1
Yuncheng (YC)	3.1	6.2	11.2	50.1*
Xiji (XJ)	2.8	6.2	11.2	19.7
Pingliang (PL)	2.8	5.6	14.0	30.5
Xifeng (XF)	2.8	6.2*	9.3	47.8
Changwu (CW)	2.5	5.1	8.0	24.2
Tongchuan (TC)	3.1	6.2	11.2	28.6
Tianshui (TS)	2.3	4.3	9.3	25.8
Baoji (BJ)	2.7	5.1	11.2	26.3*
Wugong (WG)	2.5	5.1	9.3	26.3
Xi'an (XA)	2.7	5.6	9.3	25.3

Note: * and ** represent significant trend tested at 0.1 and 0.05 significant levels, respectively.

in the variability of precipitation. Most of the stations in the study area have long-term persistence. The stations where there is no long-term persistence in the variability ($H < 0.5$) are Wuzhai and Pingliang station. The main flood season precipitation in the region shows the H value range from a minimum of 0.51 to a maximum of 0.72, indicating the trend will be maintained in the future. The H value of 0.44 for Pingliang station indicates an opposite precipitation trend in the future. The present trends of P_f and P_{mf} for most of the stations are decreasing (see Supplementary Material available online at <http://dx.doi.org/10.1155/2016/9451614>). According to above results of Hurst index, the trends of future precipitation in these stations will be persistent.

5. Conclusions

In this paper, analysis of the trends, periodic variability, and temporal-spatial patterns of the flood season precipitation and main flood season precipitation in the middle reaches of the Yellow River support the following conclusions.

TABLE 5: Hurst exponent analysis for P_f and P_{mf} during 1958–2013 in the MRYR.

Station (abbreviation)	H_1	H_2
Youyu (YY)	0.58	0.64
Hequ (HQ)	0.59	0.59
Wuzhai (WZ)	0.49	0.58
Xingxian (XX)	0.58	0.58
Yulin (YL)	0.65	0.61
Taiyuan (TY)	0.60	0.56
Hengshan (HS)	0.62	0.72
Suide (SD)	0.70	0.61
Lishi (LS)	0.60	0.58
Jiexiu (JX)	0.72	0.61
Wuqi (WQ)	0.52	0.63
Yan'an (YA)	0.64	0.56
Xixian (XX)	0.65	0.56
Linfen (LF)	0.67	0.61
Huanxian (HX)	0.58	0.53
Luochuan (LC)	0.68	0.67
Yuncheng (YC)	0.62	0.61
Xiji (XJ)	0.68	0.56
Pingliang (PL)	0.49	0.44
Xifeng (XF)	0.58	0.60
Changwu (CW)	0.53	0.51
Tongchuan (TC)	0.59	0.53
Tianshui (TS)	0.63	0.64
Baoji (BJ)	0.60	0.66
Wugong (WG)	0.73	0.70
Xi'an (XA)	0.51	0.56

Note: H_1 represented H index of P_f ; H_2 represented H index of P_{mf} .

The first three EOFs for P_f and P_{mf} were selected in this study to identify the spatial-temporal variations of the predominant components. The results indicate that the first EOFs values are all positive, which indicate that the precipitation is affected by similar large-scale circulation patterns. The second EOFs indicate north-south patterns located in the area around Linfen, Luochuan, Xifeng, and Pingliang. Moreover, the third EOFs display east-west patterns located in the area around Yulin, Suide, Luochuan, and Wugong for the study area.

The P_f and P_{mf} in the middle reaches of the Yellow River are subject to a quasi-3-year, quasi-6-year interannual periodical feature based on the EEMD analysis, whereas interdecadal scale periods are dominated by quasi-11-year and quasi-28-year. However, periodicity in most study areas is not significant.

Hurst exponent (H) analysis indicates that the H value is greater than 0.5 in most stations both for P_f and P_{mf} . Thus, the precipitation in P_f and P_{mf} will continue the current trends in the future.

Conflict of Interests

The authors declare that there is no conflict of interests regarding the publication of this paper.

Acknowledgments

This research was supported by the National Natural Science Foundation of China [41371277 and 41271295], the Key Research Program of the Chinese Academy of Sciences [KZZD-EW-04], and Special Fund for Water Conservancy Scientific Research in the Public Welfare [201501049]. The authors were grateful to the anonymous reviewers and the editors who helped improved the quality of this paper.

References

- [1] C. Rodriguez-Puebla, A. H. Encinas, S. Nieto, and J. Garmendia, "Spatial and temporal patterns of annual precipitation variability over the Iberian Peninsula," *International Journal of Climatology*, vol. 18, no. 3, pp. 299–316, 1998.
- [2] I. A. Tošić, "Spatial and temporal variability of winter and summer precipitation over Serbia and Montenegro," *Theoretical and Applied Climatology*, vol. 77, no. 1-2, pp. 47–56, 2004.
- [3] V. Barros, E. Castañeda, and M. Doyle, "Recent precipitation trends in Southern South America to the east of the Andes: an indication of a mode of climatic variability," in *Southern Hemisphere Paleo and Neoclimates*, p. 381, Springer, Berlin, Germany, 2000.
- [4] P. Coulibaly, "Spatial and temporal variability of Canadian seasonal precipitation (1900–2000)," *Advances in Water Resources*, vol. 29, no. 12, pp. 1846–1865, 2006.
- [5] H. Feidas, C. Noullopoulou, T. Makrogiannis, and E. Bora-Senta, "Trend analysis of precipitation time series in Greece and their relationship with circulation using surface and satellite data: 1955–2001," *Theoretical and Applied Climatology*, vol. 87, no. 1–4, pp. 155–177, 2007.
- [6] R. Modarres and V. de P. R. da Silva, "Rainfall trends in arid and semi-arid regions of Iran," *Journal of Arid Environments*, vol. 70, no. 2, pp. 344–355, 2007.
- [7] Q. Liu, Z. Yang, and B. Cui, "Spatial and temporal variability of annual precipitation during 1961–2006 in Yellow River Basin, China," *Journal of Hydrology*, vol. 361, no. 3-4, pp. 330–338, 2008.
- [8] Q. H. Li, Y. N. Chen, Y. J. Shen, X. G. Li, and J. H. Xu, "Spatial and temporal trends of climate change in Xinjiang, China," *Journal of Geographical Sciences*, vol. 21, no. 6, pp. 1007–1018, 2011.
- [9] C.-F. Xue, W. Hou, J.-H. Zhao, and S.-G. Wang, "The application of ensemble empirical mode decomposition method in multiscale analysis of region precipitation and its response to the climate change," *Acta Physica Sinica*, vol. 62, no. 10, Article ID 109203, 2013.
- [10] S. Yu, J. Yang, G. Liu, R. Yao, and X. Wang, "Improvement for the multi-scale periodic characteristics revealing of precipitation signals and its impact assessment on soil hydrological process by combining HHT and CWT approaches," *Natural Hazards and Earth System Science*, vol. 15, no. 3, pp. 393–407, 2015.
- [11] P. Gao, X.-M. Mu, F. Wang, and R. Li, "Changes in streamflow and sediment discharge and the response to human activities in the middle reaches of the Yellow River," *Hydrology and Earth System Sciences*, vol. 15, no. 1, pp. 1–10, 2011.
- [12] D. C. Ran, "Summary on runoff and sedimentation variation research from Hekouzhen to Longmen in the Middle Reaches of the Yellow River," *Journal of Sediment Research*, no. 3, pp. 72–81, 2000 (Chinese).

- [13] J. X. Xu, "Recent tendency of sediment reduction in the middle Yellow River and some countermeasures," *Journal of Sediment Research*, no. 2, pp. 5–10, 2004 (Chinese).
- [14] J. X. Xu, "Trend of sediment yield in the coarser sediment producing area in the middle Yellow River Basin in the Period 1997–2007 and the formative cause," *Journal of Soil and Water Conservation*, vol. 24, no. 1, pp. 1–7, 2010 (Chinese).
- [15] X. Mu, X. Zhang, H. Shao et al., "Dynamic changes of sediment discharge and the influencing factors in the yellow river, China, for the recent 90 years," *Clean—Soil, Air, Water*, vol. 40, no. 3, pp. 303–309, 2012.
- [16] K. Liang, C. Liu, X. Liu, and X. Song, "Impacts of climate variability and human activity on streamflow decrease in a sediment concentrated region in the Middle Yellow River," *Stochastic Environmental Research and Risk Assessment*, vol. 27, no. 7, pp. 1741–1749, 2013.
- [17] Y. He, X. M. Mu, G. J. Zhao, and P. Gao, "Variation of erosive rainfall and extreme rainfall based on processes of sediment discharge in the reach of Hekou-Tongguan, Yellow River," *Journal of Sediment Research*, no. 2, pp. 53–59, 2015 (Chinese).
- [18] B. J. Fu and H. Gulinck, "Land evaluation in an area of severe erosion: the Loess Plateau of China," *Land Degradation and Development*, vol. 5, no. 1, pp. 33–40, 1994.
- [19] T. C. Peterson, D. R. Easterling, T. R. Karl et al., "Homogeneity adjustments of in situ atmospheric climate data: a review," *International Journal of Climatology*, vol. 18, no. 13, pp. 1493–1517, 1998.
- [20] F. Q. Jiang, X. M. Li, B. G. Wei, R. J. Hu, and Z. Li, "Observed trends of heating and cooling degree-days in Xinjiang Province, China," *Theoretical and Applied Climatology*, vol. 97, no. 3–4, pp. 349–360, 2009.
- [21] X. Li, F. Jiang, L. Li, and G. Wang, "Spatial and temporal variability of precipitation concentration index, concentration degree and concentration period Xinjiang, China," *International Journal of Climatology*, vol. 31, no. 11, pp. 1679–1693, 2011.
- [22] Z. Li, F.-L. Zheng, W.-Z. Liu, and D. C. Flanagan, "Spatial distribution and temporal trends of extreme temperature and precipitation events on the Loess Plateau of China during 1961–2007," *Quaternary International*, vol. 226, no. 1–2, pp. 92–100, 2010.
- [23] Z. Li, "Analysis on characteristics and reasons of sediment discharge in the Hekou-Longmen Region of the Yellow River," *Yellow River*, vol. 30, no. 8, pp. 41–42, 2008.
- [24] J. E. Kutzbach, "Empirical eigenvectors of sea-level pressure, surface temperature and precipitation complexes over North America," *Journal of Applied Meteorology*, vol. 6, no. 5, pp. 791–802, 1967.
- [25] G. R. North, T. L. Bell, R. F. Cahalan, and F. J. Moeng, "Sampling errors in the estimation of empirical orthogonal functions," *Monthly Weather Review*, vol. 110, no. 7, pp. 699–706, 1982.
- [26] K. Y. Kim and G. R. North, "EOF analysis of surface temperature field in a stochastic climate model," *Journal of Climate*, vol. 6, no. 9, pp. 1681–1690, 1993.
- [27] R. Tomozeiu, M. Lazzeri, and C. Cacciamani, "Precipitation fluctuations during the winter season from 1960 to 1995 over Emilia-Romagna, Italy," *Theoretical and Applied Climatology*, vol. 72, no. 3–4, pp. 221–229, 2002.
- [28] X. Y. Song, L. J. Li, G. B. Fu et al., "Spatial-temporal variations of spring drought based on spring-composite index values for the Songnen Plain, Northeast China," *Theoretical and Applied Climatology*, vol. 116, no. 3–4, pp. 371–384, 2014.
- [29] D. H. Kim, C. Yoo, and T.-W. Kim, "Application of spatial EOF and multivariate time series model for evaluating agricultural drought vulnerability in Korea," *Advances in Water Resources*, vol. 34, no. 3, pp. 340–350, 2011.
- [30] Z. H. Wu, N. E. Huang, and X. Y. Chen, "The multi-dimensional ensemble empirical mode decomposition method," *Advances in Adaptive Data Analysis. Theory and Applications*, vol. 1, no. 3, pp. 339–372, 2009.
- [31] N. E. Huang, Z. Shen, S. R. Long et al., "The empirical mode decomposition and the Hilbert spectrum for nonlinear and non-stationary time series analysis," *Proceedings of the Royal Society of London A: Mathematical, Physical and Engineering Sciences*, vol. 454, no. 1971, pp. 903–995, 1998.
- [32] N. E. Huang and Z. Wu, "A review on Hilbert-Huang transform: method and its applications to geophysical studies," *Reviews of Geophysics*, vol. 46, no. 2, Article ID RG2006, 2008.
- [33] Z. Wu and N. E. Huang, "Ensemble empirical mode decomposition: a noise-assisted data analysis method," *Advances in Adaptive Data Analysis*, vol. 1, no. 1, pp. 1–41, 2009.
- [34] C. Qian, Z. W. Yan, and C. B. Fu, "Climatic changes in the Twenty-four Solar Terms during 1960–2008," *Chinese Science Bulletin*, vol. 57, no. 2–3, pp. 276–286, 2012.
- [35] S. Rehman, "Study of Saudi Arabian climatic conditions using Hurst exponent and climatic predictability index," *Chaos, Solitons & Fractals*, vol. 39, no. 2, pp. 499–509, 2009.
- [36] G. Sakalauskiene, "The Hurst phenomenon in hydrology," *Environmental Research, Engineering and Management*, vol. 3, no. 25, pp. 16–20, 2003.
- [37] G. R. North, T. L. Bell, R. F. Cahalan, and F. J. Moeng, "Sampling errors in the estimation of empirical orthogonal functions," *Monthly Weather Review*, vol. 110, no. 7, pp. 699–706, 1982.
- [38] X. Sun and Z. S. Lin, "A new technology HHT and its diagnosis for ENSO," *Meteorological Monthly*, vol. 32, no. 9, pp. 17–22, 2006 (Chinese).

Review Article

1600 AD Huaynaputina Eruption (Peru), Abrupt Cooling, and Epidemics in China and Korea

Jie Fei,¹ David D. Zhang,² and Harry F. Lee²

¹*Institute of Chinese Historical Geography, Fudan University, Shanghai 200433, China*

²*Department of Geography, The University of Hong Kong, Pokfulam, Hong Kong*

Correspondence should be addressed to Jie Fei; jiefei@fudan.edu.cn

Received 9 April 2015; Revised 9 July 2015; Accepted 19 August 2015

Academic Editor: Steffen Mischke

Copyright © 2016 Jie Fei et al. This is an open access article distributed under the Creative Commons Attribution License, which permits unrestricted use, distribution, and reproduction in any medium, provided the original work is properly cited.

The 1600 AD Huaynaputina eruption in Peru was one of the largest volcanic eruptions in history over the past 2000 years. This study operated on the hypothesis that this event dramatically affected the weather and environment in China and the Korean Peninsula. Over the course of this research the Chinese and Korean historical literatures as well as dendrochronology records were examined. The historical evidence points to the conclusion that the eruption was followed by an abrupt cooling period and epidemic outbreaks in 1601 AD within both China and the Korean Peninsula. These records manifested themselves in unseasonably cold weather resulting in severe killing frosts in northern China in the summer and autumn of 1601 AD. In southern China (Zhejiang and Anhui Provinces and Shanghai Municipality), July was abnormally cold with snow, with an autumn that saw anomalously hot weather. In addition, there was unseasonable snowfall that autumn within Yunnan Province. Widespread disease outbreaks occurred in August, September, and October in northern and southern China. In Korea, the spring and early summer of 1601 AD were unusually cold, and conditions led to further widespread epidemics occurring in August.

1. Introduction

Volcanic eruptions eject massive amounts of gas and ash into the stratosphere and troposphere, reducing solar insolation and resulting in climatic and environmental effects [1–8]. Major volcanic eruptions are capable of affecting short-term climatic change on hemispheric and global scales.

For example, the 1991 AD Pinatubo eruption (Philippines) caused the largest perturbation of the 20th century to the particulate content of the stratosphere; and the radiative influence of the injected particles put an end to several years of globally warm surface temperatures [9, 10]. The 1883 AD Krakatoa eruption (Indonesia) caused dimmed suns and blood red skies in the Northern Hemisphere [11]. Similar disturbances have been reported after other major volcanic eruptions, for example, 1815 AD Tambora eruption and the unidentified eruptions in 1452 AD and circa 626 AD [12–17]. Even 2000 years ago, Plutarch and others surmised that the eruption of Mount Etna in 44 BC dimmed the sun and suggested that the resulting cooling caused crops to fail and

even created famine within the Roman Empire and Egypt [6, 18]. Within China, there were dimmed suns, anomalously cold temperatures, crop failures, and famine the following year, in 43 BC, following the 44 BC Etna event [19].

Research on climatic effects using Chinese historical literature, written following major historical volcanic eruptions, has achieved encouraging progress during the past decades. Cao et al. (2012) identified evidence of climatic downturn in China following the 1815 AD Tambora eruption [20]. Fei and Zhou (2006) suggested that abrupt cooling occurred in 939–941 AD in China following the prolonged 934–939 AD Eldgjá eruption, Iceland [21].

The relationship between volcanic eruptions and abrupt cooling is therefore evident, and, recently, increasing attention has focused on the possible cause and effect relationship between volcanic eruptions and precipitation anomalies [22, 23]. It has been suggested that extreme droughts in China could be related to the volcanic eruptions during the past 500 years, because large volcanic eruptions possibly reduced the summer monsoon in East Asia [24, 25].

The epidemic effects of major volcanic eruptions have also long intrigued volcanologists [5, 26–28]. Stothers (1999) examined seven major volcanic eruptions during the past two millennia and found that most of them were followed by several years containing epidemics in Europe and the Middle East [4]. The 1783–1784 AD Laki (Lakigiga) eruption (Iceland) caused dense volcanic dry fog and a significant shift in regional climate systems that are potentially responsible for endemic diseases and high mortality rates seen in England and France during that time [29–31]. However, as a whole, the possible epidemic effects of volcanic eruptions during the past 2000 years have not been discussed in detail, and the mechanisms of contagion and spread of such epidemics have not yet been identified.

In addition, volcanic eruptions result in local disease outbreaks in the vicinity of volcanoes, due to poor hygiene and limited access to drinking water which has been contaminated with volcanic ash and debris. An example of this is following the 1815 AD Tambora volcanic eruption where populations suffering from violent diarrhea were prevalent in the vicinity of the volcano [16]. Another was a regional outbreak of measles that occurred after the eruptions of Mt. Pinatubo in 1991 AD [27].

2. The 1600 AD Huaynaputina Eruption, Peru

Huaynaputina Volcano (16.6°S, 70.9°W) is located in southern Peru, South America. The eruption in 1600 AD was the largest volcanic eruption in South America spanning the past 2000 years [32–36]. The eruption started on February 19, 1600 AD, and lasted until March [32–34, 37]. The economy of southern Peru was severely disrupted and did not recover during most of the 17th century [38, 39].

The sustained eruption column was estimated to be 27–35 km high during the Plinian phase on February 19–20, 1600 AD. The eruption reached a significantly higher altitude than the tropopause, thus making it capable of affecting the atmospheric environment on a global scale [34].

The eruption produced ~70 Mt. of global average stratospheric H₂SO₄ loading, which makes it one of the largest volcanic eruptions in world history over the past two millennia [32, 40]. For example, that of the 1815 Tambora eruption was estimated at 60 Mt. [13], 93–118 Mt. [41], and 108 Mt. [42]. However, stratospheric H₂SO₄ loading of the Huaynaputina eruption was much higher than those of the 1883 Krakatoa (22 Mt. [42]) and 1991 Pinatubo eruptions (30 Mt. [42]).

The volcanic ash from Huaynaputina formed a widespread lobe of ~95,000 km² within the 1-cm isopach [34]. Historical accounts indicate significant ash fall in Lima (~850 km north of the volcano) and on a ship 1,000 km off the Peruvian coast [32]. The fine ash and volcanic glass from the eruption were also identified in the South Pole ice core in Antarctica and possibly the GISP2 ice core in Greenland [32, 34, 43, 44].

Signals corresponding to the Huaynaputina eruption were identified in a large number of Antarctic and Greenland ice cores, thus indicating the potential global influence of the eruption. Volcanic acidity peaks corresponding to the Huaynaputina eruption were identified in the Greenland ice cores of Crete [45, 46], GRIP [47], and Summit [48]. Excess

SO₄²⁻ peaks corresponding to the Huaynaputina event were also identified in the Greenland ice cores of GISP2 [49], and Antarctic ice cores of Law Dome [50], Plateau Remote [51], SP2001 [52], PSI (near the Amundsen-Scott Base) [43], Talos Dome (East Antarctica) [53], and Dome Fuji [54].

It is well known that the other three tropical eruptions produced abrupt global cooling [13, 16, 55]. Considering the magnitude of the Huaynaputina eruption, it should have been capable of producing significant global climatic effects. Previous research has revealed that the Huaynaputina eruption was followed by abrupt cooling in many regions in the world [32, 36].

A series of dendroclimatology studies have brought robust evidence to bear to support dramatic abrupt cooling in 1601 AD. Briffa et al. (1998) suggested that the summer of 1601 AD has the potential of being the coldest on record over the past 600 years according to a synthesis of dendrochronological data in northern Eurasia and North America [55]. Scuderi (1990) identified that 1601 AD was abnormally cold according to the temperature-sensitive tree-ring chronologies in the Sierra Nevada [56]. Jones et al. (1995) synthesized a temperature-sensitive network of tree-ring chronologies in North America and Western Europe and suggested that 1601 AD possessed the summer with the most dramatic shifts to unseasonably cold weather patterns [57].

Low temperature was shown around 1600 AD in a ring-width record derived from the June–August Alpine temperature proxy over 951–1527 AD in the Swiss and Austrian Alps [58]. 1601 AD was shown to be extremely cold in the maximum latewood density data from trees at thirteen temperature-sensitive sites along the northern tree line of North America [59]. In the centre of Spain, 1601 AD was the most unfavourable for tree growth, representing the minimum index in the regional chronology [60].

Evidences of dramatic cooling in 1601 AD also exist in the light ring and frost ring chronologies, which record abnormally low temperature in growing seasons. LaMarche Jr. and Hirschboeck (1984) identified a very significant frost ring in 1601 AD in western USA [61]. Filion et al. (1986) and Yamaguchi et al. (1993) identified a significant light ring event in 1601 AD near Bush Lake, Canada [62, 63]. Hantemirov et al. (2004) also identified significant frost and light rings in 1601 AD in the Polar Urals and Yamal Peninsula in northwestern Siberia [64].

The review of historical records corresponds to a dramatic global cooling event from the data collected above, and the historical sources indicate that the summer of 1601 was unusually cold in England and Italy [65]. The winter of 1601 was very severe in Russia, Latvia, and Estonia [36]. In Sweden, record amounts of snow in the winter of 1601 were followed by a rainy spring. The resulting harvest was insufficient to feed the population leading to hunger and disease [66]. Fei and Zhou (2009) investigated the possible climatic effects in northern China following the Huaynaputina eruption. It was discovered that killing frost occurred in 1601 AD and resulted in widespread crop failures throughout the region [67].

Here we investigate the possible climatic and epidemic effects in China and Korea following the 1600 AD Peruvian Huaynaputina eruption. After a careful literature survey, we

found that significant abrupt cooling and epidemics occurred mainly in 1601 AD in China and Korea.

3. Materials and Methods

Our study of the possible climatic and epidemic effects of the Huaynaputina eruption in China and Korea is mainly based on the available historical literature. The Chinese and Korean historical texts were examined systematically. A few thousand literary sources were examined, though it turned out that only a small fraction of the historical record contains useful information.

Most of our records were discovered in the Chinese historical local gazetteers (*Di fang zhi*) (Tables 1, 2, and 3). This type of historical source material is unique and very substantial, especially for the history of the Ming (1368–1644 AD) and Qing (1644–1911 AD) dynasties. There are a few thousand extant historical local gazetteers in China [68]. The printed and/or electronic copies are available in the Libraries of Fudan University, the Libraries of the University of Science and Technology of China, and the Shanghai Library.

Some of the records were found in the historical diaries (Table 1). This type of source is particularly valuable as it contains first-hand accounts of climatic and epidemic events.

The climatological and epidemiological records in Korea were discovered in the Annals of the Choson Dynasty (also known as *Choson Wangjo Sillok*) (Table 3), which comprises 25 parts and 1,893 volumes and covers 472 years (1392–1863 AD) of the history of the Choson Dynasty (1392–1910 AD). The annals are in classical Chinese and adopt the Chinese lunar calendar. The compilations were commenced at a specific time following shortly after a king's death by the Office for Annals Compilation of Korea. Therefore the Annals of the Choson Dynasty are highly reliable. The Annals of the King Seonjo (*Seonjo Sillok*) are a part of this record. It comprises 263 volumes and covers the reign of King Seonjo (r. 1567–1608 AD).

In addition, European and American historical records of climatic and epidemic events were also examined; most of these were carried over from relevant previous studies.

Dendrochronology records were examined extensively, in order to give a general scenario of the climatic effects around the world.

Volcanic related signals in ice cores in Greenland and Antarctica were examined carefully in order to verify the potential global influence of the eruption.

4. Abrupt Cooling and Epidemics in 1601 AD in Southern China

The year of 1601 AD witnessed anomalous summer and autumn seasons in southern China. It was cold in the summer and abnormally hot in the autumn. Following the cold summer and hot autumn, widespread disease broke out (Figures 1, 2, and 3; Tables 1, 2, 3, and 4).

The contemporary record of the abnormal weather in the summer and autumn of 1601 AD was found in a book titled Notes on Experience (*Jian wen za ji*) (Figure 1). The book is actually a diary, and it was finished in circa AD 1610 by Le Li,

a retired scholar and official. (Le Li, *Jian wen za ji*. This book was written in circa 1610 AD. Here “Le” is the given name, and “Li” is the surname. Similarly hereinafter.) Le Li lived in Wuzhen (a town in Tongxiang County, Zhejiang Province) after retirement; thus the location of most of the events in the book was Wuzhen, including the record of the abnormal weather in 1601 AD.

This record is seen as the most original record of the epidemic and abnormal weather of 1601 AD, whereas similar descriptions of the event are also found in the local gazetteers of a few regions of Zhejiang Province. These regions include Hangzhou and Huzhou Prefectures (modern Hangzhou and Huzhou Cities) and Tongxiang County and Nanxun Town (modern Nanxun County of Huzhou City) (Table 1).

However, the descriptions in the Gazetteer of Shidai County (modern Shitai County, Anhui Province) and Gazetteer of Songjiang Prefecture (modern Songjiang County, Shanghai Municipality) are different from that of the Notes on Experience and should be independent from it. It is also worth noting that these two literatures were written a few decades later than the Notes on Experience (Table 1).

The spatial scale of the epidemics proved to be even larger than anticipated. We identified a plethora of records on epidemic outbreaks in 1601 AD in Anhui, Zhejiang, Fujian, Jiangxi, Hunan, and Guizhou Provinces of southern China (Figure 2). Some records indicated that the epidemics were related to drought and famine, whereas the causal link with abrupt cooling caused by the Huaynaputina event is not very clear (Table 1).

Separate from the above evidence, records were also found which described abrupt cooling which occurred in Kunming City (Yunnan Province). There was an abnormal snowfall in the autumn of 1601 AD in the area (Chengxun Fan and Jiwen Wang, General Gazetteer of Yunnan Province (*Yunnan tong zhi*) (1691), Vol. 28).

5. Abrupt Cooling and Epidemics in 1601 AD in Northern China

5.1. Historical Records. Our previous research has suggested that there were severe killing frosts in the Shanxi and Hebei Provinces in the summer and early autumn of 1601 AD (Fei and Zhou, 2009) [67]. Here we further supplemented our material with the records from Shaanxi, Gansu, and Qinghai Provinces and discovered that epidemics occurred in Shanxi and Shaanxi Provinces in 1601–1602 AD (Figures 1, 2, and 3; Tables 2 and 4). The epidemics in Shanxi and Shaanxi Provinces were possibly caused by a combination of killing frosts and drought. Supporting this information is the appearance of severe killing frosts and great epidemics in northern China in the summer and autumn of 1601 AD (Figures 1, 2, and 3; Tables 2 and 4).

It is noteworthy that killing frosts in the summer and autumn of 1601 AD in northern China were the result of outbreaks of cold waves that usually cover a large area. In some counties with records of epidemics, but without records of frost disasters (e.g., Yangqu, Qingxu Counties, and Shanxi Province), it is highly probable that frost disasters also

TABLE 1: Historical records of the abrupt cooling and epidemics in southern China in 1601 AD.

County, province	Description	Source
* Wuzhen, Hangzhou, Huzhou, Tongxiang, and Nanxun, Zhejiang Province	Wanli Reign Period, 29th year (February 3, 1601 AD–January 22, 1602 AD): it was chilly in the 6th month (June 30–July 28, 1601 AD). People took on double layered and cotton clothes. It was said that there was a heavy snow in the mountains of the Fuyang County, and the county sheriff took a tank of snow and submitted it to the province governor. It was also said that there was significant snowfall in the mountains of Hangzhou Prefecture. It turned hot in the 7th month (July 29–August 27, 1601 AD) and was still hot in the 8–9th months (August 28–October 25, 1601 AD). People even soaked in water in order to keep cool. Most of the families were hit by epidemics.	Le Li, Notes on Experience (<i>Jian wen za ji</i>) (circa 1610). Similar records are found in local gazetteers, including ① Yun Zheng et al., Gazetteer of the Hangzhou Prefecture (<i>Hangzhou fu zhi</i>) (1779), Vol. 56, ② Yuanhan Zong and Shichang Guo, Gazetteer of the Huzhou Prefecture (<i>Huzhou fu zhi</i>) (1874), Vol. 44, ③ Chen Yan, Gazetteer of the Tongxiang County (<i>Tongxiang xian zhi</i>) (1887), Vol. 20., ④ Rizhen Wang, Gazetteer of the Nanxun Town (<i>Nanxun zhen zhi</i>) (1859), Vol. 19.
* Shidai County (modern Shitai County, Anhui Province)	29th year (of the Wanli Reign Period)..., in the 6th month of this summer (June 30–July 28, 1601 AD); it was very cold. All the people took on cotton coats. Snow fell and piled up in the remote mountains. It turned hot in the 7th month (July 29–August 27, 1601 AD) and was still hot in the 8th month (August 28–September 25, 1601 AD). Most of the people fell ill in the Wu and Yue areas (including Zhejiang Province, Shanghai Municipality, and southern Jiangsu Province) and the areas to the north and south of the Yangtze River.	Zizhuang Yao and Ti Yuan Zhou, Gazetteer of the Shidai County (<i>Shidai xian zhi</i>) (1675), Vol. 2.
† Songjiang county, Shanghai Municipality	Xinchou year (i.e., the 29th year of the Wanli Reign Period) 6th month, 17th day (July 16, 1601 AD): it poured all day and all night. A flood destroyed the crops in the northern area of the county. It suddenly turned freezing cold. It was said that there was more than one <i>chi</i> (1 <i>chi</i> \approx 0.3 m) of snow in Fuyang County, Hangzhou Prefecture.	Yuegong Fang and Jiru Chen, Gazetteer of the Songjiang Prefecture (<i>Songjiang fu zhi</i>) (1630), Vol. 47.
† Kunming, Yunnan	9th month (September 26–October 25, 1601 AD): there was a heavy snowfall.	Chengxun Fan and Jiwen Wang, General Gazetteer of Yunnan Province (<i>Yunnan tong zhi</i>) (1691), Vol. 28.
* Ninggang, Jiangxi	A great epidemic. Nearly half of the people were killed.	Yuda Chen, Gazetteer of Yongning County (<i>Yongning xian zhi</i>) (1683), Vol. 1.
* Xingguo, Jiangxi	A great drought and epidemic.	Shangyuan Zhang, Gazetteer of the Lianzhui County (<i>Lianzhui zhi lin</i>) (1711), Vol. 15.
* Shicheng, Jiangxi	A great epidemic.	Yaojing Guo, Gazetteer of Shicheng County (<i>Shicheng xian zhi</i>) (1660), Vol. 8.
* Dayu, Jiangxi	There was a great epidemic in this year.	Yin Chang Chen, Gazetteer of the Dayu County (<i>Dayu xian zhi</i>) (1874), Vol. 24.
* Nankang, Jiangxi	4th month (May 2–May 31, 1601 AD): a great epidemic.	Ziyun Qiu, Gazetteer of the Nankang County (<i>Nankang xian zhi</i>) (1936), Vol. 10.
* Liancheng, Fujian	A great epidemic.	Shijin Du, Gazetteer of the Liancheng County (<i>Liancheng xian zhi</i>) (1666), Vol. 1.
* Xinhua, Hunan	When autumn came, there were drought and epidemic.	Xiaolong Yu and Wenzhu Yang, Gazetteer of the Xinhua County (<i>Xinhua xian zhi</i>) (1668), Vol. 11.
* Guizhou Province	4th month (May 2–May 31, 1601 AD): no rain. 5th month (June 1–June 29th, 1601 AD): a great famine... 7th month (July 29th–August 27th, 1601 AD): a great epidemic.	Shenji Cao and Xun Pan, General Gazetteer of Guizhou Province (<i>Guizhou tong zhi</i>) (1673), Vol. 27.

† Counties with abrupt cooling. * Counties with epidemics.

TABLE 2: Historical records of the abrupt cooling and epidemics in northern China in 1601 AD.

County, province	Description ¹	Source
†* Xincai, Henan	Since the 9th day of the 1st month (of the 29th year of the Wanli Reign Period, February 11, 1601 AD), it snowed heavily for 40 days, and the melted snow destroyed the wheat. The following epidemic killed innumerable people, and all the farmlands were deserted.	Hongxian Tan and Minfu Lü, <i>Gazetteer of the Xincai County (Xincai xian zhi)</i> (1691), Vol. 7.
†* Dingxiang, Shanxi	It did not rain in summer and autumn. There was an epidemic that killed numerous people. Even family members and relatives did not dare to have intimate physical contact with each other. There was a drought and a frost disaster that caused crop failure, and prices of crops rose to extraordinary levels.	Shijiong Wang and Hanyuan Niu, <i>Gazetteer of the Dingxiang County (Dingxiang xian zhi)</i> (1712), Vol. 7.
†* Lishi, Shanxi	A frost completely destroyed the crops (29th year of the Wanli Reign Period, 1601 AD). A great epidemic came in the spring of the 30th year of the Wanli Reign Period (1602 AD) and killed a great number of people.	Daoyi Wang, <i>Gazetteer of the Fenzhou Prefecture (Fenzhou fu zhi)</i> (1611), Vol. 16.
† Huaian, Hebei	There was a snow in the summer.	Dakun Yang and Jizeng Qian, <i>Gazetteer of the Huaian County (Huaian xian zhi)</i> (1741), Vol. 22.
† Xuanhua, Hebei	There was a frost in the summer.	Tan Chen, <i>Gazetteer of the Xuanhua County (Xuanhua xian zhi)</i> (1711), Vol. 5.
† Chicheng, Hebei	There was a frost in the summer.	Tun Zhang, <i>Gazetteer of the Longmen County (Longmen xian zhi)</i> (1712), Vol. 2.
† Yuxian, Hebei	There was a frost in the summer.	Ying Li, <i>Gazetteer of the Yu Prefecture (Yu zhou zhi)</i> (1659), Vol. 1.
† Yangyuan, Hebei	There was a frost in the summer.	Chongguo Zhang, <i>Gazetteer of the Xining County (Xining xian zhi)</i> (1712), Vol. 1.
† Laiyuan, Shanxi	A frost totally destroyed the crops.	Shizhi Liu and Wenyao Zhao, <i>Gazetteer of the Guangchang County (Guangchang xian zhi)</i> (1630).
† Guangling, Shanxi	There was a frost in the summer.	Huandou Li and Wuding Wang, <i>Gazetteer of the Guangling County (Guangling xian zhi)</i> (1685), Vol. 1.
† Xinzhou, Shanxi	A frost destroyed the crops in the 8th month (August 28–September 25th, 1601 AD).	Renlong Zhou and Gusui Dou, <i>Gazetteer of the Xin Prefecture (Xin zhou zhi)</i> (1747), Vol. 4.
† Jingle, Shanxi	A wind and frost destroyed the crop on the 25th day of the 7th month (August 22, 1601 AD). There was a great famine, and people even resorted to cannibalism.	Tuchang Huang, <i>Gazetteer of the Jingle County (Jingle xian zhi)</i> (1695), Vol. 4.
† Baode, Shanxi	A killing frost completely destroyed the crops on the 26th day of the 7th month (August 23, 1601 AD). The markets in the city were closed for nine days. People fled away and sold their children. There were victims of starvation everywhere. People were in such a weakened state they even did not care about the deaths of members of their own family.	Kechang Wang and Menggao Yin, <i>Gazetteer of the Baode Prefecture (Baode zhou zhi)</i> (1710), Vol. 3.
† Shenchi, Shanxi	A frost destroyed the crops in the 7th month (July 29–August 27th, 1601 AD). A great famine occurred in the Jingle and Shenchi counties.	Changqing Cui et al., <i>Gazetteer of the Shenchi County (Shenchi xian zhi)</i> (1880), Vol. 9.
† Zuoquan, Shanxi	A frost killed the crops in the 8th month (August 28–September 25, 1601 AD).	Tianxi Yang and Weitai Hou, <i>Gazetteer of the Liao Prefecture (Liao zhou zhi)</i> (1673), Vol. 7.
† Linxian, Shanxi	There was a bitter early frost on the 9th day of the 8th month (September 5, 1601 AD). The crops were destroyed. There was a great famine. People ate tree barks and grass roots.	Daoyi Wang, et al., <i>Gazetteer of the Fenzhou Prefecture (Fenzhou fu zhi)</i> (1611), Vol. 16.

TABLE 2: Continued.

County, province	Description [†]	Source
† Lishi, Shanxi	A frost destroyed crops in Yongning County. There was a great famine.	Daoyi Wang, et al., A Gazetteer of the Fenzhou Prefecture (<i>Fenzhou fu zhi</i>) (1611), Vol. 16.
† Xixian, Shanxi	During the last ten days of the 10th month (November 15–November 24, 1601 AD), it snowed heavily. The snow was three <i>chi</i> deep. It was considered to be a propitious omen. ... There was a frost in the 8th month (August 28–September 25th, 1601 AD) that reduced the harvest.	Yikai Qian, A Gazetteer of the Xi Prefecture (<i>Xi zhou zhi</i>) (1710), Vol. 24.
† Yulin, Shaanxi	A frost destroyed the crops in autumn.	Jicong Tan, Gazetteer of the Yansui Fort (<i>Yansui zhen zhi</i>) (1673), Vol. 5.
† Yulin, Shaanxi	There were successive snow and hail events in the 8th month (August 28–September 25, 1601 AD), and the crops were totally destroyed.	Tingyu Zhang and Zhaonan Qi, Continuation of Comprehensive Study of Documents (<i>Xu wenxian tong kao</i>) (1767), Vol. 223.
† Mizhi, Shaanxi	A frost destroyed the crops in the 7th month (July 29–August 27, 1601 AD).	Yangqi Ning, Gazetteer of Mizhi County (<i>Mizhi xian zhi</i>) (1681), Vol. 1.
† Yan'an, Shaanxi	A frost destroyed the crops in the autumn.	Hui Hong, Revised Gazetteer of Yan'an Prefecture (<i>Chongxiu Yan'an fu zhi</i>) (1802), Vol. 6.
† Ningxian, Gansu	There was a frost in the 7th month (July 29–August 27, 1601 AD).	Benzhi Zhao, New Gazetteer of the Qingyang Prefecture (<i>Xinxiu Qingyang fu zhi</i>) (1761), Vol. 37.
* Yangqu, Shanxi	There were epidemics and great famines in the 29th and 30th years of the Wanli Reign Period (i.e., 1601-1602 AD).	Mengxiong Dai, Fangtai Li and Fangfan Li, Gazetteer of the Yangqu County (<i>Yangqu xian zhi</i>) (1682), Vol. 1.
* Qingxu, Shanxi	There were a great drought and resulting epidemic.	Xunxiang Wang and Xiaozun Wang, Gazetteer of the Qingyuan Town (<i>Qingyuan xiang zhi</i>) (1882), Vol. 16.
* Linyou, Shaanxi	There were drought and epidemic outbreaks in 1601 AD in Linyou County.	Ruwei Wu and Yuantai Liu, Gazetteer of the Linyou County (<i>Linyou xian zhi</i>) (1657), Vol. 1.

[†]Counties with abrupt cooling. * Counties with epidemics.

¹If a weather event is recorded in two or more local gazetteers, the most original or the most detailed one is given.

TABLE 3: Historical records of the abrupt cooling and epidemics in Korea in 1601 AD.

Location	Description	Source
†Kangwon Prefecture, Korea	The Magistrate of the Gangneung City (<i>Gangneung Bu</i> , a city of the Kangwon Prefecture, i.e., <i>Kangwon Do</i>), Si Sin, reported that chilly wind was always blowing, and the weather was always gloomy and hazy since the late spring. The seedlings rotted and faded away. It rained and snowed on the 5th day of this month (May 6, 1601 AD). The mountains and plains were in white. This is really abnormal as it is summer now. (The date of this report was Jiawu day, 4th month, 34th year, Seonjo Reign Period, i.e., May 28, 1601 AD.)	Annals of King Seonjo, Vol. 136.
†Hwanghae Prefecture, Korea	The Governor of the Hwanghae Prefecture (<i>Hwanghae Do</i>), I-Mun Seong, reported that there were severe droughts in all of the counties from the spring to summer. It shined one moment and rained the next, and the chilly wind always blew. The wheat failed to flower, and the rice failed to grow. The paddy fields were very dry and could not be ploughed. In the seeded fields, the seeds did not sprout. We really worried about the farm work. (The date of this report was Bingshen day, 4th month, 34th year, Seonjo Reign Period, i.e., May 30, 1601 AD.)	Annals of King Seonjo, Vol. 136.
*Near Seoul, Korea	King Seonjo said that it was very hot and wet these days, and numerous people fell ill. We should take good care of ourselves, so that the patients would recover and no longer feel miserable. (The record does not mention the location. It should refer to the entire Korean Peninsula or at least the vicinity of the capital, Seoul, because this record is an order of the king.) (The date of this report was Renyin day, 7th month, 34th year, Seonjo Reign Period, i.e., August 4, 1601 AD)	Annals of King Seonjo, Vol. 139.

† Counties with abrupt cooling. * Counties with epidemics.

TABLE 4: Temporal distribution and weather background of the epidemics in China and Korea in 1601 AD.

County, province	Weather background	Time
Xincai, Henan	Cold	Spring* (February 3–May 1, 1601 AD)
Nankang, Jiangxi	n/a	4th month (May 2–May 31, 1601 AD)
Korea (State)	Abnormally hot and wet	7th month (July 29–August 27, 1601 AD)
Guizhou (Province)	Drought	7th month (July 29–August 27, 1601 AD)
Shitai, Anhui	Abnormally cold and then abnormally hot	7-8th month (July 29–September 1601 AD)
Wuzhen, Zhejiang	Abnormally cold and then abnormally hot	7-9th month (July 29–October 25, 1601 AD)
Hangzhou, Zhejiang	Abnormally cold and then abnormally hot	7-9th month (July 29–October 25, 1601 AD)
Huzhou, Zhejiang	Abnormally cold and then abnormally hot	7-9th month (July 29–October 25, 1601 AD)
Tongxiang, Zhejiang	Abnormally cold and then abnormally hot	7-9th month (July 29–October 25, 1601 AD)
Nanxun, Zhejiang	Abnormally cold and then abnormally hot	7-9th month (July 29–October 25, 1601 AD)
Xinhua, Hunan	n/a	Autumn (7th–9th month, i.e., July 29–October 25, 1601 AD)
Dingxiang, Shanxi	Drought	Autumn (7th–9th month, i.e., July 29–October 25, 1601 AD)
Xingguo, Jiangxi	Drought	n/a
Qingxu, Shanxi	Drought	n/a
Linyou, Shaanxi	Drought	n/a
Yangqu, Shanxi	n/a	n/a

* In Chinese and Korean historical literatures, particularly histories, chronicles and gazetteers, spring refers to the 1st–3rd months of the Chinese lunar calendar, and summer, autumn, and winter refer to the 4th–6th, 7th–9th, and 10th–12th months, respectively.

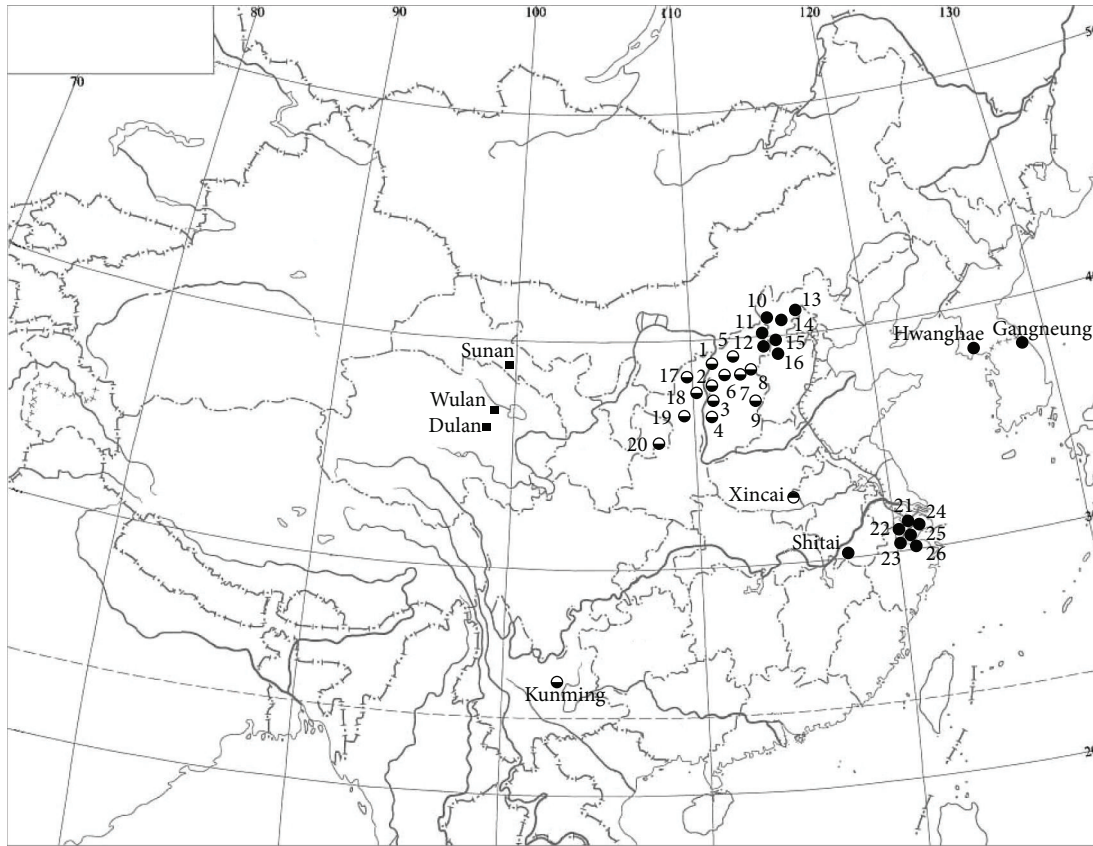
occurred in these counties if there were killing frosts in the surrounding areas.

In addition, we identified a record of disease outbreaks in early 1601 AD. In the early spring of 1601 AD, excessive snows hit Xincai County (Henan Province) and resulted in the outbreak and rapid spread of disease (Tables 2 and 4; Figures 1 and 2).

The epidemics ended in 1601 AD in China, except in the Lishi County (Shanxi Province, Table 2), where disease outbreaks were reported again in the spring of 1602 AD. There

were no further signs or data of widespread abrupt cooling and epidemics after 1602 AD.

5.2. *Dendrochronology Records on the Northeast Tibetan Plateau.* Past dendrochronological analyses were shown to be an exceptional source of information for tracking potential periods of dramatic or abrupt cooling and abnormal weather patterns. In addition, a few rigidly dated tree ring chronologies have been developed, which reveal past temperature changes on the northeast Tibetan Plateau, China (Figure 1).



- Abrupt cooling in spring, summer, and autumn
- Sites of tree ring chronologies

Abbreviations

(1) Baode	(8) Dingxiang	(15) Yuxian	(22) Huzhou
(2) Linxian	(9) Zuoquan	(16) Laiyuan	(23) Hangzhou
(3) Lishi	(10) Huai'an	(17) Yulin	(24) Songjiang
(4) Xixian	(11) Yangyuan	(18) Mizhi	(25) Wuzhen
(5) Shenchì	(12) Guangling	(19) Yan'an	(26) Tongxiang
(6) Jingle	(13) Chicheng	(20) Ningxian	
(7) Xinzhou	(14) Xuanhua	(21) Nanxun	

FIGURE 1: Abrupt cooling in 1601 AD in China and Korea. Dots denote records of abrupt cooling and epidemics, and different dots denote different seasons. Squares denote sites of relevant tree ring chronologies.

Liu et al. (2005) reconstructed the winter half-year (prior December to current April) temperature change history of Sunan County (99°56'E, 38°26'N), Gansu Province, northeast Tibetan Plateau [69]. Zhu et al. (2008) established a tree ring width chronology at Wulan County (98°40'E, 37°03'N), Qinghai Province, thus reconstructing the winter half-year (prior September to current April) temperature change history over the past 1000 years in this region [70]. Liu et al. (2009, 2011) established a new chronology of annual temperature change over the past 2485 years at Dulan and Wulan Counties (98-99°E, 36-37°N), Qinghai Province, east Tibetan Plateau [71, 72].

However, 1601-1602 AD was not abnormally cold or warm in these three chronological records.

6. Abrupt Cooling and Epidemics in Korea

After a careful literature survey, we identified a total of three records on abnormal weather and disease outbreaks in Korea in 1601 AD (Tables 3 and 4; Figures 1 and 2). Accordingly, the spring and early summer of 1601 AD were anomalously gloomy and cold. The middle summer was hot and wet, with a resulting epidemic ensuing in the prevalent conditions of the time.

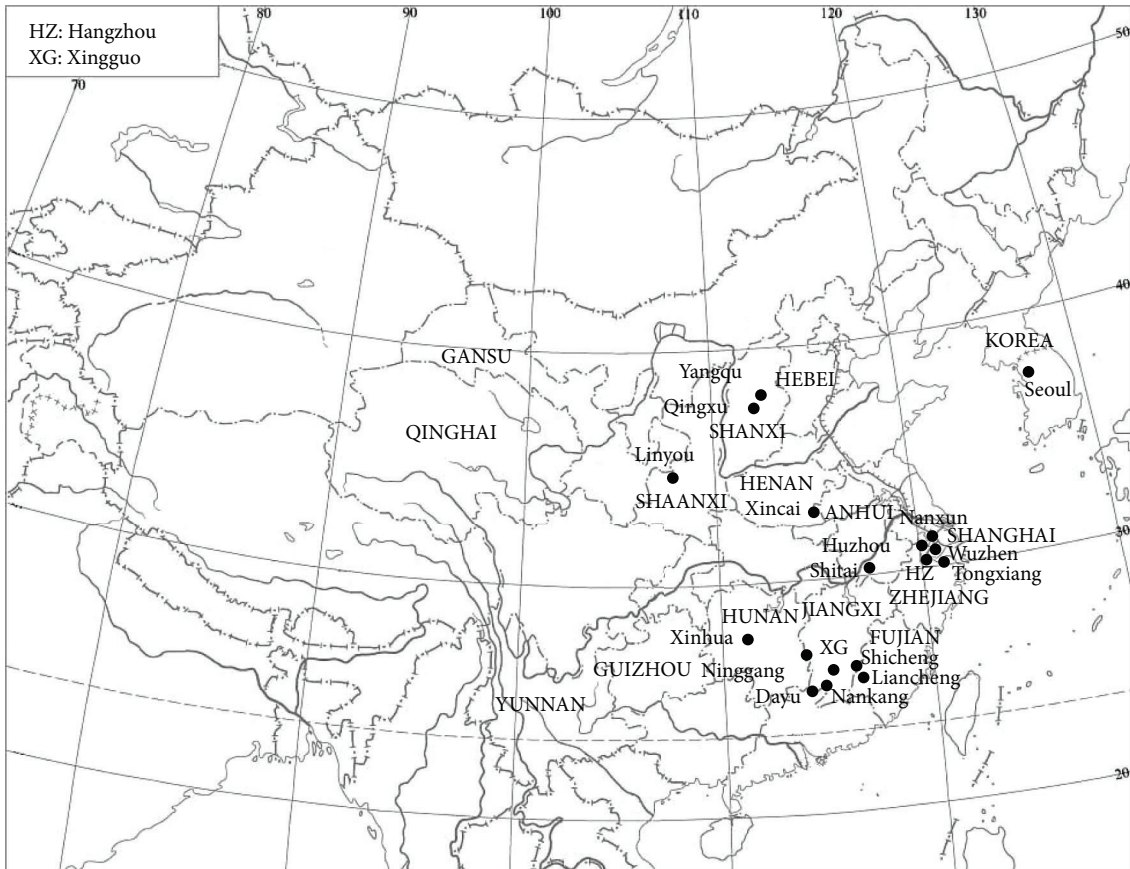


FIGURE 2: Epidemics in 1601 AD in China and Korea. Capitalized place names are Korea and provinces of China.

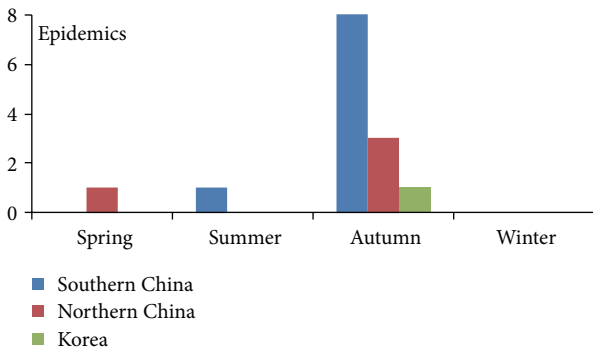


FIGURE 3: Seasonal variation of the number of records of epidemic in 1601 AD in southern China, northern China, and Korea.

7. Discussion

According to the records with detailed dates, we identify a very interesting phenomenon in many areas of China and Korea; that is, most of the epidemics occurred in the summer and autumn (Table 4, Figure 3). The areas include the Korean Peninsula and the provinces of Zhejiang, Anhui, Shanxi, Guizhou, and Hunan in China (Figure 2). The epidemics were recorded simultaneously with the abnormal weather patterns,

thus indicating a weather background and a possible causal link.

However, if the epidemics were related to the anomalous weather background, why did the epidemics break out almost simultaneously in different weather backgrounds (Table 4, Figure 3)? In Korea, the background was abnormally hot and wet weather. In Zhejiang and Anhui Provinces, the background was an abnormally cold July and a hot autumn. In Guizhou and Shanxi Provinces, the background was drought (Table 4). In Hunan province, the weather background was unidentified (Table 4).

With regard to the spatial distribution for the spread of endemic diseases, it is interesting that Korea, Zhejiang and Anhui Provinces, Shanxi Province, Guizhou, and Hunan Province are thousands of kilometres apart from each other (Figure 2). The epidemics in these four regions should be independent of one another. That is to say, weather backgrounds were different, and regions were independent; however, the records correlate multiple epidemics breaking out almost simultaneously across these regions.

It may seem to be overreaching to directly attribute the potential cause of these disease outbreaks to the 1600 AD Huaynaputina eruption. However, because the eruption reduced solar insolation and resulted in global abrupt cooling, it is not reasonable to exclude it as one of the major

causes of the epidemics in China and Korea in August, September, and October, 1600 AD. In other words, while investigating the possible causes of the epidemics, the effects of the Huaynaputina eruption should not be neglected.

8. Conclusion

Historical records on the abrupt cooling and epidemics in 1601 AD in China and Korea were investigated, and its causal relationship with the 1600 AD Peruvian Huaynaputina eruption is discussed. We suggest that abrupt cooling occurred in 1601 AD in China and Korea following the Huaynaputina eruption. Near, thereafter, widespread epidemics occurred in the summer and autumn of 1601 AD in China and Korea.

There were severe killing frosts in the summer and autumn of 1601 AD in Shanxi, Hebei, Shaanxi, and Gansu Provinces of northern China, as well as an unseasonable snow in that summer in Hebei Province.

In Zhejiang and Anhui Provinces, and Shanghai Municipality in southern China, July of 1601 AD was abnormally cold with unseasonable snows, differentiated from August, September, and October which were abnormally hot. There were widespread epidemics following this anomalous weather. Simultaneously, disease outbreaks also occurred in Guizhou and Hunan Provinces.

In Korea, the spring and early summer of 1601 AD were abnormally cold; however, middle summer was hot and wet, which was followed by epidemics.

It is worth further discussion that widespread epidemics occurred almost simultaneously in Korea and the Chinese provinces of Zhejiang, Anhui, Guizhou, Hunan, and Shanxi. Apparently, the weather background of the epidemics was different; however, we suppose that the Huaynaputina eruption possesses a major burden of responsibility for these concurrent epidemic outbreaks.

Conflict of Interests

The authors declare that there is no conflict of interests regarding the publication of this paper.

Acknowledgments

The authors gratefully acknowledge support from the National Natural Science Foundation of China (Grant no. 41202125) and the Chinese Academy of Sciences (Grant no. KLSLRC-KF-13-DX-4). Special thanks are due to Professor Clive Oppenheimer and the anonymous reviewers for the constructive comments and suggestions.

References

- [1] H. H. Lamb, "Volcanic dust in the atmosphere; with a chronology and assessment of its meteorological significance," *Philosophical Transactions of the Royal Society of London A*, vol. 266, pp. 425–533, 1970.
- [2] P. M. Kelly and C. B. Sear, "Climatic impact of explosive volcanic eruptions," *Nature*, vol. 311, no. 5988, pp. 740–743, 1984.
- [3] C. B. Sear, P. M. Kelly, P. D. Jones, and C. M. Goodess, "Global surface-temperature responses to major volcanic eruptions," *Nature*, vol. 330, no. 6146, pp. 365–367, 1987.
- [4] R. B. Stothers, "Volcanic dry fogs, climate cooling, and plague pandemics in Europe and the Middle East," *Climatic Change*, vol. 42, no. 4, pp. 713–723, 1999.
- [5] D. K. Chester, M. Degg, A. M. Duncan, and J. E. Guest, "The increasing exposure of cities to the effects of volcanic eruptions: a global survey," *Environmental Hazards*, vol. 2, no. 3, pp. 89–103, 2000.
- [6] A. Robock, "Volcanic eruptions and climate," *Reviews of Geophysics*, vol. 38, no. 2, pp. 191–219, 2000.
- [7] G. A. Zielinski, "Use of paleo-records in determining variability within the volcanism-climate system," *Quaternary Science Reviews*, vol. 19, no. 1–5, pp. 417–438, 2000.
- [8] W. S. Atwell, "Volcanism and short-term climatic change in East Asian and World history, c. 1200–1699," *Journal of World History*, vol. 12, no. 1, pp. 29–98, 2001.
- [9] M. P. McCormick, L. W. Thomason, and C. R. Trepte, "Atmospheric effects of the Mt Pinatubo eruption," *Nature*, vol. 373, no. 6513, pp. 399–404, 1995.
- [10] A. Robock, "Pinatubo eruption: the climatic aftermath," *Science*, vol. 295, no. 5558, pp. 1242–1244, 2002.
- [11] S. Self and M. R. Rampino, "The 1883 eruption of Krakatau," *Nature*, vol. 294, no. 5843, pp. 699–704, 1981.
- [12] R. B. Stothers and M. R. Rampino, "Volcanic eruptions in the Mediterranean before A.D. 630 from written and archaeological sources," *Journal of Geophysical Research*, vol. 88, no. 8, pp. 6357–6371, 1983.
- [13] R. B. Stothers, "The great Tambora eruption in 1815 and its aftermath," *Science*, vol. 224, no. 4654, pp. 1191–1198, 1984.
- [14] R. B. Stothers, "Cloudy and clear stratospheres before A.D. 1000 inferred from written sources," *Journal of Geophysical Research*, vol. 107, no. D23, article 4718, 2002.
- [15] K. D. Pang, "Climatic impact of the mid-fifteenth century Kuwae caldera formation, as reconstructed from historical and proxy data," *Eos*, vol. 74, p. 106, 1993.
- [16] C. Oppenheimer, "Climatic, environmental and human consequences of the largest known historic eruption: Tambora volcano (Indonesia) 1815," *Progress in Physical Geography*, vol. 27, no. 2, pp. 230–259, 2003.
- [17] J. B. Witter and S. Self, "The Kuwae (Vanuatu) eruption of AD 1452: potential magnitude and volatile release," *Bulletin of Volcanology*, vol. 69, no. 3, pp. 301–318, 2007.
- [18] P. Y. Forsyth, "In the wake of Etna, 44 B.C.," *Classical Antiquity*, vol. 7, no. 1, pp. 49–57, 1988.
- [19] P. J. Bicknell, "Blue suns, the son of heaven, and the chronology of the volcanic veil of the 40s B.C.," *The Ancient History Bulletin*, vol. 7, pp. 2–11, 1993.
- [20] S. Cao, Y. Li, and B. Yang, "Mt. Tambora, climatic changes, and China's decline in the nineteenth century," *Journal of World History*, vol. 23, no. 3, pp. 587–607, 2012.
- [21] J. Fei and J. Zhou, "The possible climatic impact in China of Iceland's Eldgjá eruption inferred from historical sources," *Climatic Change*, vol. 76, no. 3–4, pp. 443–457, 2006.
- [22] C. F. Mass and D. A. Portman, "Major volcanic eruptions and climate: a critical assessment," *Journal of Climate*, vol. 2, no. 6, pp. 566–593, 1989.
- [23] M. E. Mann, M. A. Cane, S. E. Zebiak, and A. Clement, "Volcanic and solar forcing of the tropical Pacific over the past 1000 years," *Journal of Climate*, vol. 18, no. 3, pp. 447–456, 2005.

- [24] C. Shen, W.-C. Wang, Z. Hao, and W. Gong, "Characteristics of anomalous precipitation events over eastern China during the past five centuries," *Climate Dynamics*, vol. 31, no. 4, pp. 463–476, 2008.
- [25] C. Shen, W.-C. Wang, Z. Hao, and W. Gong, "Exceptional drought events over eastern China During the last five centuries," *Climatic Change*, vol. 85, no. 3-4, pp. 453–471, 2007.
- [26] A. Hansell and C. Oppenheimer, "Health hazards from volcanic gases: a systematic literature review," *Archives of Environmental Health*, vol. 59, no. 12, pp. 628–639, 2004.
- [27] N. Floret, J.-F. Viel, F. Mauny, B. Hoen, and R. Piarroux, "Negligible risk for epidemics after geophysical disasters," *Emerging Infectious Diseases*, vol. 12, no. 4, pp. 543–548, 2006.
- [28] C. J. Horwell and P. J. Baxter, "The respiratory health hazards of volcanic ash: a review for volcanic risk mitigation," *Bulletin of Volcanology*, vol. 69, no. 1, pp. 1–24, 2006.
- [29] C. S. Witham and C. Oppenheimer, "Mortality in England during the 1783–4 Laki Craters eruption," *Bulletin of Volcanology*, vol. 67, no. 1, pp. 15–26, 2004.
- [30] J. Grattan, "Pollution and paradigms: lessons from Icelandic volcanism for continental flood basalt studies," *Lithos*, vol. 79, no. 3-4, pp. 343–353, 2005.
- [31] J. Grattan, R. Rabartin, S. Self, and T. Thordarson, "Volcanic air pollution and mortality in France 1783–1784," *Comptes Rendus Geoscience*, vol. 337, no. 7, pp. 641–651, 2005 (French).
- [32] S. L. de Silva and G. A. Zielinski, "Global influence of the AD 1600 eruption of Huaynaputina, Peru," *Nature*, vol. 393, no. 6684, pp. 455–458, 1998.
- [33] J.-C. Thouret, J. Davila, and J.-P. Eissen, "Largest explosive eruption in historical times in the Andes at Huaynaputina volcano, A.D. 1600, southern Peru," *Geology*, vol. 27, no. 5, pp. 435–438, 1999.
- [34] J.-C. Thouret, E. Juvigné, A. Gourgaud, P. Boivin, and J. Dávila, "Reconstruction of the AD 1600 Huaynaputina eruption based on the correlation of geologic evidence with early Spanish chronicles," *Journal of Volcanology and Geothermal Research*, vol. 115, no. 3-4, pp. 529–570, 2002.
- [35] Y. Lavallée, S. L. De Silva, G. Salas, and J. M. Byrnes, "Explosive volcanism (VEI 6) without caldera formation: insight from Huaynaputina volcano, southern Peru," *Bulletin of Volcanology*, vol. 68, no. 4, pp. 333–348, 2006.
- [36] K. Verosub and J. Lippman, "Global impacts of the 1600 eruption of Peru's huaynaputina volcano," *Eos*, vol. 89, no. 15, pp. 141–143, 2008.
- [37] N. K. Adams, S. L. De Silva, S. Self et al., "The physical volcanology of the 1600 eruption of Huaynaputina, southern Peru," *Bulletin of Volcanology*, vol. 62, no. 8, pp. 493–518, 2001.
- [38] S. L. De Silva, J. Alzueta, and G. Salas, "The socioeconomic consequences of the 1600 AD eruption of Huaynaputina," in *Volcanic Hazards and Human Antiquity*, G. Heiken and F. McCoy, Eds., Special Paper 345 of the Geological Society of America, pp. 15–24, The Geological Society of America, Boulder, Colo, USA, 2000.
- [39] R. Navarro Oviedo, L. A. Jara, J.-C. Thouret, C. Siebe, and J. Dávila, "The AD 1600 eruption of Huaynaputina as described in early Spanish gazetteers," *Boletín de la Sociedad Geológica del Perú*, vol. 90, pp. 121–132, 2000.
- [40] F. Costa, B. Scaillet, and A. Gourgaud, "Massive atmospheric sulfur loading of the AD 1600 Huaynaputina eruption and implications for petrologic sulfur estimates," *Geophysical Research Letters*, vol. 30, no. 2, p. 1068, 2003.
- [41] S. Self, R. Gertisser, T. Thordarson, M. R. Rampino, and J. A. Wolff, "Magma volume, volatile emissions, and stratospheric aerosols from the 1815 eruption of Tambora," *Geophysical Research Letters*, vol. 31, no. 20, Article ID L20608, 2004.
- [42] C. Gao, L. Oman, A. Robock, and G. L. Stenchikov, "Atmospheric volcanic loading derived from bipolar ice cores: accounting for the spatial distribution of volcanic deposition," *Journal of Geophysical Research: Atmospheres*, vol. 112, no. 9, Article ID D09109, 2007.
- [43] R. J. Delmas, S. Kirchner, J. M. Palais, and J.-R. Petit, "1000 Years of explosive volcanism recorded at the South Pole," *Tellus*, vol. 44, no. 4, pp. 335–350, 1992.
- [44] J. M. Palais, S. Kirchner, and R. J. Delmas, "Identification of some global volcanic horizons by major element analysis of fine ash in Antarctic ice," *Annals of Glaciology*, vol. 14, pp. 216–220, 1990.
- [45] C. U. Hammer, H. B. Clausen, and W. Dansgaard, "Greenland ice sheet evidence of post-glacial volcanism and its climatic impact," *Nature*, vol. 288, no. 5788, pp. 230–235, 1980.
- [46] T. J. Crowley, T. A. Criste, and N. R. Smith, "Reassessment of Crete (Greenland) ice core acidity/volcanism link to climate change," *Geophysical Research Letters*, vol. 20, no. 3, pp. 209–212, 1993.
- [47] H. B. Clausen, C. U. Hammer, S. Hvidberg et al., "A comparison of the volcanic records over the past 4000 years from the Greenland Ice Core Project and Dye 3 Greenland ice cores," *Journal of Geophysical Research*, vol. 102, no. 12, pp. 26707–26723, 1997.
- [48] S. J. Johnsen, H. B. Clausen, W. Dansgaard et al., "Irregular glacial interstadials recorded in a new Greenland ice core," *Nature*, vol. 359, no. 6393, pp. 311–313, 1992.
- [49] G. A. Zielinski, P. A. Mayewski, L. D. Meeker et al., "Record of volcanism since 7000 B.C. from the GISP2 Greenland ice core and implications for the volcano-climate system," *Science*, vol. 264, no. 5161, pp. 948–952, 1994.
- [50] A. S. Palmer, T. D. van Ommen, M. A. J. Curran, V. Morgan, J. M. Souney, and P. A. Mayewski, "High-precision dating of volcanic events (A.D. 1301–1995) using ice cores from Law Dome, Antarctica," *Journal of Geophysical Research: Atmospheres*, vol. 106, no. 22, pp. 28089–28095, 2001.
- [51] J. Cole-Dai, E. Mosley-Thompson, S. P. Wight, and L. G. Thompson, "A 4100-year record of explosive volcanism from an East Antarctica ice core," *Journal of Geophysical Research: Atmospheres*, vol. 105, no. 19, pp. 24431–24441, 2000.
- [52] D. Budner and J. Cole-Dai, "The number and magnitude of large explosive volcanic eruptions between 904 and 1865 A.D.: quantitative evidence from a new South Pole ice core," *Geophysical Monograph*, vol. 139, pp. 165–176, 2003.
- [53] B. Stenni, M. Proposito, R. Gragnani et al., "Eight centuries of volcanic signal and climate change at Talos Dome (East Antarctica)," *Journal of Geophysical Research*, vol. 107, no. 9, p. 4076, 2002.
- [54] M. Igarashi, Y. Nakai, Y. Motizuki, K. Takahashi, H. Motoyama, and K. Makishima, "Dating of the Dome Fuji shallow ice core based on a record of volcanic eruptions from AD 1260 to AD 2001," *Polar Science*, vol. 5, no. 4, pp. 411–420, 2011.
- [55] K. R. Briffa, P. D. Jones, F. H. Schweingruber, and T. J. Osborn, "Influence of volcanic eruptions on Northern Hemisphere summer temperature over the past 600 years," *Nature*, vol. 393, no. 6684, pp. 450–455, 1998.

- [56] L. A. Scuderi, "Tree-ring evidence for climatically effective volcanic eruptions," *Quaternary Research*, vol. 34, no. 1, pp. 67–85, 1990.
- [57] P. D. Jones, K. R. Briffa, and F. H. Schweingruber, "Tree-ring evidence of the widespread effects of explosive volcanic eruptions," *Geophysical Research Letters*, vol. 22, no. 11, pp. 1333–1336, 1995.
- [58] U. Büntgen, J. Esper, D. C. Frank, K. Nicolussi, and M. Schmidhalter, "A 1052-year tree-ring proxy for Alpine summer temperatures," *Climate Dynamics*, vol. 25, no. 2-3, pp. 141–153, 2005.
- [59] R. D. D'Arrigo and G. C. Jacoby, "Northern North American tree-ring evidence for regional temperature changes after major volcanic events," *Climatic Change*, vol. 41, no. 1, pp. 1–15, 1999.
- [60] M. Génova, "Extreme pointer years in tree-ring records of Central Spain as evidence of climatic events and the eruption of the Huaynaputina Volcano (Peru, 1600 AD)," *Climate of the Past*, vol. 8, no. 2, pp. 751–764, 2012.
- [61] V. C. LaMarche Jr. and K. K. Hirschboeck, "Frost rings in trees as records of major volcanic eruptions," *Nature*, vol. 307, no. 5947, pp. 121–126, 1984.
- [62] L. Filion, S. Payette, L. Gauthier, and Y. Boutin, "Light rings in subarctic conifers as a dendrochronological tool," *Quaternary Research*, vol. 26, no. 2, pp. 272–279, 1986.
- [63] D. K. Yamaguchi, L. Filion, and M. Savage, "Relationship of temperature and light ring formation at subarctic treeline and implications for climate reconstruction," *Quaternary Research*, vol. 39, no. 2, pp. 256–262, 1993.
- [64] R. M. Hantemirov, L. A. Gorlanova, and S. G. Shiyatov, "Extreme temperature events in summer in northwest Siberia since AD 742 inferred from tree rings," *Palaeogeography, Palaeoclimatology, Palaeoecology*, vol. 209, no. 1–4, pp. 155–164, 2004.
- [65] D. M. Pyle, "How did the summer go?" *Nature*, vol. 393, no. 6684, pp. 415–417, 1998.
- [66] G. Utterström, "Climatic fluctuations and population problems in early modern history," *Scandinavian Economic History Review*, vol. 3, pp. 26–41, 1955.
- [67] J. Fei and J. Zhou, "The possible climatic impact in North China of the AD 1600 Huaynaputina eruption, Peru," *International Journal of Climatology*, vol. 29, no. 6, pp. 927–933, 2009.
- [68] Beijing Astronomical Observatory and Chinese Academy of Sciences, *A Joint Catalogue of the Chinese Local Chronicles*, The Chinese Press (Zhonghua Shuju), Beijing, China, 1985 (Chinese).
- [69] X. Liu, D. Qin, X. Shao, T. Chen, and J. Ren, "Temperature variations recovered from tree-rings in the middle Qilian Mountain over the last millennium," *Science in China, Series D: Earth Sciences*, vol. 48, no. 4, pp. 521–529, 2005.
- [70] H. Zhu, Y. Zheng, X. Shao, X. Liu, Y. Xu, and E. Liang, "Millennial temperature reconstruction based on tree-ring widths of Qilian juniper from Wulan, Qinghai Province, China," *Chinese Science Bulletin*, vol. 53, no. 24, pp. 3914–3920, 2008.
- [71] Y. Liu, Z. An, H. W. Linderholm et al., "Annual temperatures during the last 2485 years in the mid-eastern tibetan plateau inferred from tree rings," *Science in China, Series D: Earth Sciences*, vol. 52, no. 3, pp. 348–359, 2009.
- [72] Y. Liu, Q. Cai, H. Song, Z. An, and H. W. Linderholm, "Amplitudes, rates, periodicities and causes of temperature variations in the past 2485 years and future trends over the central-eastern Tibetan Plateau," *Chinese Science Bulletin*, vol. 56, no. 28-29, pp. 2986–2994, 2011.

Research Article

Holocene Vegetation Succession and Response to Climate Change on the South Bank of the Heilongjiang-Amur River, Mohe County, Northeast China

Chao Zhao,^{1,2} Xiaoqiang Li,¹ Xinying Zhou,¹ Kelian Zhao,¹ and Qing Yang¹

¹Key Laboratory of Vertebrate Evolution and Human Origins of Chinese Academy of Sciences, Institute of Vertebrate Paleontology and Paleoanthropology, Chinese Academy of Sciences, Beijing 100044, China

²University of Chinese Academy of Sciences, Beijing 100049, China

Correspondence should be addressed to Xiaoqiang Li; lixiaoqiang@ivpp.ac.cn

Received 3 February 2015; Revised 24 May 2015; Accepted 31 May 2015

Academic Editor: Steffen Mischke

Copyright © 2016 Chao Zhao et al. This is an open access article distributed under the Creative Commons Attribution License, which permits unrestricted use, distribution, and reproduction in any medium, provided the original work is properly cited.

Pollen samples from peat sediments on the south bank of the Heilongjiang River in northern Northeast China (NE China) were analyzed to reconstruct the historical response of vegetation to climate change since 7800 cal yr BP. Vegetation was found to have experienced five successions from cold-temperate mixed coniferous and broadleaved forest to forest-steppe, steppe-woodland, steppe, and finally meadow-woodland. From 7800 to 7300 cal yr BP, the study area was warmer than present, and *Betula*, *Larix*, and *Picea*-dominated mixed coniferous and broadleaved forests thrived. Two cooling events at 7300 cal yr BP and 4500 cal yr BP led to a decrease in *Betula* and other broadleaved forests, whereas herbs of Poaceae expanded, leading to forest-steppe and then steppe-woodland environments. After 2500 cal yr BP, reduced temperatures and a decrease in evaporation rates are likely to have resulted in permafrost expansion and surface ponding, with meadow and isolated coniferous forests developing a resistance to the cold-wet environment. The Holocene warm period in NE China (7800–7300 cal yr BP) could have resulted in a strengthening of precipitation in northernmost NE China and encouraged the development of broadleaved forests.

1. Introduction

At present, global warming and its possible ecological consequences have become the focus for governments around the world, the scientific community, and the general public [1, 2]. In tackling core issues, it is very important to evaluate the effects of climate change accurately [3]. The Holocene is the most recent geological epoch. The early Holocene experienced increased temperatures, the mid-Holocene was warm and humid, and the late Holocene cooled [4, 5], providing research models for future climate change [6]. Land vegetation is an important part of the global ecological system and responds profoundly to climate change; exploring this relation between vegetation and climate change in critical areas has thus become an important approach in assessing the likely environmental impact of future climate change.

NE China, which has typical land ecosystems (including forests, steppes, and wetland) [7], is located on the eastern

margin of the Eurasian continent. The northern Greater Khingan Range (GKR), in the northernmost part of NE China (on the southern margins of the permafrost zone), contains cold-temperate coniferous forest. The permafrost layer is shallow and its temperature stability is relatively low in this area, so the region is highly sensitive to climate change [8–10]. Over the past century, there has been a clear degradation of permafrost in NE China. Its southern boundary has moved northward 20–30 km [11–14]. This has caused a series of ecological and hydrological changes, resulting in wetland and forest degradation and other environmental problems. Permafrost wetlands in the northern GKR have been characterized by original wetland atrophy and new wetland expansion [13, 15, 16].

In recent years, research into the Holocene environment in this area has focused more on climatic and environmental reconstruction [17, 18] and concentrated on the Sanjiang Plains in the northeast [19–21], the Changbai Mountains in

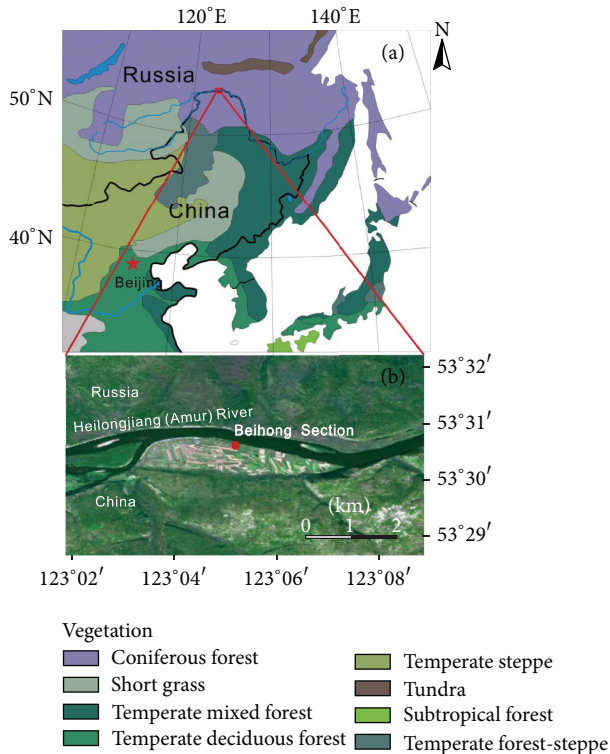


FIGURE 1: Map of the study area. (a) Red rectangle indicates the study area. (b) Red dot shows the Beihong Section.

the east [22–27], Hulun Lake in the western GKR [28, 29], Dali Lake in the southern GKR [30], Moon Lake in central GKR [31, 32], and so forth. These studies have highlighted a significant warming in the early mid-Holocene, followed by a transition to a dry-cold climate in the late Holocene.

However, a longer and more detailed vegetation history of NE China is still needed to verify vegetation succession interpretative studies and vegetative responses to climate change. There have until now been no other records sufficiently reliable for testing how cold-temperate vegetation on the northern margins of NE China has responded to Holocene climate change. This study is based on pollen records derived from Holocene peat sediments on the south bank of the Heilongjiang River. It aims to reconstruct a vegetation succession history, explore vegetation succession responses to climate change (especially during the Holocene Megathermal), and provide evidence for the evaluation of the possible effects of future climate change.

2. Materials and Methods

2.1. Study Area. The northern GKR ($52^{\circ}32'–53^{\circ}41'N$, $121^{\circ}15'–125^{\circ}58'E$) (Figure 1) is located in the transition zone between a semihumid and semiarid cold-temperate continental monsoon climate; it is controlled by the cold Siberian-Mongolian High (extremely cold and dry) in winter and is marginally affected by the Pacific High (warm and humid) in summer [7]. Based on the Mohe County meteorological station, mean annual temperature (MAT) is $-4.9^{\circ}C$, minimum temperature

is $-52.3^{\circ}C$, and the ground is frozen for up to eight months per annum. Mean annual precipitation (MAP) is 403 mm, about 80% of which is concentrated in June–September [37, 38]. In the last half century, the interannual rainfall shows fluctuation and changed between 274 mm and 635 mm [39]. The annual evaporation is ~ 1000 mm.

The Beihong Section ($53^{\circ}30'8.3''N$, $123^{\circ}5'24.5''E$, altitude: 280 m a.s.l.), which is located in the north of Beihong Village, on the southern bank of the Heilongjiang River in Mohe County, is dominated by peat sediments from the upper reaches of the Heilongjiang River (Figure 1). The Heilongjiang (Amur) Valley in northern NE China is dominated by taiga vegetation, with *Larix gmelinii* as a typical vegetation type, including *Betula Platyphylla* forest, *Pinus sylvestris* var. *mongolica* forest, *Picea* forest, and Poaceae meadow [7, 40].

The GKR has been directly administered by the central government since the Yuan Dynasty (1206–1368 CE) [41, 42]. Its native inhabitants continued to hunt and gather until the onset of the Opium Wars (1840 CE), when its forests began to undergo large-scale exploitation [7, 43, 44]. Consequently, vegetation succession in the study area has been principally affected by natural factors, with relatively weak human influence during the Holocene. It is the ideal area to study vegetation succession and its responses to climate change.

2.2. Beihong Section Sample and Pollen Analysis. The Beihong Section is 260 cm thick. The sediments are mainly peat and silt. They are delineated as follows: 0–80 cm, dark brown peat layer; 80–220 cm, light gray silty clay; 220–260 cm, gray fine sandy silt.

26 samples taken at 10 cm intervals were prepared for pollen analysis, using conventional acid-alkali treatment and heavy liquid separation [45, 46]; they were then treated by acetolysis [47]. Lycopodium tablets were added to the samples in order to estimate pollen concentrations [48]. 315–646 pollen grains were counted from each sample; pollen percentages and concentrations were calculated based on total land pollen count. TILIA software was used to draw the pollen spectra, in which a CONISS module was used to calculate distances and cluster zoning based on the square root transformation of the pollen percentage data.

Detrended correspondence analysis (DCA) and principal component analysis (PCA) have been widely used in forest ecosystem, shrub communities, meadow grasslands, and other vegetation researches [16, 49, 50]. DCA is a sort of gradient analysis method, which can arrange samples or pollen-taxa in a certain space, and the ordination axes can reflect the ecological gradient to explain the relationship between plant communities and the environment [51]; PCA is a method of statistics to focus on a few comprehensive indexes from a set of variables and was applied to extract main gradient changes in vegetation. DCA and PCA figures were created by CANOCO 4.5 based on samples and the terrestrial pollen percentage data (of percentage $>3\%$). PCA function in SPSS was used to generate the PCA F1 values, extracting more comprehensive information on the environment [22].

2.3. Chronology. Macroremains of leaves and peat selected from the samples were examined to obtain an accurate

TABLE 1: AMS ^{14}C dating results from the Beihong Section.

Sample	Laboratory code	Depth (cm)	Sample type	^{14}C ages (yr BP)	$\delta^{13}\text{C}$ (‰VPDB)	Calibrated ^{14}C ages (cal yr BP)
BH-16	378769	75	Macro-remains of leaves	3970 ± 30	-28.8	4524-4401
BH-32	379976	155	Peat	6200 ± 30	-25.4	7179-7000
BH-48	376264	238	Macro-remains of leaves	6770 ± 30		7669-7580

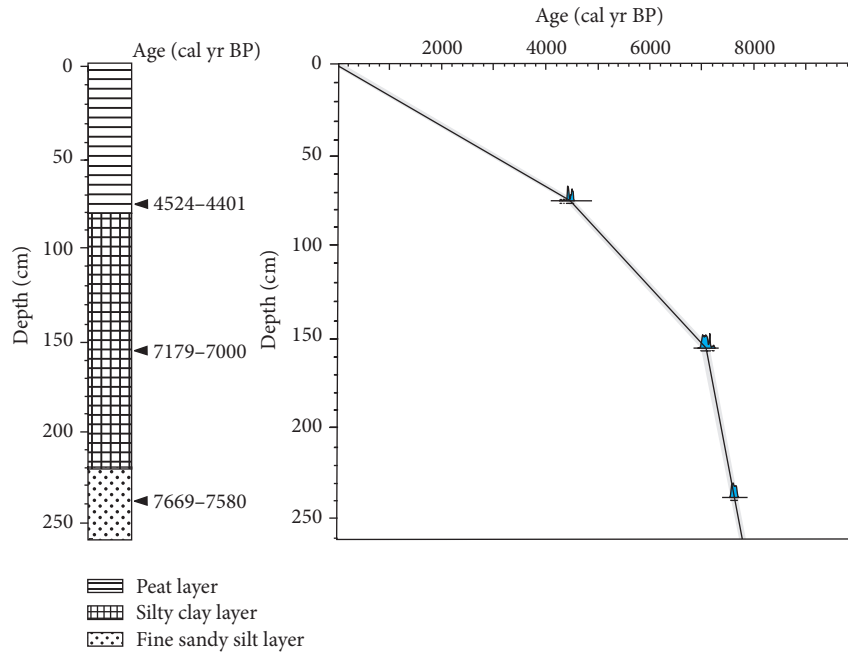


FIGURE 2: Beihong Section and age-depth model.

age-depth framework. AMS ^{14}C dating was conducted at the Beta Analytic Radiocarbon Dating Laboratory in America, and three AMS ^{14}C ages at depths of 75 cm, 155 cm, and 238 cm were obtained. Radiogenic ^{14}C ages were calibrated to calendar ages based on IntCal13 [52] and an age-depth model was produced using OxCal4.2.4 [35] (Table 1). The Beihong Section shows a positive correlation between age and depth.

A chronosequence for the Beihong Section was established using linear interpolation and extrapolation methods based on three samples. The age of the base (260 cm) was calculated as 7800 cal yr BP; the top consists of modern deposits. Consequently, the Beihong Section presents a historically continuous sedimentary sequence (Figure 2). The sedimentation rate is higher in the lower segment of the section. The average sediment rate is 0.16 cm/yr between 260 cm and 155 cm and falls to an average of 0.02 cm/yr from 155 cm to 0 cm; as a consequence the lower segment of the section has a higher resolution than the upper part.

3. Results

3.1. Pollen Assemblages in the Beihong Section. 53 families and genera of pollen were identified in the Beihong Section (Table 2). They are mainly broadleaved tree pollen (19%–54%) and herb pollen (28%–64%); *Betula* pollen (10%–45%)

was the commonest of the broadleaved tree pollen, and Poaceae pollen was the most prominent of the herb pollen, with content ranging from 3% to 36%. Total pollen concentrations exhibited considerable variation, ranging from 2.9×10^2 to 1.9×10^6 grains/g.

Based on chronological changes in pollen percentages, five successions can be recognized from pollen spectra (Figure 3).

In zone 1 (260–190 cm, 7800–7300 cal yr BP), *Betula*, *Larix*, *Picea*, *Alnus*, Cupressaceae, *Pinus*, and other kinds of tree pollen dominate pollen assemblages (55%–66%); of these, broadleaved tree pollen percentages, especially of *Betula* (22%–45%), were extremely high. Coniferous tree pollen content (10%–27%), mainly *Larix* (7%–16%) and *Picea* (2%–7%), was relatively high. Shrub and herb pollen percentages fluctuated from 34% to 45% and were dominated by Liliaceae pollen (1%–19%), with some *Artemisia* (3%–11%), Chenopodiaceae (2%–5%), and Poaceae pollen (3%–16%). Total pollen concentrations (2.9×10^2 – 2.0×10^4 grains/g) were relatively low.

In zone 2 (190–80 cm, 7300–4500 cal yr BP), spectra were dominated by Poaceae, *Artemisia*, Chenopodiaceae, and other kinds of herb pollen, with their total content ranging from 44% to 50%. Poaceae pollen percentages (9%–28%) clearly increased, whereas Liliaceae pollen content (0–6%)

TABLE 2: Pollen types in the Beihong Section.

Conifers	<i>Pinus</i> , <i>Picea</i> , <i>Larix</i> , and Cupressaceae
Broadleaved trees	<i>Quercus</i> , <i>Betula</i> , <i>Salix</i> , <i>Populus</i> , <i>Ulmus</i> , <i>Alnus</i> , <i>Corylus</i> , <i>Carpinus</i> , <i>Juglans</i> , <i>Castanea</i> , and Aceraceae.
Shrubs and herbs	Ericaceae, <i>Artemisia</i> , Chenopodiaceae, Poaceae, Leguminosae, <i>Thalictrum</i> , Caryophyllaceae, Compositae, Rosaceae, <i>Sanguisorba</i> , Liliaceae, <i>Plantago</i> , Umbelliferae, <i>Ephedra</i> , Polygonaceae, Oleaceae, Cyperaceae, Ranunculaceae, <i>Tamarix</i> , Dipsacaceae, and so forth.
Ferns	Polypodiaceae, Athyriaceae, <i>Selaginella</i> , and so forth.

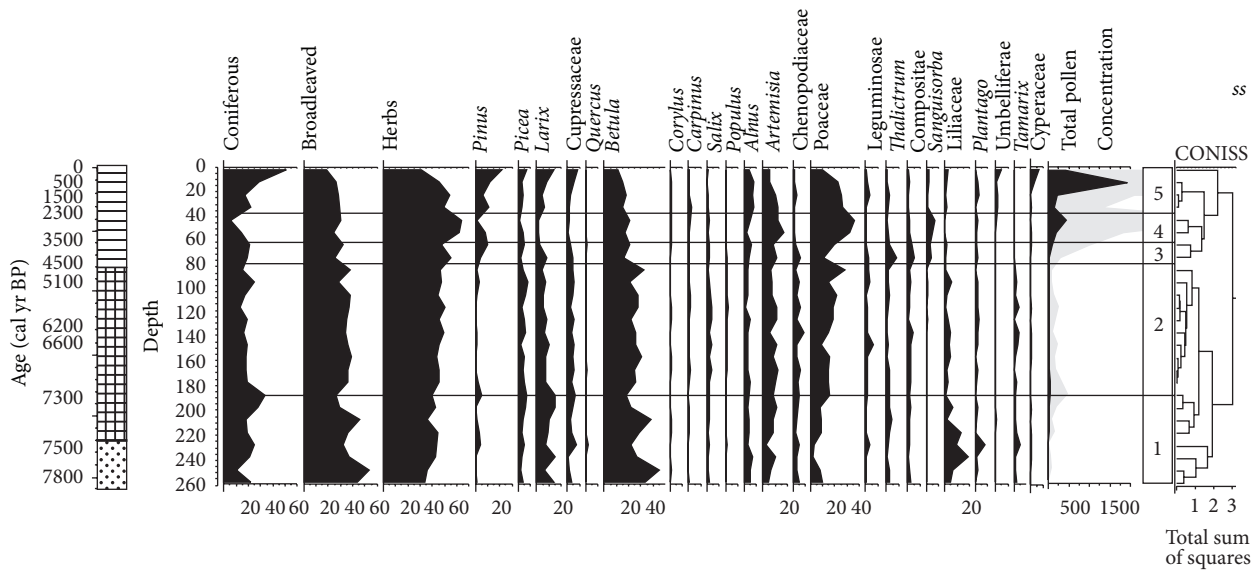


FIGURE 3: Pollen percentages and concentrations for the Beihong Section (the gray values to the right are magnified tenfold to emphasize changes in concentration).

decreased. In contrast, tree pollen content decreased markedly, with *Larix* (5%–10%), *Betula* (21%–32%), and *Pinus* pollen percentages (0–4%) dropping markedly. Total pollen concentrations (6.7×10^3 – 4.5×10^4 grains/g) were relatively low.

In zone 3 (80–60 cm, 4500–3500 cal yr BP), this period was characterized by high percentages (48%–55%) of herb pollen, principally *Thalictrum* (3%–9%), Compositae (4%–5%), *Sanguisorba* (3%–4%), and *Artemisia* (8%–11%); Poaceae pollen content (11%–20%) decreased noticeably. Coniferous (19%–21%) and broadleaved tree pollen content (26%–32%) decreased, with *Betula* (17%–20%) and *Picea* pollen percentages (3%–5%) falling markedly. Total pollen concentrations (2.9×10^4 – 10.0×10^4 grains/g) increased slightly.

In zone 4 (60–40 cm, 3500–2300 cal yr BP), Herb pollen, dominated by Poaceae, *Artemisia*, and *Sanguisorba*, reached its peak values at 62%–64%; among them Poaceae (32%–36%), *Artemisia* (12%–18%), and *Sanguisorba* (5%–7%) pollen markedly increased, while Chenopodiaceae pollen content (about 1%) decreased. Coniferous tree pollen (6%–14%) decreased noticeably, with *Larix*, Cupressaceae, and *Picea* pollen falling to their lowest values, while *Pinus* pollen increased (1%–8%). Total pollen concentrations rose (1.8×10^5 – 4.3×10^5 grains/g).

In zone 5 (40–0 cm, 2300 cal yr BP–modern), coniferous tree pollen (17%–51%), especially *Pinus* pollen percentages (6%–21%), increased greatly, with some emergence of *Larix* (4%–13%) and *Picea* (3%–6%). Broadleaved tree pollen (29%–19%) decreased, especially *Betula* pollen content (18%–11%), which fell to its lowest value for the entire section. Herb pollen percentages (31%–55%) decreased, but Cyperaceae, *Plantago*, and Umbelliferae content increased to some extent. Total pollen concentrations (1.3×10^5 – 1.9×10^6 grains/g) increased.

3.2. DCA and PCA Results. Of the 26 samples taken from top to bottom of Beihong Section, 31 families and genera were analyzed using DCA. The first two ordination axes were drawn on a two-dimensional ordination map (Figure 4). The score value of each sample was distributed regularly on the plane composed of the first and second principal axes. Samples from the five pollen assemblages yielded separate, individual clusters, and these clear differences verified the accuracy of the zoning (Figure 3).

According to PCA results for the principal families and genera (Figure 5), the first two principal component axes accounted for 79% of all the variables (the first axis for 69% and the second for 10%). *Pinus*, *Betula*, Chenopodiaceae, and Ericaceae are the four main taxa of the original

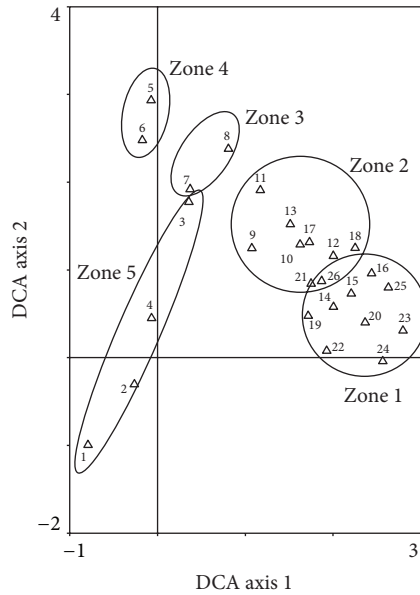


FIGURE 4: DCA results for 26 representative plant community samples from the Beihong Section.

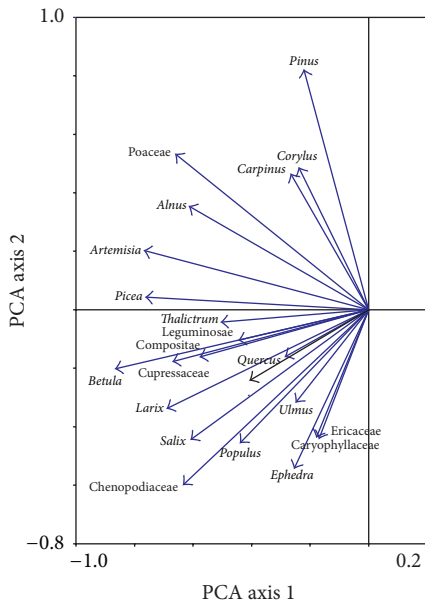


FIGURE 5: PCA results for principal pollen from the Beihong Section.

data matrix, whose vector lengths represent their degree of effect and significance, while the importance of other taxa decreases accordingly. Relations between the main taxa present a certain regularity. The plants that registered the highest positive scores for the first component axis included Ericaceae, Caryophyllaceae, and other plant types; *Betula*, *Picea*, and other vegetation types yielded the lowest scores. *Pinus* and Poaceae scored the highest positive values on the second component axis; Chenopodiaceae, *Ephedra*, and other vegetation types scored lowest here.

4. Discussion

Stalagmite, ice core, ocean, lake sediment, and other high resolution records show that there was a significant warm period in the mid-Holocene, similar to a scenario encompassing a 1-2°C increase in average global temperatures [5, 53-55]. Marcott et al. suggested that, based on 73 globally discrete records, temperatures during 10000-5000 cal yr BP were 0.7°C warmer than the late Holocene [4]. The reconstruction of the vegetation succession on the southern bank of the Heilongjiang River in northern NE China since 7800 cal yr BP provides an important basis for establishing climate and environment change and their effect on vegetation in a cold-temperate region in the Holocene.

Pollen analysis is the technique most widely used and pollen data are most reliable for the reconstruction of paleovegetation and paleoclimate. Understanding the relation between modern pollen and vegetation is a prerequisite for interpreting fossil pollen records correctly and improving the accuracy of past vegetation type and paleoclimate reconstruction [56-58].

4.1. Pollen Source in Beihong Section. The lithology changed from fine detritus gyttja at the bottom to decomposed peat in the Beihong Section (Figure 2). It may indicate that the environment of sedimentation changed over time and this lithologic transition probably occurred as the site changed from lake to swamp [59].

Source areas and relative pollen representation are shown to depend on basin size [60]. In Beihong Section, 220-260 cm gray fine sandy silt may indicate the enhancement of water-carrying capacity. This may induce a relatively low total pollen concentration because of the poor depositional environment (Figure 3). In addition, surface pollen assemblages in the marsh always includes a large number of regional pollen types usually from aquatic plants [61]; meanwhile, the total pollen concentrations may increase due to favorable depositional environment (Figure 3).

Nevertheless, studies on alluvial pollen show that the differences between alluvial pollen assemblages are the result of different pollen origins [34]. Most studies in different environment of sedimentation show that despite containing some exotic ingredients, the modern pollen assemblages can reflect characteristics of plant community in the immediate area, and the main vegetation zones along the regional can be distinguished by their modern pollen spectra [33, 36, 56-58, 61-65]. Therefore, the transitions of the pollen assemblages of the terrestrial pollen percentage (with the pollen sum excluding aquatics) in Beihong Section are mainly the result of the vegetation succession in the study area.

4.2. Modern Pollen Representation and Climatic Implications. Surface pollen studies have established that there is a relationship among the pollen percentages as well as vegetation type and regional climate [64]. The studies on vegetation and modern pollen distribution show that pollen assemblages are correlated well with the vegetation types in NE China [33, 36, 63].

In addition, *Betula* and *Pinus* pollen is overrepresented. The existence of birch forests was thus indicated only when the *Betula* content exceeded 40%. Pine forest might exist when *Pinus* pollen percentages are more than 30%. Poaceae and *Larix* pollen is of low representative feature. *Larix* pollen contents accounted for only 15% in larch forest [57, 62, 66]. A higher proportion of Poaceae (24%) was the main characteristic of wetland shrub. Poaceae pollen contents are <10% in Poaceae grassland, with *Artemisia* and Chenopodiaceae pollen percentages being more than half of the total. Hence, a high representation of *Artemisia* and Chenopodiaceae was found. Cyperaceae and *Ephedra* appeared in the middle or low relative representation values [33, 57].

Larix gmelinii and *Pinus sylvestris* var. *mongolica* are dominated in cold-temperate zone. The relationship among *Pinus* pollen, temperature, and humidity is more complex. *Pinus* pollen contents rise rapidly with increasing humidity [36]. The distribution of spruce is in cold-temperate zone (average temperature is 0–8°C) in the northern part of NE China; others grow in the cold-wet subalpine zone between 1000 and 2000 m [67]. The abundance of *Picea* pollen generally increases along with the humidity rise [68]. The *Betula* pollen count in topsoil of northern China is affected mainly by annual precipitation and will rise consistent with the increase of the amount of precipitation [67, 68].

Poaceae pollen is abundant in fossil records and is often used as a paleoclimatic indicator [69]. Poaceae pollen always concentrated in low temperature and high humidity area or semiarid warm zone, and its abundance increases with the decrease of temperature, as well as the increase of precipitation in low temperature and high humidity area [67]. The abundances of Chenopodiaceae and *Ephedra* pollen increased with increasing aridity; Compositae and *Plantago* pollens appear at low temperature and high humidity area [67, 68].

4.3. Vegetation Succession in Beihong Area. Based on the pollen assemblages and the modern pollen analysis, the vegetation history in Beihong area has experienced five chronosequences since 7800 cal yr BP.

- (1) In 7800–7300 cal yr BP, *Betula* pollen percentage is at the highest level of the section, up to 45%. *Larix* content (7%–16%) is also relatively high. The pollen assemblage may indicate that the study area developed *Larix* and *Betula* dominated cold-temperate coniferous and broadleaved mixed forest.
- (2) In 7300–4500 cal yr BP, herb pollens increase (>44%). Poaceae pollen percentages range from 9% to 28%, while *Betula* (<32%), *Larix* (<10%), *Pinus* pollen (<4%), and other tree pollen contents decreased markedly, suggesting a forest-steppe vegetation type.
- (3) In 4500–3500 cal yr BP, herb pollen increases, including *Thalictrum*, Compositae, *Sanguisorba*, and *Artemisia*. Tree pollen percentages decrease markedly, with *Betula* pollen ranging from 17% to 20%. Pollen assemblages indicate steppe-woodland.

(4) In 3500–2300 cal yr BP, pollen records reveal Poaceae (32%–36%), *Artemisia*, and *Sanguisorba* dominated steppe vegetation type.

(5) In 2300 cal yr BP-modern, pollen assemblages indicate that Poaceae, Cyperaceae, and other mesophytophyte-dominated meadow vegetation developed, along with an expansion in isolated coniferous forests composed largely of *Pinus* pollen (up to 21%). These pollen assemblages are characterized by meadow-woodland vegetation.

4.4. Vegetation Response to Climate Change. Climate change has an important impact on terrestrial ecosystems [70–72]. Similarly, vegetation successions in different regions are a good indicator of climate change and are an important index for revealing the environmental impact of climate change. Fossil pollen diagrams can be assumed to reflect information about natural vegetation dynamics and provide the evidence for the behavior of plant taxa when subjected to major climatic and environmental changes in the past [64].

The vegetation history mainly experienced a clear decrease in *Betula* and other broadleaved trees, while Poaceae-dominated herbs increased in the study area (Figure 3). The pollen samples exhibited five vegetation successions, from coniferous and deciduous mixed forest at the section's base, upward to forest-steppe, steppe-woodland, steppe, and meadow-woodland, transitioning from a forest vegetation cover, resistant to a cold-dry environment to meadow-woodland vegetation and then to cold-wet environs (Figure 4). These vegetation types and the succession process had similar records at high latitudes.

Herbaceous plants, such as Cyperaceae and Poaceae, are the most important components of wetland communities [73]. Alpine vegetation occurs from the treeline to the snow line, whose important taxa include Cyperaceae, Poaceae, Compositae, Ericaceae, Caryophyllaceae, and Rosaceae [74]. The Holocene pollen diagram from eastern Canadian Arctic Island showed that there was virtually no *Betula* pollen present in very cold temperature, while Poaceae pollen with varying amounts of Ericaceae and Caryophyllaceae dominated the pollen assemblages [75]. Vegetation history of the western America in the Holocene shows that the lower subalpine communities are usually closed forests, and upper communities are steppe-woodland and shrublands. Based on the meteorological data of Changbai Mountain, the distribution age of *Betula ermanii* was in the trend of decreasing with elevation rising in the ecotone between *Betula ermanii* and alpine tundra [76]. Therefore, vegetation dominated by *Betula* might reflect a relatively warmer environment than the later meadow-woodland community in Beihong Section.

Consequently, DCA reflected a clear relation between different plant communities as well as between plant communities and the environment. The first axis can reflect the temperature gradients for different plant communities, with ability to resist the cold strengthening leftward along the axis; the second axis can indicate changes in humidity, with a plant community's ability to withstand drought strengthening

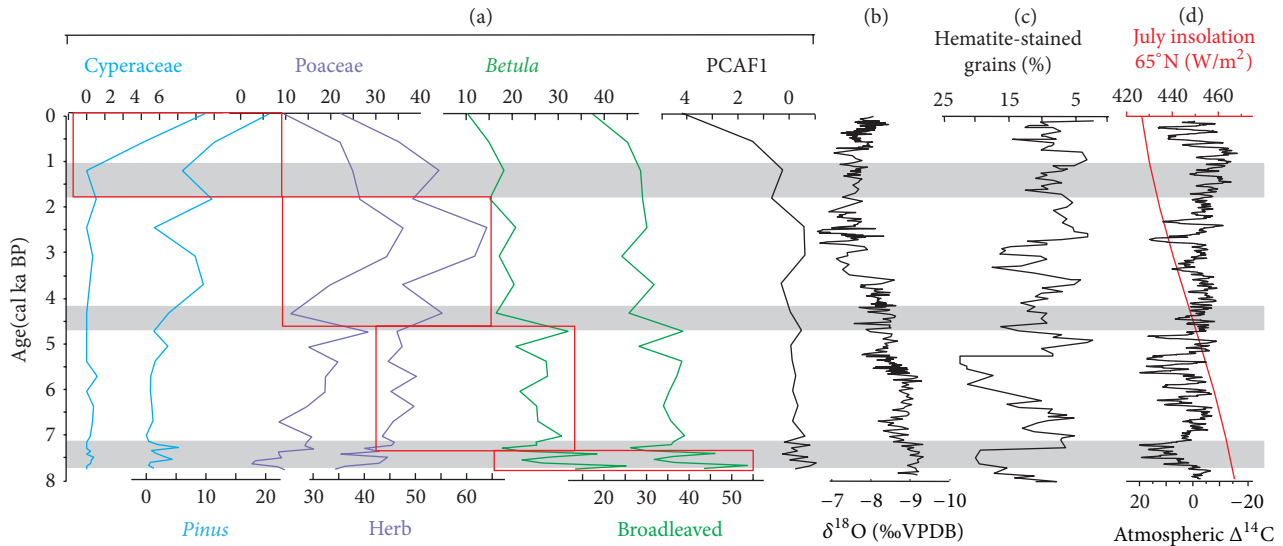


FIGURE 6: Comparison of principal pollen percentages and the PCA F1 curve from the Beihong Section with other selected proxy records. (a) Pollen index from the Beihong Section. From the right to left are the PCA F1 curve, the percentage curves of broadleaved trees, *Betula*, herb, Poaceae, *Pinus*, and Cyperaceae. (b) Dongge Cave D4 [33]. (c) Holocene drift ice record for the MC52-VM29-191 North Atlantic core [34]. (d) Northern Hemisphere July insolation at 65°N [35] and the residual atmospheric $\Delta^{14}\text{C}$ record (~2000-year moving average) [36]. The lateral gray bands trace the interconnection between climate cooling, drift ice, a weakened EASM, reduced insolation activity, and the principal pollen taxa changes in this study. The red boxes show the main indicator plants of vegetation type conversion.

upward along the axis. The first principal component of PCA reflected temperatures and the second changes in humidity.

The PCA F1 scores of the taxa on the first principal component axis better reflected the pollen percentage variations with temperature; that is, higher values may represent cold and lower values warm climates (Figure 5). The PCA F1 curve thus revealed that temperatures have fluctuated downward decreased since 7800 cal yr BP (Figure 6), in tandem with reductions in insolation in northern hemisphere high latitudes [77].

In order to better reflect the response of vegetation to climate change, the principal pollen percentages and the PCA F1 curve from the Beihong Section were compared with high-resolution climate indices from other regions (Figure 6). Results suggested that the warmest and wettest stage in the Holocene occurred at ~7800–7300 cal yr BP, when MAT and MAP suited the growth of coniferous and broadleaved mixed forest in the study area. After 7300 cal yr BP, a decrease in *Betula* and other broadleaved trees and an increase in Poaceae and other herbs, as well as in *Pinus*, Cyperaceae, and other plants resistant to the cold-wet environs of the late Holocene, correspond to documented cooling events and reduced insolation activity [78].

The Beihong Section shows that the area had developed *Betula*, *Larix*, and *Picea*-dominated coniferous and broadleaved mixed forests, with Liliaceae prevalent in the undergrowth during 7800–7300 cal yr BP. Such vegetation indicates a warm and humid climate and essentially agrees with the findings of many other surveys, such as those conducted at Hulun Lake in the western GKR [29], the Qindeli Section on the Sanjiang Plains [20], Hokkaido Island

[79], the Kuril Islands [80], the eastern Siberian Yakutia Lake [61], and Sakhalin [79].

At ~7300 cal yr BP and ~4500 cal yr BP, warmth-loving broadleaved trees clearly decreased in number in the study area, while cold-tolerant herbs increased (Figure 6). Vegetation cover changed from mixed coniferous and broadleaved forest to forest-steppe and steppe-woodland. The two significant cooling events which had a profound impact on vegetation succession are consistent with the significant ice event identified in North Atlantic records [81] and with the weakened East Asian Summer Monsoon (EASM) revealed in stalagmite oxygen isotope records from Dongge Cave [5, 82]. At ~2500–1500 cal yr BP, broadleaved trees, Poaceae, and mesophytes-xerophytes taxa declined, while *Pinus* and Cyperaceae vegetation expanded. Plant type was affected by paludification, indicating that global climate cooling had a profound influence on vegetation.

The cooling event at ~7300 cal yr BP, which resulted in a vegetation succession from mixed coniferous and broadleaved forest to forest-steppe, also appears in pollen records from Moon Lake in the central GKR [31] and the Buguldeika Core from Baikal Lake [83]. The cooling event at ~4500 cal yr BP, which may have global parallels, appears in the pollen records from Erlongwan Maar Lake [84], the Gushantun Bog in Jilin [85], and Hokkaido in Japan [86]. Vegetation shows a succession from forest-steppe to steppe-woodland. The cooling during ~2500–1500 cal yr BP in the Beihong area is also apparent in paleoenvironmental records from Hulun Lake in the western GKR [29], Moon Lake in the central GKR [31], Dali Lake in the southern GKR [30], Jingpo Lake in NE China [24], and Hokkaido Island in Japan [79, 80].

Many studies show that there is a complex interaction of climatic and ecological processes in boreal permafrost formation and degradation [73, 87, 88]. Permafrost is directly influenced by climate; climate and permafrost are among the principal driving forces of vegetation establishment and successional change across Siberia [89, 90]. The investigation of potential vegetation cover progression during the Siberian Bioclimatic Model shows that permafrost is predicted to thaw. The future much warmer and drier climate would be suitable for the forest-steppe ecotone and grasslands rather than forests, and water-stress-tolerant light larch (*Larix dahurica*) taiga will continue to be the dominant zoniobiome over eastern Siberia [89].

Accordingly, it can be predicted that falling global temperatures and a weakening EASM gave rise to decreased rates of evaporation and an increase in effective humidity levels in the late Holocene. At the same time, an expansion in permafrost led to precipitation and runoff being unable to seep underground, causing surface ponding, marsh expansion, and peat development [13]. As a result, the vegetation type changed gradually to meadow and swamp-meadow, with isolated areas of cold-wet tolerant coniferous woodland [91] and a severe reduction in warmth-loving broadleaved trees. The long-term data from our studies (especially during the Holocene Megathermal) in the permafrost ecosystem suggest that responses of vegetation to climate warming might be the thaw of permafrost which will be deep enough to sustain the growth of *Betula* and *Larix* dominated taiga in south bank of Heilongjiang-Amur River [89].

5. Conclusions

The pollen records of peat sediments from the southern bank of the Heilongjiang River in northernmost NE China show that the period 7800–7300 cal yr BP was the warmest and wettest stage of the Holocene. At that time, the study area developed *Betula* and *Larix*-dominated mixed coniferous and broadleaved forest. This indicates that increases in temperature and precipitation were conducive to the growth of broadleaved forests in the study area. At ~7300 cal yr BP and ~4500 cal yr BP, two significant cooling events resulted in a reduction in broadleaved forests and an expansion of herbs, with a vegetation succession into forest-steppe and then steppe-woodland. After a decrease in temperatures during ~2500–1500 cal yr BP, the vegetation type changed into meadow, accompanied by the development of “islands” of cold-wet tolerant coniferous forest. In the late Holocene, lower global temperatures and a weakening EASM led to decreases in evaporation and increases in effective humidity; the expansion of permafrost might have hindered the infiltration of precipitation and runoff, causing surface ponding and an expansion in marsh and meadow vegetation.

Conflict of Interests

The authors declare that there is no conflict of interests regarding the publication of this paper.

Acknowledgments

The authors sincerely thank the editor and other anonymous two reviewers for their thoughtful reviews and constructive suggestions, which helped to improve the paper. This research was supported by the CAS Strategic Priority Research Program (Grant no. XDA01020304), the National Basic Research Program of China (Grant no. 2015CB953803), and the National Natural Science Foundation of China (Grant no. 41372175). The authors thank Hanbin Liu and Qiang Gao for assistance with fieldwork.

References

- [1] Intergovernmental Panel on Climate Change (IPCC), *Climate Change 2013: The Physical Sciences Basis*, Cambridge University Press, New York, NY, USA, 2013.
- [2] M. E. Mann, Z. H. Zhang, M. K. Hughes et al., “Proxy-based reconstructions of hemispheric and global surface temperature variations over the past two millennia,” *Proceedings of the National Academy of Sciences of the United States of America*, vol. 105, no. 36, pp. 13252–13257, 2008.
- [3] Z. L. Ding, X.-N. Duan, Q.-S. Ge, and Z.-Q. Zhang, “On the major proposals for carbon emission reduction some related issues,” *Science in China Series D: Earth Sciences*, vol. 39, no. 12, pp. 1659–1671, 2009.
- [4] S. A. Marcott, J. D. Shakun, P. U. Clark, and A. C. Mix, “A reconstruction of regional and global temperature for the past 11,300 years,” *Science*, vol. 339, no. 6124, pp. 1198–1201, 2013.
- [5] Y.-J. Wang, H. Cheng, R. L. Edwards et al., “The holocene Asian monsoon: links to solar changes and North Atlantic climate,” *Science*, vol. 308, no. 5723, pp. 854–857, 2005.
- [6] Y. F. Shi, Z. C. Kong, S. M. Wang et al., “The climate variation and important events during Holocene Megathermal in China,” *Science in China Series B*, vol. 22, no. 12, pp. 1300–1308, 1992.
- [7] Y. L. Zhou, Y. G. Zu, D. Yu et al., *Geography of the Vegetation in Northeast China*, Science Press, Beijing, China, 1997.
- [8] X. C. Wu, H. Y. Liu, D. L. Guo, O. A. Anenkhonov, N. K. Badmaeva, and D. V. Sandanov, “Growth decline linked to warming-induced water limitation in Hemi-Boreal forests,” *PLoS ONE*, vol. 7, no. 8, Article ID e42619, 2012.
- [9] M. Lu, F. Zhang, and S.-Z. Feng, “Climate change and its impact on the agriculture of the Greater Khingan Range area in recent 30 years,” *Climate in Inner Mongolia*, no. 3, pp. 35–37, 2005.
- [10] G.-L. Tang and G.-Y. Ren, “Reanalysis of surface air temperature change of the last 100 years over China,” *Climatic and Environmental Research*, vol. 10, no. 4, pp. 791–798, 2005.
- [11] H.-J. Jin, S.-P. Yu, D.-X. Guo, L.-Z. Lu, and Y.-W. Li, “Degradation of permafrost in the Da and Xiao Hinggan Mountains, northeast China, and preliminary assessment of its trend,” *Journal of Glaciology and Geocryology*, vol. 28, no. 4, pp. 467–476, 2006.
- [12] J. Shi, G. Y. Wang, C.-Y. Du, and P. Wang, “Distribution and characteristic of permafrost of Heilongjiang Province,” *Heilongjiang Meteorology*, vol. 3, pp. 32–34, 2003.
- [13] M. Zhou, X.-X. Yu, L. Feng, L.-H. Wang, and P.-S. Na, “Effects of permafrost and wetland in forests in Great Xing’an Mountains on ecology and environment,” *Journal of Beijing Forestry University*, vol. 25, no. 6, pp. 91–93, 2003.
- [14] J. Tan and X.-H. Li, “The impact of the climate warming on degradation the Great Hinggan Mountains permafrost

- and northward movement of *Larix gmelinii*,” *Inner Mongolia Forestry Investigation and Design*, vol. 1, pp. 25–31, 1995.
- [15] Y.-Z. Zhao, Z.-L. Gao, M. Zhao, and L. Wang, “The influence of climate change on forest and wetland ecosystems at Mohe region,” *Science & Technology Information*, pp. 449–450, 2012.
- [16] S. Ju, X.-Z. Li, Y.-M. Hu et al., “Classification, species diversity, and species distribution gradient of permafrost wetland plant communities in Great Xing’an Mountains valleys of Northeast China,” *Chinese Journal of Applied Ecology*, vol. 20, no. 9, pp. 2049–2056, 2009.
- [17] G.-Y. Ren, “Changes in forest cover in China during the Holocene,” *Vegetation History and Archaeobotany*, vol. 16, no. 2-3, pp. 119–126, 2007.
- [18] G.-Y. Ren, “Wetness changes of the Holocene in northeast China,” *Geological Review*, vol. 45, no. 3, pp. 255–264, 1999.
- [19] C. Y. Gao, K. S. Bao, Q. X. Lin et al., “Characterizing trace and major elemental distribution in late Holocene in Sanjiang Plain, Northeast China: paleoenvironmental implications,” *Quaternary International*, vol. 349, pp. 376–383, 2014.
- [20] X.-Q. Li, H.-L. Zhao, M.-H. Yan, and S.-Z. Wang, “Fire variations relationship among fire and vegetation and climate during Holocene at Sanjiang Plain, Northeast China,” *Scientia Geographica Sinica*, vol. 25, no. 2, pp. 177–182, 2005.
- [21] S. Q. Zhang, W. Deng, M. H. Yan, X. Q. Li, and S. Z. Wang, “Pollen record and forming process of the peatland in late Holocene in the north bank of Xingkai Lake, China,” *Wetland Science*, vol. 2, no. 2, pp. 110–115, 2004.
- [22] D. K. Xu, H. Y. Lu, G. Q. Chu et al., “500-year climate cycles stacking of recent centennial warming documented in an East Asian pollen record,” *Scientific Reports*, vol. 4, article 3611, 2014.
- [23] J. Zhu, J. Mingram, and A. Brauer, “Early Holocene aeolian dust accumulation in northeast China recorded in varved sediments from Lake Sihailongwan,” *Quaternary International*, vol. 290–291, pp. 299–312, 2013.
- [24] C. H. Li, Y. H. Wu, and X. H. Hou, “Holocene vegetation and climate in Northeast China revealed from Jingbo Lake sediment,” *Quaternary International*, vol. 229, no. 1-2, pp. 67–73, 2011.
- [25] B. Hong, C. Q. Liu, Q. H. Lin et al., “Temperature evolution from the $\delta^{18}\text{O}$ record of Hani peat, Northeast China, in the last 14000 years,” *Science in China, Series D: Earth Sciences*, vol. 52, no. 7, pp. 952–964, 2009.
- [26] Y. T. Hong, B. Hong, Q. H. Lin et al., “Synchronous climate anomalies in the western North Pacific and North Atlantic regions during the last 14,000 years,” *Quaternary Science Reviews*, vol. 28, no. 9-10, pp. 840–849, 2009.
- [27] M. Stebich, J. Mingram, J. Han, and J. Liu, “Late Pleistocene spread of (cool-)temperate forests in Northeast China and climate changes synchronous with the North Atlantic region,” *Global and Planetary Change*, vol. 65, no. 1-2, pp. 56–70, 2009.
- [28] R.-L. Wen, J. L. Xiao, Z. G. Chang et al., “Holocene precipitation and temperature variations in the East Asian monsoonal margin from pollen data from Hulun Lake in northeastern Inner Mongolia, China,” *Boreas*, vol. 39, no. 2, pp. 262–272, 2010.
- [29] R.-L. Wen, J.-L. Xiao, Z.-G. Chang et al., “Holocene climate changes in the mid-high-latitude-monsoon margin reflected by the pollen record from Hulun Lake, northeastern Inner Mongolia,” *Quaternary Research*, vol. 73, no. 2, pp. 293–303, 2010.
- [30] J. L. Xiao, B. Si, D. Y. Zhai, S. Itoh, and Z. Lomtadidze, “Hydrology of Dali lake in central-eastern Inner Mongolia and Holocene East Asian monsoon variability,” *Journal of Paleolimnology*, vol. 40, no. 1, pp. 519–528, 2008.
- [31] J. Wu and Q. Liu, “Charcoal-recorded climate changes from Moon Lake in Late Glacial, Chinese,” *Earth Science—Journal of China University of Geosciences*, vol. 37, no. 5, pp. 947–954, 2012.
- [32] Q. Liu, Q. Li, L. Wang, and G. Q. Chu, “Stable carbon isotope record of bulk organic matter from a sediment core at Moon Lake in the middle part of the Daxing’an Mountain Range, northeast China during the last 21 ka,” *Quaternary Sciences*, vol. 30, no. 6, pp. 1069–1077, 2010.
- [33] Y. Li, X. Zhang, and G. Zhou, “Quantitative relationships between vegetation and several pollen taxa in surface soil from North China,” *Chinese Science Bulletin*, vol. 45, no. 16, pp. 1519–1523, 2000.
- [34] S. A. Hall, “Pollen analysis and paleoecology of alluvium,” *Quaternary Research*, vol. 31, no. 3, pp. 435–438, 1989.
- [35] C. B. Ramsey and S. Lee, “Recent and planned developments of the program OxCal,” *Radiocarbon*, vol. 55, no. 2-3, pp. 720–730, 2013.
- [36] Q. H. Xu, Y. C. Li, X. L. Yang, and Z. H. Zheng, “Quantitative relationship between pollen and vegetation in northern China,” *Science in China, Series D: Earth Sciences*, vol. 50, no. 4, pp. 582–599, 2007.
- [37] L. L. Wang, X. M. Shao, L. Huang, and E. Y. Liang, “Tree-ring characteristics of *Larix emelinii* and *Pinus sylvestris* var. mongolica and their response to climate in Mohe, China,” *Acta Phytocologica Sinica*, vol. 29, no. 3, pp. 380–385, 2005.
- [38] D. X. Guo, S. L. Wang, G. W. Lu, J. B. Dai, and E. Y. Li, “Division of permafrost regions in Daxiao Hinggan Ling northeast China,” *Journal of Glaciology and Geocryology*, vol. 3, no. 3, pp. 1–9, 1981.
- [39] H. L. Gui, X. H. Zhang, C. H. Wang, L. Huang, and G. S. Wu, “Mohe County climate change trend analysis during the last 50 years,” *Modernization Agriculture*, no. 6, pp. 24–26, 2009.
- [40] Editorial Committee of Vegetation Map of China. Chinese Academy of Sciences, *Vegetation Map of the People’s Republic of China (1:1000,000)*, Geological Publishing House, Beijing, China, 2007.
- [41] Y. Lan, *Chinese Historical Geography*, Higher Education Press, Beijing, China, 2002.
- [42] J. S. Feng, “The origin of the Oroqen nationality,” *Jilin Normal University Journal*, no. 2, pp. 77–85, 1979.
- [43] G. Y. Ren, “Decline of the mid-to late Holocene forests in China: climatic change or human impact?” *Journal of Quaternary Science*, vol. 15, no. 3, pp. 273–281, 2000.
- [44] S. G. Zhu, “Vegetation changes during the history in Northeast China,” *Journal of Chinese Historical Geography*, vol. 4, pp. 105–119, 1992.
- [45] X.-Q. Li and N.-Q. Du, “The acid-alkali-free analysis of Quaternary pollen,” *Acta Botanica Sinica*, vol. 41, no. 7, pp. 782–784, 1999.
- [46] K. Feagri and J. Iversen, *Textbook of Pollen Analysis*, Blackwell, Oxford, UK, 3rd edition, 1989.
- [47] G. Erdtman, “The acetolysis method. A revised description,” *Svensk Botanisk Tidskrift*, vol. 54, pp. 561–564, 1960.
- [48] R. M. Peck, “A comparison of four absolute pollen preparation techniques,” *New Phytologist*, vol. 73, no. 3, pp. 567–587, 1974.
- [49] B.-R. Chen, Y.-X. Zhu, H. B. Zhang, L. Zhou, and X. P. Xin, “Quantitative classification and ordination of eadow grassland vegetations in Hulunber,” *Journal of Wuhan Botanical Research*, vol. 26, no. 5, pp. 476–481, 2008.

- [50] X. C. Wang, "A pollen profile from the permafrost region in southwest Yukon territory and its paleoenvironmental significance," *Journal of Glaciology and Geocryology*, vol. 11, no. 2, pp. 99–112, 1989.
- [51] M. O. Hill and H. G. Gauch Jr., "Detrended correspondence analysis: an improved ordination technique," *Vegetatio*, vol. 42, no. 1–3, pp. 47–58, 1980.
- [52] P. J. Reimer, E. Bard, A. Bayliss et al., "IntCal13 and Marine13 radiocarbon age calibration curves 0–50,000 years cal BP," *Radiocarbon*, vol. 55, no. 4, pp. 1869–1887, 2013.
- [53] Intergovernmental Panel on Climate Change (IPCC), *Climate Change 2007: The Physical Sciences Basis*, Cambridge University Press, New York, NY, USA, 2007.
- [54] M. Tan, A. Baker, D. Genty, C. Smith, J. Esper, and B. Cai, "Applications of stalagmite laminae to paleoclimate reconstructions: comparison with dendrochronology/climatology," *Quaternary Science Reviews*, vol. 25, no. 17–18, pp. 2103–2117, 2006.
- [55] D. X. Yuan, H. Cheng, R. L. Edwards et al., "Timing, duration, and transitions of the last interglacial Asian monsoon," *Science*, vol. 304, no. 5670, pp. 575–578, 2004.
- [56] Z. Zheng, K. Y. Huang, Q. H. Xu et al., "Comparison of climatic threshold of geographical distribution between dominant plants and surface pollen in China," *Science in China, Series D: Earth Sciences*, vol. 51, no. 8, pp. 1107–1120, 2008.
- [57] Y. Zhao and U. Herzschuh, "Modern pollen representation of source vegetation in the Qaidam Basin and surrounding mountains, north-eastern Tibetan Plateau," *Vegetation History and Archaeobotany*, vol. 18, no. 3, pp. 245–260, 2009.
- [58] Q. Xu, F. Tian, M. J. Bunting et al., "Pollen source areas of lakes with inflowing rivers: modern pollen influx data from Lake Baiyangdian, China," *Quaternary Science Reviews*, vol. 37, pp. 81–91, 2012.
- [59] D. S. Sea and C. Whitlock, "Postglacial vegetation and climate of the Cascade Range, central Oregon," *Quaternary Research*, vol. 43, no. 3, pp. 370–381, 1995.
- [60] I. C. Prentice, "Pollen representation, source area, and basin size: toward a unified theory of pollen analysis," *Quaternary Research*, vol. 23, no. 1, pp. 76–86, 1985.
- [61] S. Sugita, "A model of pollen source area for an entire lake surface," *Quaternary Research*, vol. 39, no. 2, pp. 239–244, 1993.
- [62] M. J. Bunting, M.-J. Gaillard, S. Sugita, R. Middleton, and A. Broström, "Vegetation structure and pollen source area," *The Holocene*, vol. 14, no. 5, pp. 651–660, 2004.
- [63] C. Prentice, "Records of vegetation in time and space: the principles of pollen analysis," in *Vegetation History*, vol. 7 of *Handbook of Vegetation Science*, pp. 17–42, Springer, Dordrecht, The Netherlands, 1988.
- [64] B. V. Odgaard, "Fossil pollen as a record of past biodiversity," *Journal of Biogeography*, vol. 26, no. 1, pp. 7–17, 1999.
- [65] S. H. Yu, Z. Zheng, K. Y. Huang, and M. I. Skrypnikova, "Modern pollen distribution in the Heilongjiang-Amur cold-temperate regions of China and Russia," *Acta Palaeontologica Sinica*, vol. 51, no. 3, pp. 370–384, 2012.
- [66] X. J. Sun, F. Y. Wang, and C. Q. Song, "Pollen-climate response surfaces of selected taxa from Northern China," *Science in China, Series D: Earth Sciences*, vol. 39, no. 5, pp. 486–493, 1996.
- [67] H. Y. Liu and Y. Y. Li, "Pollen indicators of climate change and human activities in the semi-arid region," *Acta Palaeontologica Sinica*, vol. 48, no. 2, pp. 211–221, 2009.
- [68] X. H. Wu, "A study of palaeotemperatures recorded by the Pleistocene *Picea-Abies* floras in east and southwest China," *Bulletin of the Institute of Geomechanics CAGS*, vol. 6, pp. 155–166, 1985.
- [69] M. B. Bush, "On the interpretation of fossil Poaceae pollen in the lowland humid neotropics," *Palaeogeography, Palaeoclimatology, Palaeoecology*, vol. 177, no. 1–2, pp. 5–17, 2002.
- [70] J. Y. Fang, Y. H. Tang, J. D. Lin, and G. M. Jiang, *Global Ecology: Climate Change and Ecological Responses*, Higher Education Press, Beijing, China, 2000.
- [71] P. J. Bartlein, I. C. Prentice, and T. Webb III, "Climatic response surfaces from pollen data for some eastern North American taxa," *Journal of Biogeography*, vol. 13, no. 1, pp. 35–57, 1986.
- [72] B. Huntley and H. J. B. Birks, *An Atlas of Past and Present Pollen Maps for Europe: 0–13000 B.P.*, Cambridge University Press, Cambridge, UK, 1983.
- [73] A. Miola, A. Bondesan, L. Corain et al., "Wetlands in the Venetian Po Plain (northeastern Italy) during the Last Glacial Maximum: interplay between vegetation, hydrology and sedimentary environment," *Review of Palaeobotany and Palynology*, vol. 141, no. 1–2, pp. 53–81, 2006.
- [74] R. G. Baker, "Holocene vegetational history of the western United States," in *Late-Quaternary Environments of the United States: The Late Pleistocene*, vol. 1, p. 109, University of Minnesota Press, 1983.
- [75] J. T. Andrews, W. N. Mode, and P. T. Davis, "Holocene climate based on pollen transfer functions, eastern Canadian Arctic," *Arctic and Alpine Research*, vol. 12, no. 1, pp. 41–64, 1980.
- [76] Z. Yang-Jian, D. Li-Min, and P. Jie, "The trend of tree line on the northern slope of Changbai Mountain," *Journal of Forestry Research*, vol. 12, no. 2, pp. 97–100, 2001.
- [77] A. Berger and M. F. Loutre, "Insolation values for the climate of the last 10 million years," *Quaternary Science Reviews*, vol. 10, no. 4, pp. 297–317, 1991.
- [78] P. J. Reimer, M. G. L. Baillie, E. Bard et al., "Residual delta ^{14}C around 2000 year moving average of IntCal04," *Radiocarbon*, vol. 46, no. 3, pp. 1029–1058, 2000.
- [79] Y. Igarashi and A. E. Zharov, "Climate and vegetation change during the late Pleistocene and early Holocene in Sakhalin and Hokkaido, northeast Asia," *Quaternary International*, vol. 237, no. 1–2, pp. 24–31, 2011.
- [80] N. G. Razjigaeva, L. A. Ganzey, T. A. Grebennikova et al., "Holocene climatic changes and vegetation development in the Kuril Islands," *Quaternary International*, vol. 290–291, pp. 126–138, 2013.
- [81] G. Bond, W. Showers, M. Cheseby et al., "A pervasive millennial-scale cycle in North Atlantic holocene and glacial climates," *Science*, vol. 278, no. 5341, pp. 1257–1266, 1997.
- [82] C. A. Dykoski, R. L. Edwards, H. Cheng et al., "A high-resolution, absolute-dated Holocene and deglacial Asian monsoon record from Dongge Cave, China," *Earth and Planetary Science Letters*, vol. 233, no. 1–2, pp. 71–86, 2005.
- [83] P. Tarasov, E. Bezrukova, E. Karabanov et al., "Vegetation and climate dynamics during the Holocene and Eemian interglacials derived from Lake Baikal pollen records," *Palaeogeography, Palaeoclimatology, Palaeoecology*, vol. 252, no. 3–4, pp. 440–457, 2007.
- [84] Y. Y. Liu, S. Q. Zhang, J. Q. Liu, H. T. You, and J. T. Han, "Vegetation and environment history of Erlongwan Maar Lake during the late Pleistocene on pollen record," *Acta Micropalaeontologica Sinica*, vol. 25, no. 3, pp. 274–280, 2008.
- [85] J. L. Liu, "Vegetational and climatic changes at Gushantun bog in Jilin, NE China since 13,000 yr BP," *Acta Palaeontologica Sinica*, vol. 28, no. 4, pp. 495–511, 1989.

- [86] Y. Igarashi, "Holocene vegetation and climate on Hokkaido Island, northern Japan," *Quaternary International*, vol. 290-291, pp. 139-150, 2013.
- [87] Y. L. Shur and M. T. Jorgenson, "Patterns of permafrost formation and degradation in relation to climate and ecosystems," *Permafrost and Periglacial Processes*, vol. 18, no. 1, pp. 7-19, 2007.
- [88] P. Camill and J. S. Clark, "Long-term perspectives on lagged ecosystem responses to climate change: permafrost in boreal peatlands and the grassland/woodland boundary," *Ecosystems*, vol. 3, no. 6, pp. 534-544, 2000.
- [89] A. J. Soja, N. M. Tchepakova, N. H. F. French et al., "Climate-induced boreal forest change: predictions versus current observations," *Global and Planetary Change*, vol. 56, no. 3-4, pp. 274-296, 2007.
- [90] N. M. Tchepakova, E. Parfenova, and A. J. Soja, "The effects of climate, permafrost and fire on vegetation change in Siberia in a changing climate," *Environmental Research Letters*, vol. 4, no. 4, Article ID 045013, 2009.
- [91] C. C. Mou, "Succession of *Larix olgensis* and *Betula platyphylla*-marsh ecotone communities in Changbai Mountain," *Chinese Journal of Applied Ecology*, vol. 14, no. 11, pp. 1813-1819, 2003.

Research Article

Determination of the Effect of Water Depth and Flow Velocity on the Quality of an In-Stream Habitat in Terms of Climate Change

V. Macura,¹ Z. Štefunková,² and A. Škrinár¹

¹*Department of Land and Water Resources Management, Faculty of Civil Engineering, Slovak University of Technology in Bratislava, Radlinského 11, 813 68 Bratislava, Slovakia*

²*Department of Hydraulic Engineering, Faculty of Civil Engineering, Slovak University of Technology in Bratislava, Radlinského 11, 813 68 Bratislava, Slovakia*

Correspondence should be addressed to A. Škrinár; andrej.skrinar@stuba.sk

Received 2 February 2015; Revised 4 June 2015; Accepted 14 June 2015

Academic Editor: Zhongping Lai

Copyright © 2016 V. Macura et al. This is an open access article distributed under the Creative Commons Attribution License, which permits unrestricted use, distribution, and reproduction in any medium, provided the original work is properly cited.

The study is focused on the objectification of an assessment of the quality of an in-stream habitat in mountain and piedmont streams by the decision-making Instream Flow Incremental Methodology (IFIM) due to climate change. The quality of the habitat was assessed on the basis of a bioindication, represented by ichthyofauna. Sixty-four reaches of 47 watercourses in five river basins in Slovakia, in which ichthyologic, topographic, and hydraulic measurements were performed, were evaluated. The effect of the physical characteristics of the stream channel on the quality of the in-stream habitat has been verified on a number of reference reaches in which the measurements were performed at different water levels. From the set of the data measured, an analysis aimed at determining the impact of individual characteristics on the quality of an in-stream habitat has been carried out. The results show the optimum ratio of the weights of the flow velocity and water depth for an assessment of the quality of an in-stream habitat due to climate change.

1. Introduction

Water management planning and decision-making should be based on the forecasting or modeling of the quality of an aquatic habitat, for example, the impact of water take-offs, river training, river restoration, or the effects of climate change. Based on the modeling of trends in the habitat quality, data can be obtained which should characterize the impact of these changes on the aquatic ecosystem. The results of the modeling are important in the decision-making process of water management solutions. The models are mainly based on hydrological, morphological, and hydraulic parameters affecting the distribution and abundance of organisms in the stream, or in other words, the bioindication, for example, comprehensive monitoring of the aquatic environment using bioindication by macrophytes, macroinvertebrates, and fish by Friberg et al. [1]. In the last 40 years considerable efforts have been spent to develop supporting mechanisms used

in determining the flow regimes necessary for protecting and improving water resources as described by Jowett [2], Hardy [3], or Tharme [4]. The results show that of all the aquatic organisms, fish react most sensitively to morphological changes.

At the beginning of our research the macrozoobenthos was studied along with the ichthyofauna. The invertebrates responded to changes in flow and hydraulic changes as discussed by Mérigoux et al. [5] or Hodkinson and Jackson [6] but were less sensitive to morphological changes in regulated mountain streams. Fish were sensitive to these changes as shown by Slavík et al. [7], and they also sensitively responded to changes in water temperature and discharges as discussed by Lamouroux et al. [8]. The sensitivity of fish caused by river regulation was also confirmed in a study of Macura et al. [9].

Different species prefer different habitats, while the age of a fish has a significant impact on its habitat preferences.

Particular species and age groups prefer various flow velocities, depths, and types of substrate [10]. Therefore, the spatial distribution of combinations of hydraulic parameters plays an important role in the availability of a suitable in-stream habitat. Among the wide range of various models intended for the modeling of a habitat quality IFIM is the most widely used in the United States and one of the most popular models in the world [4]. A very good overview of the overall philosophy, history, and development of IFIM is given in [11]. The IFIM methodology has been gradually evolving into a tool intended for planning water management strategies. For example, variations in the individual components of an ecosystem due to climate change count among the most recent topics. A number of studies have been developed on the impact of climate change on periods of drought and minimum flows, which are essential for an aquatic habitat, such as scientific articles [12–14]. The quantification of these changes on the level of their effect on different types of bioindicators requires a detailed characterization of a whole set of factors, which is a difficult task. Such results may be very important strategically, as they allow for proposing concrete restoration measures to mitigate the effects of climate change. The study gives a particular example of modeling the quality of an in-stream habitat as a result of climate change.

2. Materials and Methods

2.1. Characteristics of Modeling the Quality of an Aquatic Habitat. The ecological status of a stream is influenced by many factors; the most important one is the biotope of the fauna and flora of the aquatic area. The in-stream habitat structure has a substantial impact on the organization and structure of biological communities as discussed by Maddock [15]. The aim of modeling the quality of a habitat is mainly to provide a basis for the evaluation or forecasting of biological changes, which should constitute a potential impact on the ecology that is important in the decision-making process of the management of the in-stream quality. In this study the Riverine HABitat SIMulation model (RHABSIM) [16–18], which is based on the IFIM methodology, was used for modeling the habitat quality. The model was developed in order to improve the possibility of determining the rate of the influence of different ways of water use on a stream channel. It is an integrated set of one-dimensional hydraulic models and microhabitat simulation models intended for determining the quality of an aquatic habitat based on the preferences of fish for a wider range of discharges. The basic biotic characteristics are the habitat suitability curves of particular fish species.

2.2. Habitat Suitability Curves (HSCs). Habitat suitability curves (HSCs) express the preferences of different types of habitat by particular fish species. They are based on the assumption that each fish species (or other bioindicators) prefers a particular combination of abiotic environmental parameters such as flow velocity and water depth, cover places, type of bottom substrate, water temperature or quality, and the like.

The curves for flow velocity and water depth are the most widely used expressions of habitat preferences in the RHABSIM model. These curves are continuous, because the velocities and depths between all the nodes may be interpolated. Suitability curves, along with the hydraulic and topographic characteristics, allow for quantifying the quality of an aquatic habitat in the form of area weighted suitability.

2.3. Area Weighted Suitability (AWS). Area weighted suitability (AWS) is defined as the total area of the water level, which is adjusted by the suitability ratio of the individual parameters (flow velocity, water depth, cover places, etc.). This procedure is implemented by individual cells that represent microhabitats with the same characteristics. AWS shows the changes in a habitat quality with respect to the variable parameters, which are typically the discharges or changes in the morphology of the river bed. The representation of AWS by the stream length mostly has the shape of a mosaic setup of cells (Figures 6–10).

The importance of AWS has been discussed for many years. Many scientists have evaluated the correlation between AWS and a fish population or biomass, particularly in relation to the discharges, for example, Bovee [19], Conder and Annear [20], Jowett [21], Nehring and Anderson [22], and Gallagher and Gard [23], although this interpretation of a habitat quality has certain imperfections which have been highlighted by others [24–28].

When considering the representativeness of the ichthyofauna as a bioindicator, it should be noted that the term “fish” does not include only one species but is a large, morphologically, physiologically, and ecologically variable group of aquatic vertebrates living in various habitats. Ultimately, fish are the best bioindicators of morphological changes in a stream channel.

2.4. Methods. To determine the influence of various parameters on the quality of an in-stream aquatic area, the following procedure was chosen:

- (i) Selection of reference reaches for a generalization of biotic characteristics.
- (ii) Ichthyological sampling and a hydraulic survey aimed at a determination of the HSCs of individual fish species.
- (iii) Assessment of the hydraulic characteristics of the reference reaches.
- (iv) Verification of the HSCs.
- (v) Determination of the AWS.
- (vi) Examination of the influence of abiotic parameters on the HSCs.
- (vii) Determination of the weights of the basic abiotic habitat characteristics based on the data measured.

2.5. Selection of the Reference Stream Reaches. Selection was mainly focused on smaller mountain and piedmont brooks. The reaches were selected on the basis of the structure and abundance of the ichthyofauna. The selected watercourses

TABLE 1: Characteristics of the reference reaches in the Váh River basin.

Watercourse	Channel character	Rkm	Q [m ³ ·s ⁻¹]	Drainage area [km ²]	Reach length [m]	B _p [m]	h _{max} [m]	h _p [m]	h _p ^{max} [m]	v _{max} [m·s ⁻¹]	v _p [m·s ⁻¹]	v _p ^{max} [m·s ⁻¹]	i _p
Drietomica	Regulated	3.1	0.38	90.3	100	4.2	0.61	0.43	0.52	0.536	0.378	0.482	0.007
Drietomica	Natural	5.2	0.38	82.495	241	4.8	0.68	0.46	0.56	0.724	0.329	0.463	0.006
Hradnianska	Natural	5.7	0.142	32.143	124.8	3.4	0.3	0.11	0.19	0.764	0.388	0.547	0.008
Hybica 1	Natural	0.8	0.429	44.784	111.4	6.13	0.78	0.26	0.48	0.772	0.281	0.415	0.007
Hybica 2	Regulated	3.75	0.324	35.284	74.8	4.25	0.34	0.16	0.24	0.675	0.391	0.527	0.006
Kamečnica	Natural	10.6	0.112	12.772	94.2	2	0.21	0.12	0.18	0.756	0.402	0.482	0.031
Klačianska	Natural	0.18	0.346	27.17	96.3	4.19	0.36	0.15	0.22	0.912	0.51	0.706	0.007
Lesnianska 1	Regulated	0.8	0.167	25.26	50.2	4.23	0.33	0.13	0.23	0.765	0.284	0.329	0.021
Lesnianska 2	Natural	3.4	0.135	20.887	117.6	5.3	0.41	0.09	0.16	1.044	0.377	0.634	0.016
Manínsky potok	Natural	3.7	0.245	9.588	95.2	3.97	0.47	0.15	0.26	0.791	0.37	0.552	0.02
Petrovička 1	Natural	3.05	0.08	64.175	86.2	5.31	0.11	0.04	0.08	0.651	0.312	0.464	0.022
Petrovička 2	Regulated	5.55	0.029	33.465	63.4	2.03	0.12	0.06	0.11	0.645	0.201	0.316	0.01
Teplička 1	Regulated	7.4	0.29	55.406	60	5.56	0.39	0.19	0.36	0.357	0.196	0.325	0.006
Teplička 2	Natural	10.2	0.283	51.081	69.4	5.14	0.8	0.2	0.34	0.926	0.31	0.441	0.022
Veselianska 1	Natural	3.76	1.225	85.869	143.1	11.36	0.62	0.27	0.45	0.898	0.384	0.566	0.01
Veselianska 2	Natural	7.6	0.905	69.116	98.6	12.93	0.68	0.24	0.45	0.481	0.247	0.379	0.011
Vrzavka	Natural	4.8	0.09	10	78.8	3.36	0.14	0.06	0.11	0.844	0.363	0.553	0.015
Vôdky	Natural	2.1	0.221	15.792	167	3.02	0.22	0.13	0.2	0.736	0.47	0.649	0.018
Zázrivka 1	Natural	7.9	1.025	76.473	100.7	13.57	0.61	0.2	0.39	0.994	0.353	0.545	0.014
Zázrivka 2	Natural	0.3	1.441	96.094	98.6	13.21	0.48	0.22	0.37	0.764	0.416	0.607	0.012
Vadičovský potok	Natural	1.1	0.223	39.39	103.5	4.32	0.25	0.1	0.17	0.821	0.458	0.675	0.017

of all the river basins are shown in Figure 1 with the main characteristics of the reference reaches in the Váh River basin given in Table 1. Besides Váh, watercourses belonging to four other river basins were evaluated: Dunajec and Poprad basin, Nitra basin, Bodrog basin, and Hron basin. These are not listed in detail.

2.6. Ichthyological Sampling and Hydraulic Survey. The ichthyologic measurements were aimed at determining the HSCs of the individual fish species. The ichthyological sampling as well as the topographic measurements was carried out during the summer months due to the need to monitor the conditions of the in-stream habitats during minimum flows. The ichthyological data were collected by the Hans-Grassl ELT62II-HI electrofishing device. The flow velocities, water depths, and character of the microhabitat (type of cover and bottom substrate) were recorded at all the points of the fish capture. The flow velocities were measured by hydrometric propellers, and the topography of the riverbed was measured by the Leica Flexline TS02 total station with an angle accuracy of 3".

2.7. Hydraulic Characteristics of the Selected Stream Reaches. The hydraulics of a river channel determine the quality of a habitat suitable for ichthyofauna. Habitat suitability curves for the flow velocity and water depths represent a biotic component of the method. The peaks of the curves were

compared, that is, spots with the highest occurrence of the species in particular depths at certain velocities, which are referred to as the velocity parameter (P_v) and the depth parameter (P_d).

The Pearson product-moment correlation coefficient (r) was used for the measurement of the correlation relationship between the parameters mentioned. Cohen [29] states out the evaluation of Pearson's r as follows: no correlation: 0.0 to 0.09 (−0.09 to 0.0), small degree of correlation: 0.1 to 0.3 (−0.3 to −0.1), medium degree of correlation: 0.3 to 0.5 (−0.5 to −0.3), and large degree of correlation: 0.5 to 1.0 (−1.0 to −0.5). The regulated and natural reaches of the streams were distinguished for the purposes of the statistical analysis. The database was divided into three files: a file of regulated reaches, a file of natural streams, and a file of all the reaches created by the union of natural and regulated stream reaches.

Correlation relationships were determined between the parameters of P_v and P_d with the slope of the energy line (i) and the M -constant (M), which is equivalent to the Chézy coefficient (C). The M -constant depends on the discharges and heights of the water levels, similar to the Chézy coefficient. A more detailed description of the M -constant is given in the literature [30].

The M -constant was calculated from K. V. Grišani's equation:

$$M = \frac{R(g \cdot B)^{1/4}}{Q^{1/2}}, \quad (1)$$

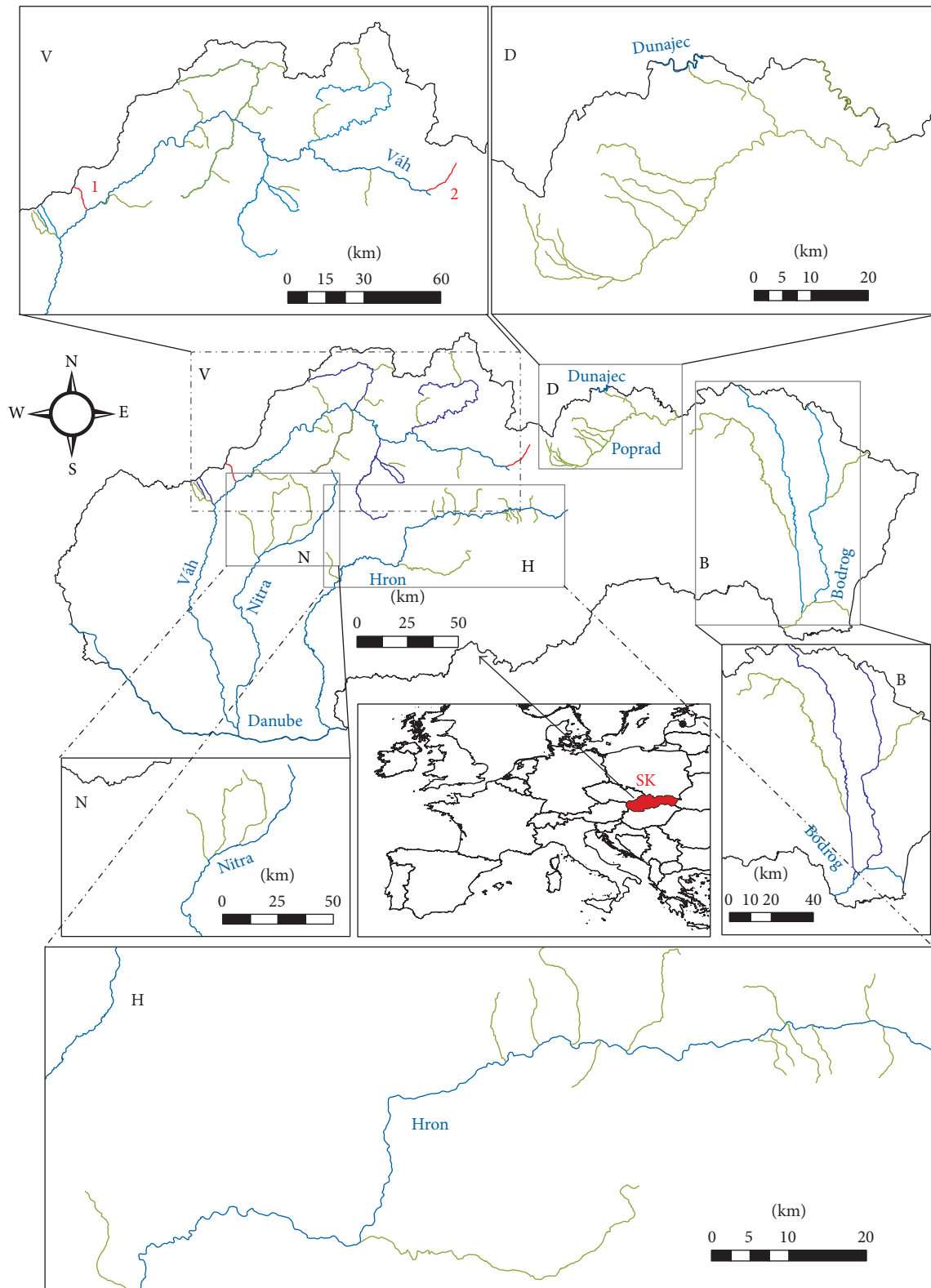


FIGURE 1: Map of the selected watercourses (SK: Slovak Republic, V: Váh basin, D: Dunajec and Poprad basin, N: Nitra basin, B: Bodrog basin, H: Hron basin, 1: Drietomica, and 2: Hybica; the blue lines indicate rivers; the green lines indicate the selected watercourses).

TABLE 2: Comparison of the Pearson correlation coefficient (r) for the brown trout between the following variables: velocity parameter (P_v), depth parameter (P_d), the M -factor (M), and hydraulic slope of the energy line (i).

Set of watercourses	P_v - M	P_d - M	P_v - i	P_d - i
(1) All the watercourses	0.06	0.14	-0.24	-0.14
(2) Regulated channels	0.64	-0.28	-0.33	0.15
(3) Natural channels	0.13	0.52	-0.17	-0.30

where g is the acceleration of gravity [$\text{m}\cdot\text{s}^{-2}$], B is the channel width at the water level [m], R is the hydraulic radius [m], and Q is the discharge [$\text{m}^3\cdot\text{s}^{-1}$].

From the statistical assessment (Table 2), it follows that

- (i) a strong correlation in the relationship of P_v - M ($r = 0.64$) was shown in the regulated streams. On the contrary, the correlation relationship of P_d - M was small ($r = -0.28$). The reason for this result is that the regulated streams have prismatic channels with a small range of water depths. Therefore, the fish, especially brown trout (*Salmo trutta m. fario*), prefer biotopes based on flow velocity,
- (ii) the opposite effect occurred in natural channels, since there was a degree of correlation demonstrated in the relationship of P_d - M as large ($r = 0.52$) and the correlation in the relationship of P_v - M as small (0.13). This result is directly related to the morphological characteristics of a natural stream channel. Trout prefer cover places with sufficient depths. Flow velocity is not crucial in reaches with larger depths, because there are generally low velocities in these spots (cover places).
- (iii) In the set of all the watercourses (regulated and natural) no correlation has been proved.

The results shown in Table 2 directly confirmed the sensitivity of the trout as a bioindicator for habitat parameters that are dominant at characteristic reaches. An important fact is that there was a relationship between the morphological parameters of the channel and the microhabitat preference by brown trout as a bioindicator of environmental quality.

2.8. Influence of Abiotic Parameters on the HSCs. The aim of our further research was to determine whether there is a correlation between the shape of the HSCs and the abiotic parameters of in-stream habitats. Data from the database of the field measurements at the watercourses listed in Table 1 were used for the analysis. Only those streams where brown trout occurred in such numbers that it was possible to reliably determine the suitability curves for the depths were evaluated. The results were verified using the data of the Drietomica brook. Comprehensive field measurements were carried out for three different water levels.

The depth parameters (dependent variable) were correlated with the average maximum depths (independent variable). The average maximum depths were determined by averaging the maximum depth at each cross section of the

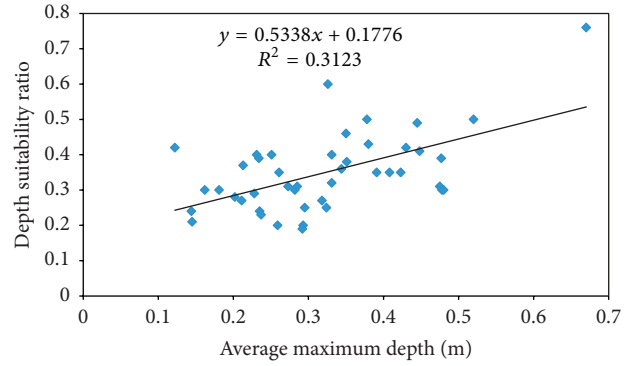


FIGURE 2: Correlation between the mean maximum depths and depth parameters for the brown trout.

selected reach. Graph of the correlation between the mean maximum depths and the depth parameters for the brown trout is shown in Figure 2.

The correlation coefficient evaluated from all the watercourses has a value of 0.55, which indicates a large degree of dependence. Since there are also regulated reaches in the database, the correlation coefficient was evaluated separately for the reaches with a natural character. In this case, r took the value of 0.67, which was close to a very high degree of dependence. From the results it can be concluded that the shape of the HSCs is greatly influenced by the average maximum depths of a channel.

2.9. Verification of the HSCs Using the Example of the Drietomica Brook. The Drietomica brook was selected to be the verification reach since it is a mountain stream with a variable morphology and has a minimum impact from human activities. In the years 2004–2013, a detailed field survey was carried out, which focused on a comprehensive evaluation of the quality of the aquatic habitat by the RHABSIM model. A set of topographical, hydrometrical, and ichthyological measurements aimed at evaluating the quality of the in-stream habitat of various types of fish covers was realized. These data formed the basis of a detailed analysis of the reference reach at the Drietomica brook with the aim of optimizing the ratio of $W_V : W_D$. Three various discharges along with the water-level regimes were measured: $Q_1 = 0.55 \text{ m}^3\cdot\text{s}^{-1}$, corresponding to the discharge of Q_{180d} , $Q_2 = 1.48 \text{ m}^3\cdot\text{s}^{-1}$, corresponding to the discharge of Q_{60d} , and $Q_3 = 0.08 \text{ m}^3\cdot\text{s}^{-1}$, representing the discharge of Q_{365d} . For each discharge ichthyological sampling was performed that focused on the habitat preferences by the ichthyofauna to derive the HSCs. From the measurements for the three various water levels, the HSCs for the brown trout (Figures 3 and 4) were determined.

The HSCs for the water depths in Figure 3 and the flow velocities in Figure 4 show that the changes in habitat preferences indicated the same trends as the changes in the water level. Specifically, during a discharge of $Q = 0.085 \text{ m}^3\cdot\text{s}^{-1}$, the water depths in cover places varied from 0.15 m to 0.60 m, while during the highest measured discharge of $Q =$

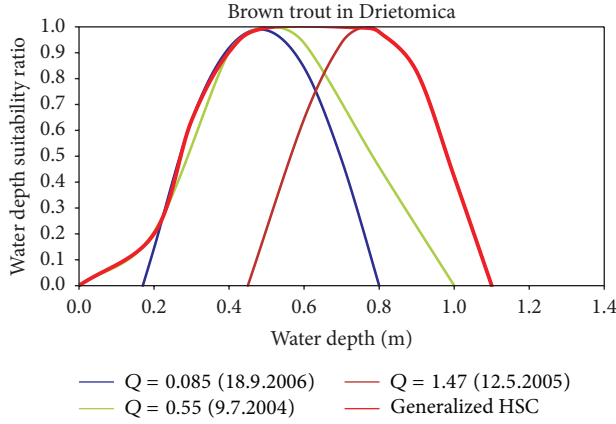


FIGURE 3: Suitability curves of the brown trout for the water depths during three various discharges and the resulting generalized suitability curve.

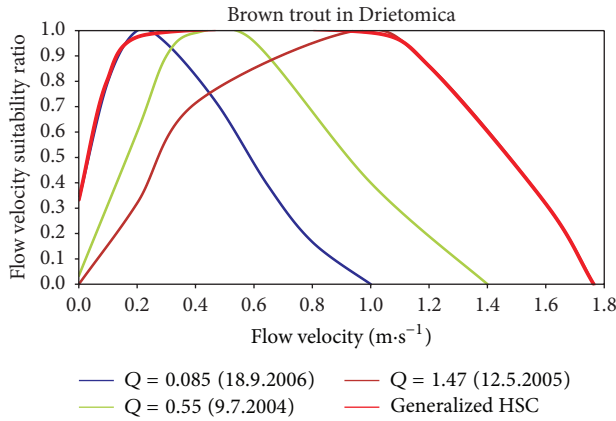


FIGURE 4: Suitability curves of the brown trout for the flow velocities during three various discharges and the resulting generalized suitability curve.

$1.47 \text{ m}^3 \cdot \text{s}^{-1}$ they varied from 0.45 m to 0.85 m. Thus, the difference in the P_D was 25 cm. Changes in the water levels during the above discharges varied from 0.2 to 0.3 m in particular cross sections. Hence, the changes in the water levels were similar to the changes in the P_D . We obtained similar results by comparing the changes in the P_V and the maximum flow velocities. The above analysis leads us to a conclusion that in habitats with acceptable velocities: fish do not change their cover places (an acceptable flow velocity is one that does not prevent the fish specimen from the long-term use of a microhabitat). In other words, with an increasing discharge a certain fish specimen prefers the same microhabitat until it is forced to switch to another cover (current shadow) by high velocities.

2.10. Evaluation of the AWS. The AWS is the result of a simulation process in the RHABSIM model. Based on the hydraulic parameters, an index from the HSCs of individual species (separately for the flow velocities and water depths, or other factors) is assigned to each individual microhabitat

cell at the reference reach. The so-called combined suitability factor (CSF) is calculated by multiplying the flow velocity and water depth suitability values:

$$\text{CSF} = V \cdot D \cdot A, \quad (2)$$

where V is the velocity suitability value, D is the depth suitability value, and A is the suitability value for additional habitat attributes (cover, bottom substrate, etc.).

This method considers each variable to have the same weight. From the preceding text it follows that the water depth affects the quality of the habitat more significantly than the flow velocity and that it is similar with different types of fish covers. It is necessary to consider the different weights for each parameter. Therefore, we recommend the CSF to be evaluated according to

$$\text{CSF} = \frac{(V \cdot W_V) + (D \cdot W_D) + (A \cdot W_A)}{(W_V + W_D + W_A)}, \quad (3)$$

where W_V is the weighting factor for flow velocity, W_D is the weighting factor for water depth, and W_A is the weighting factor for additional attribute (any weight from 0.1 to 1.0 can be assigned to each factor). The AWS is then determined by multiplying the water surface of the particular cells and their CSF:

$$\text{AWS} = S_b \cdot \text{CSF}, \quad (4)$$

where S_b is the area of the water surface of the cells [m^2] and CSF is the combined suitability factor.

The total of the area weighted suitability is determined by the sum of the partial AWSs. RHABSIM allows for a representation of habitat suitability for individual cross sections for each water level and fish species, as well as a situational projection of the suitability ratio in the context of the surface area in the individual cells.

The AWS was investigated by changing the weights of the flow velocity and water depth suitability values. The effect of this balance was analyzed according to (3) and its modification having the form

$$\text{CSF} = (V^{W_V} \cdot D^{W_D} \cdot A^{W_A}). \quad (5)$$

Provided that all of the weights are nonnegative, the following may be stated:

$$W_V + W_D + W_A = 1. \quad (6)$$

The third additional attribute (A) and its weight (W_A) may represent a type of cover or substrate. The velocity fields at the selected reaches were verified at the water levels, which were measured during the ichthyological survey. The biotic area was represented by normalized HSCs.

Comparison of the results evaluated in accordance with (3) and (5) showed minimum differences. We used the CSF evaluation by (3). In the text below the calculation of the AWS according to (2) is referred to as Method 1, and the calculation of the AWS according to (3) is referred to as Method 2.

From the AWS values modeled by Method 1, it follows that the results do not match the actual status of the habitat.

When combining a suitable parameter (water depth) and a less suitable parameter (flow velocity), the total AWS of this method is unsuitable, or the suitability is low. It is necessary to recall that the RHABSIM model does not provide other options. Therefore, we have created our own AWS assessment procedure for the application of Method 2.

As mentioned above, the water depth has a significantly greater effect on the quality of the habitat than it does on velocity. Correct determination of the weights of these parameters is an essential step towards the objectification of the AWS according to Method 2.

Optimum ratio of $W_D : W_V$ was derived from the five reference reaches in three streams (Slatina, Drietomica, and Udava). The reference reaches were subdivided into particular microhabitats that have been identified and marked in the field. During the ichthyologic survey the water depths and flow velocities were measured at the sites of the catch of each fish and have been associated with a specific microhabitat. These data were compared to the results from the RHABSIM model at different ratios of weights. A comparison of the suitability values and number of fish caught showed the best match at a ratio of $W_D : W_V = 8 : 2$.

The AWS was evaluated by the two methods mentioned above: Method 1 according to (2) and Method 2 according to (3) (ratio $W_D : W_V = 8 : 2$). The HSCs for the entire range of discharges for depth and velocity shown in Figures 3 and 4 by the red line were used for the evaluation of the habitat quality. Typical riffle and pool habitats were selected to determine the AWS. Table 3 indicates the percentage differences of the AWS evaluated by Methods 1 and 2 with the ratio of the weights $W_D : W_V = 8 : 2$. For the calculation of the difference, the following relationship was used:

$$\Delta = \frac{AWS_{met.2} - AWS_{met.1}}{AWS_{met.2}} \cdot 100, \quad (7)$$

where Δ is the percentage difference of the AWS by Methods 1 and 2 [%], $AWS_{met.1}$ is the area weighted suitability as determined by Method 1 [m^2/m], and $AWS_{met.2}$ is the area weighted suitability as determined by Method 2 [m^2/m].

Differences in the resulting AWSs are given in Table 3, wherein the average difference was 31.6% in the riffle habitats. Reaches with pool habitats were evaluated by the same method with differences of 12.9%. The results have indicated that there is a significant difference between the methods used. Comparison of the AWS by Methods 1 and 2 for all the cross sections of the Drietomica brook is shown in Figure 5.

3. Discussion

Despite the uncertainty in future trends of climate and land use change and in species responses to these interacting drivers, it is important to attempt to understand these effects; otherwise current conservation practice may become ineffective. Inappropriate habitat management could exacerbate biodiversity declines [31]. Petts [32] notes that the expert judgment is always important regardless of the tool and the method used for determining the minimum flow. From a water management point of view, it is important to

characterize the shape of the HSCs in the range of minimum flows. The effect of the discharge and the shape of the HSCs on the habitat quality were analyzed at the reference reach of the Drietomica brook. The first stage was to evaluate the quality of the habitat for the discharge of $Q = 0.085 \text{ m}^3 \cdot \text{s}^{-1}$ and $Q = 1.48 \text{ m}^3 \cdot \text{s}^{-1}$ using the HSCs derived from the same discharge. A comparison of the results in Figures 6 and 7 shows that the habitat quality for the velocity parameter was very good for both discharges, but concerning the depth parameter, the habitat quality paradoxically decreases when the water depths increase. However, when we used the $Q = 0.085 \text{ m}^3 \cdot \text{s}^{-1}$ curve for the $Q = 1.48 \text{ m}^3 \cdot \text{s}^{-1}$ discharge, the habitat quality for the depth parameter was logically increasing, but on the contrary it was decreasing for the velocity parameter (Figure 8). The same trend in both parameters was also confirmed for a discharge of $Q = 2.235 \text{ m}^3 \cdot \text{s}^{-1}$ (Figures 9 and 10).

The above results provide a logical explanation: in a period of minimum flows fish prefer cover places with maximum depths. During a slight increase in a discharge, the fish remains in the same habitat. This means that for a fish caught at the same location, the higher depth is recorded; therefore, the preferred depth increases with an increase in the discharge; this trend is also confirmed in Figure 3. From these results it can be stated that the HSCs should be derived for the minimum flows, and the peak of the curve should be shifted to an area where the fish is forced to find another cover place because of the higher velocities. These curves are shown in Figures 3 and 4 marked with a red line. The ideal situation would be to have a set of measurements from the minimum flow to the discharge when the habitat preference of the fish is changed based on the velocities. Hence, the rising part of the curve would be derived at the minimum flow conditions, while the descending part should be derived at the conditions which lead to relocations of a fish population. The determination of such a discharge would be extremely difficult for a number of reasons. In our case, the discharge of $Q = 1.48 \text{ m}^3 \cdot \text{s}^{-1}$ was used for the descending part of the curve (Figure 3).

The quality of the habitat determined by such a modified HSC has a logical development. That is, for the depth parameter the quality of the habitat increases with an increasing discharge. The quality of the habitat for the velocity parameter has a similar development. This means that there were no observed relocations of the fish population during $Q = 1.48 \text{ m}^3 \cdot \text{s}^{-1}$. Also, in this case it may be stated that the trout preferred a habitat according to the water depths and that the impact of the flow velocities on the quality of the habitat was indirect. In terms of the flow velocity there are two limiting factors. During the small velocities (the rising part of the HSC), it is a change in the quality of the riverbed material. During the low velocities sedimentation processes occur. The natural sand-gravel substrate is covered by a fine material, which has a negative impact on the quality of the habitat (during flow velocities lower than $0.1 \text{ m} \cdot \text{s}^{-1}$ in a modified HSC). The flow velocities that maintain the natural character of the riverbed are suitable in the microhabitat. During higher velocities (descending part of the HSC), the limiting factor is the ability of fish to withstand the streamflow up to the

TABLE 3: Percentage difference of the AWS evaluated by Methods 1 and 2 with the ratio of weights $W_D : W_V = 8 : 2$.

Cross section number	Riffles			Pools with greater depths		
	AWS met.1 [m ² /m]	AWS met.2 [m ² /m]	Δ [%]	AWS met.1 [m ² /m]	AWS met.2 [m ² /m]	Δ [%]
3				0.53	0.82	35
4				1.42	2.01	29.4
5				3.33	4.69	29
6				2.75	5.17	46.8
13	1.39	2.93	52.5			
14	13.28	22.02	39.7			
15	13.68	31.72	56.9			
20				27.67	29.09	4.9
21				9.7	10.56	8.1
22				9.75	10.48	7
23				12.54	13.13	4.5
24				14.04	14.51	3.3
28				4.18	4.56	8.3
29				7.15	7.91	9.6
30	17.78	21.81	18.5			
31	20.9	24.88	16			
32				8.5	10.05	15.4
33				4.63	5.09	9
34				1.78	1.92	7.2
35				6.71	7.3	8.1
36				9.44	10.82	12.8
37				7.96	8.58	7.2
38				3.71	4.01	7.5
39				4.8	5.15	6.8
40				4.84	5.18	6.6
41				2.18	2.34	6.9
42				12.44	13.07	4.9
43				10.75	11.69	8
44				4.62	5.07	8.9
47	10.33	13.61	24.1			
48	14.73	19.41	24.1			
49	9.02	12.34	26.9			
50				2.18	2.77	21.4
51	2.02	2.61	22.6			
52	2.91	4.27	31.8			
53	2.68	4.06	33.9			
54	4.13	5.6	26.3			
55				6.9	7.71	10.5
56	9.97	13.5	26.2			
57	18.71	23.72	21.1			
58	11.74	14.21	17.4			
59	1.41	1.87	24.6			
60	7.69	10.96	29.8			
61	10.66	16.66	36			
62	4.47	9.15	51.1			
63	1.6	2.7	40.8			
64	3.08	4.38	29.7			
65	0.32	1.33	76			
67				3.41	4.62	26.2

TABLE 3: Continued.

Cross section number	Riffles			Pools with greater depths		
	AWS met.1 [m ² /m]	AWS met.2 [m ² /m]	Δ [%]	AWS met.1 [m ² /m]	AWS met.2 [m ² /m]	Δ [%]
68				3.96	4.59	13.7
70				5.56	6.25	11
71				4.59	5.2	11.7
72				11.44	12.65	9.6
74	9.49	12.39	23.4			
75	2.84	3.42	17			
76	2.28	2.84	19.7			
77	0.97	1.49	35			
78	1.22	1.65	26.1			
79	1.43	1.96	27			
80	4.84	7.34	34.1			
81	3.2	5.29	39.5			
Average	31.6	12.9				

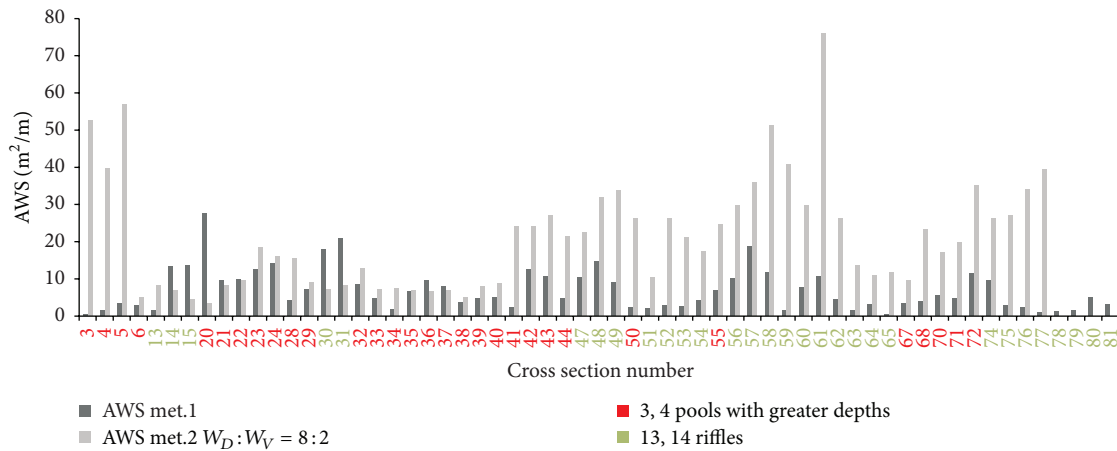


FIGURE 5: Comparison of the AWSs computed by Methods 1 and 2 (weights ratio $W_D : W_V = 8 : 2$) for the particular cross sections at the Drietomica reach.

values where the fish are forced to leave their positions for the high flow velocities and find a cover place in the current shadow. It is necessary to note that, for the purposes of water management, the rising part of the curve is crucial, as it characterizes the quality of the habitat under the maximum stress of the biota. Although the fish are forced to switch their habitat due to higher flow velocities, there are sufficient cover opportunities that create favorable conditions in the natural flow. Therefore, the descending part of the curve has no significant impact on the habitat evaluation. It has been reported that flood conditions have no significant negative impact on fish populations.

In addition to the evaluation of a simple case of changes in the quality of an aquatic habitat due to discharge variations, it is possible to solve a much more difficult task, the impact of climate change on the quality of an aquatic habitat. Addressing this issue will be documented further by a case study on the specific reach.

4. Case Study: Modeling the Quality of an In-Stream Habitat under the Influence of Climate Change on the Hybica River

The impact of climate change on the particular components of an ecosystem belongs among hot topics. Various studies of the impact of climate change demonstrate an increase in weather extremes that have an impact on human health (increasing mortality, illness from extreme weather) and the availability of food, water, and energy supplies [33]. One of the most determinative changes in weather extremes that we can expect is a protraction of drought seasons and the more frequent occurrence of minimum flows. Many scientific studies have paid attention to this topic, including [12–14]. Reducing discharges and a protraction of drought seasons may also have an impact on the quality of an aquatic habitat. This topic has not often been discussed [26, 34, 35]. Therefore,

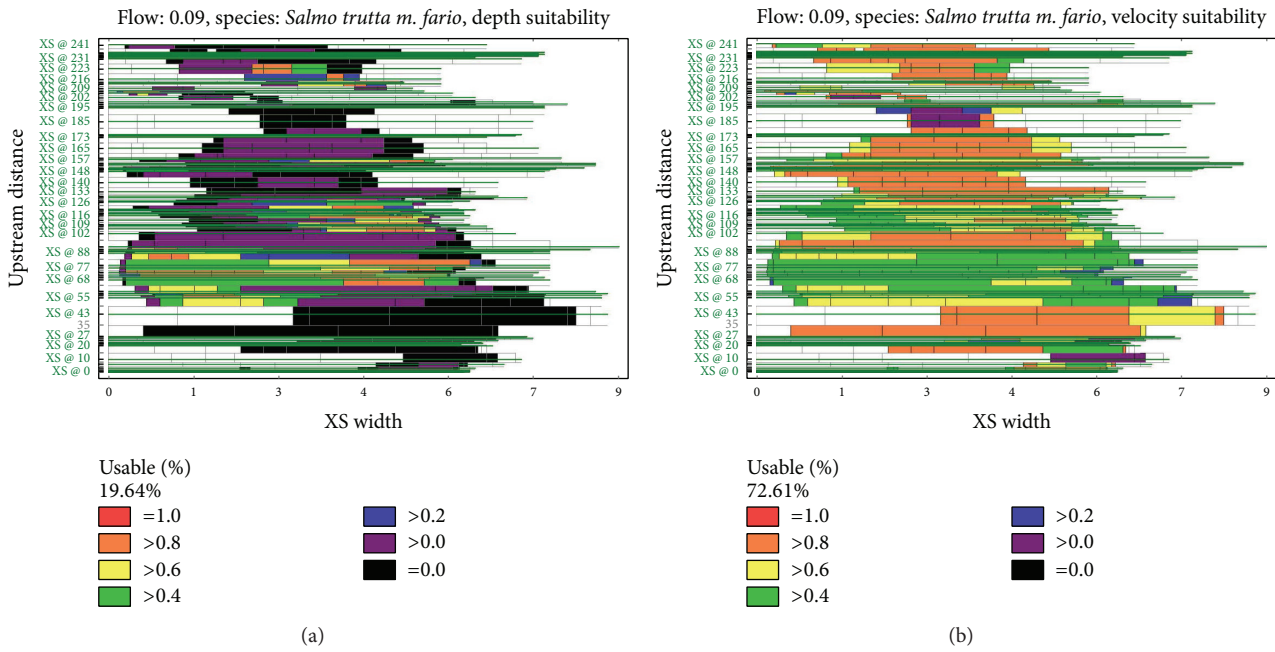


FIGURE 6: AWS during the discharge of $Q = 0.085 \text{ m}^3 \cdot \text{s}^{-1}$ using the HSCs evaluated during the discharge of $Q = 0.085 \text{ m}^3 \cdot \text{s}^{-1}$. (a) Water depth suitability, (b) flow velocity suitability. Habitat quality is scaled; black color represents an unsuitable habitat, while the red color represents the most suitable habitat.

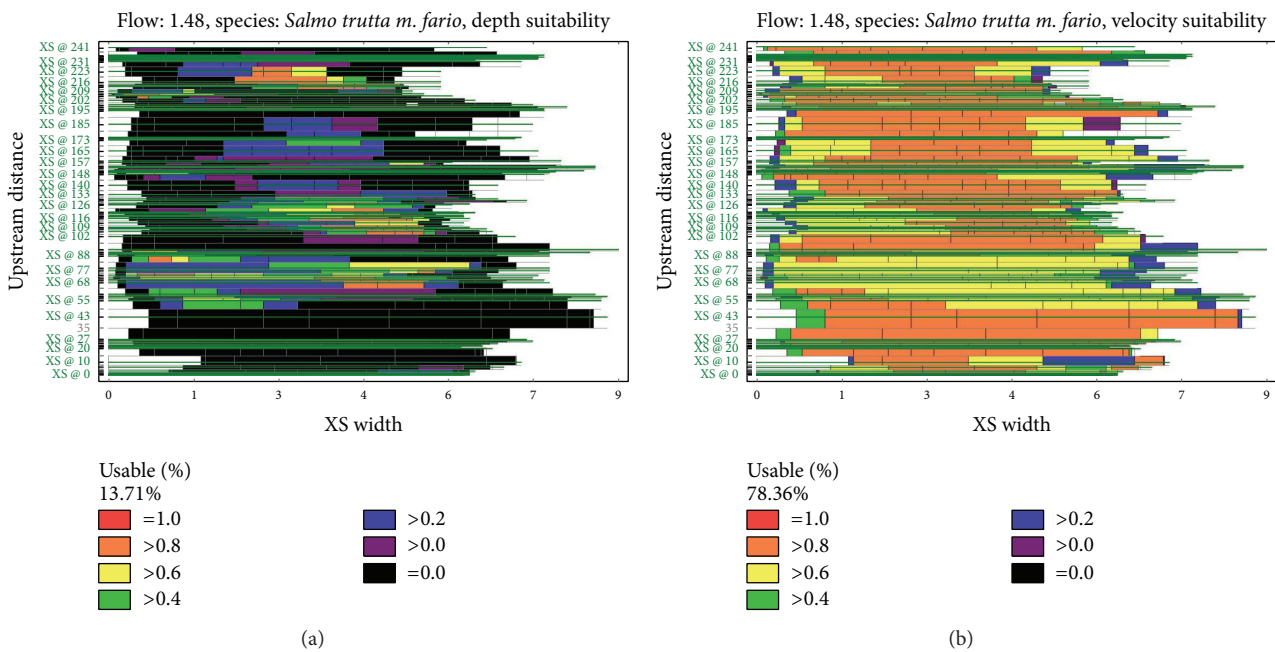


FIGURE 7: AWS during the discharge of $Q = 1.48 \text{ m}^3 \cdot \text{s}^{-1}$ using the HSCs evaluated during the discharge of $Q = 1.48 \text{ m}^3 \cdot \text{s}^{-1}$. (a) Water depth suitability, (b) flow velocity suitability.

this issue will be documented in this study at the specific reach.

The methodology for solving this issue has been divided into three areas. The first one was the calibration and validation of the Hron [36] and WetSpa [37] rainfall-runoff

models, processing the outputs from the ALADIN-Climate [38], KNMI and MPI [39] climate models, and a simulation of the altered minimum flows. The second area was focused on the measurement of abiotic and biotic characteristics and modeling in-stream habitat quality. In the study this method

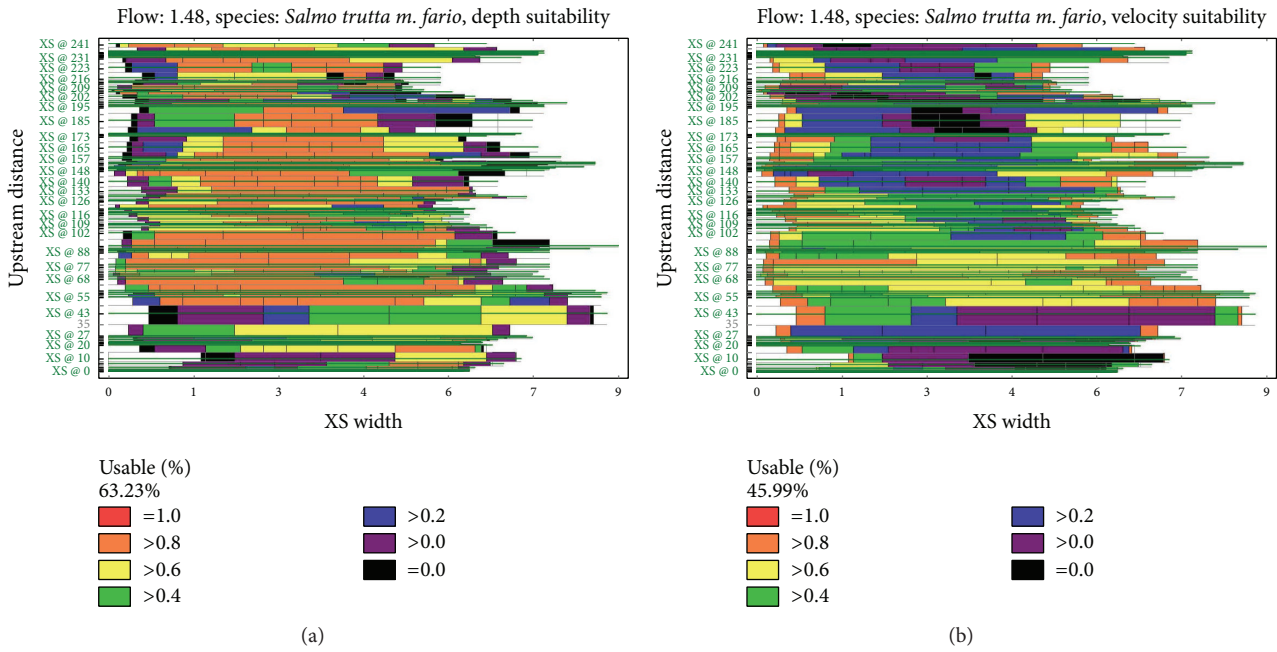


FIGURE 8: AWS during the discharge of $Q = 1.48 \text{ m}^3 \cdot \text{s}^{-1}$ using the HSCs evaluated during the discharge of $Q = 0.085 \text{ m}^3 \cdot \text{s}^{-1}$. (a) Water depth suitability, (b) flow velocity suitability.

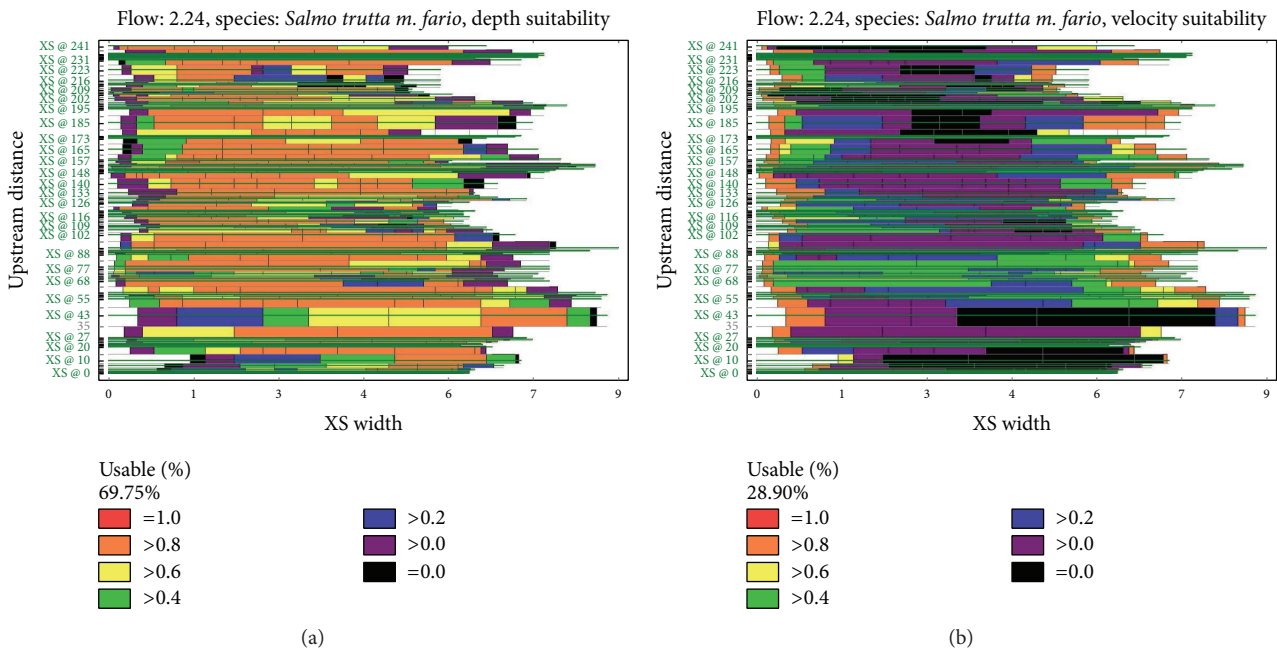


FIGURE 9: AWS during the discharge of $Q = 2.235 \text{ m}^3 \cdot \text{s}^{-1}$ using the HSCs evaluated during the discharge of $Q = 0.085 \text{ m}^3 \cdot \text{s}^{-1}$. (a) Water depth suitability, (b) flow velocity suitability.

was applied to the specific example of the Hybica River. The first stage of the simulation of the trend of minimum flows under the climate change scenario was executed as follows:

- (i) Parameters of the rainfall-runoff model of the Hybica basin were calibrated based on the measured data of air temperature, precipitation, and discharges from

the period of 01.11.1994–31.10.2002 using several rain gauging stations (Kráľova Lehota, Čierny Váh, Podbanské, and Hybe) and climate stations (Liptovský Hrádok, Podbanské).

- (ii) Mean daily discharges for two future time periods (2021–2050 and 2071–2100) and the reference

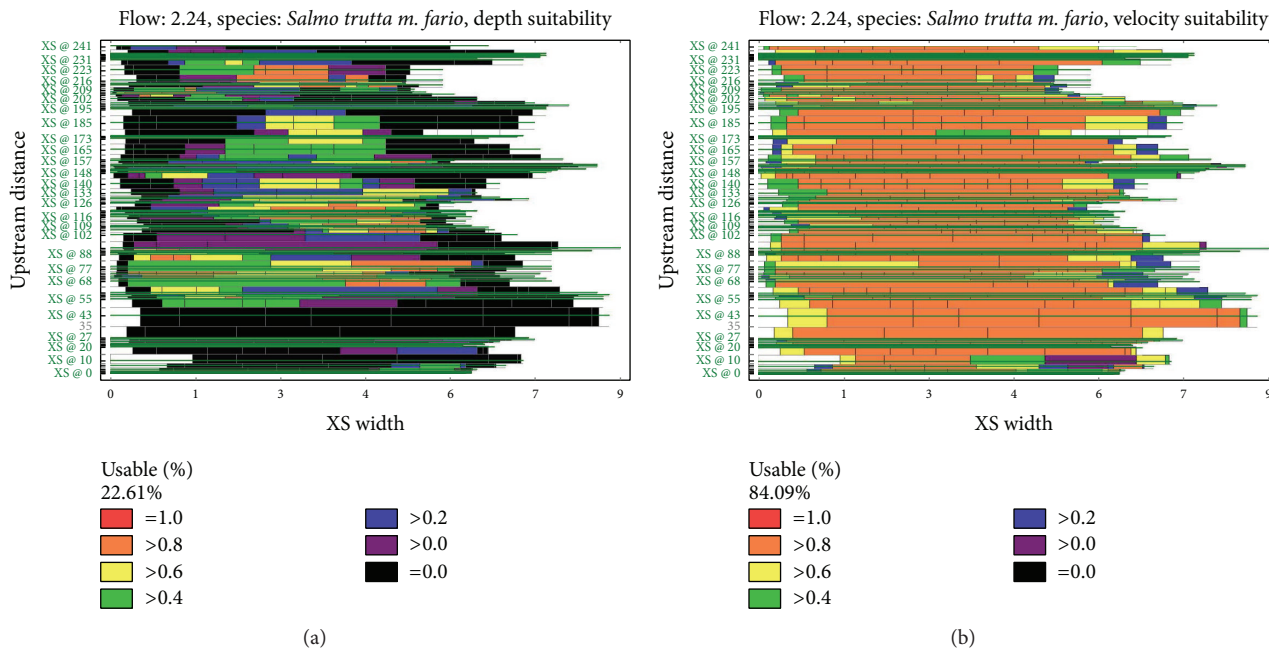


FIGURE 10: AWS during the discharge of $Q = 2.235 \text{ m}^3 \cdot \text{s}^{-1}$ using the HSCs evaluated during the discharge of $Q = 1.48 \text{ m}^3 \cdot \text{s}^{-1}$. (a) Water depth suitability, (b) flow velocity suitability.

period (1961–1990) for the Hybica River basin were simulated. The simulation results were statistically compared with the measured values of mean daily minimum flows in the calibration period. Based on the high correspondence between the simulated and measured minimum flows, the mean daily minimum flows for the future time periods were determined.

- (iii) The impact of changes in the flow regime on the quality of the aquatic habitat at Hybica River as a result of climate change was investigated.

Hybica is a right tributary of the Váh River with a length of 18.7 km and a catchment area of 44.71 km². The morphology of the riverbed is very rugged and produces a varied range of microhabitats. For the selected reach sudden changes in the curvature and vertical alignment of the bottom are characteristic. The average slope of the channel is 0.7%. The shores are covered by deciduous trees and bushes that create shade in a significant part of the channel. The ichthyological and topographical research was carried out in the reference reach of the stream with a length of 113 m. The species and quantitative composition of the ichthyofauna were as follows:

- Brown trout (*Salmo trutta m. fario*), 42 pcs.
- Carpathian sculpin (*Cottus poecilopus*), 19 pcs.
- Grayling (*Thymallus thymallus*), 17 pcs.

4.1. Modelling of the Minimum Flows for the Hybica River Basin for Future Time Periods. For the modeling of the flows for the Hybica River basin, two different rainfall-runoff models were tested, the WetSpa distributed model and the

Hron conceptual model. Calibration of the model parameters was carried out on the basis of the measured data of the air temperature and precipitation at the different stations from 1.11.1994 to 31.10.2002. The calibration was focused on achieving the best correlation between the measured and simulated mean daily discharges during the summer period. The period from May until August was considered as the summer period. Based on the measured data it was determined that the most frequent occurrence of minimum flows and also the most demanding conditions for biota occur in August. For this reason, not only was the calibration coefficient of the Nash Sutcliffe (N-S) correlation important, but also, in particular, the graphic compliance of the measured and simulated mean daily discharges of this month was also important.

The Hron model achieved a higher degree of consistency between the measured and simulated mean daily discharges compared with the WetSpa model for the summer season observed. Therefore, for the evaluation of the impact of climate change on the quality of the in-stream habitat, the Hron rainfall-runoff model was used.

The N-S correlation coefficient did not achieve a globally high degree of conformity (N-S = 0.67), due to the fact that during the calibration, particular attention was paid to the graphic compliance of the minimum mean daily flows, and the maximum flows were ignored. The choice of model parameters was adapted to this kind of calibration. The results of the comparison of the measured and simulated flows showed that in the month of August, almost total agreement between the simulated and measured long-term mean monthly and daily discharges has been achieved (Figure 11(a)).

The compliance was not achieved just for the long-term mean monthly and daily values but also was reached for

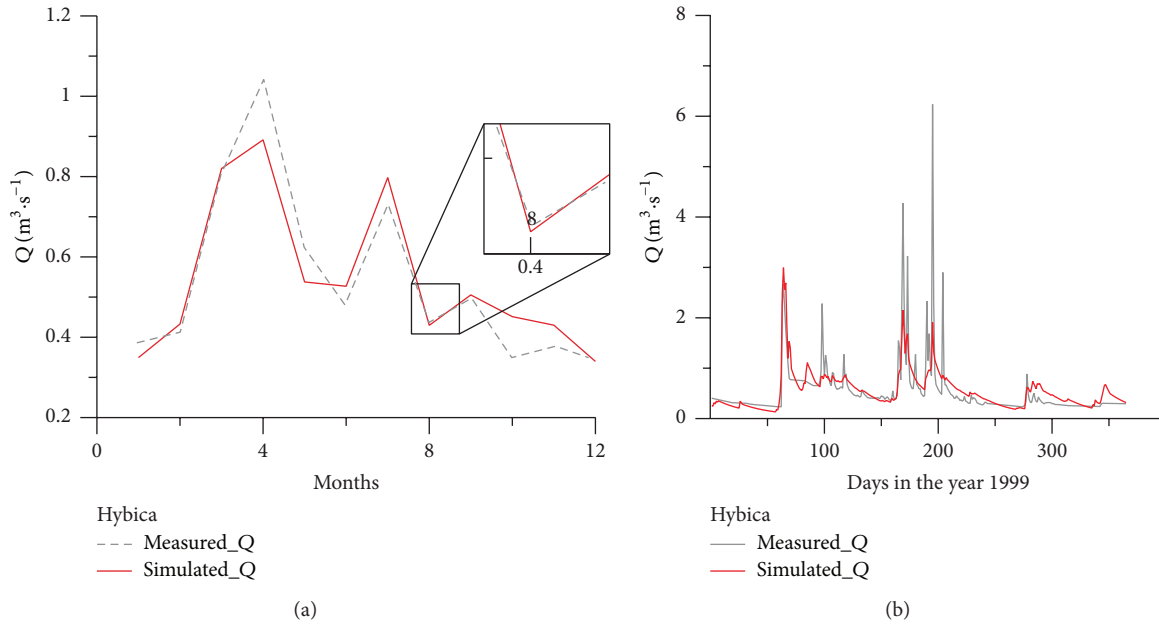


FIGURE 11: Results of the comparison by the Hron model as (a) the monthly average discharges in the closing profile of the Hybica basin and as (b) the mean daily discharges in the closing profile for the year 2000.

the concrete value of the mean daily minimum flow, which occurred in the measured and the simulated periods on the same day (27.8.1995). The measured mean daily minimum flow was equal to $0.156 \text{ m}^3 \cdot \text{s}^{-1}$, and the simulated mean daily minimum flow was $0.151 \text{ m}^3 \cdot \text{s}^{-1}$. Other summer months showed a similar consistency of long-term mean monthly and daily flows.

Based on the calibrated parameters of the models, the simulation was performed for the reference period 1961–1990 and the two future time periods of 2021–2050 and 2071–2100. For the choice of the most extreme climate change scenario, the simulation of the flow changes for the Váh River basin, where the Hybica River is located, was performed. Out of the three climate change scenarios (ALADIN-Climate, KNMI, and MPI), the ALADIN-Climate scenario was selected for assessing the impact of climate change on the quality of the in-stream habitat for the Hybica River. This scenario assumes the most extreme decrease in flows for the future periods compared to the KNMI and MPI scenarios (Figure 12).

Next, the minimum mean daily discharges of each 30-year period for the Hybica River were evaluated, because the minimum water levels are the most crucial for the aquatic biota. For the period 2021–2050, the minimum average daily discharge was $0.17 \text{ m}^3 \cdot \text{s}^{-1}$, which occurred specifically on August 29, 2025, and for the period from 2071 to 2100, it was the flow equal to $0.06 \text{ m}^3 \cdot \text{s}^{-1}$, which, based on the simulation, occurred on 22 August 2079. In the period 1961–1990, the lowest simulated mean daily flow was $0.22 \text{ m}^3 \cdot \text{s}^{-1}$.

It can be concluded that according to the results the flows in the summer periods in the future will decrease. The results are documented on the map of the runoff changes by 2100 compared to the reference period 1961–1990. From this map it is clear that the flow will decrease, especially in the

TABLE 4: The m -day discharges in the reference reach of the Hybica River (m is the periodicity of achieving or exceeding the discharge).

m [day]	30	90	180	270	330	355	364
Q_m [$\text{m}^3 \cdot \text{s}^{-1}$]	2.319	0.952	0.471	0.24	0.139	0.083	0.037

high mountain areas (Figure 13). Such results have been also documented in the newest studies such as [40–42] and many others.

4.2. *Assessment of the Quality of the In-Stream Habitat of the Hybica River.* The ichthyological survey of the selected reaches was oriented towards determination of the suitability curves for the individual fish species. The data were obtained by electrofishing similarly as in [43].

The topographical measurement of the individual reaches was adapted to the requirements of the hydraulic modeling. Cross sections were measured by leveling; at the characteristic profiles the water level was fixed to static points, which accelerated the measurement of the water level regimes at different flows.

The quality of the habitat was evaluated at different discharges. These were not chosen randomly, but the real values of the m -day discharges were used (Table 4). Determination of the m -day discharges was realized in cooperation with the Slovak Hydrometeorological Institute in Bratislava. The evaluation was in accordance with the STN 75 1410-1 national standard, where the method of interpolation between two gauging stations was used.

4.3. *Impact of Changes in the Flow Regime, as a Result of Climate Change, on the Quality of the Biota of the Hybica River.* The impact of climate change will mainly be reflected

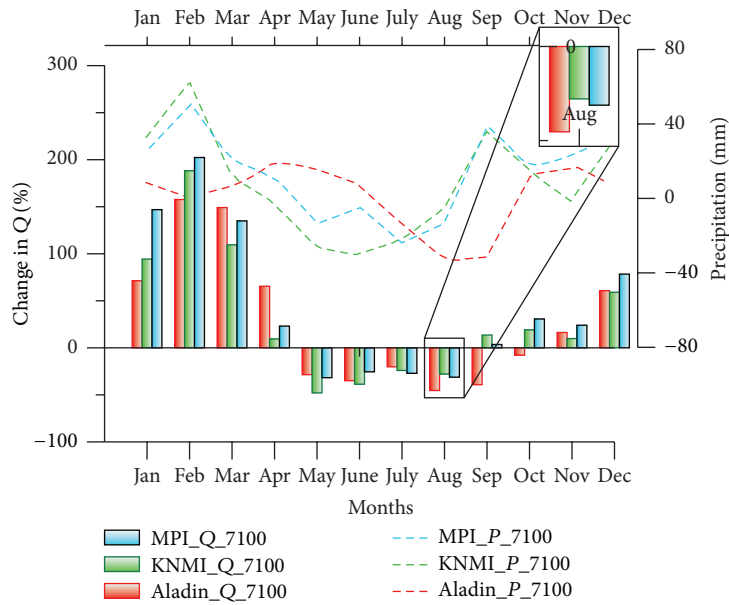


FIGURE 12: Evaluation of changes in precipitation and discharges in the closing profile of the Váh basin by the year 2100 as a change against the reference period 1961–1990 using the WetSpa hydrological model and individual scenarios.

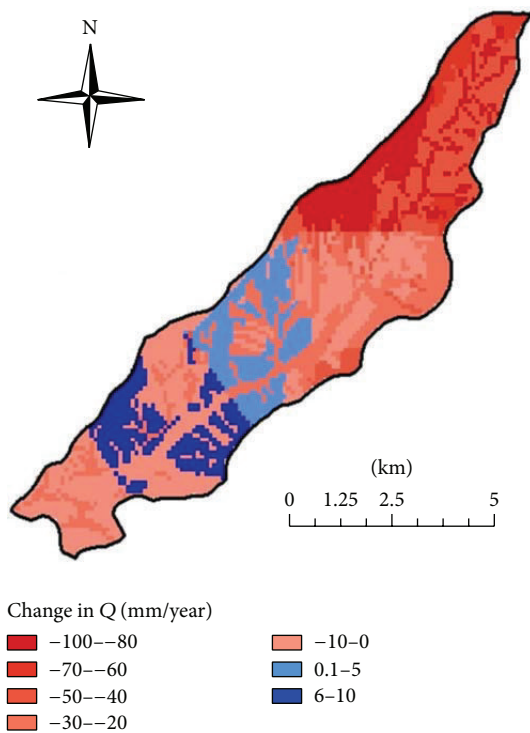


FIGURE 13: Changes in the mean annual surface runoff in the Hybica basin in the period 2071–2100 compared to the reference period 1961–1990.

in aquatic areas by changing of the flow, which has a direct impact on the abiotic characteristics of the channel. The biotic habitat parameters are represented by fish as bioindicators of the in-stream habitat quality. The relationship

between the abiotic and biotic characteristics is represented by the suitability curves of the individual species. The most demanding area in the modeling of an aquatic habitat is the determination of the HSCs. These were derived from an ichthyological survey conducted by the Department of Land and Water Resources Management, Slovak University of Technology in Bratislava, in cooperation with the Slovak Agricultural University in Nitra directly at the reference reaches of the Hybica River. The topographical characteristics were determined by leveling and water-level regime has been verified on the basis of the hydrometry and measurements of the water levels at each cross section. This is a set of data which allows us to model the quality of the habitat in the RHABSIM model.

Figure 14 shows a gradual change in the quality of the aquatic habitat according to the modified discharge. The change in the quality of the aquatic habitat was simulated for the discharges that have been assessed as the minimum daily flows for each evaluated 30-year period.

During minimum flows, the quality of microhabitats where the biota is focused is important. The remaining part of the channel does not have a significant impact on the conservation of the in-stream biota. In other words, it is important that the stream provides a satisfactory habitat (level of suitability of more than 0.4).

Figures 14(b) and 14(c) show that the quality of the aquatic habitat for the two future periods modeled decreases with a decreasing mean daily minimum discharge compared to the reference period (discharge of $0.22 \text{ m}^3 \cdot \text{s}^{-1}$, which occurred at the time of the ichthyological measurements). At a discharge of $0.17 \text{ m}^3 \cdot \text{s}^{-1}$ (Q_{330}), the quality of the habitat where the biota is concentrated did not change significantly. At the discharge of $0.06 \text{ m}^3 \cdot \text{s}^{-1}$ (Q_{355}) a significant change occurred. A suitable habitat was reduced to only one cell. This means that this

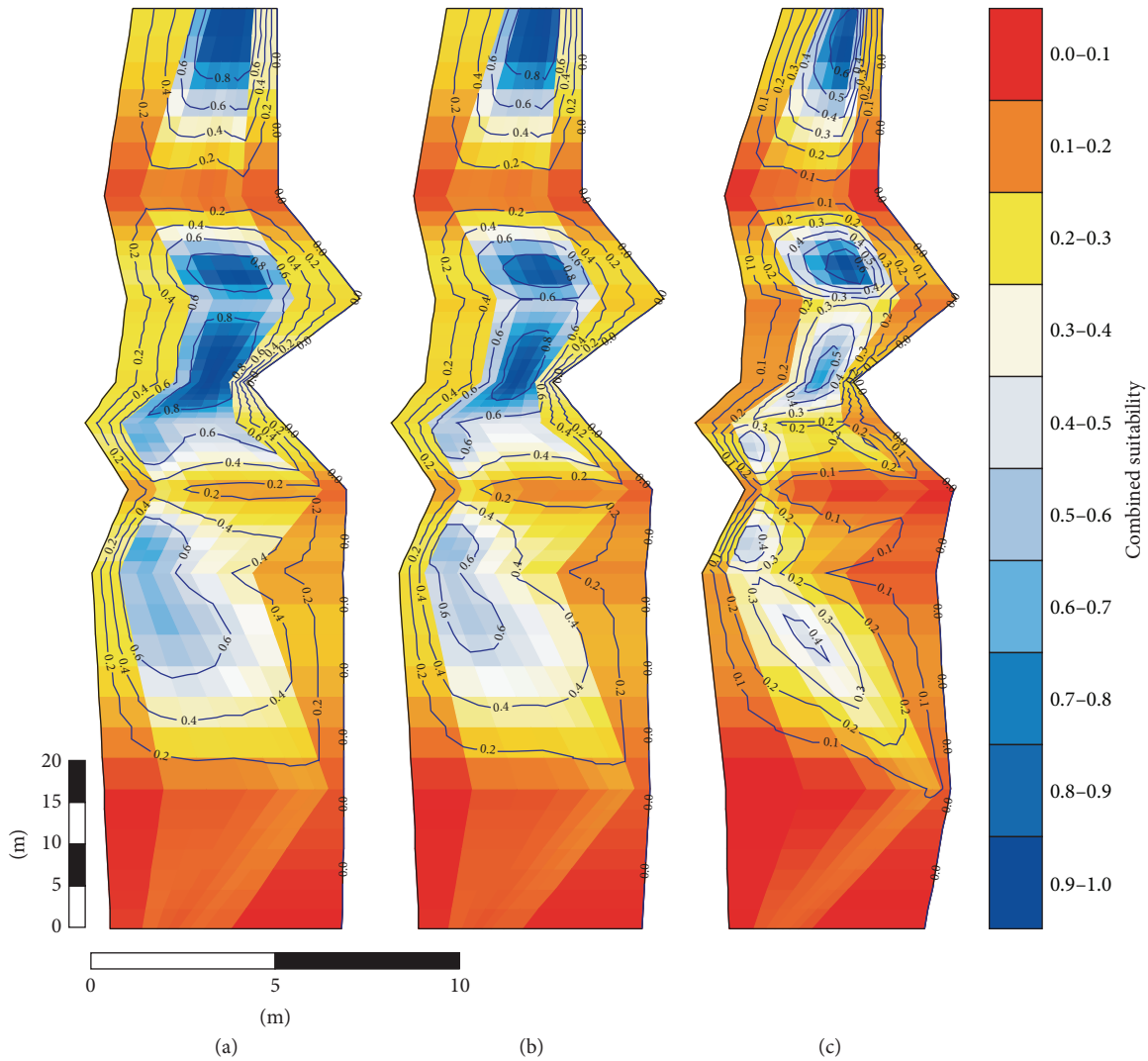


FIGURE 14: Evaluation of the quality of the in-stream habitat by the RHABSIM model in the Hybica River for the discharge of (a) $Q = 0.22 \text{ m}^3 \cdot \text{s}^{-1}$ (1961–1990), (b) $Q = 0.17 \text{ m}^3 \cdot \text{s}^{-1}$ (2021–2050), and (c) $Q = 0.06 \text{ m}^3 \cdot \text{s}^{-1}$ (2071–2100).

discharge would have a significant impact not only on the reduction of the in-stream habitat, but also on the biodiversity in this reach. On the basis of these results we can conclude that according to the ALADIN-Climat scenario we could expect significant changes in the quality of the aquatic habitat for the future time period of 2071–2100.

5. Conclusions

Analysis of the relationship between the shape of the HSCs and the abiotic parameters of the in-stream habitat showed that the shapes of the curves are strongly related to the relevant parameters, in particular to the water depth and flow velocity. These two characteristics define the shape of the HSCs, which represent a wider range of discharges. Further analysis was aimed at evaluating the AWS in terms of the impact of the water depth and flow velocity. The results show

that the water depth has a significantly greater effect on the quality of the in-stream habitat than the flow velocity and that the optimum ratio between these parameters is as follows: $W_D : W_V = 8 : 2$.

There is little information about the modeling of the quality of an in-stream habitat in terms of the trends in climate change. The described methodology enhances the ability to obtain such information. The results show that climate change may cause significant modifications in the ecosystem of watercourses. Based on these results it is possible to design and evaluate restorative measures that could mitigate the impact of climate change on the in-stream areas of watercourses.

Conflict of Interests

The authors declare that there is no conflict of interests regarding the publication of this paper.

Acknowledgments

This study has been jointly supported by the Slovak Research and Development Agency under Contract no. APVV-0303-11 and by the Scientific Grant Agency under Contracts no. VEGA 1/0625/15 and VEGA 1/0665/15.

References

- [1] N. Friberg, A. Baatrup-Pedersen, M. L. Pedersen, and J. Skriver, "The new Danish stream monitoring programme (NOVANA)—preparing monitoring activities for the Water Framework Directive era," *Environmental Monitoring and Assessment*, vol. 111, no. 1–3, pp. 27–42, 2005.
- [2] I. G. Jowett, "Instream flow methods: a comparison of approaches," *Regulated Rivers: Research & Management*, vol. 13, no. 2, pp. 115–127, 1997.
- [3] T. B. Hardy, "The future of habitat modeling and instream flow assessment techniques," *Regulated Rivers: Research & Management*, vol. 14, no. 5, pp. 405–420, 1998.
- [4] R. E. Tharme, "A global perspective on environmental flow assessment: emerging trends in the development and application of environmental flow methodologies for rivers," *River Research and Applications*, vol. 19, no. 5–6, pp. 397–441, 2003.
- [5] S. Mérigoux, N. Lamouroux, J.-M. Olivier, and S. Dolédec, "Invertebrate hydraulic preferences and predicted impacts of changes in discharge in a large river," *Freshwater Biology*, vol. 54, no. 6, pp. 1343–1356, 2009.
- [6] I. D. Hodgkinson and J. K. Jackson, "Terrestrial and aquatic invertebrates as bioindicators for environmental monitoring, with particular reference to mountain ecosystems," *Environmental Management*, vol. 35, no. 5, pp. 649–666, 2005.
- [7] O. Slavík, L. Bartoš, and D. Mattas, "Does stream morphology predict the home range size in burbot?" *Environmental Biology of Fishes*, vol. 74, no. 1, pp. 89–98, 2005.
- [8] N. Lamouroux, J.-M. Olivier, H. Capra, M. Zylberblat, A. Chandesris, and P. Roger, "Fish community changes after minimum flow increase: testing quantitative predictions in the Rhône River at Pierre-Bénite, France," *Freshwater Biology*, vol. 51, no. 9, pp. 1730–1743, 2006.
- [9] V. Macura, A. Škrinár, K. Kaluz, M. Jačová, and M. Škrovinová, "Influence of the morphological and hydraulic characteristics of mountain streams on fish habitat suitability curves," *River Research and Applications*, vol. 28, no. 8, pp. 1161–1178, 2012.
- [10] J. A. Thomas and K. D. Bovee, "Application and testing of a procedure to evaluate transferability of habitat suitability criteria," *Regulated Rivers: Research & Management*, vol. 8, no. 3, pp. 285–294, 1993.
- [11] C. B. Stalnaker, B. L. Lamb, J. Henriksen, K. Bovee, and J. Bartholow, "The instream flow incremental methodology: a primer for IFIM," Biological Report 29, National Biological Service, 1995.
- [12] C.-Y. Xu, "Modelling the effects of climate change on water resources in central Sweden," *Water Resources Management*, vol. 14, no. 3, pp. 177–189, 2000.
- [13] O. B. Haddad, M. Jahandideh-Tehrani, and M. A. Mariño, "Discussion of 'investigating the vulnerability of dry-season water supplies to climate change: a case study of the Gwangdong reservoir drought management system, Korea' by Donghoon Cha; Sangeun Lee; and Heekyung Park," *Water Resources Management*, vol. 27, no. 7, pp. 1893–1896, 2013.
- [14] F. Fung, G. Watts, A. Lopez, H. G. Orr, M. New, and C. Extence, "Using large climate ensembles to plan for the hydrological impact of climate change in the freshwater environment," *Water Resources Management*, vol. 27, no. 4, pp. 1063–1084, 2013.
- [15] I. Maddock, "The importance of physical habitat assessment for evaluating river health," *Freshwater Biology*, vol. 41, no. 2, pp. 373–391, 1999.
- [16] D. Ayllón, A. Almodóvar, G. G. Nicola, and B. Elvira, "Interactive effects of cover and hydraulics on brown trout habitat selection patterns," *River Research and Applications*, vol. 25, no. 8, pp. 1051–1065, 2009.
- [17] D. Ayllón, A. Almodóvar, G. Nicola, and B. Elvira, "Modelling brown trout spatial requirements through physical habitat simulations," *River Research and Applications*, vol. 26, no. 9, pp. 1090–1102, 2010.
- [18] D. Ayllón, A. Almodóvar, G. G. Nicola, and B. Elvira, "The influence of variable habitat suitability criteria on PHABSIM habitat index results," *River Research and Applications*, vol. 28, no. 8, pp. 1179–1188, 2012.
- [19] K. D. Bovee, "Use of the instream flow incremental methodology to evaluate the influence of microhabitat variability on trout populations in four Colorado streams," in *Proceedings of the Western Division of the American Fisheries Society*, pp. 227–257, Albuquerque, NM, USA, 1988.
- [20] A. L. Conder and T. C. Annear, "test of weighted usable area estimates derived from a PHABSIM model for instream flow studies on trout streams," *North American Journal of Fisheries Management*, vol. 7, no. 3, pp. 339–350, 1987.
- [21] I. G. Jowett, "Models of the abundance of large brown trout in New Zealand rivers," *North American Journal Fisheries Management*, vol. 12, pp. 417–432, 1992.
- [22] R. B. Nehring and R. M. Anderson, "Determination of population-limiting critical salmonid habitats in Colorado streams using the Physical Habitat Simulation system," *Rivers*, vol. 4, no. 1, pp. 1–19, 1993.
- [23] S. P. Gallagher and M. F. Gard, "Relationship between chinook salmon (*Oncorhynchus tshawytscha*) redd densities and PHABSIM-predicted habitat in the Merced and Lower American rivers, California," *Canadian Journal of Fisheries and Aquatic Sciences*, vol. 56, no. 4, pp. 570–577, 1999.
- [24] D. Mathur, W. H. Bason, E. J. Purdy Jr., and C. A. Silver, "A critique of the in stream flow incremental methodology," *Canadian Journal of Fisheries and Aquatic Sciences*, vol. 42, no. 4, pp. 825–831, 1985.
- [25] D. Mathur, W. H. Bason, E. J. Purdy Jr., and C. A. Silver, "Reply to 'in defense of the instream flow incremental methodology,'" *Canadian Journal of Fisheries and Aquatic Sciences*, vol. 43, no. 5, pp. 1084–1094, 1986.
- [26] J. L. Meyer, M. J. Sale, P. J. Mulholland, and N. L. Poff, "Impacts of climate change on aquatic ecosystem functioning and health," *Journal of the American Water Resources Association*, vol. 35, no. 6, pp. 1373–1386, 1999.
- [27] D. Scott and C. S. Shirvell, "A critique of the instream flow incremental methodology and observations on flow determination in New Zealand," in *Regulated Streams*, J. Craig and J. B. Kemper, Eds., pp. 27–43, Springer, New York, NY, USA, 1987.
- [28] C. S. Shirvell, "Ability of PHABSIM to predict chinook salmon spawning habitat," *Regulated Rivers: Research & Management*, vol. 3, no. 1, pp. 277–289, 1989.
- [29] J. Cohen, *Statistical Power Analysis for the Behavioral Sciences*, Lawrence Earlbaum Associates, Hillsdale, NJ, USA, 2nd edition, 1988.

- [30] K. V. Grišanin, *Dinamika ruslovykh potokov*, Gidrometeoizdat, Leningrad, Russia, 1981.
- [31] T. H. Oliver and M. D. Morecroft, "Interactions between climate change and land use change on biodiversity: attribution problems, risks, and opportunities," *Wiley Interdisciplinary Reviews: Climate Change*, vol. 5, no. 3, pp. 317–335, 2014.
- [32] G. E. Petts, "Instream flow science for sustainable river management," *Journal of the American Water Resources Association*, vol. 45, no. 5, pp. 1071–1086, 2009.
- [33] Z. Li, X. Deng, J. Huang, R. Zhang, and J. Huang, "Critical studies on integrating land-use induced effects on climate regulation services into impact assessment for human well-being," *Advances in Meteorology*, vol. 2013, Article ID 831250, 14 pages, 2013.
- [34] T. Beechie, H. Imaki, J. Greene et al., "Restoring salmon habitat for a changing climate," *River Research and Applications*, vol. 29, no. 8, pp. 939–960, 2013.
- [35] C. T. Graham and C. Harrod, "Implications of climate change for the fishes of the British Isles," *Journal of Fish Biology*, vol. 74, no. 6, pp. 1143–1205, 2009.
- [36] P. Valent, J. Szolgay, and C. Rivero, "Split sample calibration of the HBV model using artificially generated flows," in *Proceedings of the HydroCarpath, Catchment Processes in Regional Hydrology: From Experiment to Modeling in Carpathian Drainage Basins*, p. 5, University of West Hungary, Sopron, Hungary, October 2012.
- [37] Z.-M. Wang, O. Batelaan, and F. De Smedt, "A distributed model for water and energy transfer between soil, plants and atmosphere (WetSpa)," *Physics and Chemistry of the Earth*, vol. 21, no. 3, pp. 189–193, 1996.
- [38] P. Skalák, P. Štěpánek, and A. Farda, "Validation of ALADIN-Climat/CZ for present climate (1961–1990) over the Czech Republic," *Időjárás*, vol. 122, no. 3-4, pp. 191–201, 2008.
- [39] Z. Štefunková, K. Hlavčová, and M. Lapin, "Runoff change scenarios based on regional climate change projections in mountainous basins in Slovakia," *Contributions to Geophysics and Geodesy*, vol. 43, no. 4, pp. 327–350, 2013.
- [40] C. Schneider, C. L. R. Laizé, M. C. Acreman, and M. Flörke, "How will climate change modify river flow regimes in Europe?" *Hydrology and Earth System Sciences*, vol. 17, no. 1, pp. 325–339, 2013.
- [41] W. J. Fisk, "Review of some effects of climate change on indoor environmental quality and health and associated no-regrets mitigation measures," *Building and Environment*, vol. 86, pp. 70–80, 2015.
- [42] M. Höglind, S. M. Thorsen, and M. A. Semenov, "Assessing uncertainties in impact of climate change on grass production in Northern Europe using ensembles of global climate models," *Agricultural and Forest Meteorology*, vol. 170, pp. 103–113, 2013.
- [43] N. Lamouroux, H. Capra, M. Pouilly, and Y. Souchon, "Fish habitat preferences in large streams of southern France," *Freshwater Biology*, vol. 42, no. 4, pp. 673–687, 1999.

Research Article

Numerical Modeling of Topography-Modulated Dust Aerosol Distribution and Its Influence on the Onset of East Asian Summer Monsoon

Hui Sun¹ and Xiaodong Liu^{1,2}

¹SKLLQG, Institute of Earth Environment, Chinese Academy of Sciences, Xi'an 710061, China

²CAS Center for Excellence in Tibetan Plateau Earth Sciences, Beijing 100101, China

Correspondence should be addressed to Hui Sun; sunhui@ieecas.cn

Received 29 April 2015; Revised 1 September 2015; Accepted 17 September 2015

Academic Editor: Steffen Mischke

Copyright © 2016 H. Sun and X. Liu. This is an open access article distributed under the Creative Commons Attribution License, which permits unrestricted use, distribution, and reproduction in any medium, provided the original work is properly cited.

A regional climate model coupled with a dust module was used to simulate dust aerosol distribution and its effects on the atmospheric heat source over the TP, East Asian summer monsoon onset, and precipitation in East Asia modulated by the uplift of the northern TP. We carried out four experiments, including a modern (i.e., high-mountain) experiment with (HMD) and without (HM) the major deserts in Northwest China and a low-mountain experiment with (LMD) and without (LM) the deserts. The results show that dust greatly increases in the Taklamakan Desert accompanied with the uplift of the northern TP, and the increase exceeds $150 \mu\text{g kg}^{-1}$ in spring. A strong cyclone in the Tarim Basin produced by the uplifted northern TP enhances dust emissions in the Taklamakan Desert in summer. Meanwhile, the dust loading over the TP also increases induced by the uplift of the northern TP, causing the heat source over the TP decreased. Under the condition of the northern TP uplift to present altitude, dust delays the East Asia summer monsoon onset by two pentads and one pentad, respectively, in the southern and northern monsoon regions and greatly suppresses precipitation in East Asia compared with results in the low terrain experiments.

1. Introduction

Dust aerosol receives much attention due to its substantial effects on the environment and climate [1]. It not only adversely affects air quality and endangers human health [2, 3] but also impacts biogeochemical cycles and ocean CO₂ uptake [4, 5]. Additionally, it can change regional and even global climate through modifying the radiation balance and cloud-precipitation physics [6–8].

Important progress focusing on the East Asian dust cycle, dust radiative effects, and its effects on the East Asian monsoon has been made recently using various global and regional climate models [9–16]. The distribution of dust aerosol can directly determine its induced climatic effects, and so some scientists have studied the impacts of various factors on the distribution of dust, including meteorological parameters [17], dust sources [18], and different underlying surfaces [19]. There are two large deserts located in East Asia: the Taklamakan Desert and the Gobi Desert [20].

The distribution of dust aerosol in Asia is closely related to the activity of strong dust storms which mainly occur in spring in East Asia [21–23].

Dust can influence the climate through direct and indirect effects [6–8]. Dust aerosol can change atmospheric temperatures via its direct radiative effects [24, 25] and, meanwhile, satellite observations show that the dust load over the Tibetan Plateau (TP) can be transported from the Taklamakan Desert [26], meaning that the heat source over the TP can be influenced by such dust radiative effects. Meanwhile, numerous studies have shown that variation in the heat source over the TP bears a close relationship with East Asian summer monsoon onset in late spring or early summer [27–29]. Previous research shows that aerosol can change the heat source over the TP and further influences the Asia summer monsoon [30]. Therefore, it is crucial to determine the distribution of dust over the TP, as it can indirectly impact upon East Asian summer monsoon onset through modifying the heat source over the TP.

On the other hand, the uplift of the TP, as one of the most important geological events in Cenozoic era, has had profound influences on the Asian and global climate and environment evolution in geological periods [31]. Presently, most studies show that the TP uplift is phased and process, and some researches show that the uplift of northern TP and its nearby mountains has mainly occurred since the Miocene [31]. Meanwhile, the major Asian inland deserts may form and develop with the northern TP uplifting.

Recently, Shi et al. [32] carried out a numerical simulation of the impacts of the uplifting of the TP on the dust cycle in Asia using a GCM, and their results showed that topography has a great effect on dust sedimentation in East Asia. Liu et al. [33], using the latest version of RegCM4.1/Dust, studied the impacts of the uplifting of the northern TP on regional climate, and their research indicated that uplift of the northern TP is closely related with inland desert formation. However, they did not analyze how the northern TP uplift modulates the distribution of dust in East Asia, nor did they discuss the effects of dust on the heat source over the TP and ultimately how it induces anomalies in East Asia summer monsoon onset.

In this paper, therefore, we conduct a set of sensitivity experiments under conditions of low and high orography in the northern TP using a regional climate model with and without the dust module to further discuss two main issues: (1) How does the northern TP modulate the dust distribution in East Asia? (2) What are the impacts of dust effects on the heat source over the TP and East Asia summer monsoon onset under different terrain settings? This study will help to deep explore the modulation of topography on dust-monsoon relationship and also to understand the paleoclimate change in East Asia.

2. Numerical Model and Experiment Design

2.1. Numerical Model. RegCM4.1/Dust is a hydrostatic, sigma vertical coordinate model, based on the major physical parameterizations of RegCM3 [34]. The dynamical framework in RegCM4.1/Dust is similar to the mesoscale model MM5 [35] and it adopts CCM3 [36] for atmospheric radiative transfer processes at solar (SW) and thermal (LW) wavelengths. In addition, the Biosphere-Atmosphere Transfer Scheme (BATSle) [37] is coupled in the model to diagnose the land surface processes. The mass flux scheme of Grell et al. [38] and the subgrid explicit moisture scheme of Pal et al. [39] are used to describe cumulus convective precipitation and nonconvective precipitation, respectively.

The coupled dust module of RegCM4.1 based on the dust producing model of Marticorena and Bergametti [40] and Alfaro and Gomes [41], generally includes dust emission, transport, and deposition processes. Parameterization of the dust emission processes comprises four components [14, 42]. First, each model grid cell is classified either as desert or as nondesert and the soil characteristics including texture, particle size, and composition in each model grid cell are specified based on the USDA textural classification. Second, dust emission is represented as a function of a threshold value, surface roughness, and soil moisture. Third, horizontal

mass flux is represented as a function of friction velocity [42]. Finally the vertical flux corresponding to each emission mode is obtained. The dust particles in the dust module are divided to four size bins (or modes): the fine (0.01–1.0 μm), accumulation (1.0–2.5 μm), coarse (2.5–5 μm), and giant (5.0–20.0 μm). Dust transport, deposition, and removal processes are given by Solmon et al. [43], Qian et al. [44], and Qian and Giorgi [45]. The dust mixing ratio is represented by the tracer transport equation:

$$\frac{\partial \chi^i}{\partial t} = -\bar{V} \cdot \nabla \chi^i + F_H^i + F_V^i + F_c^i + S^i - R_{\text{Wls}}^i - R_{\text{Wc}}^i - D_d^i, \quad (1)$$

where $-\bar{V} \cdot \nabla \chi^i$ is advection, F_H^i is horizontal turbulent diffusion, F_V^i is vertical turbulent diffusion, and F_c^i is convective transport [43–45]. R_{Wls}^i and R_{Wc}^i are the wet removal terms represented by large-scale and convective rain [46, 47]. D_d^i is dry deposition represented by assuming fixed deposition velocities over land and water.

The δ -Eddington approximation is employed by RegCM4 for radiative flux calculations. The calculation of dust SW radiation uses an asymmetry factor, single scattering albedo, and mass extinction coefficient based on Mie theory. The dust LW radiation is accounted for introducing the dust emissivity given by Kiehl et al. [36].

2.2. Model Sensitivity Tests. Four experiments were performed in this study (Table 1), the first three of which followed the protocol of Liu et al. [33], while the fourth was a newly designed experiment. The first is the modern (i.e., high-mountain) experiment, in which all of boundary conditions including terrain are set to the present-day state and the dust emissions from the major deserts in northwest China (HMD) are opened. The second is the high-mountain experiment with modern terrain stage but an absence of East Asian inland deserts (HM). The third is the low-mountain experiment with reduced topography in the northern TP (by as much as 2400 m) and also an absence of deserts (LM). The final one is the low-mountain experiment with the same terrain conditions as LM but with dust emissions from the major deserts of East Asia opened up (LMD). Therefore, by comparing the results of HMD minus HM (hereafter HMD – HM) and those of LMD minus LM (hereafter LMD – LM), we can determine the distribution of dust in East Asia and its related effects on East Asia summer monsoon onset as modulated by the uplift of the northern TP and its nearby major mountains.

The initial and lateral boundary conditions for the model were extracted from the National Centers for Environmental Prediction, Department of Energy (NCEP–DOE) Atmospheric Model Intercomparison Project (AMIP-II) reanalysis (R-2) [48], and the default land use types were based on Global Land Cover Characterization (GLCC) data [49]. Soil texture data were from the USDA texture classification [50]. The sea surface temperature (SST) is from the National Oceanic and Atmospheric Administration SST dataset [51]. Each simulation began on January 1, 1988, and ran until

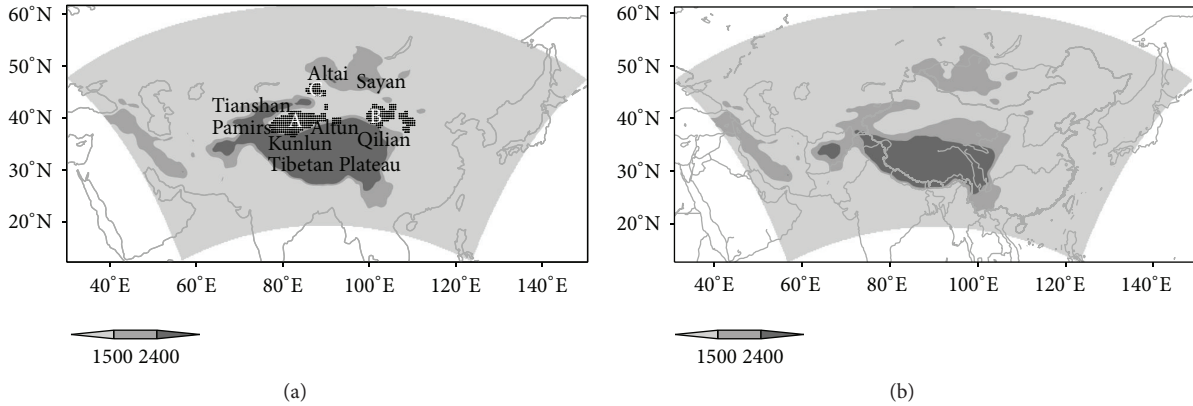


FIGURE 1: (a) Modern terrain used in HMD and HM and the locations of the major mountain ranges. The dotted areas indicate the three major deserts in China. A = southern Xinjiang in the Taklamakan desert; B = western Inner Mongolia in the Gobi desert; C = northern Xinjiang in the Gurbantunggut Desert. (b) Lowered terrain distribution used in LM and LMD. The lightest grey region in (a, b) is the model domain.

TABLE 1: Information on the topography and dust emissions in the experiments.

Experiment name	Topography	Emissions from the major deserts
HMD	Modern (high-mountain)	Open
HM	Modern (high-mountain)	Closed
LMD	Lowered	Open
LM	Lowered	Closed

December 31, 2009; however, only the last 20 years is analyzed, leaving the first two years as model spin-up time. The model center is located at 40°N and 90°E, with 160 grid cells in the W-E direction and 95 in the N-S direction. The interval of model integration time is 1 minute. Model horizontal resolution is 50 km. It was run in its standard configuration of 18 vertical σ -layers, with the model top at 10 hPa. Besides the change of terrain and deserts, all experiments used the same conditions. Only the dust direct effect is included in this study.

The height of the lowered region in LMD and LM was 1500 m plus 20% of the modern terrain altitude. The reduced area was mainly located in the northern TP and its nearby mountains, including the Pamir Plateau, the Tianshan Mountain, the Kunlun Mountain, the Altun Mountain, the Qilian Mountain, the Altai Mountains, and the Sayan Mountains (Figure 1). In order to close the dust emissions in HM and LM, the land cover types of the Taklamakan Desert, Gurbantunggut Desert, and Gobi Desert are replaced with nearby vegetation types.

2.3. Observation Data. Three datasets are used in this study for comparison with the RegCM4.1/Dust simulated results. The first is monthly mean surface air temperature and precipitation data, with a high resolution of $0.5^\circ \times 0.5^\circ$, provided by the Climate Research Unit (CRU), University of East Anglia [52]. The second is the NCEP-DOE reanalysis

($2.5^\circ \times 2.5^\circ$) wind fields at 850 hPa [48]. The third is the Multiangle Imaging Spectroradiometer (MISR) aboard the NASA Earth Observation System's Terra satellite Level 3 monthly mean aerosol optical depth (AOD) from 2000 to 2009.

3. Validation

Spring and summer are not only the seasons of strong dust emissions in East Asia but also the seasons of Asian monsoon onset and prevalence. So, model performance during this period directly affects the predication of dust climatic effects. The comparison between the CRU observed and HMD simulated surface temperature in spring and summer is illustrated in Figure 2. Both spring and summer surface temperatures simulated by HMD are consistent with those of CRU observation. In spring, the model successfully captures the major patterns of surface temperature distribution, including a reasonable northwest-southeast gradient, minimum temperature center in the TP and Mongolia, and maximum temperature center in south China and north India. However, it simulates a cold bias of 1–3°C in northwest China (Figures 2(a) and 2(b)). The simulation is better in summer than in spring, and the maximum temperature center in the Thar Desert located in northwest India is well captured compared with the observation (Figures 2(c) and 2(d)). Our simulation only includes dust aerosol, and there are other kinds of aerosols in the atmosphere. However, the CRU observation includes comprehensive effects of all aerosols (dust, black carbon, organic carbon, sulphate, and sea salt). Sandstorm mainly outbreaks in spring in northwestern China, so the cold bias in northwest China is from the dust cooling effect. Meanwhile, dust storm activities decrease in summer, and the cold bias weakens in summer. Therefore, the simulation is better in summer than in spring.

The comparison between observed and simulated 850 hPa wind and precipitation in spring and summer is illustrated in Figure 3. Southeasterly winds and southwest wind prevail in south China and to the south of the TP in spring, respectively. The region to the north of the Yangtze

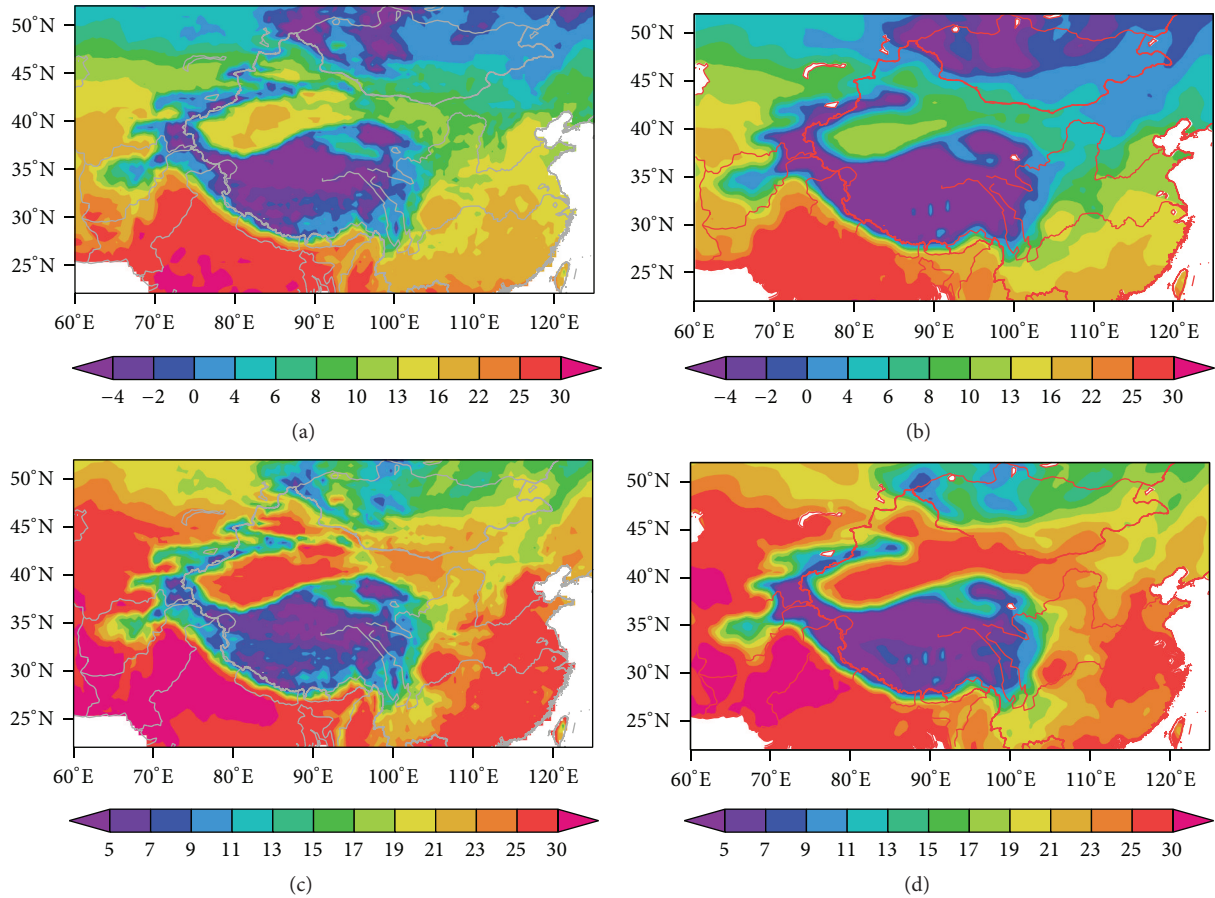


FIGURE 2: Observed (a, c) and simulated (b, d) surface mean temperature (units: °C) in spring (a, b) and summer (c, d).

river is affected by strong northwest wind (Figure 3(a)). In summer, northwest wind weakens in north China, and the southerly wind is enhanced in south China, accompanied by the outbreak of the East Asia summer monsoon. The southerly wind is divided into two branches: one moves across the southeast coast of China and eventually enters the East China Sea, while the other continues to north, passing over central China, and then changes into a southwesterly wind before entering into north and northeast China (Figure 3(c)). Compared with the NCEP observation, RegCM4.1/Dust basically captures the above major features of 850 hPa wind during spring and summer (Figures 3(b) and 3(d)).

RegCM4.1/Dust also captures well the characteristics of the precipitation distribution in East Asia. In spring, the maximum center of precipitation is mainly located in south China, the southeast of the Himalaya Mountains, and the Pamirs Plateau (Figure 3(a)). The precipitation rate is less than 1.5 mm day^{-1} over the TP, northern India, and the areas to the north of the Yangtze river. The model results are consistent with the above precipitation distribution, albeit an overestimation of precipitation is apparent in the Pamirs Plateau, Tianshan Mountains, and southeast Himalaya Mountains, and an underestimation in southeast China (Figure 3(b)). The simulation of summer precipitation

is better than that in spring, in which there is a slight overestimation in the Tianshan Mountains, northern TP, and south China (Figure 3(b)). The terrain of the TP is quite complicated, and the cumulus convection parameterization applied in this extremely complex area has high sensitivity [53]. Therefore, the overestimated precipitation over the TP and its nearby mountains comes from the cumulus parameterization scheme chosen in RegCM4.1/Dust, namely, the Grell scheme with Fritsch-Chappell closure. On the other hand, the bias in south China mainly relates to the model physics scheme applied in this area: for example, the Grell mass flux scheme may be more suitable for the midlatitudes rather than tropical and subtropical areas of China [54].

The rainy season in East Asia usually starts from late spring to summer under the influences of the East Asia summer monsoon and the Indian monsoon. The RegCM4.1 simulated precipitation seasonal variation is well consistent with those of CRU observed in northern and southern China, which indicates that our simulation is reliable (Figure 4).

The distribution of MISR-observed aerosol AOD and model-simulated dust AOD is illustrated in Figure 5. The comparison shows that the patterns of model-simulated dust AOD are consistent with those of the MISR observation in spring and summer. The model successfully captures the maximum center of dust AOD in the Taklamakan Desert in

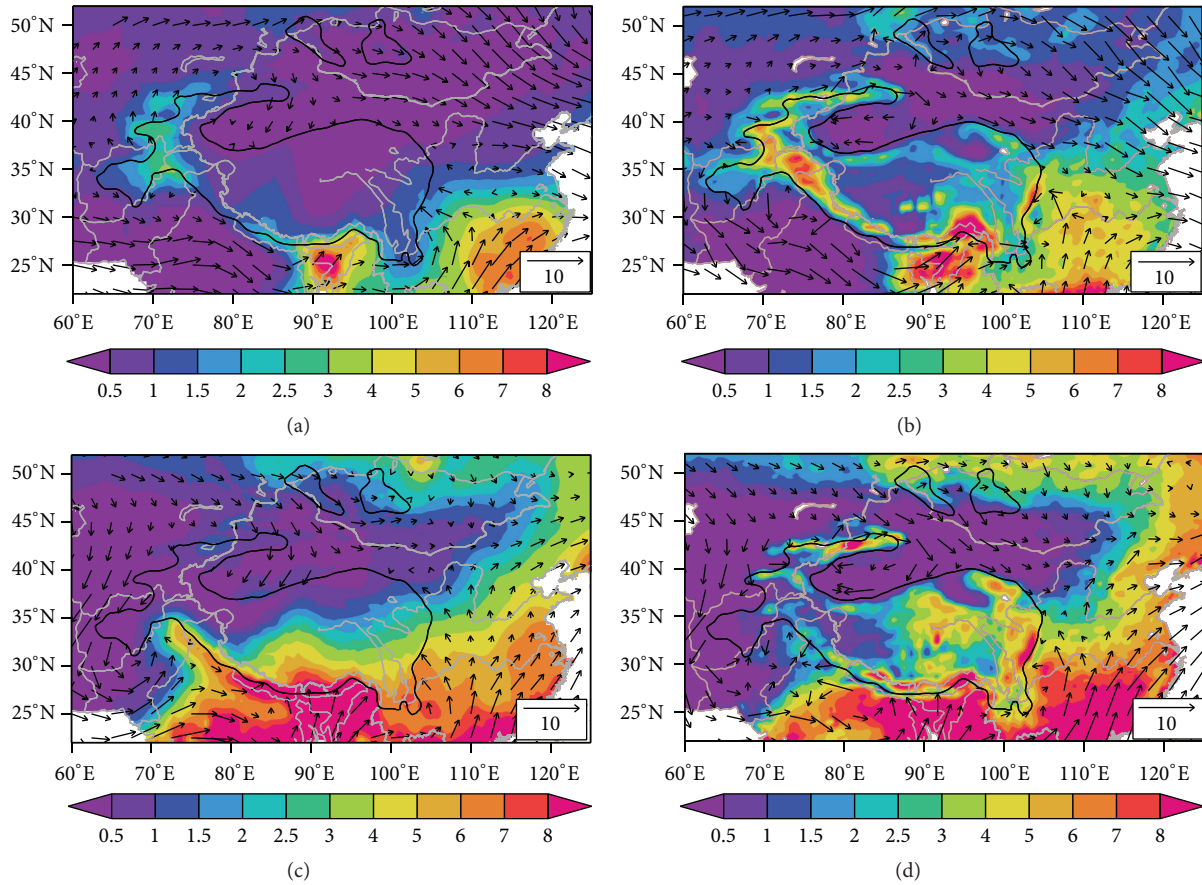


FIGURE 3: Observed (a, c) and simulated (b, d) mean precipitation rate (units: mm day^{-1}) and 850 hPa wind (units: m s^{-1}) in spring (a, b) and summer (c, d). The black lines are the terrain contours of 2000 m.

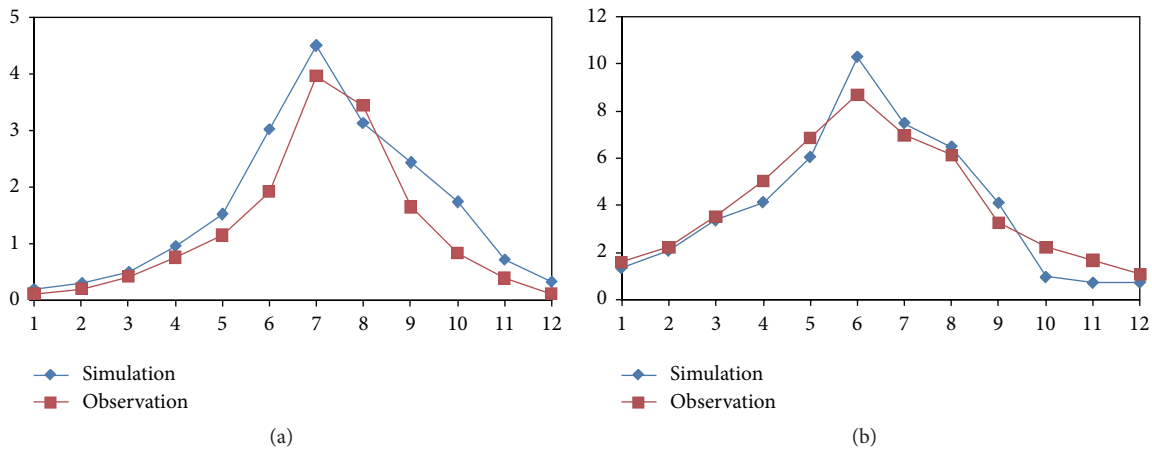


FIGURE 4: Comparison between RegCM4.1 simulated and CRU observed annual cycles of monthly precipitation (mm/day) regional averaged for the north China (a) ($38^{\circ}\text{--}42^{\circ}\text{N}$, $110^{\circ}\text{--}120^{\circ}\text{E}$) and south China ($25^{\circ}\text{--}30^{\circ}\text{N}$, $110^{\circ}\text{--}115^{\circ}\text{E}$).

spring and summer. However, it overestimates the dust AOD in the Gobi and Gurbantunggut Desert. The simulation of dust AOD in summer is better than that in spring. It should be noted that only dust aerosol is featured in our experiment, so the heavy MISR AOD in eastern and southwest China (left panels in Figure 5) is not consistent with the model

simulation. Our simulation might overestimate the AOD in the three dust source centers; the possible reason comes from the overestimation of giant aerosol ($5.0\text{--}20.0\ \mu\text{m}$) and the uncertainty in characterizing soil property. Meanwhile, the model does not describe the presence of additional aerosol types as well as background aerosols; this may also be

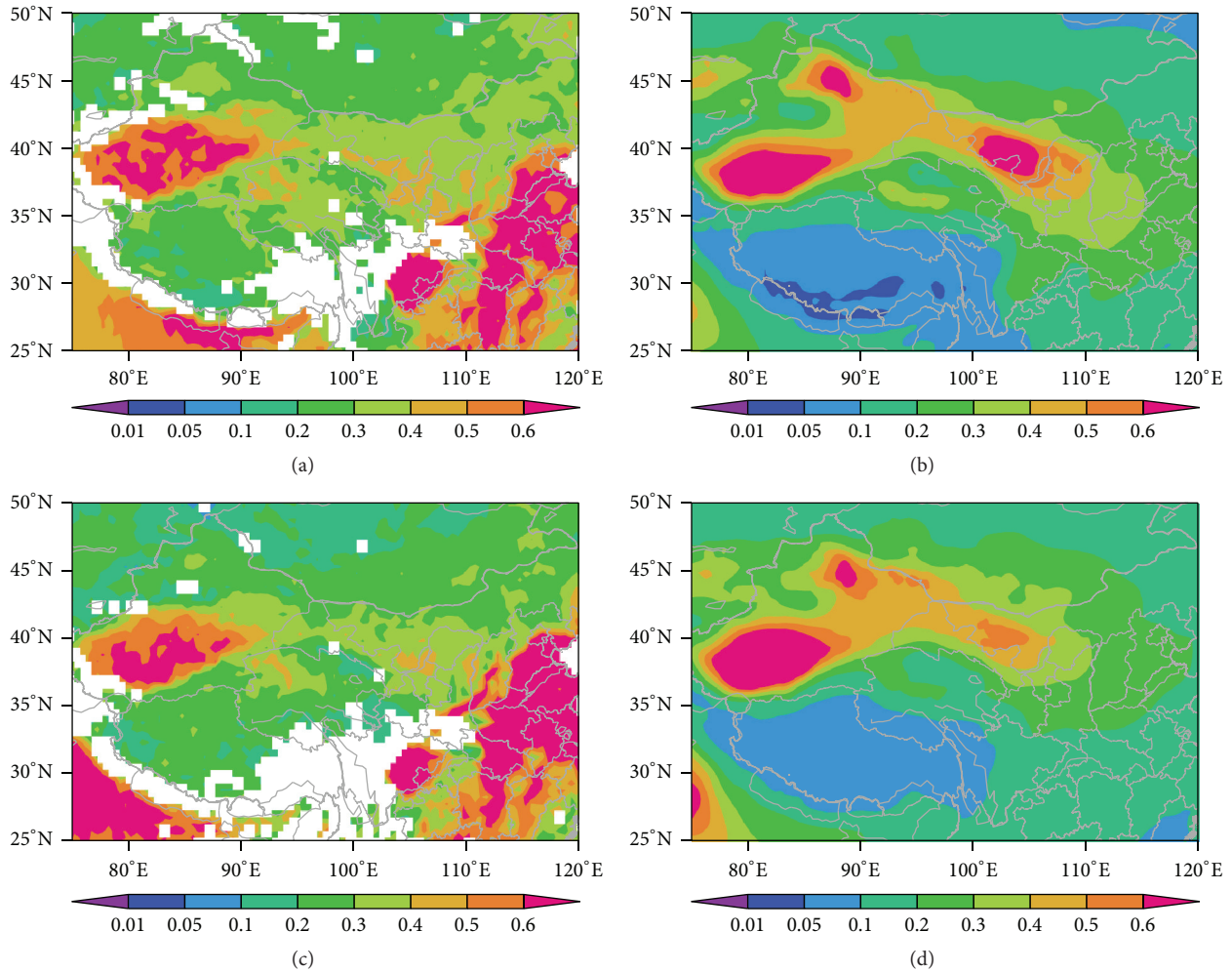


FIGURE 5: MISR-observed aerosol optical depth (a, c) and simulated dust AOD (b, d) averaged in spring (a, b) and summer (c, d) during 2000–2009.

an indication of relatively weak long range dispersal of dust plume by the model [14]. Besides, Sun et al. [15] have detailed and compared the same model (RegCM4) simulated results of control run with various observations on the regional scale of Asia and found that the performance of RegCM4 is basically good. Overall, the control simulated result is reasonable when compared with observations or other model results.

4. Results and Analyses

4.1. Impacts of Topography on the Distribution of Dust in East Asia. The uplifting of the northern TP and its nearby major mountains significantly influences the distribution of dust in East Asia. The dust mixing ratio at 600 hPa is higher in the Taklamakan and Gobi Desert in spring than in summer in HMD – HM, with their center values greater than $150 \mu\text{g kg}^{-1}$ (Figure 6(a)). In summer, the dust mixing ratio is relatively lower than that in spring over the two deserts (Figure 6(b)). However, in LMD – LM, the dust mixing ratio is lower in the above two deserts in both spring and summer

(Figures 6(c) and 6(d)). Besides, uplift of the northern TP causes the dust mixing ratio to increase greatly in the northern TP (Figure 6(e)), and this enhancement is discussed further, in detail, below. The dust mixing ratio only increases markedly in the Taklamakan Desert in summer between HMD – HM and LMD – LM (Figure 6(f)).

The seasonal variation of the regional mean dust column burden averaged in the Taklamakan Desert in the four different experiments is illustrated in Figure 7. The dust source has an important effect on the maintenance of the dust cycle in East Asia. Both HMD and LMD capture the highest dust emissions in spring in the Taklamakan Desert, but the experiments with an absence of deserts all missed this feature. Besides, it is interesting to note that the differences between HMD and HM are greater than the differences between LMD and LM in summer (Figure 7(a)). The formation of cyclonic circulation in the Tarim Basin, induced by uplifting of the northern TP and its nearby major mountains, may be a reason for the higher dust production there in summer. This is discussed further in Section 4.3.

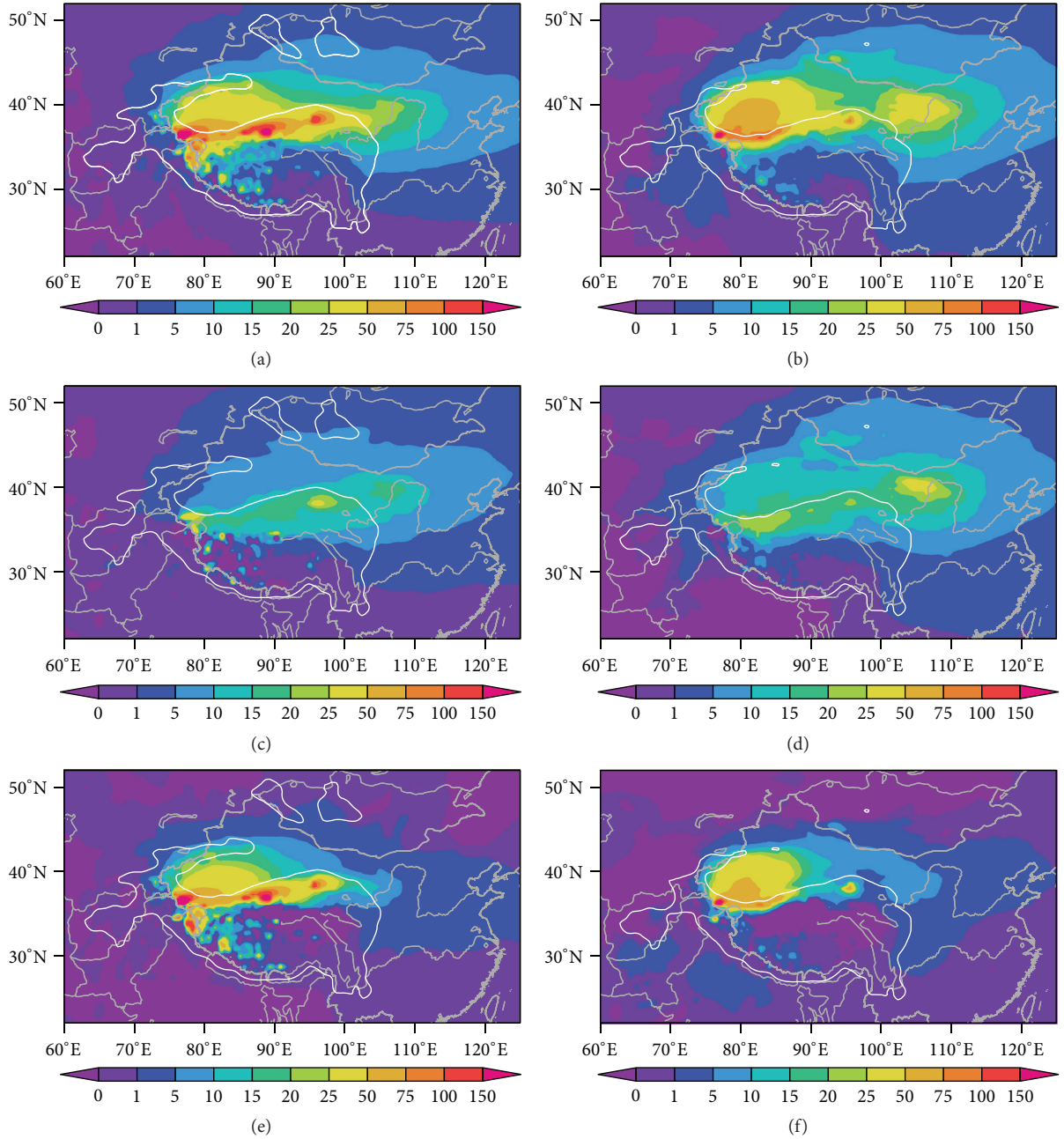


FIGURE 6: Dust mixing ratio changes at 600 hPa ($\mu\text{g kg}^{-1}$) between different numerical experiments in spring (a, c, e) and summer (b, d, f): (a, b) HMD – HM; (c, d) LMD – LM; (e, f) (HMD – HM) minus (LMD – LM).

As mentioned, Figure 6 shows that the topography also significantly influences the dust distribution in the TP in spring. Therefore, we further analyzed the differences in the dust vertical profile between the different experiments, as shown in Figure 8. In HMD – HM (Figure 8(a)), the dust mixing ratio is highest in the western TP and the center values reach $40 \mu\text{g kg}^{-1}$. The values in the central and eastern TP range from 20 to $30 \mu\text{g kg}^{-1}$ and the dust concentration is higher between 400 hPa and the near-surface layer of the TP (Figure 8(a)). In LMD – LM, the dust concentration is lower over the TP and the dust vertical mixing is weak (Figure 8(b)).

The differences between HMD – HM and LMD – LM show that the uplifting of the northern TP and its nearby major mountains enhances the dust load over the TP (Figure 8(c)).

4.2. Dust Effects on the Heat Source over the TP Modulated by Topography. The differences in dust load between HMD and HM are greater than those between LMD and LM over the TP (Figure 8), and dust can directly modify atmosphere-earth radiation [55, 56]. Therefore, the dust effects on the heat source over the TP may differ in the high- and low-mountain experiments. We use 600 hPa atmospheric temperature to

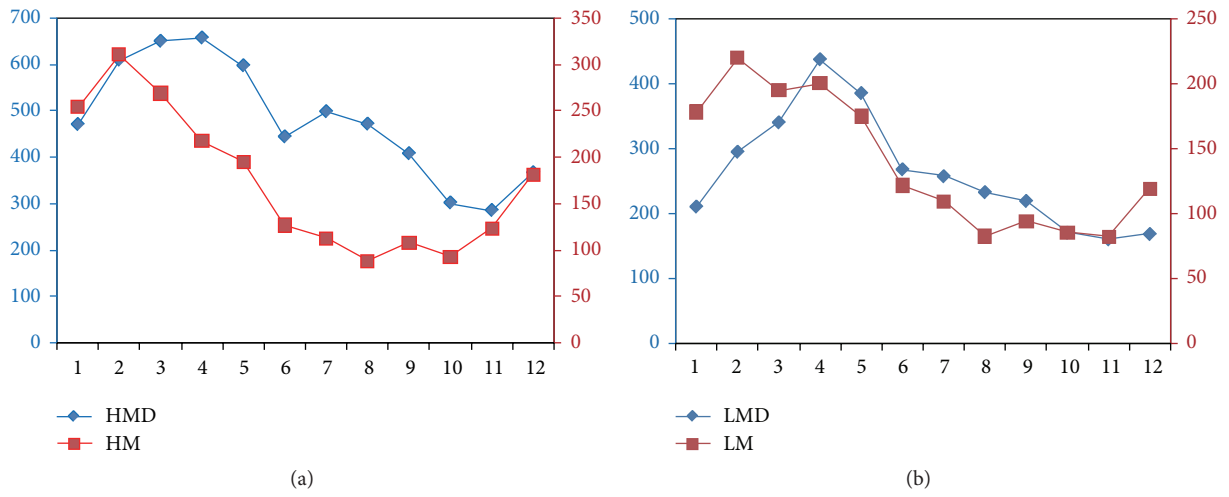


FIGURE 7: Annual cycles of monthly dust column burden (mg m^{-2}) regionally averaged for the Taklamakan Desert ($37^{\circ}\text{--}42^{\circ}\text{N}$, $78^{\circ}\text{--}87^{\circ}\text{E}$) in (a) HMD and HM and (b) LMD and LM.

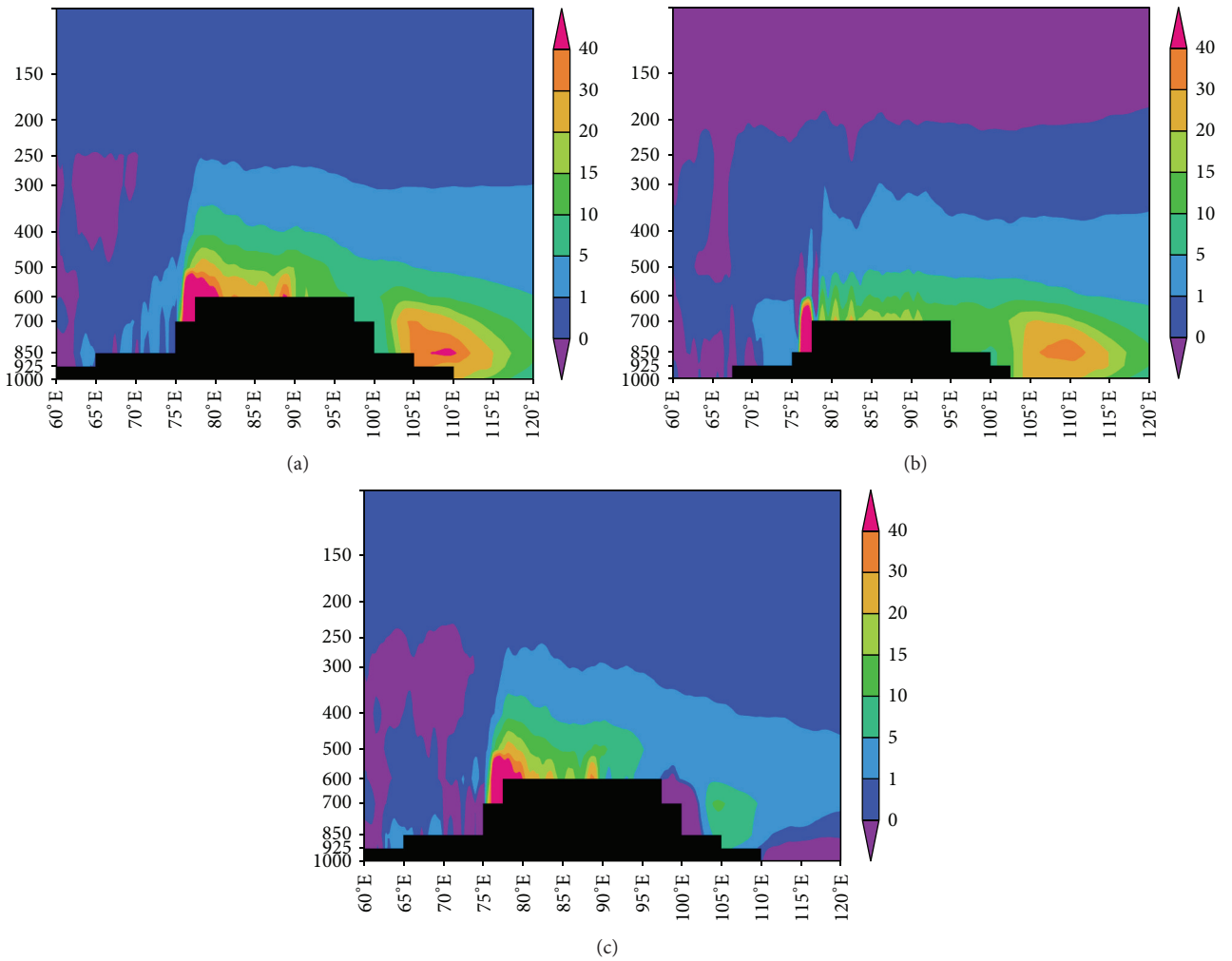


FIGURE 8: Longitude-height ($32^{\circ}\text{--}37^{\circ}\text{N}$) DMR ($\mu\text{g kg}^{-1}$) changes between different experiments in spring: (a) HMD – HM; (b) LMD – LM; (c) HMD – HM minus LMD – LM.

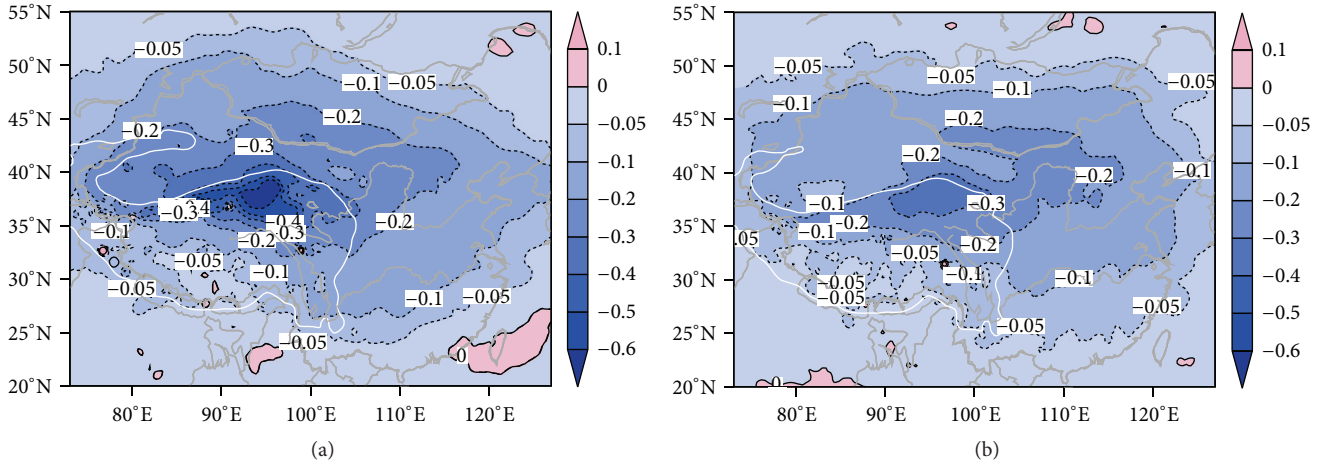


FIGURE 9: Atmospheric temperature changes at 600 hPa over the TP in spring (units: °C) between different numerical experiments: (a) HMD – HM; (b) LMD – LM.

simply represent the heat source over the TP, following Liu and Wang [57].

The heat source over the TP substantially decreases in the northern TP due to the high dust load between HMD and HM (Figure 9(a)), in which the decrease can exceed 0.6°C. It also decreases between LMD and LM, but the reduction is not significant compared with that between HMD and HM due to the low dust load (Figure 9(b)).

We further analyzed the variation in the heat source over the northern TP (hereafter NTP-HT) during the period of East Asia summer monsoon onset (Figure 10). The NTP-HT greatly decreases due to dust from the 27th to the 48th pentad in both the high- and low-mountain experiments, but the decreasing effect on the NTP-HT in HMD – HM is quite a lot stronger than those in LMD – LM due to the high dust content over the TP with the uplift of the northern TP.

4.3. Dust Effects on the East Asia Summer Monsoon and Its Onset Modulated by Topography. In HMD, north and south China are affected by westerly and southwesterly winds, respectively, and there is strong cyclonic circulation in the Tarim Basin (Figure 11(a)). Without the major deserts of northwest China, the cyclonic circulation and northwesterly winds weaken (Figure 11(b)). In HMD – HM, dust weakens the East Asia summer monsoon and causes strong cyclonic circulation over the Tarim Basin. Therefore, dust emissions are still stronger in summer over the Taklamakan Desert due to the strong updraft induced by the cyclonic activity (Figures 6(e) and 7(a)). Both LMD and LM capture the major features of the East Asia summer monsoon (Figures 11(b) and 11(d)), but there is no cyclonic circulation over the Tarim Basin. Therefore, the dust concentration is lower over the Taklamakan Desert (Figure 7(b)). Both the high- and low-mountain experiments show that dust weakens the East Asia summer monsoon, which is in agreement with previous studies [15, 58].

Because of the close relationship between the heat source of the TP and East Asia summer monsoon onset, we analyzed

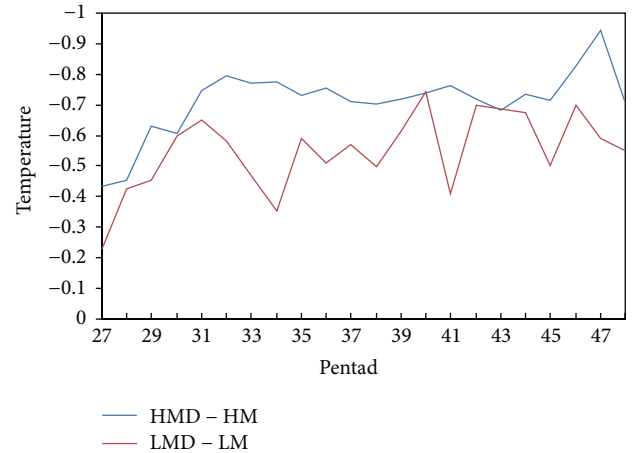


FIGURE 10: Regional mean atmospheric temperature (°C) change at 600 hPa averaged in the northern TP (34°–38°E, 90°–105°N).

the dust effects on East Asia summer monsoon onset under the high- and low-mountain settings. The index of East Asia summer monsoon onset that we used followed the definition of Wang and Ho [59], as follows:

$$RR_i = R_i - R_{JAN}, \quad i = 1, 2, \dots, 73, \quad (2)$$

where RR_i is the relative pentad mean rainfall rate. In the Northern Hemisphere, R_i is the pentad mean rainfall rate and R_{JAN} is the pentad mean rainfall rate of January. If RR_i is greater than 6 mm day^{-1} , then the onset of the East Asia summer monsoon begins. Pentad is five days, and there are 6 pentads in one month.

Following Liu and Yin [60], we chose two key monsoon regions of East Asia: a southern monsoon region (22°–30°N, 105°–120°E) and northern monsoon region (34°–42°N, 105°–120°E). Figure 12 shows the variation in East Asia summer monsoon onset index averaged in the southern monsoon region. Onset of the East Asia summer monsoon begins in

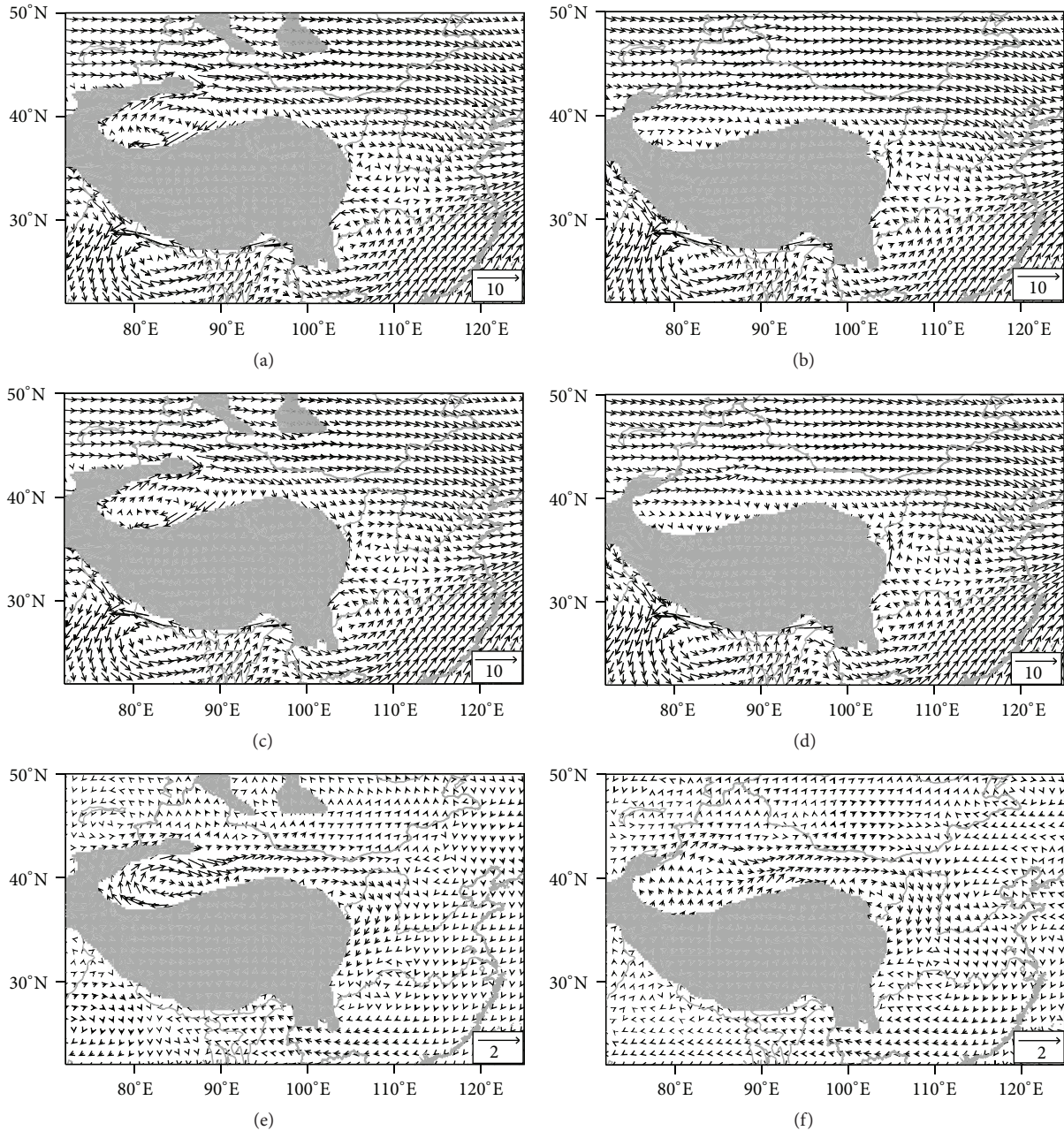


FIGURE 11: 700 hPa wind field averaged in summer (June to August) in (a) HMD, (b) HM, (c) LMD, (d) LM, (e) HMD–HM, and (f) LMD–LM. The grey area represents the topography below 700 hPa.

the 29th pentad in HM but is two pentads later in HMD. The onset of the East Asia summer monsoon begins in the 31st pentad in LM but in the 32nd in LMD. The results demonstrate that dust can delay the onset of the East Asia summer monsoon, but the delaying effect of dust in HMD – HM is stronger than that in LMD – LM.

The dust effect on East Asia summer monsoon onset in the northern monsoon region is illustrated in Figure 13. The onset of the East Asia summer monsoon in this region starts in the 36th pentad in both HM and LM, while dust delays the monsoon onset by one pentad in both HMD and LMD compared with HM and LM. The sensitivity of

the dust-induced East Asia summer monsoon onset anomalies to the topography change in the northern monsoon region is lower than that in the southern monsoon region.

4.4. Impacts of the Effects of Dust on Precipitation Induced by Topography Changes. The regional monthly mean of precipitation averaged in north and south China in the four experiments is illustrated in Figure 14. Dust hinders precipitation over north and south China due to the delaying effect of dust on the onset of monsoon in both the high- and low-mountain experiments. The suppression effects in HMD – HM are much stronger than in LMD – LM in

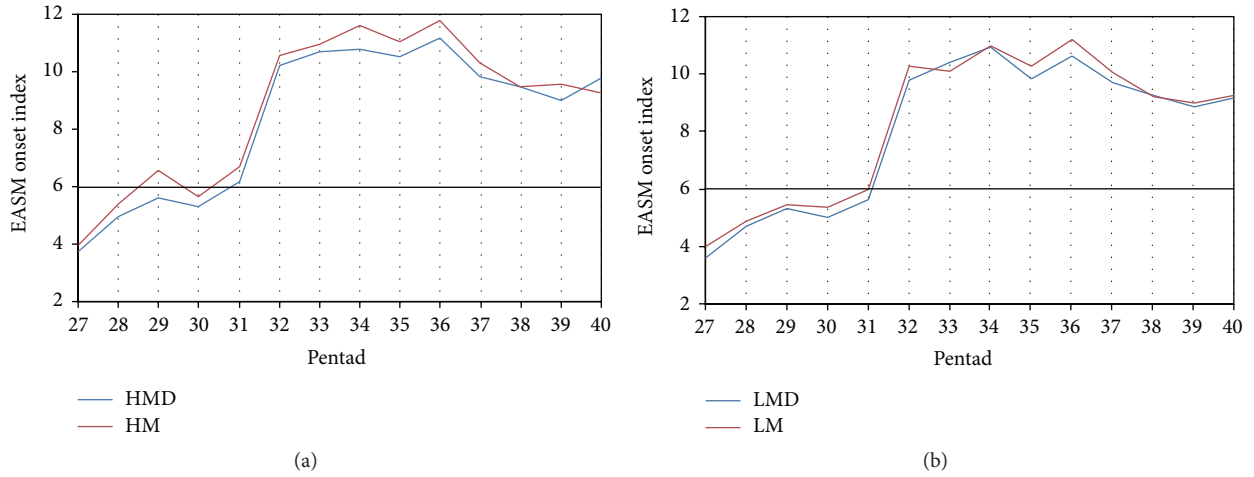


FIGURE 12: East Asia summer monsoon onset index averaged in the southern monsoon region (22° – 30° N, 105° – 120° E) in (a) HMD and HM and (b) LMD and LM.

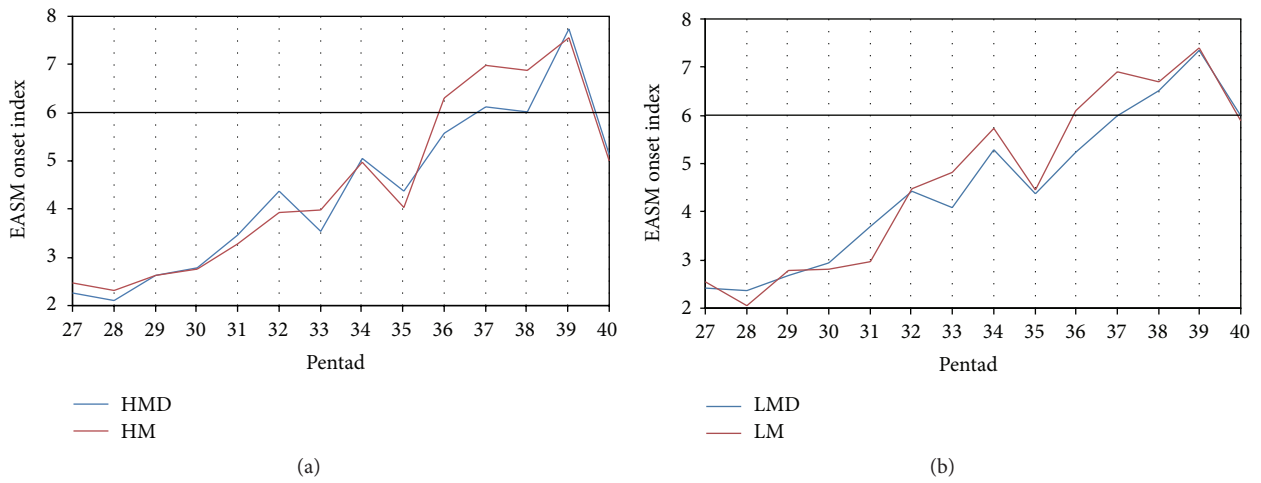


FIGURE 13: As in Figure 10 but for the northern monsoon region (34° – 42° N, 105° – 120° E).

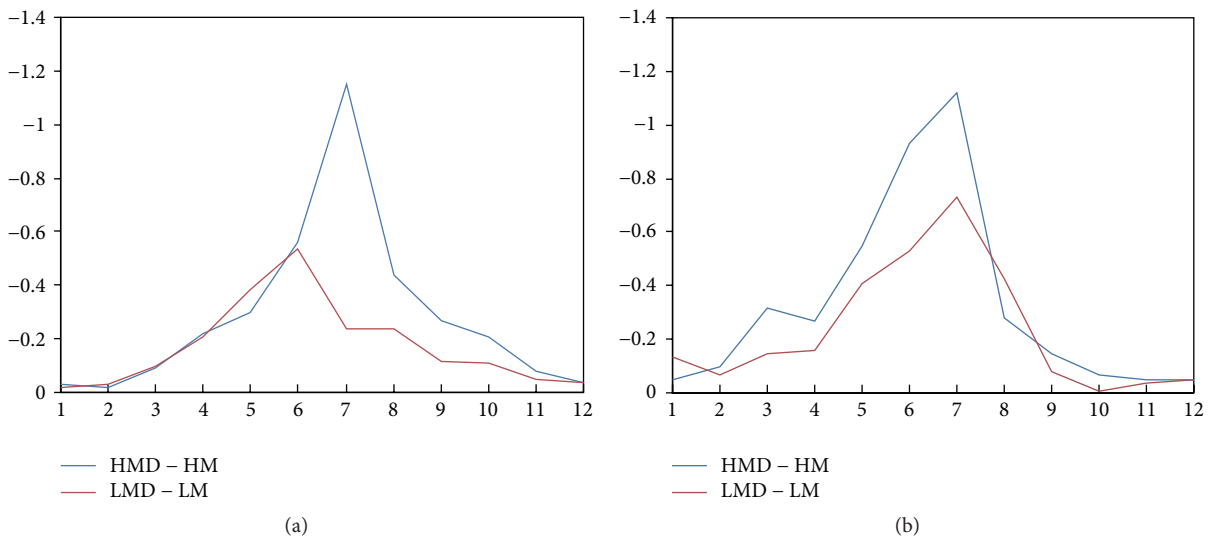


FIGURE 14: Regional mean precipitation rate (mm day^{-1}) averaged in the rainy season (May to August) in north China (a) (38° – 42° N, 110° – 120° E) and south China (25° – 30° N, 110° – 115° E) in the four different experiments.

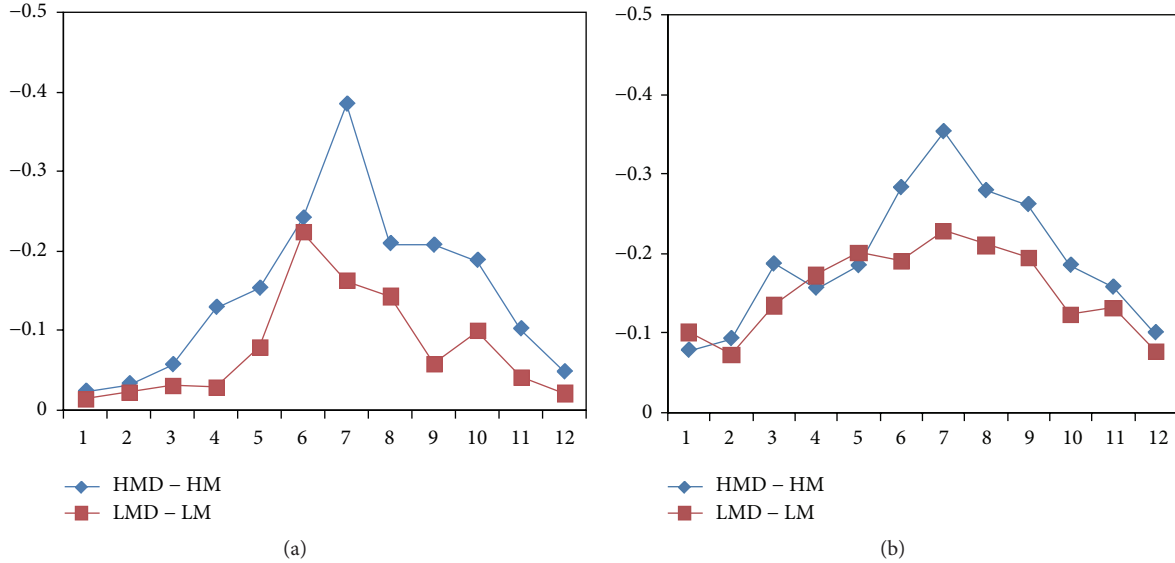


FIGURE 15: Regional mean water vapor mixing ratio (g kg^{-1}) at 850 hPa averaged in the rainy season (May to August) in north China (a) ($38^{\circ}\text{--}42^{\circ}\text{N}$, $110^{\circ}\text{--}120^{\circ}\text{E}$) and south China ($25^{\circ}\text{--}30^{\circ}\text{N}$, $110^{\circ}\text{--}115^{\circ}\text{E}$) in the four different experiments.

both north and south China. The differences in precipitation in north China are substantially in July in HMD – HM, while for south China the differences are markedly from spring to summer (March to July). The influences of dust on the precipitation induced by the modified topography in south China are stronger than those in north China, because the delaying effects on the onset of the East Asia summer monsoon in south China are stronger than those in north China.

Our simulation did not include the dust indirect effect, but it is interesting to note that the previous research demonstrated that the indirect effect of aerosols from central eastern China also reduces Asian monsoon strength and precipitation [58]. The main reason for the reduction of the precipitation in East Asia is that dust cooling effect created cyclone-anticyclone-cyclone flow pattern emanating from the dust source region to the East China Sea and weakened the East Asia summer monsoon [15]. Besides, we analyzed the water vapor mixing ratio and found that the change characteristic of water mixing ratio in the above two regions also decreased (Figure 15). The reduction of the water vapor mixing ratio induced by dust between the modern terrain experiments is more than that between the low terrain experiments, which is consistent with the changes in precipitation.

5. Discussion and Conclusions

In this study, the latest version of RegCM4.1/Dust was used to study how the northern TP and its nearby major mountains modulate the dust distribution in East Asia. The dust effects on the heat source over the TP and, ultimately, the related onset of the East Asia summer monsoon under different terrain settings were then analyzed. The simulations showed that the dust load in northwest China during spring increases

greatly in the Taklamakan Desert in HMD – HM compared to LMD – LM. The increase can exceed $150 \mu\text{g kg}^{-1}$ in spring. Interestingly, the dust concentration is higher in the Taklamakan Desert during summer in HMD–HM compared to LMD – LM. The formation of cyclonic circulation in summer, induced by the uplifting of the northern TP and its nearby major mountains, is the reason for this higher dust production in the Taklamakan Desert (Figure 11(e)). Due to the absence of uplifting of the northern TP and its nearby major mountains, there is no mechanism for dust emission in summer over the Tarim Basin (Figure 11(f)). Additionally, the dust loading over the TP is sensitive to the northern TP changes. It is higher in HMD – HM and lower in LMD – LM, over the TP.

The uplift of the northern TP causes the dust loading over the TP to increase, and dust cooling effect causes the radiation absorbed by the TP to reduce. Therefore, dust aerosol causes the heat source over the TP to decrease in both the high- and low-mountain experiments. The reduction in HMD – HM is much larger than in LMD – LM, reaching -0.6°C in the northern TP. Due to the weakening of the heat source over the TP induced by dust, the onset of the East Asia summer monsoon is delayed in both the high- and low-mountain experiments. The effect of dust on East Asia summer monsoon onset is stronger in HMD – HM than in LMD – LM. Dust delays the onset of the East Asia summer monsoon over the northern and southern monsoon region in East Asia by two pentads and one pentad, respectively, in HMD – HM, while in LMD – LM the delay is one pentad in both the northern and southern monsoon region. It also weakens the East Asia summer monsoon in both the high- and low-mountain experiments, which is consistent with previous research [15, 58].

Furthermore, dust suppresses precipitation in both the high- and low-mountain experiments, but the suppression

effects are stronger in HMD – HM than in LMD – LM. In north China, the suppression effect is markedly in July in HMD – HM, while in south China it is markedly from March to July. The dust effects on precipitation in south China are more sensitive to the topography change than in north China.

Most previous studies have focused on the dust cycle and its radiative effects on temperature, precipitation, and the East Asia summer monsoon. A recent modeling work using RegCM4.1/Dust studied the relationships among topography, inland deserts, and regional climate evolution in East Asia and found that the topography is closely related to dust change in East Asia [33]. Besides, to date, simulation work using high-resolution regional climate modeling, in the context of dust effects on the heat source over the TP and its effect on East Asia summer monsoon onset, is rare. Dust can influence the climate through direct and indirect effects, and the uplift of the TP is proved to have great effects on the global and regional climate [31]. However, most previous researches only focus on one of the above two factors. On the one hand, this study helps to figure out combined effects of dust and the TP uplifting on the East Asia summer climate, while, on the other hand, it has a certain referential significance for the quantification of the topography-modulated dust distribution and its effects on the onset of the East Asia summer monsoon, as well as understanding the aeolian dust effects on the East Asian climate.

However, the analysis about the interactions between dust aerosols and meteorological factors in the simulation has some deficiencies. First, RegCM4.1/Dust only includes the direct radiative effect of dust aerosol. Thus, we acknowledge that these preliminary results on the effects of dust on the heat source over the TP and the related onset of the East Asia summer monsoon are uncertain. The findings need to be evaluated using models that include both direct and indirect dust effects. Second, dust effects are sensitive to aerosol optical properties assumed in the model, and the value of single scattering albedo in Asia desert is still uncertain [61]. The results in this study also need to be validated by sensitivity experiments with different aerosol properties. Third, the simulation only includes dust aerosol, but there are other kinds of aerosols in the atmosphere. Accordingly, we plan to carry out experiments with all major types of aerosols in the future to further evaluate the results. Finally, the uncertainty from the model cumulus parameterization schemes should also be considered in future work.

Conflict of Interests

The authors declare that there is no conflict of interests regarding the publication of this paper.

Acknowledgments

The authors thank the anonymous reviewers for their constructive comments and suggestions to improve the paper. This work was jointly supported by the Strategic Priority Research Program of the Chinese Academy of Sciences (XDB03020601), the National Science Foundation of China

(41572150, 41405093), the CAS/SAFEA International Partnership Program for Creative Research Teams (KZZD-EW-TZ-03), and the West Light Foundation of the Chinese Academy of Sciences.

References

- [1] T. L. Zhao, S. L. Gong, X. Y. Zhang, A. Abdel-Mawgoud, and Y. P. Shao, "An assessment of dust emission schemes in modeling east Asian dust storms," *Journal of Geophysical Research: Atmospheres*, vol. 111, no. 5, Article ID D05S90, 2006.
- [2] R. A. VanCuren, "Asian aerosols in North America: extracting the chemical composition and mass concentration of the Asian continental aerosol plume from long-term aerosol records in the western United States," *Journal of Geophysical Research*, vol. 108, article 4623, 2003.
- [3] K. W. Kim, Y. J. Kim, and S. J. Oh, "Visibility impairment during Yellow Sand periods in the urban atmosphere of Kwangju, Korea," *Atmospheric Environment*, vol. 35, no. 30, pp. 5157–5167, 2001.
- [4] N. M. Mahowald, S. Engelstaedter, C. Luo et al., "Atmospheric iron deposition: global distribution, variability, and human perturbations," *Annual Review of Marine Science*, vol. 1, pp. 245–278, 2009.
- [5] R. Duce, P. S. Liss, J. T. Merrill, E. L. Atlas, and P. Buat-Menard, "The atmospheric input of trace species to the world ocean," *Global Biogeochemical Cycles*, vol. 5, no. 3, pp. 193–259, 1991.
- [6] I. Tegen and A. A. Lacis, "Modeling of particle size distribution and its influence on the radiative properties of mineral dust aerosol," *Journal of Geophysical Research: Atmospheres*, vol. 101, no. 14, pp. 19237–19244, 1996.
- [7] R. L. Miller, I. Tegen, and J. Perlwitz, "Surface radiative forcing by soil dust aerosols and the hydrologic cycle," *Journal of Geophysical Research D: Atmospheres*, vol. 109, no. 4, pp. D04203–24, 2004.
- [8] D. Rosenfeld, "Suppression of rain and snow by urban and industrial air pollution," *Science*, vol. 287, no. 5459, pp. 1793–1796, 2000.
- [9] Y. P. Shao, Y. Yang, J. J. Wang et al., "Northeast Asian dust storms: real-time numerical prediction and validation," *Journal of Geophysical Research*, vol. 108, article 4691, 2003.
- [10] I. Uno, S. Satake, G. R. Carmichael et al., "Numerical study of Asian dust transport during the springtime of 2001 simulated with the Chemical Weather Forecasting System (CFORS) model," *Journal of Geophysical Research D: Atmospheres*, vol. 109, no. 19, Article ID D19S24, 2004.
- [11] S. L. Gong and X. Y. Zhang, "CUACE/Dust—an integrated system of observation and modeling systems for operational dust forecasting in Asia," *Atmospheric Chemistry and Physics*, vol. 8, no. 9, pp. 2333–2340, 2008.
- [12] J. H. Sun and L. N. Zhao, "Numerical simulation of two East Asian dust storms in spring 2006," *Earth Surface Processes and Landforms*, vol. 33, no. 12, pp. 1892–1911, 2008.
- [13] C. H. Zhou, S. L. Gong, X. Y. Zhang et al., "Development and evaluation of an operational SDS forecasting system for East Asia: CUACE/Dust," *Atmospheric Chemistry and Physics*, vol. 8, no. 4, pp. 787–798, 2008.
- [14] D. F. Zhang, A. S. Zakey, X. J. Gao, F. Giorgi, and F. Solmon, "Simulation of dust aerosol and its regional feedbacks over East Asia using a regional climate model," *Atmospheric Chemistry and Physics*, vol. 9, no. 4, pp. 1095–1110, 2009.

- [15] H. Sun, Z. Pan, and X. Liu, "Numerical simulation of spatial-temporal distribution of dust aerosol and its direct radiative effects on East Asian climate," *Journal of Geophysical Research: Atmospheres*, vol. 117, no. 13, Article ID D13206, 2012.
- [16] S. Y. Chen, C. Zhao, Y. Qian et al., "Regional modeling of dust mass balance and radiative forcing over East Asia using WRF-Chem," *Aeolian Research*, vol. 15, pp. 15–30, 2014.
- [17] Q. Mu and H. Liao, "Simulation of the interannual variations of aerosols in China: role of variations in meteorological parameters," *Atmospheric Chemistry and Physics*, vol. 14, no. 18, pp. 9597–9612, 2014.
- [18] Z. G. Shi and X. D. Liu, "Distinguishing the provenance of fine-grained eolian dust over the Chinese Loess Plateau from a modelling perspective," *Tellus B: Chemical and Physical Meteorology*, vol. 63, no. 5, pp. 959–970, 2011.
- [19] I. Uno, K. Harada, S. Satake, Y. Hara, and Z. Wang, "Meteorological characteristics and dust distribution of the Tarim Basin simulated by the nesting RAMS/CFORS dust model," *Journal of the Meteorological Society of Japan A*, vol. 83, no. 3, pp. 219–239, 2005.
- [20] X. K. Xu and H. Chen, "Influence of vegetations and snow cover on sand-dust events in the west of China," *Chinese Science Bulletin*, vol. 51, no. 3, pp. 331–340, 2006.
- [21] W. Chen, D. W. Fryear, and Z. Yang, "Dust fall in the Taklamakan desert of China," *Physical Geography*, vol. 20, no. 3, pp. 189–224, 1999.
- [22] J. Sun, M. Zhang, and T. Liu, "Spatial and temporal characteristics of dust storms in China and its surrounding regions, 1960–1999: relations to source area and climate," *Journal of Geophysical Research: Atmospheres*, vol. 106, no. 10, Article ID 2000JD900665, pp. 10325–10333, 2001.
- [23] X. Y. Zhang, R. Arimoto, and Z. S. An, "Dust emission from Chinese desert sources linked to variations in atmospheric circulation," *Journal of Geophysical Research: Atmospheres*, vol. 102, no. 23, pp. 28041–28047, 1997.
- [24] R. L. Miller and I. Tegen, "Climate response to soil dust aerosols," *Journal of Climate*, vol. 11, no. 12, pp. 3247–3267, 1998.
- [25] K. M. Shell and R. C. J. Somerville, "Direct radiative effect of mineral dust and volcanic aerosols in a simple aerosol climate model," *Journal of Geophysical Research*, vol. 112, no. 3, Article ID D03205, 2007.
- [26] J. P. Huang, Y. Minnis, Q. Tang et al., "Summer dust aerosols detected from CALIPSO over the Tibetan Plateau," *Geophysical Research Letter*, vol. 34, no. 18, Article ID L18805, 2007.
- [27] T. C. Yeh and Y. X. Gao, *Meteorology of the Qinghai-Xizang (Tibet) Plateau*, Science Press, 1979.
- [28] M. Yanai, C. Li, and Z. Song, "Seasonal heating of the Tibetan Plateau and its effects on the evolution of the Asian summer monsoon," *Journal of the Meteorological Society of Japan*, vol. 70, no. 1, pp. 319–351, 1992.
- [29] M. Yanai and G. X. Wu, "Role of the Tibetan plateau on Asia monsoon," in *The Asian Monsoon*, B. Wang, Ed., pp. 513–629, Springer, 2006.
- [30] K. M. Lau, M. K. Kim, and K. M. Kim, "Asian summer monsoon anomalies induced by aerosol direct forcing: the role of the Tibetan Plateau," *Climate Dynamics*, vol. 26, no. 7–8, pp. 855–864, 2006.
- [31] X. D. Liu and B. W. Dong, "Influence of the Tibetan Plateau uplift on the Asian monsoon-arid environment evolution," *Chinese Science Bulletin*, vol. 58, no. 34, pp. 4277–4291, 2013.
- [32] Z. G. Shi, X. D. Liu, Z. S. An, B. Q. Yi, P. Yang, and N. Mahowald, "Simulated variations of eolian dust from inner Asian deserts at the mid-Pliocene, last glacial maximum, and present day: contributions from the regional tectonic uplift and global climate change," *Climate Dynamics*, vol. 37, no. 11–12, pp. 2289–2301, 2011.
- [33] X. D. Liu, H. Sun, Y. F. Miao, B. W. Dong, and Z. Y. Yin, "Impacts of uplift of northern Tibetan Plateau and formation of Asian inland deserts on regional climate and environment," *Quaternary Science Reviews*, vol. 116, pp. 1–14, 2015.
- [34] J. S. Pal, F. Giorgi, X. Q. Bi et al., "Regional climate modeling for the developing world: the ICTP RegCM3 and RegCNET," *Bulletin of the American Meteorological Society*, vol. 88, no. 9, pp. 1395–1409, 2007.
- [35] G. A. Grell, J. Dudhia, and D. R. Stauffer, "Description of the fifth generation Penn State/NCAR Mesoscale Model (MM5)," NCAR Technical Report TN-398+STR, National Center for Atmospheric Research, Boulder, Colo, USA, 1994.
- [36] J. Kiehl, J. Hack, G. Bonan et al., "Description of the NCAR community climate model (CCM3)," Tech. Rep., National Center for Atmospheric Research, Boulder, Colo, USA, 1996.
- [37] R. E. Dickinson, A. Henderson-Sellers, and P. J. Kennedy, "Biosphere-atmosphere transfer scheme (bats) version 1e as coupled to the NCAR community climate model," NCAR Technical Report TN-387+STR, National Center for Atmospheric Research, Boulder, Colo, USA, 1993.
- [38] G. A. Grell, "Prognostic evaluation of assumptions used by cumulus parameterizations," *Monthly Weather Review*, vol. 121, no. 3, pp. 764–787, 1993.
- [39] J. S. Pal, E. E. Small, and E. A. B. Eltahir, "Simulation of regional-scale water and energy budgets: representation of subgrid cloud and precipitation processes within RegCM," *Journal of Geophysical Research: Atmospheres*, vol. 105, no. 24, pp. 29579–29594, 2000.
- [40] B. Marticorena and G. Bergametti, "Modeling the atmospheric dust cycle: 1. Design of a soil-derived dust emission scheme," *Journal of Geophysical Research*, vol. 100, no. 8, pp. 16415–16430, 1995.
- [41] S. C. Alfaro and L. Gomes, "Modeling mineral aerosol production by wind erosion: emission intensities and aerosol size distributions in source areas," *Journal of Geophysical Research: Atmospheres*, vol. 106, no. 16, Article ID 2000JD900339, pp. 18075–18084, 2001.
- [42] A. S. Zakey, F. Solmon, and F. Giorgi, "Implementation and testing of a desert dust module in a regional climate model," *Atmospheric Chemistry and Physics*, vol. 6, no. 12, pp. 4687–4704, 2006.
- [43] F. Solmon, F. Giorgi, and C. Liousse, "Aerosol modelling for regional climate studies: application to anthropogenic particles and evaluation over a European/African domain," *Tellus, Series B: Chemical and Physical Meteorology*, vol. 58, no. 1, pp. 51–72, 2006.
- [44] Y. Qian, F. Giorgi, Y. Huang, W. Chameides, and C. Luo, "Regional simulation of anthropogenic sulfur over East Asia and its sensitivity to model parameters," *Tellus B*, vol. 53, no. 2, pp. 171–191, 2001.
- [45] Y. Qian and F. Giorgi, "Interactive coupling of regional climate and sulfate aerosol models over eastern Asia," *Journal of Geophysical Research: Atmospheres*, vol. 104, no. 6, pp. 6477–6499, 1999.
- [46] F. Giorgi and W. L. Chameides, "Rainout lifetimes of highly soluble aerosols and gases as inferred from simulations with

- a general circulation model,” *Journal of Geophysical Research*, vol. 91, no. 13, pp. 14367–14376, 1986.
- [47] F. Giorgi, “Two-dimensional simulations of possible mesoscale effects of nuclear war fires. I: model description,” *Journal of Geophysical Research*, vol. 94, no. 1, pp. 1127–1144, 1989.
- [48] M. Kanamitsu, W. Ebisuzaki, J. Woollen et al., “NCEP–DOE AMIP-II reanalysis (R-2),” *Bulletin of the American Meteorological Society*, vol. 83, no. 11, pp. 1631–1643, 2002.
- [49] T. R. Loveland, B. C. Reed, J. F. Brown et al., “Development of a global land cover characteristics database and IGBP DISCover from 1km AVHRR data,” *International Journal of Remote Sensing*, vol. 21, no. 6-7, pp. 1303–1330, 2000.
- [50] USDA, *Soil Taxonomy, A Basic System of Soil Classification for Making and Interpreting Soil Surveys*, US Government Printing Office, Washington, DC, USA, 1999.
- [51] R. W. Reynolds, N. A. Rayner, T. M. Smith, D. C. Stokes, and W. Q. Wang, “An improved in situ and satellite SST analysis for climate,” *Journal of Climate*, vol. 15, no. 13, pp. 1609–1625, 2002.
- [52] T. D. Mitchell and P. D. Jones, “An improved method of constructing a database of monthly climate observations and associated high-resolution grids,” *International Journal of Climatology*, vol. 25, no. 6, pp. 693–712, 2005.
- [53] C. T. Wang and L. Yu, “Sensitivity of regional climate model to different cumulus parameterization schemes in simulation of the Tibetan Plateau climate,” *Chinese Journal of Atmospheric Sciences*, vol. 35, no. 6, pp. 1132–1144, 2011 (Chinese).
- [54] D.-F. Zhang, X.-J. Gao, L.-C. Ouyang, and W.-J. Dong, “Simulation of present climate over East Asia by a regional climate model,” *Journal of Tropical Meteorology*, vol. 14, no. 1, pp. 19–23, 2008.
- [55] I. N. Sokolik, D. M. Winker, G. Bergametti et al., “Introduction to special section: outstanding problems in quantifying the radiative impacts of mineral dust,” *Journal of Geophysical Research: Atmospheres*, vol. 106, no. 16, pp. 18015–18027, 2001.
- [56] Y. Balkanski, M. Schulz, T. Claquin, and S. Guibert, “Reevaluation of Mineral aerosol radiative forcings suggests a better agreement with satellite and AERONET data,” *Atmospheric Chemistry and Physics*, vol. 7, no. 1, pp. 81–95, 2007.
- [57] X. D. Liu and Y. Wang, “Contrasting impacts of spring thermal conditions over Tibetan Plateau on late-spring to early-summer precipitation in southeast China,” *Atmospheric Science Letters*, vol. 12, no. 3, pp. 309–315, 2011.
- [58] X. D. Liu, X. N. Xie, Z.-Y. Yin, C. H. Liu, and A. Gettelman, “A modeling study of the effects of aerosols on clouds and precipitation over East Asia,” *Theoretical and Applied Climatology*, vol. 106, no. 3-4, pp. 343–354, 2011.
- [59] B. Wang and L. Ho, “Rainy season of the Asian-Pacific summer monsoon,” *Journal of Climate*, vol. 15, no. 4, pp. 386–398, 2002.
- [60] X. Liu and Z.-Y. Yin, “Sensitivity of East Asian monsoon climate to the Tibetan Plateau,” *Palaeogeography, Palaeoclimatology, Palaeoecology*, vol. 183, no. 3-4, pp. 223–245, 2002.
- [61] H. Sun and X. D. Liu, “Numerical simulation of the direct radiative effects of dust aerosol on the East Asian winter monsoon,” *Advances in Meteorology*, vol. 2015, Article ID 142617, 15 pages, 2015.

Research Article

Universal Power Law for Relationship between Rainfall Kinetic Energy and Rainfall Intensity

Seung Sook Shin,¹ Sang Deog Park,² and Byoung Koo Choi³

¹Disaster Prevention Research Institute, Gangneung-Wonju National University, Gangneung 210-702, Republic of Korea

²Department of Civil Engineering, Gangneung-Wonju National University, Gangneung 210-702, Republic of Korea

³Department of Forest Environment Protection, Kangwon National University, Chuncheon 200-701, Republic of Korea

Correspondence should be addressed to Byoung Koo Choi; bkchoi@kangwon.ac.kr

Received 5 February 2015; Revised 24 May 2015; Accepted 28 May 2015

Academic Editor: Hongming He

Copyright © 2016 Seung Sook Shin et al. This is an open access article distributed under the Creative Commons Attribution License, which permits unrestricted use, distribution, and reproduction in any medium, provided the original work is properly cited.

Rainfall kinetic energy has been linked to linear, exponential, logarithmic, and power-law functions using rainfall intensity as an independent variable. The power law is the most suitable mathematical expression used to relate rainfall kinetic energy and rainfall intensity. In evaluating the rainfall kinetic energy, the empirical power laws have shown a larger deviation than other functions. In this study, universal power law between rainfall kinetic energy and rainfall intensity was proposed based on the rainfall power theory under an ideal assumption that drop-size is uniformly distributed in constant rainfall intensity. An exponent of the proposed power law was 11/9 and coefficient was estimated at 10.3 from the empirical equations of the existing power-law relation. The rainfall kinetic energy calculated by universal power law showed >95% concordance rate in comparison to the average values calculated from exponential and logarithmic functions used in soil erosion model such as USLE, RUSLE, EUROSEM, and SEMMA and <5% relative difference as compared to the average rainfall kinetic energies calculated by other empirical functions. Therefore, it is expected that power law of ideal assumption may be utilized as a universal power law in evaluating rainfall kinetic energy.

1. Introduction

Soil erosion is a natural process in all landform evolution and soil degradation along with various environmental problems. In water erosion, the impact of raindrop on the soil surface disperses soil aggregates. The rainfall kinetic energy is one of the useful indicators in the potential ability of rainfall for separating soil particles from the soil surface. Basically, the rainfall kinetic energy results from the kinetic energy of individual raindrops that strikes the soil. The calculation of the rainfall kinetic energy requires drop-size, drop-velocity, and drop-volume measurements as well as drop-size distribution (DSD). DSD data has been obtained using various techniques such as filter paper, flour pellet, camera, optical array, and meteorological radar [1–7]. The rainfall kinetic energy can be calculated by the measured DSD combined with empirical $V_t(D)$ laws [8–10], direct measurement using a pressure transducer or acoustic devices

[11, 12] or using an Optical Spector Pluviometer allowing the real time measurement of drop-size and drop-velocity [7]. Many empirical equations of the rainfall kinetic energy (E_k) linked to the easily available rainfall intensity (I) are proposed on the basis of drop-size and drop-velocity measurements. The empirical equations for the rainfall kinetic energy in various mathematical expressions have been developed in the form of power-law, exponential, logarithmic, and linear functions.

In the empirical soil erosion models, the rainfall kinetic energy has been used as erosivity factor of splash erosion, sheet erosion, and rill erosion modeling [13–16]. USLE [13], soil erosion models based on agricultural area in the United States, used a logarithmic function of rainfall kinetic energy developed by Wischmeier and Smith [13], and RUSLE [14] used an exponential function proposed by Brown and Foster [17]. Under the assumption based on the DSD measurements [18], EUROSEM [15], the representative soil erosion model

in Europe, used a logarithmic function presented by Brandt [19]. SEMMA [16] developed in South Korea adopted an exponential function of Van Dijk et al. [20]. However, they require the validation in a wide range of environmental settings since these functions were focused on restricted areas with different environmental settings and measurement technique.

There are no distinct criteria on what is the most suitable function as rainfall erosivity factor of the soil erosion. Many researchers suggested that the maximum value of the rainfall kinetic energy exists in the natural rainfall events [3, 17, 21–24]. The exponential function which converges to the limited value was judged to be function that better describes the relationship between rainfall kinetic energy and rainfall intensity [3, 25] because there is no upper limit in the power-law, logarithmic, and linear functions. Van Dijk et al. [20] proposed a general equation of the exponential type from the measured data through a literature review on the relationship between rainfall kinetic energy and rainfall intensity. The empirical power-law relation from the observation of rainfall intensity and radar reflectivity factors using a statistical model of the DSD was presented by Smith and de Veaux [26]. In particular, Salles et al. [27] proved that the time-specific kinetic energy is the most appropriate expression of the empirical law between rainfall kinetic energy and rainfall intensity in the statistical and physical basis and presented that the power law between rainfall kinetic energy and rainfall intensity is the most suitable mathematical function as considering the DSD models.

The existing empirical equations between rainfall kinetic energy and rainfall intensity showed significantly different coefficients according to geographical location and measurement technique. Therefore, it is not easy to apply in other countries or regions having different types of rainfall [4, 20, 28]. In particular, power law in calculation of rainfall kinetic energy shows larger deviation compared to exponential and logarithmic functions [26, 29]. There were few cases that the power law had been used as rainfall erosivity index in developed soil erosion models although it is simple and suitable mathematical expression. Therefore, it is necessary to present the representative power law obtained from various rainfall kinetic energy equations. This study attempts to propose a new equation of power law based on the rainfall power theory under the ideal assumption that drop-size is uniformly distributed in constant rainfall intensity. In addition, our newly proposed power law is evaluated through comparing with existing empirical equations.

2. Theory

2.1. Relationship between Rainfall Kinetic Energy and Rainfall Intensity. In general, the relationships between rainfall kinetic energy and rainfall intensity are presented in the form of exponential [4, 17, 24, 28, 30–34], logarithmic [3, 13, 28, 34–37], linear [24, 28, 38–40], and power-law [26, 28, 29, 33, 41, 42] functions.

The rainfall kinetic energy can be expressed in two ways of volume-specific and time-specific kinetic energy. The volume-specific kinetic energy is expressed as the amount

of rainfall kinetic energy expended per unit volume of rain [13, 20, 36, 43] while time-specific kinetic energy is the rate of expenditure of rainfall kinetic energy or rainfall power and expressed as rainfall kinetic energy expended per unit area and per unit time [3, 26, 29]. In the relationship between rainfall kinetic energy and rainfall intensity, the two expressions of volume-specific rainfall kinetic energy $E_{k\text{-mm}}$ ($\text{J}/\text{m}^2/\text{mm}$) and time-specific rainfall kinetic energy $E_{k\text{-time}}$ ($\text{J}/\text{m}^2/\text{h}$) are related to each other through the rainfall intensity as shown in the following:

$$E_{k\text{-time}} = IE_{k\text{-mm}}. \quad (1)$$

As reported by Sempere-Torres et al. [39], the scatterplots of $E_{k\text{-time}}-I$ have less heteroscedasticity than those of $E_{k\text{-mm}}-I$, and $E_{k\text{-mm}}$ is more sensitive to the DSD of rainfall [27] so that the connection of $E_{k\text{-time}}$ with I is more suitable compared to $E_{k\text{-mm}}$. Therefore, this study investigates the relationship between time-specific rainfall kinetic energy (hereafter, E_k) and rainfall intensity.

Exponential, logarithmic, linear, and power-law functions of time-specific rainfall kinetic energy can be expressed as general equations using empirical coefficients of a , b , and c as shown in the following equations:

$$E_k = aI(1 - be^{-cI}), \quad (2)$$

$$E_k = I(a + b \log I), \quad (3)$$

$$E_k = a(I - b), \quad (4)$$

$$E_k = aI^b. \quad (5)$$

Reported empirical relationships between rainfall kinetic energy and rainfall intensity are summarized in Table 1. In case of exponential function developed widely, only reliable functions organized by Salles et al. [27] and Van Dijk et al. [20] were reported as considering the range of rainfall intensity and the number of observations and determination coefficient of measured data. Also, the linear and logarithmic function include the reliable empirical equations along with equations organized by Salles et al. [27]. Representative forms of the power law include six typical power laws presented using DSD data from the Illinois State Water Survey of the United States [26] and six different sets on power law between rainfall related variables and rainfall intensity were presented based on different assumptions regarding the rainfall intensity dependence of the DSD parameters [29]. With continuous and direct drop-size and drop-velocity measurements, kinetic energy equations recently developed in the Republic of Korea were organized in Table 1 [33, 34, 42].

2.2. Review of Mathematical Power Laws. Many researchers demonstrated that a power law is the most suitable mathematical function between rainfall kinetic energy and rainfall intensity [27, 44]. Therefore, the power law presented by Salles et al. [27] is summarized in these passages to understand a mathematically rational power law used to link I with E_k .

TABLE 1: Empirical relationships between time-specific rainfall kinetic energy (E_k , J/m²/h) and rainfall intensities (I , mm/h).

Equation forms	References	a	b	c	I (mm/h)	Number observation	Location/altitude
Exponential function	Blanchard, 1953 [30]	23.7	0.710	0.031	0-127	29	Honolulu, Hawaii, USA/670-2250 m
	Kinnell, 1981 [3]	29.3	0.281	0.018	2-309	200	Miami, Florida, USA/3 m
	Rosewell, 1986 [24]	29.2	0.894	0.048	19-229	50	Rhodesia from Hudson [11]/1230 m
	Brown and Foster, 1987 [17]	29.0	0.596	0.040	1-146	13,438	Gunnedah, Australia/305 m
	McIsaac, 1990 [4]	26.4	0.669	0.349	1-161	6,360	Brisbane, Australia/25 m
	Azevedo Coutinho and Pereira Tomás, 1995 [31]	29.0	0.720	0.050	0-250	315	MS, USA/180 m
	Jayawardena and Rezaur, 2000 [32]	29.2	0.510	0.011	2-170	19,000	Majuro, Marshall Islands/3 m
	Fornis et al., 2005 [28]	28.8	0.450	0.033	1-194	18,021	Pina Range/Fort Sherman, Panama/50 m
	Lim et al., 2012 [33]	35.9	0.559	0.034	0-120	8190	Mértola, Algarve, Portugal/21 m
	Lee and Won, 2013 [34]	36.8	0.691	0.038	0-150	18	Hong Kong/50 m
Logarithmic function	Wischmeier and Smith, 1958 [13]	30.8	0.550	0.031	0-142	5822	Cetral, Cebu, Philippine/44 m
	Onaga et al., 1988 [35]	30.3	0.730	0.130	0-142	1,841	Chungcheong, South Korea/58 m
	Zanchi and Torri, 1980 [36]	30.0	0.740	0.068	1-108	25,017	Gangwon, South Korea/842 m
	Kinnell, 1981 [3]	11.9	8.73	n.a	n.a	n.a	Washington, USA; from Laws and Parsons [2]
	Brandt, 1990 [37]	9.81	10.6	n.a	n.a	n.a	Okinawa, Japan
	Fornis et al., 2005 [28]	9.81	11.25	n.a	1-140	n.a	Firenze, Central Italy/90 m
	Lee and Won, 2013 [34]	17.1	5.23	n.a	2-309	315	Miami, Florida/3 m
	Hudson, 1965 [38]	9.71	9.26	n.a	19-227	200	Rhodesia from Hudson [11]/1230 m
	Kinnell, 1981 [3]	8.95	8.44	n.a	0-105	92	USA, DSD from Marshall and Palmer [18]/35 m
	Rosewell, 1986 [24]	11.93	7.82	n.a	0-142	5822	Cetral, Cebu, Philippine/44 m
Linear function	Hudson, 1965 [38]	6.04	12.37	n.a	1-108	25,017	Gangwon, South Korea/842 m
	Kinnell, 1981 [3]	29.9	4.29	n.a	n.a	n.a	Zimbabwe
	Rosewell, 1986 [24]	30.1	5.48	n.a	2-309	315	Miami, Florida, USA/3 m
	Sempere-Torres et al., 1992 [39]	29.9	4.29	n.a	19-227	200	Rhodesia from Hudson [11]/1230 m
	Usón and Ramos, 2001 [40]	24.5	1.25	n.a	1-146	13,438	Gunnedah, Australia/305 m
	Fornis et al., 2005 [28]	24.8	1.29	n.a	1-161	6,360	Brisbane, Australia/25 m
	Wischmeier and Smith, 1958 [13]	34.0	5.59	n.a	20-100	n.a	Cevennes, France
	Onaga et al., 1988 [35]	23.4	0.77	n.a	0-20	n.a	North-East, Spain

TABLE 1: Continued.

Equation forms	References	a	b	c	I (mm/h)	Number observation	Location/altitude
		13.0	1.21		n.a	n.a	Oregon, USA
		11.0	1.23		n.a	n.a	Alaska, USA
		18.0	1.24		n.a	n.a	Arizona, USA
	Smith and de Veaux, 1992 [26]	11.0	1.17		n.a	n.a	New Jersey, USA
		10.0	1.18		0–240	n.a	North Carolina, USA
		11.0	1.14		n.a	n.a	Florida, USA
		7.20	1.32				
		8.53	1.29				
		8.46	1.17				
		8.89	1.28		0–105	92	Based on Marshall and Palmer [18] parameterization/35 m
	Uijlenhoet and Stricker, 1999 [29]	10.8	1.06				
		7.74	1.35				
		11.0	1.25		n.a	n.a	Northern Mississippi, USA
	Steiner and Smith, 2000 [41]	12.1	1.19		0–142	5822	Cetral, Cebu, Philippine/44 m
	Fornis et al., 2005 [28]	9.6	1.19		0–38	423	Gyeonggi, South Korea/115 m
	Kim et al., 2010 [42]	15.1	1.13		0–142	1,841	Chungcheong, South Korea/58 m
	Lim et al., 2012 [33]						

Power Law
function

The time-specific rainfall kinetic energy E_k (J/m²/h), the rainfall kinetic energy flux density [41, 45], is calculated by the DSD and drop-velocity measurement data:

$$E_k = 3.6 \times 10^{-3} \frac{\rho\pi}{12} \sum_i X(D_i) D_i^3 V_t^2(D_i), \quad (6)$$

where ρ is the water density (kg/m³) in standard conditions, D_i is a diameter of raindrop (cm), $X(D_i)$ is the number of drops with diameter D_i arriving per unit time and per unit area, and $V_t(D)$ is the terminal fall velocity of a raindrop with diameter D_i .

Rainfall intensity I (mm/h) is derived from the droplet flux density:

$$I = 3.6 \frac{\pi}{6} \sum_i X(D_i) D_i^3. \quad (7)$$

Sempere-Torres et al. [44, 46] mentioned the various mathematical expressions of the DSD described by exponential, gamma, lognormal, or Weibull distribution functions [18, 47–49] and presented that all DSD models follow the power law as the most appropriate relationship between E_k and I . The general formulation of the DSD using I as reference variable is expressed as follows:

$$N(D, I) = I^\alpha g(DI^{-\beta}). \quad (8)$$

The general formulation of an analytical relation between E_k and I is expressed by raindrop flux density replacing DSD and the terminal fall velocity:

$$E_k = 3.6 \times 10^3 \frac{\rho\pi}{12} I^\alpha \int_{D_{\min}}^{D_{\max}} g(DI^{-\beta}) D^3 V_t^2(D) dD. \quad (9)$$

Using a terminal fall velocity $V_t(D) = a_0 D^{b_0}$ and the variable $x = DI^{-\beta}$ (9) becomes

$$E_k = 3.6 \times 10^3 \frac{\rho\pi}{12} I^{\alpha+\beta(4+3b_0)} \int_{x_{\min}}^{x_{\max}} g(x) x^{3(b_0+1)} dx. \quad (10)$$

The remaining terms except I are defined as A being a constant. If $V_t(D)$ proposed by Atlas and Ulbrich [50] is used, A and E_k can be expressed simply as follows:

$$E_k = AI^{1+1.34\beta}. \quad (11)$$

The exponent of the relation between E_k and I depends on only one variable β . In various climate conditions, the coefficient A is well expressed by gamma distribution with a single free variable μ presented by Sempere-Torres et al. [46] or Salles et al. [51]. Therefore, the coefficient A is simply expressed below:

$$A = 1288.17\mu^{-1.34}. \quad (12)$$

Finally, the power law of E_k (J/m²/h) presented by Salles et al. [27] is described as follows:

$$E_k = 1288.17\mu^{-1.34} I^{1+1.34\beta}. \quad (13)$$

In the presented E_k - I relationship, the parameters μ and β are linked to the type of microphysical process related to the growth of raindrops [27]. In the previously reported studies, μ is applicable to the range between 30 and 40. Typical values around 30 are related to convective rainfall [44, 46, 51] and the values $\mu = 40$ and $\mu = 50$ are commonly associated with stratified rainfall [18] and drizzle [52], respectively. Regarding the parameter β , Marshall and Palmer [18] reported values around 0.12 to 0.15 are suitable to convection rainfall and the value $\beta = 0.21$ is related to a wide range of stratified rainfall. In the general form of given power law in (5), the coefficient and exponent are transformed into mathematical power functions of Salles et al. [27] as shown below:

$$\begin{aligned} a &= 1288.17\mu^{-1.34}, \\ b &= 1 + 1.34\beta. \end{aligned} \quad (14)$$

The coefficient a of the power law is 13.5 for convective rainfall and 9.2 for the wide range of stratified rainfall. The exponent b varies from 1.0 to 1.4, and the values around 1 are suitable for strong rainfall.

3. Establishment of Ideal Equation for Rainfall Power

Despite the definition of the functional relationship between rainfall kinetic energy and rainfall intensity, exponents and coefficients of the power law are largely different depending on parameters such as rainfall type, geographical location, and measurement techniques. Therefore, a general equation which represents empirical power law is required to evaluate soil erosion in the area where there is no measurement data of rainfall kinetic energy. The power of raindrop falling on the surface soil is derived theoretically under the ideal assumption that the diameter of raindrop is uniform for constant rainfall intensity. This assumption is based on the judgment that the error caused by this ideal assumption would be smaller than the difference in rainfall kinetic energies estimated by various types of empirical power law [26, 29].

The power of raindrop particles striking on the surface soil is defined by the multiplication of the force and terminal velocity of freefalling raindrop:

$$P_R = \sum F_R V_t(D), \quad (15)$$

where rainfall power P_R is the expended energy per unit area and per time (J/m²/s), the force of rainfall F_R is the water weight per unit area (N/m²), and $V_t(D)$ is the terminal velocity of raindrop (m/s).

Atlas and Ulbrich [50] have suggested the power law based on the terminal velocity data presented by Gunn and Kinzer [9]; the terminal fall velocity is proportional to the diameter of raindrop:

$$V_t(D) = 17.67D^{0.67}, \quad (16)$$

where D is mean diameter (cm) of uniform raindrop.

A freefalling raindrop is affected by gravity and the resistance force. The velocity of a falling raindrop keeps the steady condition when two forces are equal. The terminal fall velocity can be expressed as reported by Zhou et al. [53]:

$$V_t(D) = \left(\frac{D^2 \rho g}{6K} \right)^{1/3}, \quad (17)$$

where g is the acceleration by gravity (m/s^2) and K is the constant in the certain range of raindrop diameter (kg s/m^3). Therefore, the relationship of the terminal velocity and raindrop diameter is expressed as $V_t(D) \propto D^{2/3}$.

If the raindrop flux density $X(D)$ is the number of raindrops with a uniform diameter D per unit area and per unit time, rainfall intensity equation can be expressed simply as follows:

$$I = \frac{\pi}{0.6} X(D) D^3. \quad (18)$$

The above equation is expressed into the equation of uniform diameter of raindrop as follows:

$$D = \left[\frac{I}{0.6\pi X(D)} \right]^{1/3}. \quad (19)$$

The uniform diameter in (19) is substituted in the terminal velocity of (16) and it is then substituted in rainfall power equation as follows:

$$P_R = 17.67 \left[\frac{I}{0.6\pi X(D)} \right]^{2/9} \sum F_R. \quad (20)$$

Since the weight of rainfall per unit area is the product of the specific weight and rainfall amount, it is derived from

$$\sum F_R = 10^{-3} \gamma_w R, \quad (21)$$

where γ_w is the unit weight of raindrop water (N/m^3) and the amount of rainfall R (mm) has relationship of $R = I \cdot t$ with rainfall intensity.

When the weight of rainfall in (21) is substituted in the rainfall power equation, it is expressed as in the following:

$$P_R = \frac{150t}{X(D)^{2/9}} I^{11/9}. \quad (22)$$

If the equation of rainfall power per unit area ($\text{J/m}^2/\text{s}$) is converted to the equation of time-specific rainfall kinetic energy ($\text{J/m}^2/\text{h}$), and time t is 1 hour, the ideal equation of rainfall power is derived as follows:

$$E_k = \frac{150}{X(D)^{2/9}} I^{11/9}. \quad (23)$$

Therefore, time-specific rainfall kinetic energy (E_k) from rainfall power theory is proportional to 11/9 power of rainfall intensity I and is in inverse proportion to 2/9 power of the number of raindrops, $X(D)$.

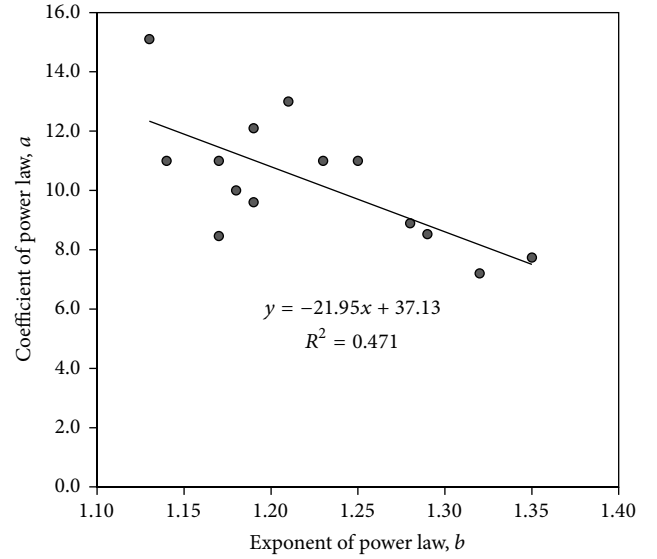


FIGURE 1: Relationship between coefficients and exponents of empirical power laws.

The exponent 11/9 of rainfall power function was theoretically derived from ideal assumption that the drop-size is uniform in constant I . The coefficient can be calculated if the number of raindrops is identified. DSD to describe a population of falling drops obviously depends on the diameter and I [44] influenced by location, climate, and rainfall type [44]. Therefore, the coefficient can be obtained from the power laws developed based on empirically available DSD expressed by many researchers. In Table 1, the maximum ($a = 18.0$, $b = 1.24$) and minimum ($a = 10.8$, $b = 1.06$) kinetic energy equations which show > 30% difference from the calculated rainfall kinetic energies are excluded from regression analysis of empirical power laws. The linear regression equation ($r = 0.686$, $p = 0.0068$) from reliable power law is shown as in Figure 1. The coefficient a was 10.3 when the exponent ($b = 11/9$) for ideal power law was substituted in the linear regression equation ($a = -21.95b + 37.13$). Thus, the power law of time-specific rainfall kinetic energy by ideal assumption is proposed as follows:

$$E_k = 10.3I^{11/9}. \quad (24)$$

4. Evaluations and Discussions

We compared the relationship between existing empirical equations and the ideal equation of rainfall power to evaluate the availability as the universal power law.

The average value of rainfall energies calculated by 13 exponential functions [4, 17, 24, 28, 30–34] presented in Table 1 was fitted with the result simulated by the ideal power law of rainfall power ($a = 10.3$, $b = 11/9$) in Figure 2(a). The rainfall energy calculated by the ideal power law was distributed within the range of standard deviation of exponential functions. In case of rainfall intensity < 80 mm/h, the average value by exponential functions was greater than that of ideal power law while ideal power law had relatively

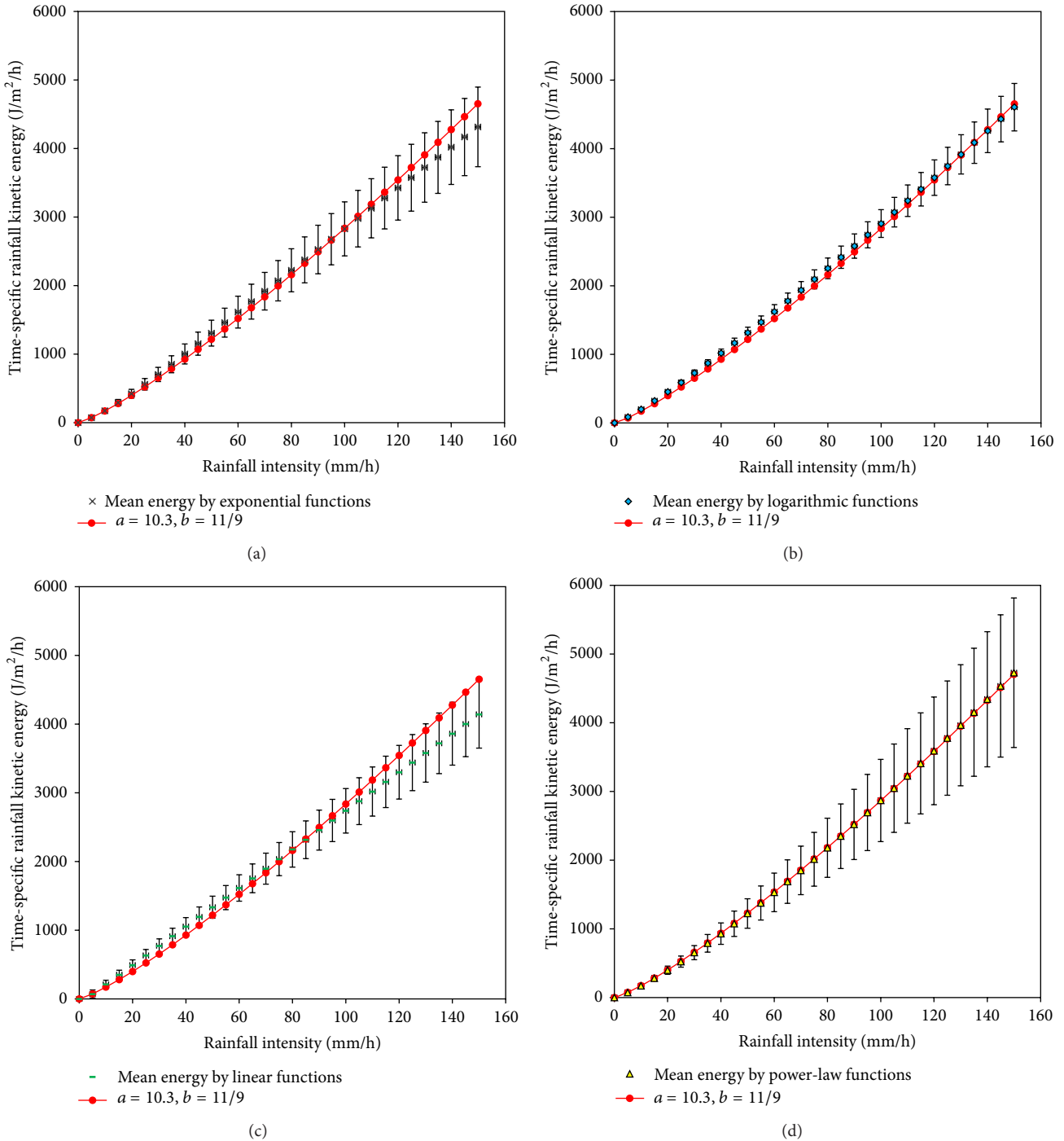


FIGURE 2: Comparisons of time-specific rainfall kinetic energies calculated by the ideal power law and the exponential functions (a), the logarithmic functions (b), the linear functions (c), and the power-law functions (d).

greater rainfall energy after $I > 100$ mm/h as the exponential function converges to the limited value in higher rainfall intensity [3, 25].

Comparison between the ideal equation and 8 logarithmic functions [3, 13, 28, 34–37] is presented in Figure 2(b). The average energy by logarithmic functions was relatively

greater than that of the ideal power law; however, the relative difference was minor.

In case of linear functions with the lowest utilization as an equation of rainfall kinetic energy, the average energy by the linear functions [24, 28, 38–40] became smaller than that of the ideal equation at $I > 90$ mm/h, and the relative difference

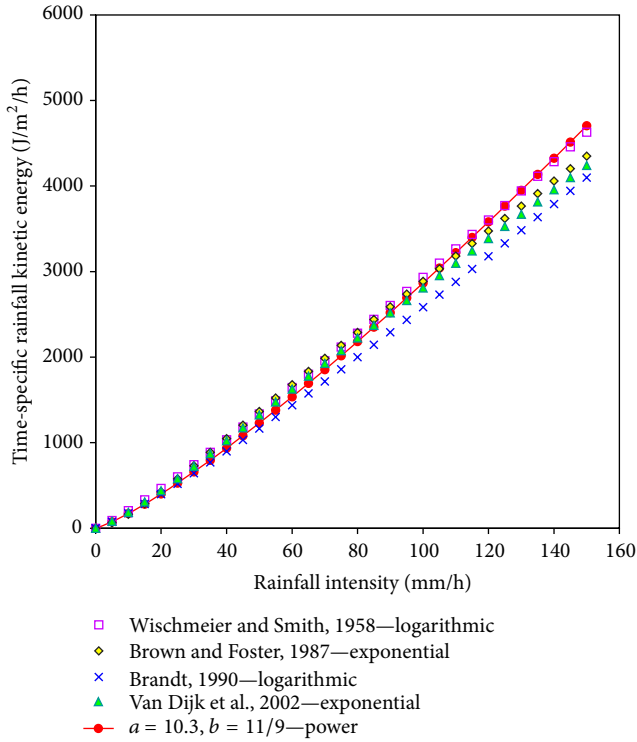


FIGURE 3: Comparison between time-specific kinetic energies calculated by empirical equations used in soil erosion models and time-specific kinetic energy simulated by universal power law according to rainfall intensity.

was largest compared to other functions at the maximum rainfall intensity (150 mm/h) (Figure 2(c)).

The rainfall energy simulated by the ideal power law and the average rainfall energy calculated from power laws [26, 28, 29, 33, 41, 42] showed the greatest deviation of rainfall kinetic energy as shown in Figure 2(d). The average energy calculated by 14 power laws excluding the maximum and minimum kinetic energy equations shown in Table 1 is approximated to the values from the ideal power law. The mean exponent and coefficient deduced from existing power laws were 1.221 ± 0.068 and 10.33 ± 2.16 , respectively, which coincide approximately with the exponent 11/9 and coefficient 10.3 of the ideal power law indicating universal power law.

To utilize the universal power law as an erosivity factor of soil erosion models, it is necessary to conduct a comparative review throughout various rainfall kinetic energy equations used in existing soil erosion models. USLE [13] and EUROSEM [15] used logarithmic functions presented by Wischmeier and Smith [13] and Brandt [19], respectively, and RUSLE [14] and SEMMA [16] used exponential functions developed by Brown and Foster [17] and Van Dijk et al. [20], respectively. Comparison of results simulated from these equations and ideal power law is shown in Figure 3. The simulation results showed that universal power law appears closer to logarithmic function of Wischmeier and Smith [13]. With $I > 100$ mm/h, its calculation was found to be greater than other equations. However, the relative difference

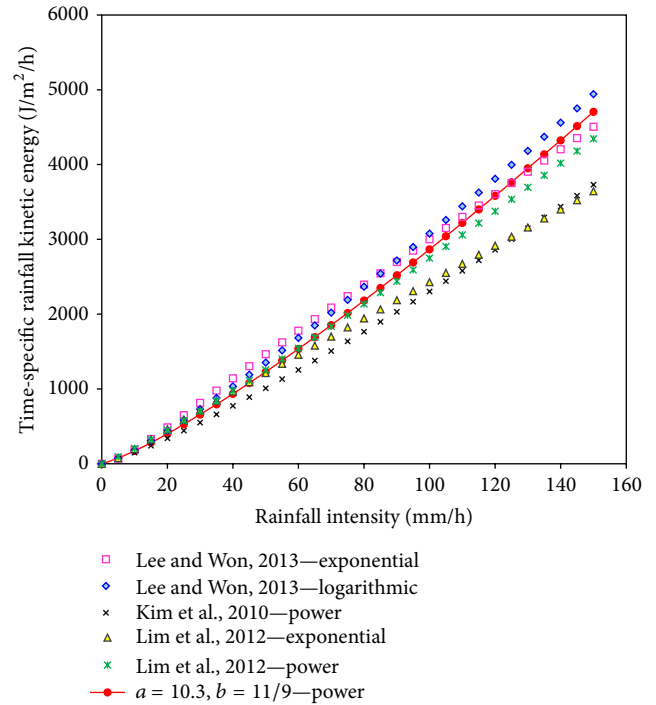


FIGURE 4: Comparison of time-specific kinetic energies between empirical equations presented in South Korea and universal power law.

with these rainfall energy equations showed reasonable value (4.8%).

The logarithmic, exponential, and power-law functions of the rainfall kinetic energies calculated by continuous DSD measurement data were presented by Kim et al. [42], Lim et al. [33], and Lee and Won [34] in South Korea's representative sites. The rainfall kinetic energies simulated from those equations and universal power law are shown in Figure 4. The results simulated from power law by Lim et al. [33] and exponential and logarithmic functions by Lee and Won [34] showed relatively small difference as compared with the values calculated by universal power law.

Comparison of the average rainfall kinetic energies between various empirical equations and the universal equation was conducted to evaluate whether the universal power law can be used as a representative power law of erosivity factor on soil erosion. The relative difference between the rainfall kinetic energies was calculated in range of $20 \text{ mm/h} \leq I < 160 \text{ mm/h}$ (Table 2). The relative difference was most significant in case of a linear function at $I = 20 \text{ mm/h}$ while $I > 100 \text{ mm/h}$; the energy of universal power law was found to be relatively greater. Power law showed the smallest relative difference which had the average relative difference of 0.06%. Moreover, exponential function used frequently in soil erosion models had small average relative difference (0.32%). Many studies confirmed that there is the maximum value of rainfall kinetic energy and determined that the exponential function with upper limit better describes the relationship between rainfall kinetic energy and rainfall intensity as compared to logarithmic, linear, and power-law

TABLE 2: Relative differences in kinetic energy between universal power law and average kinetic energies evaluated by empirical equations.

Rainfall intensity (mm/h)	Relative difference with exponential function (%)	Relative difference with logarithmic function (%)	Relative difference with linear function (%)	Relative difference with power law (%)
20	-5.40	-12.96	-22.61	0.85
40	-7.18	-8.69	-12.59	0.58
60	-5.09	-5.67	-5.17	0.33
80	-1.93	-3.34	0.27	0.11
100	1.32	-1.46	4.48	-0.09
120	4.33	0.13	7.88	-0.27
140	7.03	1.49	10.72	-0.43
160	9.44	2.69	13.13	-0.58
Ave.	0.32	-3.48	-0.49	0.06
S.D.	5.79	5.02	11.53	0.47

functions with no upper limit [3, 17, 21–25]. In addition, Van Dijk et al. [20] proposed a general exponential equation based on comprehensive measurement data by reviewing literature. Actually, the kinetic energy of freefalling raindrops has the upper limit due to limited maximum size of raindrop in the order of 6–8 mm [2, 10, 52]. However, power law simulated excessively in high rainfall intensity may be more useful than exponential function in evaluating soil erosion because sediment transport capacity of running water increases with the rainfall kinetic energy. Interrill erosion model linked to power-law relationship with rainfall intensity has been adopted that the exponent of power law was approximated by ≥ 2 [54–56]. Therefore, the universal power law that used ideal assumption would take great advantages in utilization as erosivity factor to determine a quantitative assessment of soil erosion.

5. Conclusion

The empirical rainfall kinetic energy equations determined by the characteristics of the DSD have a variety of functional forms. In case of power laws, especially, the relative deviations of calculated energies depend on the exponents and coefficients of power laws. This study proposed a representative power law. The time-specific rainfall kinetic energy equation based on the power theory was derived through the ideal assumption that the drop-size is uniformly distributed under the constant rainfall intensity. The exponent of ideal power law was 11/9, and the coefficient was 10.3 which obtained from the relationship between exponents and coefficients of existing empirical power laws. The rainfall energy calculated by ideal equation was compared with results simulated by existing exponential, logarithmic, linear, and power-law functions. The logarithmic function showed the smallest deviation as compared to the ideal power law. The ideal equation in $I > 100$ mm/h overestimated in comparison with exponential and linear functions. The mean rainfall kinetic energy calculated from empirical power laws corresponded approximately with the results of ideal power law. This supports that the ideal equation can be a universal form of the power law. The universal power law in comparison with

rainfall kinetic energy equations used in typical soil erosion models showed that the relative difference was within 5%, and there was no significant deviation in relationship with equations of rainfall kinetic energy presented by DSD measurement. It was also confirmed that the relative differences in the average rainfall kinetic energy between various empirical equations and universal equation of rainfall power law were not significant. These results prove that the universal power law can represent the existing empirical power laws. There was a trend that the kinetic energy by universal power law had relatively overestimated as compared to other empirical equations in $I > 100$ mm/h. However, this result supports the conclusion that it can be more useful in the development of soil erosion models due to significant increase in sediment yield by increasing transport capacity of surface runoff in the high rainfall intensity ($I > 100$ mm/h).

Conflict of Interests

The authors declare that there is no conflict of interests regarding the publication of this paper.

Acknowledgment

This research was supported by Basic Science Research Program through the National Research Foundation of Korea (NRF) funded by the Ministry of Education, Science and Technology (no. 2013R1A1A3011962).

References

- [1] M. J. Hall, "Use of the stain method in determining the drop size distribution of coarse liquid sprays," *Transactions of the American Society of Agricultural Engineers*, vol. 13, pp. 33–37, 1970.
- [2] J. O. Laws and D. A. Parsons, "The relation of raindrop size to intensity," *Transactions of the American Geophysical Union*, vol. 26, pp. 452–460, 1943.
- [3] P. I. A. Kinnell, "Rainfall intensity-kinetic energy relationships for soil loss prediction," *Soil Science Society of America Journal*, vol. 45, no. 1, pp. 153–155, 1981.

- [4] G. F. McIsaac, "Apparent geographic and atmospheric influences on raindrop sizes and rainfall kinetic energy," *Journal of Soil & Water Conservation*, vol. 45, no. 6, pp. 663–666, 1990.
- [5] T.-I. Wang, K. B. Earnshaw, and R. S. Lawrence, "Path-averaged measurements of rain rate and raindrop size distribution using a fast-response optical sensor," *Journal of Applied Meteorology*, vol. 18, no. 5, pp. 654–660, 1979.
- [6] A. J. Illingworth and C. J. Stevens, "An optical disdrometer for the measurement of raindrop size spectra in windy conditions," *Journal of Atmospheric and Oceanic Technology*, vol. 4, no. 3, pp. 411–421, 1987.
- [7] C. Salles and J. Poesen, "Performance of an optical spectro pluviometer in measuring basic rain erosivity characteristics," *Journal of Hydrology*, vol. 218, no. 3–4, pp. 142–156, 1999.
- [8] J. O. Laws, "Measurements of the fall-velocity of water-drops and raindrops," *Eos, Transactions American Geophysical Union*, vol. 22, pp. 709–721, 1941.
- [9] R. Gunn and G. D. Kinzer, "The terminal velocity of fall for water droplets in stagnant air," *Journal of Meteorology*, vol. 6, no. 4, pp. 243–248, 1949.
- [10] K. V. Beard, "Terminal velocity and shape of cloud and precipitation drops aloft," *Journal of the Atmospheric Sciences*, vol. 33, no. 5, pp. 851–864, 1976.
- [11] N. W. Hudson, "An introduction to the mechanics of soil erosion under conditions of sub-tropical rainfall," *Transactions of the Rhodesia Scientific Association*, vol. 49, pp. 15–25, 1961.
- [12] A. W. Jayawardena and R. B. Rezaur, "Measuring drop size distribution and kinetic energy of rainfall using a force transducer," *Hydrological Processes*, vol. 14, no. 1, pp. 37–49, 2000.
- [13] W. H. Wischmeier and D. D. Smith, "Rainfall energy and its relationship to soil loss," *Transactions of the American Geophysical Union*, vol. 39, no. 2, pp. 285–291, 1958.
- [14] K. G. Renard, G. R. Foster, G. A. Weesies, D. K. McCool, and D. C. Yoder, "Predicting soil erosion by water: a guide to conservation planning with the Revised Universal Soil Loss Equation (RUSLE)," in *US Department of Agriculture Handbook 703*, US Department of Agriculture, Agricultural Search Service, Washington, DC, USA, 1997.
- [15] R. P. C. Morgan, J. N. Quinton, R. E. Smith et al., "The European soil erosion model (EUROSEM): a dynamic approach for predicting sediment transport from fields and small catchments," *Earth Surface Processes and Landforms*, vol. 23, no. 6, pp. 527–544, 1998.
- [16] S. D. Park, K. S. Lee, and S. S. Shin, "A statistical soil erosion model for burnt mountain areas in Korea—RUSLE approach," *Journal of Hydrologic Engineering*, vol. 17, no. 2, pp. 292–304, 2012.
- [17] L. C. Brown and G. R. Foster, "Storm erosivity using idealized intensity distributions," *Transactions of the American Society of Agricultural Engineers*, vol. 30, no. 2, pp. 379–386, 1987.
- [18] J. S. Marshall and W. M. Palmer, "The distribution of raindrop with size," *Journal of Meteorology*, vol. 5, pp. 165–166, 1948.
- [19] C. J. Brandt, "The size distribution of throughfall drops under vegetation canopies," *CATENA*, vol. 16, no. 4–5, pp. 507–524, 1989.
- [20] A. I. J. M. Van Dijk, L. A. Bruijnzeel, and C. J. Rosewell, "Rainfall intensity-kinetic energy relationships: a critical literature appraisal," *Journal of Hydrology*, vol. 261, no. 1–4, pp. 1–23, 2002.
- [21] N. W. Hudson, "Raindrop size distribution in high intensity storms," *Rhodesian Journal of Agricultural Research*, vol. 1, pp. 6–11, 1963.
- [22] P. C. Baruah, *An investigation of drop size distribution of rainfall in Thailand [M.S. thesis]*, Asian Institute of Technology, Bangkok, Thailand, 1973.
- [23] C. E. Carter, J. D. Greer, H. J. Braud, and J. M. Floyd, "Raindrop characteristics in south central United States," *Transactions of the American Society of Agricultural Engineers*, vol. 17, no. 6, pp. 1033–1037, 1974.
- [24] C. J. Rosewell, "Rainfall kinetic energy in eastern Australia," *Journal of Climate & Applied Meteorology*, vol. 25, no. 11, pp. 1695–1701, 1986.
- [25] W. H. Wischmeier and D. D. Smith, "Predicting rainfall erosion losses," in *Agriculture Handbook No. 537*, U.S. Department of Agriculture, Washington, DC, USA, 1978.
- [26] J. A. Smith and R. D. de Veaux, "The temporal and spatial variability of rainfall power," *Environmetrics*, vol. 3, no. 1, pp. 29–53, 1992.
- [27] C. Salles, J. Poesen, and D. Sempere-Torres, "Kinetic energy of rain and its functional relationship with intensity," *Journal of Hydrology*, vol. 257, no. 1–4, pp. 256–270, 2002.
- [28] R. L. Fornis, H. R. Vermeulen, and J. D. Nieuwenhuis, "Kinetic energy-rainfall intensity relationship for Central Cebu, Philippines for soil erosion studies," *Journal of Hydrology*, vol. 300, no. 1–4, pp. 20–32, 2005.
- [29] R. Uijlenhoet and J. N. M. Stricker, "A consistent rainfall parameterization based on the exponential raindrop size distribution," *Journal of Hydrology*, vol. 218, no. 3–4, pp. 101–127, 1999.
- [30] D. C. Blanchard, "Raindrop size-distribution in Hawaiian rains," *Journal of Meteorology*, vol. 10, no. 6, pp. 457–473, 1953.
- [31] M. Azevedo Coutinho and P. Pereira Tomás, "Characterization of raindrop size distributions at the Vale Formoso Experimental Erosion Center," *CATENA*, vol. 25, no. 1–4, pp. 187–197, 1995.
- [32] A. W. Jayawardena and R. B. Rezaur, "Drop size distribution and kinetic energy load of rainstorms in Hong Kong," *Hydrological Processes*, vol. 14, no. 6, pp. 1069–1082, 2000.
- [33] Y. S. Lim, J. W. Kim, J. K. Kim, and B. I. Park, "Evaluation of kinetic energy of raindrops at Daejeon city using laser-optical disdrometer," *Journal of the Korean Geomorphological Association*, vol. 19, no. 2, pp. 133–143, 2012.
- [34] J. S. Lee and J. Y. Won, "Analysis of the characteristic of monthly rainfall erosivity in Korea with derivation of rainfall energy equation," *Journal of Korean Society of Hazard Mitigation*, vol. 13, no. 3, pp. 177–184, 2013.
- [35] K. Onaga, K. Shirai, and A. Yoshinaga, "Rainfall erosion and how to control its effects on farmland in Okinawa," in *Land Conservation for Future Generation*, S. Rimwanich, Ed., pp. 627–639, Department of Land Development, Bangkok, Thailand, 1988.
- [36] C. Zanchi and D. Torri, "Evaluation of rainfall energy in central Italy," in *Assessment of Erosion*, M. de Boodt and D. Gabriels, Eds., pp. 133–142, Wiley, Toronto, Canada, 1980.
- [37] C. J. Brandt, "Simulation of the size distribution and erosivity of raindrops and throughfall drops," *Earth Surface Processes & Landforms*, vol. 15, no. 8, pp. 687–698, 1990.
- [38] N. W. Hudson, *The influence of rainfall mechanics on soil erosion [MSc. thesis]*, Cape Town University, Cape Town, South Africa, 1965.
- [39] D. Sempere-Torres, C. Salles, J. D. Creutin, and G. Delrieu, "Quantification of soil detachment by raindrop impact: performance of classical formulae of kinetic energy in Mediterranean storms. Erosion and sediment transport monitoring programs in river basin," *IASH Publications*, vol. 210, pp. 115–124, 1992.

- [40] A. Usón and M. C. Ramos, "An improved rainfall erosivity index obtained from experimental interrill soil losses in soils with a mediterranean climate," *CATENA*, vol. 43, no. 4, pp. 293–305, 2001.
- [41] M. Steiner and J. A. Smith, "Reflectivity, rain rate, and kinetic energy flux relationships based on raindrop spectra," *Journal of Applied Meteorology*, vol. 39, no. 11, pp. 1923–1940, 2000.
- [42] J. K. Kim, D. Y. Yang, and M. S. Kim, "Evaluating physical characteristics of raindrop in Anseong Gyeonggi province," *Journal of the Korean Geomorphological Association*, vol. 17, no. 1, pp. 49–57, 2010.
- [43] P. I. A. Kinnell, "The problem of assessing the erosive power of rainfall from meteorological observations," *Soil Science Society of America*, vol. 37, no. 4, pp. 617–621, 1973.
- [44] D. S. Torres, J. M. Porrà, and J. D. Creutin, "A general formulation for raindrop size distribution," *Journal of Applied Meteorology*, vol. 33, no. 12, pp. 1494–1502, 1994.
- [45] L. V. Madden, L. L. Wilson, and N. Ntahirpera, "Calibration and evaluation of an electronic sensor for rainfall kinetic energy," *Phytopathology*, vol. 88, no. 9, pp. 950–959, 1998.
- [46] D. Sempere-Torres, J. M. Porrà, and J.-D. Creutin, "Experimental evidence of a general description for raindrop size distribution properties," *Journal of Geophysical Research D: Atmospheres*, vol. 103, no. 2, pp. 1785–1797, 1998.
- [47] A. C. Best, "The size distribution of raindrops," *Quarterly Journal of The Royal Meteorological Society*, vol. 76, pp. 16–36, 1950.
- [48] C. W. Ulbrich, "Natural variations in the analytical form of the raindrop size distribution," *Journal of Climate & Applied Meteorology*, vol. 22, no. 10, pp. 1764–1775, 1983.
- [49] G. Feingold and Z. Levin, "The lognormal fit to raindrop spectra from frontal convective clouds in Israel," *Journal of Climate & Applied Meteorology*, vol. 25, no. 10, pp. 1346–1363, 1986.
- [50] D. Atlas and C. W. Ulbrich, "Path- and area-integrated rainfall measurement by microwave attenuation in the 1-3cm band," *Journal of Applied Meteorology*, vol. 16, pp. 1322–1331, 1977.
- [51] C. Salles, D. Sempere-Torres, and J. D. Creutin, "Characterisation of raindrop size distribution in Mediterranean climate: analysis of the variations on the Z-R relationship," in *Proceedings of the 29th Conference on Rada Meteorology*, pp. 671–673, AMS, Montreal, Canada, July 1999.
- [52] J. Joss and A. Waldvogel, "Raindrop size distribution and sampling size errors," *Journal of the Atmospheric Sciences*, vol. 26, no. 3, pp. 566–569, 1969.
- [53] G. Zhou, X. Wei, and J. Yan, "Impacts of eucalyptus (*Eucalyptus exserta*) plantation on sediment yield in Guangdong Province, Southern Chin—a kinetic energy approach," *CATENA*, vol. 49, no. 3, pp. 231–251, 2002.
- [54] L. D. Meyer, "How rain intensity affects rill erosion," *Transaction American Society of Agricultural Engineers*, vol. 24, no. 6, pp. 1472–1475, 1981.
- [55] C. C. Truman and J. M. Bradford, "Relationships between rainfall intensity and the interrill soil loss-slope steepness ratio as affected by antecedent water content," *Soil Science*, vol. 156, no. 6, pp. 405–413, 1993.
- [56] A. J. Parsons and P. M. Stone, "Effects of intra-storm variations in rainfall intensity on interrill runoff and erosion," *CATENA*, vol. 67, no. 1, pp. 68–78, 2006.

Research Article

NDVI Variation and Its Responses to Climate Change on the Northern Loess Plateau of China from 1998 to 2012

Tingting Ning,^{1,2} Wenzhao Liu,¹ Wen Lin,^{1,2} and Xiaoqiang Song³

¹State Key Laboratory of Soil Erosion and Dryland Farming on the Loess Plateau, Institute of Soil and Water Conservation, Chinese Academy of Sciences and Ministry of Water Resources, Yangling, Shaanxi 712100, China

²University of the Chinese Academy of Sciences, Beijing 100049, China

³Soil and Water Conservation Bureau of Shaanxi Province, Xian, Shaanxi 710004, China

Correspondence should be addressed to Wenzhao Liu; wzliu@ms.iswc.ac.cn

Received 30 January 2015; Revised 23 April 2015; Accepted 30 April 2015

Academic Editor: Steffen Mischke

Copyright © 2015 Tingting Ning et al. This is an open access article distributed under the Creative Commons Attribution License, which permits unrestricted use, distribution, and reproduction in any medium, provided the original work is properly cited.

This study analyzed temporal and spatial changes of normalized difference vegetation index (NDVI) on the northern Loess Plateau and their correlation with climatic factors from 1998 to 2012. The possible impacts of human activities on the NDVI changes were also explored. The results showed that (1) the annual maximum NDVI showed an upward trend. The significantly increased NDVI and decreasing severe desertification areas demonstrate that the vegetation condition improved in this area. (2) Over the past decades, climate tended to be warmer and drier. However, the mean temperature significantly decreased and precipitation slightly increased from 1998 to 2012, especially in spring and summer, which was one of the major reasons for the increase in the annual maximum NDVI. Compared to temperature, vegetation was more sensitive to precipitation changes in this area. The NDVI and annual precipitation changes were highly synchronous over the first half of the year, while a 1-month time lag existed between the two variables during the second half of the year. (3) Positive human activities, including the “Grain for Green” program and successful environmental treatments at coal mining bases, were some of the other factors that improved the vegetation condition.

1. Introduction

Vegetation is the main component of terrestrial ecosystems on earth and plays an important role in the water, energy exchange, and biogeochemical cycles on terrestrial surfaces [1]. Linking soil, atmosphere, and moisture [2, 3], vegetation plays an irreplaceable role in maintaining climate stability, regulating the carbon balance, and reducing global-scale greenhouse gases [4]. However, vegetation is sensitive to climate changes. Vegetation dynamics and the responses to climate changes have been recognized as one of the core issues of global change in terrestrial ecosystems [5].

Due to high spatial and temporal resolutions and accuracy, remotely sensed data can provide technical support for monitoring vegetation dynamics at large scales. The normalized difference vegetation index (NDVI) was proposed by Rouse et al. based on red and near-infrared reflectance [6]. The NDVI has been frequently used for studying vegetation dynamics because it is highly correlated with the

photosynthetic capacity, the leaf area index, biomass, and net primary productivity [7]. The NDVI ranges from -1 to 1 . Higher positive NDVI values correspond to higher vegetation coverage and activity [8]. Negative NDVI values indicate the presence of clouds, snow, water, or a bright, nonvegetated surface [9]. Moreover, the NDVI has been widely used to assess the net primary productivity of vegetation (NPP) [10, 11] and crop production [12, 13] and to indicate the feedback effects of vegetation on local climates [14–16]. In addition, the NDVI has also been used to improve predictions and impact assessments related to disturbances, such as droughts [17] and floods [18].

Over the past 20 years, many scholars have conducted extensive research regarding surface vegetation coverage at different spatial and temporal scales based on NDVI time series data. Their research has shown that global vegetation activity has been gradually increasing, especially in northern middle-high latitude regions [19–21]. And similar results have been observed on the Tibet Plateau [22], the Loess

Plateau [23, 24] and over southwestern [25], central, and northwestern China [4, 26]. Conversely, decreasing NDVI trends have been detected in many regions, such as in the southwestern United States [27], northeastern Thailand [28], the upper catchments of the Yellow River [29], and the Lancang River source region [30].

In addition, the relationship between the NDVI and climatic factors has been explored by scholars at both local and regional scales since the 1980s. However, the mechanisms of the vegetative response to climate change are uncertain [31], and the results from previous studies have varied due to different vegetation characteristics, regions, and study methods. For example, Schultz and Halpert found that the global-scale NDVI data are not highly correlated with precipitation, although they did not correlate the data with temperature [32]. Liu et al. reported that vegetation coverage in the arid, western regions of northeastern Asia exhibits a strongly positive correlation with precipitation, while spatial changes in the NDVI, which are influenced by temperature in the region, are less pronounced [33]. He et al. examined the seasonal and inter-annual relationships between vegetation and climate data from 1985 to 2007 over Canadian ecosystems. Their results suggested that the relationship between the NDVI and temperature is stronger than that with precipitation [34]. Clearly, the key climate factors impacting the NDVI vary by region. Therefore, it is essential to conduct regional-scale research.

The northern Loess Plateau (Figure 1), which is located in the middle reach of the Yellow River, has a semiarid climate with an annual mean precipitation of 300 to 500 mm and an annual mean temperature of 6–9°C. This region is subject to soil erosion; numerous soil conservation measures have been implemented. Moreover, it is the largest coal mining region in China, with coal reserves accounting for 60% of the national total [35]. Both erosion and mining, which can be linked to human activities, have seriously altered surface conditions. Therefore, due to the combined impacts of climate change and human activities, it has become necessary to study the vegetation condition changes in this area in recent years. Based on the SPOT-VEGETATION DN, precipitation, and temperature data, this study investigated the spatial and temporal changes of the NDVI, precipitation and temperature over the past 15 years. We also explored the relationship between the NDVI and climate factors. Finally, based on two land-use maps, we analyzed the possible influence of human activities on the NDVI. This information can be useful when assessing the effects of ecological construction and for providing a scientific basis for corresponding policies.

2. Data and Methods

2.1. *Dataset.* The data used in this study were as follows:

- (1) NDVI data from 1998 to 2012 were obtained from SPOT-4 VGT-DN. The SPOT-4 satellite was launched in March 1998, having 10-day composite temporal resolution and 1-km² spatial resolution. The stretched values range from 0 to 255. The true NDVI values were restored with the following equation, which was

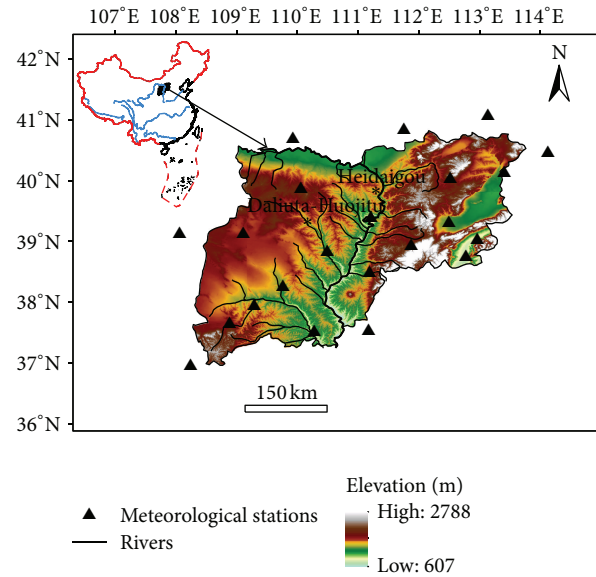


FIGURE 1: Location of the study area.

developed by the image processing and archiving center, VITO, Belgium (<http://www.vgt.vito.be/>):

$$\text{NDVI} = \text{DN} \times 0.004 - 0.1, \quad (1)$$

where DN is the digital count number used for storage.

- (2) Monthly precipitation and temperature from 22 weather stations were obtained from the China Meteorological Administration for the period of 1957 to 2012 and has been carried out quality control. A few missing data were interpolated based on values from neighboring stations over the same period. The IDW (Inverse Distance Weighted) interpolation method was used to interpret the spatial distribution of monthly and annual precipitation and temperature.
- (3) Two land-use maps (i.e., from 1997 and 2010) were used in this study. They were produced from Landsat Thematic Mapper (TM) images using the visual interpretation method. During the interpretation process, the practical field survey was considered, and land-use styles were classified into multiple categories, including farmland, forestland, grassland, water bodies, urban and built-up land, and unused land.

We also selected Heidaigou (111.22°E–111.33°E, 39.72°N–39.82°N) and Daliuta-Huojiu (110.05°E–110.12°E, 39.17°N–39.37°N), which represent the largest opencast mine and well mine bases in this area, respectively, to analyze their temporal NDVI variations as compared with those for the entire study area.

2.2. Methods

2.2.1. *Monthly and Annual NDVI.* The maximum value compositing (MVC) procedure, as described by Holben [36], was

used to merge NDVI values from 10 consecutive days to produce NDVI values for each month and year. The MVC method was found to be a reliable procedure for detecting changes in vegetation coverage and has been widely used to obtain monthly and annual NDVI values [37–40].

2.2.2. Calculation of NDVI Trends. To further investigate the yearly maximum NDVI trends, linear trends were examined on a perpixel basis from 1998 to 2012. This calculation is as follows:

$$\theta_{\text{slope}} = \frac{n \times \sum_{i=1}^n i \times \text{NDVI}_i - \sum_{i=1}^n i \sum_{i=1}^n \text{NDVI}_i}{n \times \sum_{i=1}^n i^2 - (\sum_{i=1}^n i)^2}, \quad (2)$$

where n represents the number of study years and NDVI_i is the maximum NDVI in the i th year. $\theta_{\text{slope}} > 0$ means that the NDVI over n years increased. The opposite relationship signifies a decreasing trend. The F test was used to examine the significance of these trends. Depending on the significance level of a given pixel, it was filtered into one of five classes: extremely significant increase (ESI) or decrease (ESD) ($P < 0.01$), significant increase (SI) or decrease (SD) ($0.01 < P < 0.05$), or no significant change (NSC) ($P > 0.05$).

2.2.3. Classification of Desertification Land. Previous research has shown that there is a linear relation between vegetation indices (e.g., the NDVI) and vegetation coverage. Therefore, the NDVI can be converted into vegetation coverage. Then, the study area, which has various vegetation coverages, can be classified according to desertification grading standards [41].

2.2.4. Partial Correlation Analysis Model. A coefficient of partial correlation is determined based on the simple correlation coefficient. The partial correlation coefficient of the NDVI and temperature or precipitation is defined as follows:

$$R_{xy \cdot z} = \frac{R_{xy} - R_{xz}R_{yz}}{\sqrt{(1 - R_{xz}^2)(1 - R_{yz}^2)}}, \quad (3)$$

where $R_{xy \cdot z}$ is the partial correlation coefficient between variables x and y when z is constant. Moreover, R_{xy} , R_{xz} , and R_{yz} represent the simple correlation coefficients between variables x and y , y and z , and x and z , respectively.

3. Results and Discussion

3.1. Temporal and Spatial Variation Characteristics of the NDVI

3.1.1. Spatial Distribution of the Annual Maximum NDVI. The spatial distribution of the annual maximum NDVI in the study area is shown in Figure 2(a). The NDVI gradually decreased from east to west, exhibiting evident spatial heterogeneities. For the entire region, the mean annual maximum NDVI from 1998 to 2012 was 0.44, ranging from 0.07 to 0.82. For the Heidaigou and Daliuta-Huojitu coal mining areas, the annual maximum NDVI values over the 15-year study

period were 0.36 and 0.38, respectively. The greatest NDVI values were located in mountainous and hilly regions in the southeastern portion of the study area. The sparse deciduous broad-leaved forest, including *Pinus tabulaeformis*, Poplar-birch, and *Larix principis-rupprechtii*, and secondary shrub-grassland are the dominant vegetation types. The lowest NDVI values were found in Jungar Banner, Ejin Horo Banner, and Wushen Banner in Inner Mongolia, as well as northern portions of Shaanxi province. Most areas of the northern Loess Plateau are typical semiarid temperate steppe areas, where the dominant vegetation can be characterized as shrub and semiarid herb; the main plant communities include the *Stipa* plant community, *Thymus serpyllum* community, *Caragana* community, *Sabina vulgaris* community, and *Artemisia ordosica* community.

3.1.2. Temporal and Spatial Variation of the NDVI. From 1998 to 2012, the NDVI exhibited an increasing trend in the study area, with a rate of increase of 0.09 per decade (Figure 2(b)). The annual maximum NDVI at the Heidaigou mining base exhibited an upward trend at a rate of 0.03 per decade, which was slower than the trend for the entire study area. The Daliuta-Huojitu coal mining base exhibited a trend of 0.12 per decade, which increased faster than the trend for the entire study area. The significance level for the NDVI trend is shown in Figure 2(c). Over the entire region, the areas where the NDVI exhibited ESI and SI trends accounted for 56.4% and 17.2% of the total area, respectively. Meanwhile, the areas where the NDVI exhibited NSC trends accounted for 26% of the total area, and the percentage of areas with SC and ESC trends was very small (less than 1%). At the Heidaigou mining base, the percentages of the area characterized as SI and ESI were only 17.4% and 9%, respectively, while NSC accounted for 50% of the area. At the Daliuta-Huojitu mining base, the vegetation coverage was found to be more abundant, and more than 95% of this area was classified as ESC.

Spatially (Figure 2(c)), the areas where the NDVI exhibited ESI trends from 1998 to 2012 were primarily distributed in northern Shaanxi province and the southeast edge of Mu Us Sandy Land. Areas where the NDVI exhibited SD trends were primarily located near Xingxian and Wuzhai in Shanxi and parts of Jungar Banner in Inner Mongolia. The areas where the NDVI exhibited NSC trends were primarily distributed near Youyu and Datong in Shanxi, and Liangcheng, Lingle, and the Qingshui River in Inner Mongolia. Furthermore, the annual maximum NDVI time series in the study area from 1998 to 2012 can be divided into three periods (Figure 2(d)). The regional average NDVI decreased from 1998 to 2001, then increased continuously from 2002 to 2008, and increased again from 2009 to 2012, although significant fluctuations were observed during this time period. The NDVI values at Heidaigou and Daliuta-Huojitu also exhibited similar three-stage variations, although the values were lower than the area average over the past 15-year period. The greatest annual NDVI occurred in 2012 for both the entire study area and the two coal mining areas. Moreover, excluding the period from 1998 to 2001, the NDVI at Daliuta-Huojitu was higher than that at Heidaigou.

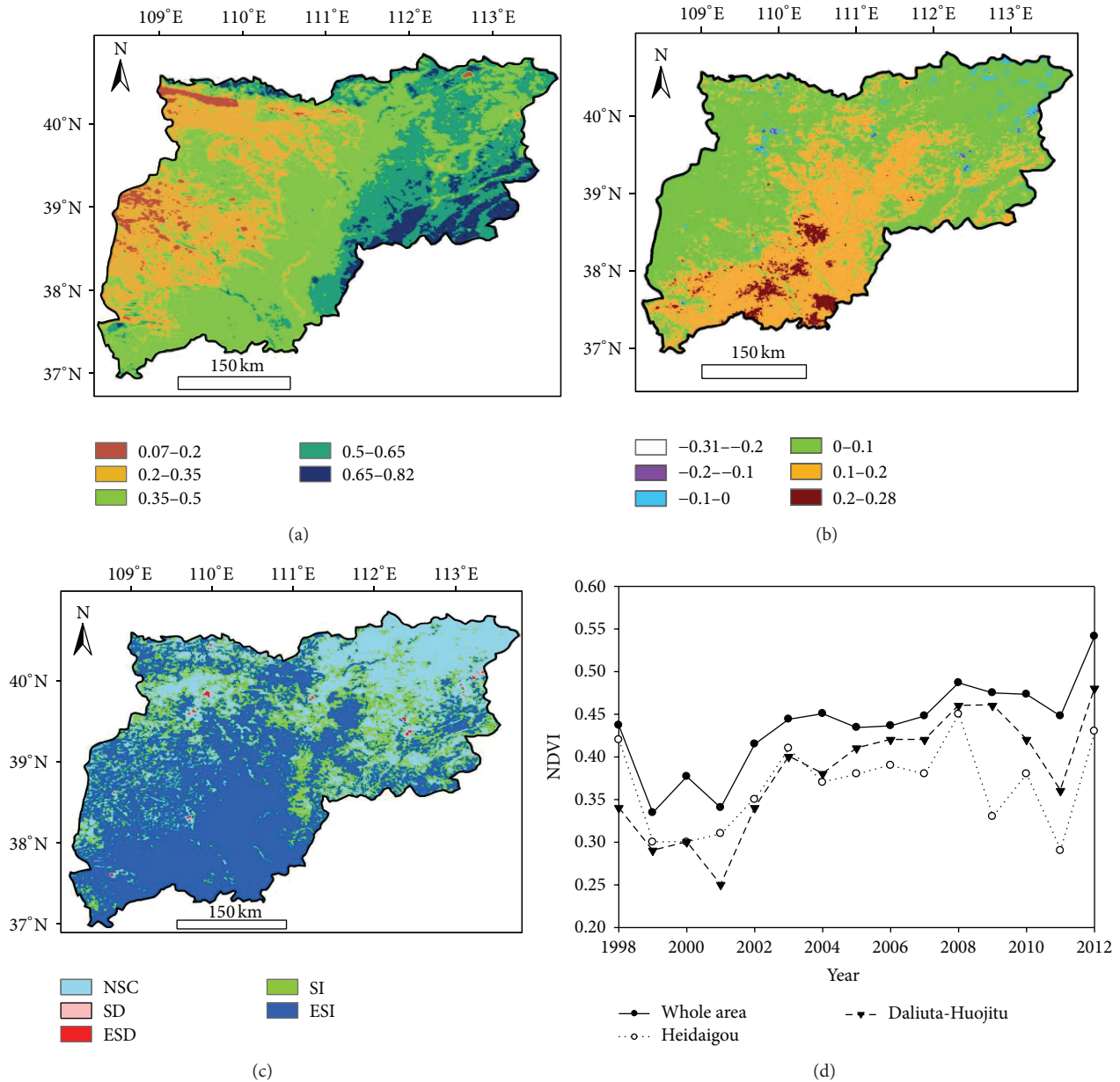


FIGURE 2: (a) The spatial distribution of the annual maximum NDVI; (b) the NDVI trends; (c) the significance level of the NDVI trends; and (d) the interannual NDVI changes for the northern Loess Plateau from 1998 to 2012.

3.1.3. The Dynamic Change of Desertification Land. According to the relationship between the NDVI and vegetation coverage [41], the study area can be divided into 5 grades, including slight, light, moderate, severe, and extremely severe desertification (Table 1). The proportional changes of land area for the different types of desertification are shown in Figure 3. Most areas in this region were characterized as exhibiting moderate and light desertification, accounting for 39.7% and 30.6% of the entire area, respectively. Areas of extremely severe and slight desertification were smaller, accounting for only 2.4% and 0.7% of the entire area, respectively.

Over the 15-year study period, extremely severe, moderate, and slight desertification areas slightly changed, while severe and light desertification areas significantly changed. Meanwhile, severe desertification areas decreased significantly ($P < 0.05$) from 54.7% in 1999 to 8.9% in 2012, which is an average of 2.1%/yr. Light desertification areas increased significantly ($P < 0.01$) from 36.7% in 1998 to 61% in 2012, which is an average of 2.2%/yr. At the Heidaigou and Daliuta-Huojiu coal mining locations, most areas were considered moderate desertification, accounting for 70.8% and 92.0% of the entire study area, respectively.

TABLE 1: Gradation standard for land desertification.

Desertification grade	Vegetation coverage	NDVI
Extremely severe	<0.1	<0.19
Severe	0.1–0.3	0.19–0.34
Moderate	0.3–0.5	0.34–0.51
Light	0.5–0.7	0.51–0.78
Slight	>0.7	0.78–0.83

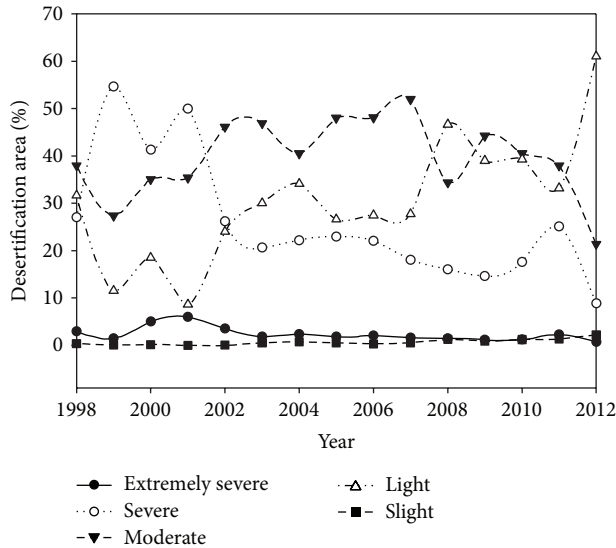


FIGURE 3: The proportional changes of land area for the different types of desertification on the northern Loess Plateau from 1998 to 2012.

3.2. Relationship between the NDVI and Climatic Factors

3.2.1. Annual Correlations between the NDVI and Climate.

From 1957 to 2012, the annual mean temperature (TEM) significantly increased over the entire study area at a rate of $0.24^{\circ}\text{C}/10\text{ yr}$ ($P < 0.05$) (Figure 4(a)). The annual precipitation (PRE) slightly decreased, at a rate of $9.16\text{ mm}/10\text{ yr}$ (Figure 4(b)). These rates indicate that a warming and drying trend occurred during the 56-year period. However, from 1998 to 2012, the average TEM of the study area was 8.8°C and exhibited a significant downward trend at the rate of $-0.61^{\circ}\text{C}/10\text{ yr}$ ($P < 0.05$). The TEM gradually decreased from the southwest to the northeast. The lowest TEM was located in the northeast region, with an annual average of less than 7°C , while the highest TEM was located in the southwest, with an annual average exceeding 10°C (Figure 4(c)). On an interannual time scale, the partial correlation coefficient of the NDVI and the TEM for the entire region was -0.29 . The areal percentage of the regions where the NDVI exhibited a negative correlation with the TEM was 86.62% (11.78% , $P < 0.05$; 72.47% , $P < 0.01$). These areas were primarily located in the western and southern regions of the study area. The areal percentage of the regions where a significantly positive correlation existed between the NDVI and the TEM was less than 1% ; these areas were primarily distributed in the northeast (Figure 5(a)).

From 1998 to 2012, the mean annual PRE for the region was 387.2 mm and it exhibited insignificant increasing trend at a rate of $52\text{ mm}/10\text{ yr}$ ($P > 0.05$). As shown in Figure 4(d), the PRE gradually decreased from the southeast to northwest; the smallest PRE was measured in the northwest, with an annual average of less than 360 mm . The greatest PRE was measured in the southeast, with an annual average of more than 420 mm . The partial correlation coefficient of the NDVI and the PRE for the entire region was 0.51 . The areal percentage of the regions where the NDVI exhibited a positive correlation with the PRE was 99.33% (30.04% , $P < 0.05$; 20.12% , $P < 0.01$), and the correlation coefficient between the NDVI and the PRE exhibited a strong increasing trend from the southwest to the northeast (Figure 5(b)). On the northern Loess Plateau, the correlation with the annual NDVI was stronger for precipitation than for temperature over the 15-year period. This finding can be explained by the fact that the study area is primarily located in arid and semiarid climate regimes, where precipitation is the limiting factor for vegetation growth and vegetation is more sensitive to precipitation changes. In general, higher temperatures will accelerate the evaporation process, which results in water scarcity and prohibits vegetation growth [42]. However, there was a significant decrease in temperature and a weak increase in precipitation in the study area from 1998 to 2012. These trends are good for vegetation growth and represent one of the major reasons for the increase in the annual NDVI.

3.2.2. Monthly Relationship between the NDVI and Climate.

The maximum monthly NDVI over the 15-year study period was observed on the northern Loess Plateau in August, which was largely controlled by the hydrothermal conditions during this period (Figure 6). Most areas of the northern Loess Plateau are considered to have a temperate continental grassland climate. In the summer (June to August), the climate is governed by marine air masses and prevailing easterly and southeasterly winds, which are characterized by high temperatures and copious rainfall. Approximately two-thirds of the annual precipitation is concentrated in the summer, which benefits vegetation growth. Furthermore, spring precipitation also increased at a rate of $2.45\text{ mm}/10\text{ yr}$ from 1998 to 2012, which is important for the accumulation of biomass production.

The effect of climatic factors on the NDVI may differ according to the growth phase [43]. Therefore, we performed partial correlation analyses for the monthly NDVI, temperature, and precipitation to determine the monthly and seasonal differences (Figure 7). The average correlation between the monthly NDVI and the TEM across the study area was -0.14 , which was weaker than that for an interannual time scale (-0.29) (Figure 7(a)). The areal percentage of the regions where the NDVI exhibited a negative correlation with the TEM was 58.32% . The percentage of significantly positive correlated areas did not exceed 1% , which was substantially less than that for an interannual time scale. In contrast, the correlation between the monthly NDVI and PRE was stronger than that for an interannual time scale (Figure 7(b)). For the study area average, the correlation coefficient was

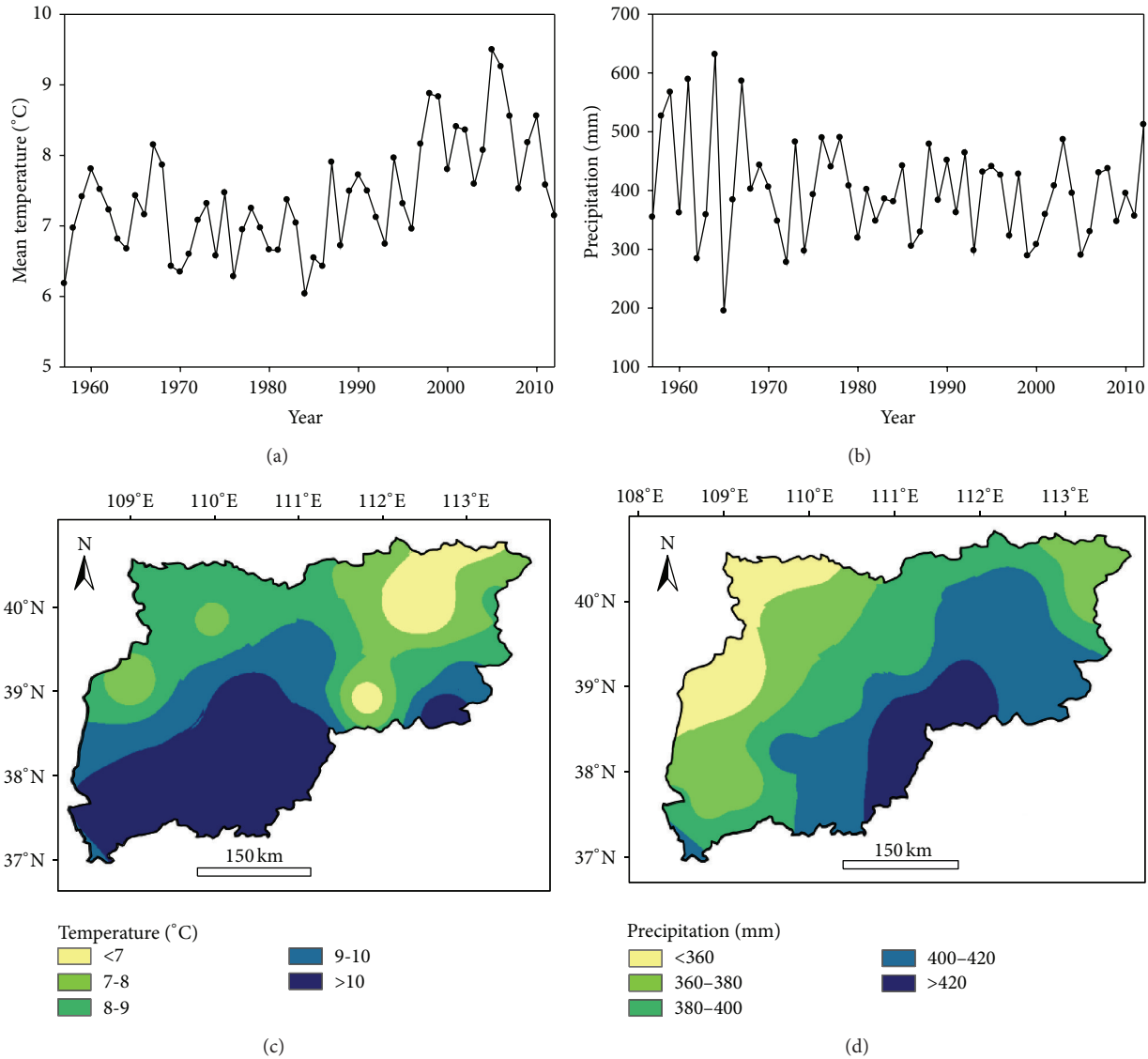


FIGURE 4: The temporal variation of interannual (a) temperature and (b) precipitation from 1957 to 2012; spatial change in the (c) annual mean temperature and (d) annual precipitation on the northern Loess Plateau from 1998 to 2012.

0.78, and the areal percentage of the regions where the NDVI exhibited a positive correlation with the PRE was 99.99% (41.28%, $P < 0.05$; 55.26%, $P < 0.01$). These results further suggest that the PRE was the dominant factor controlling plant growth because it was very sensitive to PRE changes.

3.2.3. Time Lag Effect of NDVI-PRE Relationship. According to Figure 6, the NDVI and the PRE exhibited similar temporal variations during the first half of the year. While in the latter half of the year, the NDVI response to the PRE exhibited a 1-month time lag. To further examine the synchrony and time-lag effects of the PRE and NDVI dynamics, we calculated the partial correlation coefficient between the NDVI and the PRE for the same month in the first half and the last half of the year and the NDVI for a particular month and the PRE for the preceding month in the last half of the year, respectively. The results showed that in the first half of the year, the average

correlation between the NDVI and the PRE over the study area for the same month was 0.90, and the areal percentage of the areas where the NDVI exhibited a significantly positive correlation with the PRE exceeded 55% of total study area ($P < 0.05$). This finding suggests that the NDVI was sensitive to the PRE of the same month in this period, which is similar to the results shown in Figure 6. Because the PRE in this period was small, the precipitation could be fully utilized by plants and converted to biomass production over short time periods.

The correlation between the NDVI of a particular month and the PRE of the preceding month in the last half of the year was 0.43, which was greater than that between the NDVI and the PRE for the same month in this period (0.33). The areal percentage of significantly positive correlated areas also increased ($P < 0.05$), demonstrating that a 1-month lag time existed between the NDVI and the PRE during the last half

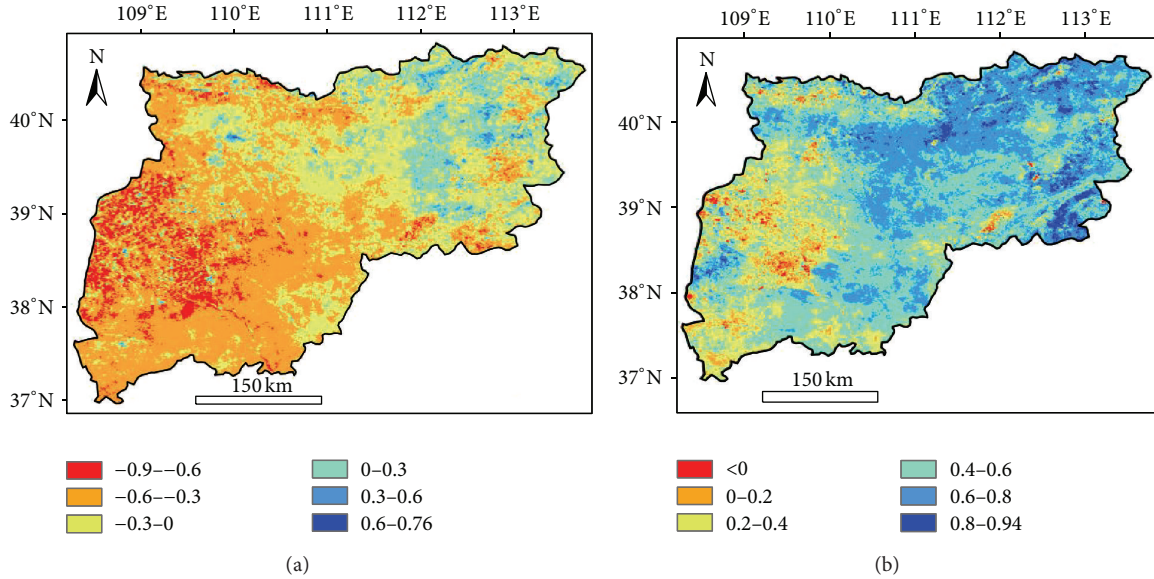


FIGURE 5: Correlation between the annual NDVI and annual (a) mean temperature and (b) precipitation on the northern Loess Plateau from 1998 to 2012.

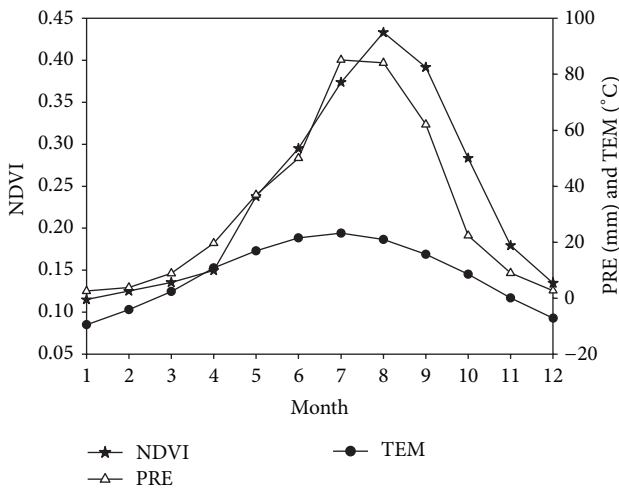


FIGURE 6: The monthly NDVI, precipitation, and temperature on the northern Loess Plateau from 1998 to 2012.

of the year. This lag can be explained by the fact that in this period, the PRE was large and could not be totally used by plants over short time periods. And the time required for the plants to use the water for production was approximately 1 month.

3.3. Influence of Human Activities on the NDVI

3.3.1. The Impacts of the “Grain for Green” Program. Climate change was found to be the most important factor influencing the spatial and temporal changes in vegetation coverage. However, human activities are also major driving factors and cannot be neglected. The Loess Plateau is well known for

its intensive soil erosion, contributing 90% of the sediments in the Yellow River [44]. In an attempt to reduce the soil erosion rate, the Chinese government launched the “Grain for Green” program (GGP) in 1999. The goals of this program were to increase forest coverage and mitigate soil erosion by converting agricultural lands on steep slopes to forests and grasslands [45]. Recently, several researchers have examined the effects of the GGP program. For example, Xiao used a variety of satellite data products from MODIS to assess the biophysical consequences of the GGP. He found that the average tree coverage in the plateau substantially increased, and the GGP led to significant increases in the enhanced vegetation index (EVI) and leaf area index (LAI) [23]. Tang et al. analyzed the spatial differences related to land-use change on Loess Plateau region from 1996 to 2005. They noted that farmland areas on the Loess Plateau decreased significantly, while forested areas increased significantly [46].

To further demonstrate the improvements in the vegetation condition on the northern Loess Plateau from 1997 to 2010, we studied the dynamic land-use change in the study area. Table 2 shows that the main land-use types in the study area were grassland, farmland, and forestland, which combined to account for 85.58% and 84.79% of the total area of the study region in 1997 and 2010, respectively. Forestland areas increased the most, that is, from 10140.58 km² in 1997 to 12373.57 km² in 2010, with an average annual increase of 159.50 km². Although grassland areas decreased the most, from 45.80% of the region in 1997 to 44.04% in 2010, the total area of forestland and grassland increased from 54.81% in 1997 to 55.04% in 2010. Farmland areas decreased at a rate of 81.38 km²/yr. These variations in land-use characteristics were similar to the results of Tang et al. [46]. Furthermore, the annual maximum NDVI exhibited a significantly increasing trend for forestland and grassland ($P < 0.05$). It can be

TABLE 2: Changes in land-cover area on the northern Loess Plateau region between 1997 and 2010.

Land type	Area in 1997 (km ²)	Area ratio in 1997 (%)	Area in 2010 (km ²)	Area ratio in 2010 (%)
Farmland	34604.82	30.76	33465.49	29.75
Forestland	10140.58	9.01	12373.57	11.00
Grassland	51520.69	45.80	49540.2	44.04
Water bodies	1935.73	1.72	1986.34	1.77
Urban and built-up land	1549.50	1.38	1942.18	1.73

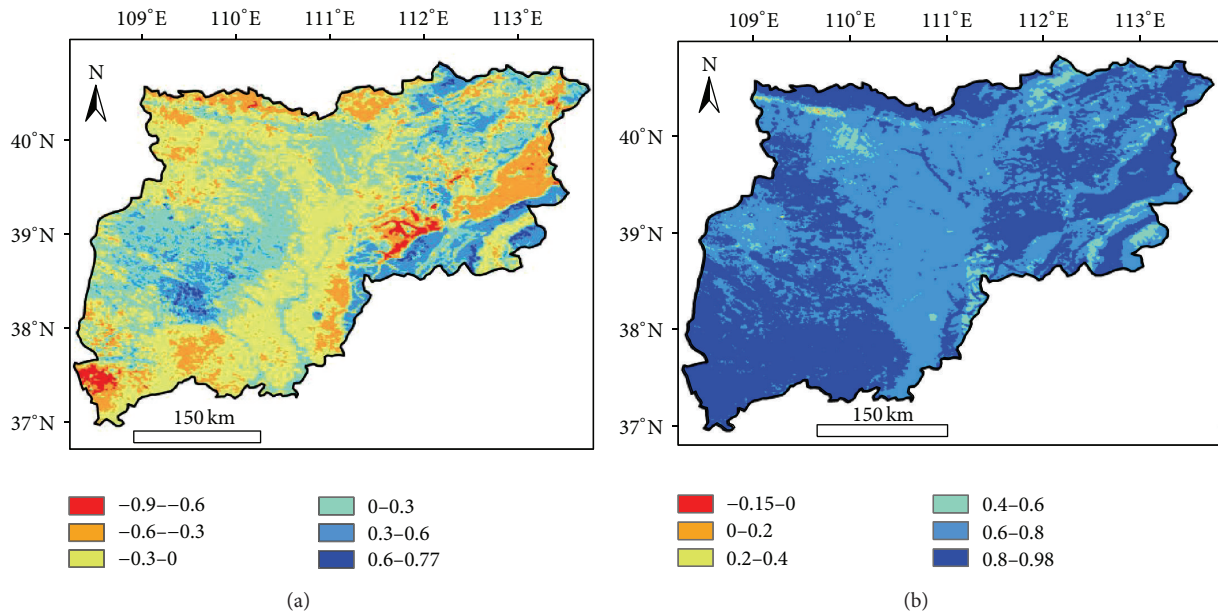


FIGURE 7: Correlation relationship between the monthly NDVI and monthly (a) mean temperature and (b) precipitation on the northern Loess Plateau from 1998 to 2012.

concluded that the increasing NDVI trend and land-use changes indicate that the GGP was successful over the 15-year study period on the northern Loess Plateau.

Although the farmland areas decreased from 1998 to 2010, its NDVI increased significantly over the 15-year study period ($P < 0.05$). This change can be explained by agricultural activities, such as the use of fertilizer and pesticides, the construction of water conservation facilities, and intensive agricultural management, which led to increases in grain yields and/or biomass production, thus increasing the NDVI in these areas. The Hetao Plain, which is located on the northern Loess Plateau, is one such example. From 1982 to 2005, the grain yield increased, reaching a steady state in the late 1990s. Simultaneously, the vegetation coverage in this area also increased and was positively correlated with the grain yield [47].

3.3.2. The Impacts of Coal Mining. The NDVI values at the two coal mining bases were lower than those for the entire study area. At Heidaigou, the NDVI was the lowest, especially over the most recent 10 years, which was largely due to massive open-pit mining. During opencast mining, the surface soil layer and vegetation are completely destroyed by mechanical excavation. Moreover, water resources, including

groundwater, soil water and surface water, and soil quality are also influenced by coal mining, thus affecting vegetation growth. But it is noting that the NDVI values at the two coal mining bases also increased over the recent 15 years, which was due to mine protection investments and successful environmental treatments. Using the Shenfu-Dongsheng coal mine base as an example, the coal company invested 0.45 yuan per ton of coal for environmental protection. As coal production increases, so does the amount of funds used to protect coal mining areas, which has guaranteed the sustainability and stabilization of greening and environmental treatments and has played an important role in improving vegetation coverage at coal mining bases.

4. Conclusions

This study combined SPOT VEGETATION and climatic factor data from 1998 to 2012 to analyze spatial and temporal vegetation variations in the context of climate change. We also explored the potential impacts of human activities on the observed NDVI changes on the northern Loess Plateau. Our conclusions are as follows.

The spatial distribution of the annual maximum NDVI on the northern Loess Plateau exhibited obvious heterogeneity.

The NDVI gradually decreased from east to west. The annual maximum NDVI was 0.44, increasing at a rate of 0.09 per decade. The areas where the NDVI significantly increased accounted for 73.6% of the total area, and severe desertification areas decreased significantly ($P < 0.05$) from 54.7% in 1999 to 8.9% in 2012 (a rate of 2.1%/yr). This result indicates that the vegetation condition has improved in this area. Although the NDVI values at the two coal mining bases increased over the 15-year study period, they were all lower than the values for the entire study area, which was largely due to massive open-pit mining.

From 1998 to 2012, the temperature significantly decreased at a rate of $-0.61^{\circ}\text{C}/10$ yr, while the precipitation slightly increased at a rate of 52 mm/10 yr. The precipitation also increased in spring and summer, which promoted vegetation growth and represents one of the major reasons for the increase in the annual NDVI. The correlation with the annual NDVI was stronger for precipitation than temperature, indicating that vegetation is more sensitive to precipitation changes in this area. The NDVI and PRE changed synchronously during the first half of the year, while a 1-month lag time existed between the NDVI and PRE during the last half of the year.

From 1998 to 2012, the total areas of forestland and grassland increased, and the annual maximum NDVI exhibited an increasing trend for these two land-use types ($P < 0.05$), indicating that the GGP was successful over the 15-year study period on the northern Loess Plateau. Although the farmland areas decreased, its NDVI increased significantly over the 15-year study period ($P < 0.05$), which can be explained by positive agricultural activities. Moreover, the NDVI improvements at the two coal mining bases were related to environmental protection investments and successful environmental treatments. Therefore, we conclude that positive human activities were another reason for the vegetation condition improvements.

Conflict of Interests

The authors declare that there is no conflict of interests regarding the publication of this paper.

Acknowledgments

This study was supported by the the CAS Action-Plan for Western Development (KZCX2-XB3-13) and Water conservancy science and technology project of Shaanxi Province. The authors also highly appreciated the editor and two anonymous reviewers for their thoughtful comments that were of big help in improving the paper.

References

- [1] J. Peng, Z. Liu, Y. Liu, J. Wu, and Y. Han, "Trend analysis of vegetation dynamics in Qinghai-Tibet Plateau using Hurst Exponent," *Ecological Indicators*, vol. 14, no. 1, pp. 28–39, 2012.
- [2] H. Godínez-Alvarez, J. E. Herrick, M. Mattocks, D. Toledo, and J. van Zee, "Comparison of three vegetation monitoring methods: their relative utility for ecological assessment and monitoring," *Ecological Indicators*, vol. 9, no. 5, pp. 1001–1008, 2009.
- [3] X. W. Chuai, X. J. Huang, W. J. Wang, and G. Bao, "NDVI, temperature and precipitation changes and their relationships with different vegetation types during 1998–2007 in Inner Mongolia, China," *International Journal of Climatology*, vol. 33, no. 7, pp. 1696–1706, 2013.
- [4] S. Piao and J. Fang, "Seasonal changes in vegetation activity in response to climate changes in China between 1982 and 1999," *Acta Geographica Sinica*, vol. 58, no. 1, pp. 119–125, 2003.
- [5] B. Fu, S. Li, X. Yu et al., "Chinese ecosystem research network: progress and perspectives," *Ecological Complexity*, vol. 7, no. 2, pp. 225–233, 2010.
- [6] J. W. Rouse Jr., R. Haas, J. Schell et al., "Monitoring vegetation systems in the Great Plains with ERTS," *NASA Special Publication*, vol. 351, p. 309, 1974.
- [7] C. Li, J. Qi, L. Yang et al., "Regional vegetation dynamics and its response to climate change—a case study in the Tao River Basin in Northwestern China," *Environmental Research Letters*, vol. 9, no. 12, Article ID 125003, 2014.
- [8] J. Fang, S. Piao, J. He, and W. Ma, "Increasing terrestrial vegetation activity in China, 1982–1999," *Science in China Series C: Life Sciences*, vol. 47, no. 3, pp. 229–240, 2004.
- [9] Z. Yin and T. H. Lee Williams, "Obtaining spatial and temporal vegetation data from Landsat MSS and AVHRR/NOAA satellite images for a hydrologic model," *Photogrammetric Engineering and Remote Sensing*, vol. 63, no. 1, pp. 69–77, 1997.
- [10] C. Liu, X. Dong, and Y. Liu, "Changes of NPP and their relationship to climate factors based on the transformation of different scales in Gansu, China," *CATENA*, vol. 125, pp. 190–199, 2015.
- [11] S. L. Piao, J. Y. Fang, and J. S. He, "Variations in vegetation net primary production in the Qinghai-Xizang Plateau, China, from 1982 to 1999," *Climatic Change*, vol. 74, no. 1–3, pp. 253–267, 2006.
- [12] F. Rembold and F. Maselli, "Estimation of inter-annual crop area variation by the application of spectral angle mapping to low resolution multitemporal NDVI images," *Photogrammetric Engineering and Remote Sensing*, vol. 72, no. 1, pp. 55–62, 2006.
- [13] M. S. Mkhabela, P. Bullock, S. Raj, S. Wang, and Y. Yang, "Crop yield forecasting on the Canadian Prairies using MODIS NDVI data," *Agricultural and Forest Meteorology*, vol. 151, no. 3, pp. 385–393, 2011.
- [14] D.-Y. Gong and P.-J. Shi, "Northern hemispheric NDVI variations associated with large-scale climate indices in spring," *International Journal of Remote Sensing*, vol. 24, no. 12, pp. 2559–2566, 2003.
- [15] D. A. Walker, H. E. Epstein, G. J. Jia et al., "Phytomass, LAI, and NDVI in northern Alaska: relationships to summer warmth, soil pH, plant functional types, and extrapolation to the circumpolar arctic," *Journal of Geophysical Research D: Atmospheres*, vol. 108, no. 2, pp. 10–15, 2003.
- [16] J. Y. Zhang, W. J. Dong, C. B. Fu, and L. Wu, "The influence of vegetation cover on summer precipitation in China: a statistical analysis of NDVI and climate data," *Advances in Atmospheric Sciences*, vol. 20, no. 6, pp. 1002–1006, 2003.
- [17] R. P. Singh, S. Roy, and F. Kogan, "Vegetation and temperature condition indices from NOAA AVHRR data for drought monitoring over India," *International Journal of Remote Sensing*, vol. 24, no. 22, pp. 4393–4402, 2003.

- [18] Q. Wang, M. Watanabe, S. Hayashi, and S. Murakami, "Using NOAA AVHRR data to assess flood damage in China," *Environmental Monitoring and Assessment*, vol. 82, no. 2, pp. 119–148, 2003.
- [19] R. B. Myneni, C. D. Keeling, C. J. Tucker, G. Asrar, and R. R. Nemani, "Increased plant growth in the northern high latitudes from 1981 to 1991," *Nature*, vol. 386, no. 6626, pp. 698–702, 1997.
- [20] A. Kawabata, K. Ichii, and Y. Yamaguchi, "Global monitoring of interannual changes in vegetation activities using NDVI and its relationships to temperature and precipitation," *International Journal of Remote Sensing*, vol. 22, no. 7, pp. 1377–1382, 2001.
- [21] J. Xiao and A. Moody, "Geographical distribution of global greening trends and their climatic correlates: 1982–1998," *International Journal of Remote Sensing*, vol. 26, no. 11, pp. 2371–2390, 2005.
- [22] S. Liang, J. Chen, X. Jin et al., "Regularity of vegetation coverage changes in the Tibetan Plateau over the last 21 years," *Advances in Earth Science*, vol. 22, no. 1, pp. 33–40, 2007.
- [23] J. F. Xiao, "Satellite evidence for significant biophysical consequences of the 'Grain for Green' Program on the Loess Plateau in China," *Journal of Geophysical Research: Biogeosciences*, vol. 119, no. 12, pp. 2261–2275, 2014.
- [24] T. Wang, X. Kou, Y. Xiong, P. Mou, J. Wu, and J. Ge, "Temporal and spatial patterns of NDVI and their relationship to precipitation in the loess plateau of China," *International Journal of Remote Sensing*, vol. 31, no. 7, pp. 1943–1958, 2010.
- [25] M. T. Schnur, H. Xie, and X. Wang, "Estimating root zone soil moisture at distant sites using MODIS NDVI and EVI in a semi-arid region of southwestern USA," *Ecological Informatics*, vol. 5, no. 5, pp. 400–409, 2010.
- [26] X. Chen and R. Yu, "Spatial and temporal variations of the vegetation growing season in warm-temperate eastern China during 1982 to 1999," *Acta Geographica Sinica*, vol. 62, no. 1, pp. 41–51, 2007.
- [27] D. C. Sohoulane Djebou, V. P. Singh, and O. W. Frauenfeld, "Vegetation response to precipitation across the aridity gradient of the southwestern United states," *Journal of Arid Environments*, vol. 115, pp. 35–43, 2015.
- [28] W. Thavornntam and N. Tantemsapya, "Vegetation greenness modeling in response to climate change for Northeast Thailand," *Journal of Geographical Sciences*, vol. 23, no. 6, pp. 1052–1068, 2013.
- [29] R. Cao, W. Jiang, L. Yuan, W. Wang, Z. Lv, and Z. Chen, "Inter-annual variations in vegetation and their response to climatic factors in the upper catchments of the Yellow River from 2000 to 2010," *Journal of Geographical Sciences*, vol. 24, no. 6, pp. 963–979, 2014.
- [30] X. Liu, J. Zhang, X. Zhu et al., "Spatiotemporal changes in vegetation coverage and its driving factors in the Three-River Headwaters Region during 2000–2011," *Journal of Geographical Sciences*, vol. 24, no. 2, pp. 288–302, 2014.
- [31] J. Wang, P. M. Rich, and K. P. Price, "Temporal responses of NDVI to precipitation and temperature in the central Great Plains, USA," *International Journal of Remote Sensing*, vol. 24, no. 11, pp. 2345–2364, 2003.
- [32] P. A. Schultz and M. S. Halpert, "Global analysis of the relationships among a vegetation index, precipitation and land surface temperature," *International Journal of Remote Sensing*, vol. 16, no. 15, pp. 2755–2777, 1995.
- [33] Y. Liu, X. Wang, M. Guo, H. Tani, N. Matsuoka, and S. Matsumura, "Spatial and temporal relationships among NDVI, climate factors, and land cover changes in Northeast Asia from 1982 to 2009," *GIScience & Remote Sensing*, vol. 48, no. 3, pp. 371–393, 2011.
- [34] Y. He, X. Guo, P. Dixon, and J. F. Wilmshurst, "NDVI variation and its relation to climate in Canadian ecozones," *The Canadian Geographer*, vol. 56, no. 4, pp. 492–507, 2012.
- [35] G. Tian, X. Shang, J. Li et al., "A strategic study of coal exploitation in Shanxi, Shannxi and Inner Mongolia," *Coal Geology of China*, vol. 20, no. 3, pp. 1–15, 2008.
- [36] B. N. Holben, "Characteristics of maximum-value composite images from temporal AVHRR data," *International Journal of Remote Sensing*, vol. 7, no. 11, pp. 1417–1434, 1986.
- [37] S. Chamailé-Jammes and H. Fritz, "Precipitation-NDVI relationships in eastern and southern African savannas vary along a precipitation gradient," *International Journal of Remote Sensing*, vol. 30, no. 13, pp. 3409–3422, 2009.
- [38] Y. He, X. Guo, P. Dixon, and J. F. Wilmshurst, "NDVI variation and its relation to climate in Canadian ecozones," *Canadian Geographer*, vol. 56, no. 4, pp. 492–507, 2012.
- [39] M. Lanfredi, R. Lasaponara, T. Simoniello, V. Cuomo, and M. Macchiato, "Multiresolution spatial characterization of land degradation phenomena in southern Italy from 1985 to 1999 using NOAA-AVHRR NDVI data," *Geophysical Research Letters*, vol. 30, no. 2, 2003.
- [40] J. Sun, G. Cheng, W. Li, Y. Sha, and Y. Yang, "On the variation of NDVI with the principal climatic elements in the Tibetan Plateau," *Remote Sensing*, vol. 5, no. 4, pp. 1894–1911, 2013.
- [41] Y. Song and M. Ma, "Study on vegetation cover change in northwest China based on SPOT VEGETATION data," *Journal of Desert Research*, vol. 27, no. 1, pp. 90–94, 2007.
- [42] E. G. Jobbágy, O. E. Sala, and J. M. Paruelo, "Patterns and controls of primary production in the Patagonian steppe: a remote sensing approach," *Ecology*, vol. 83, no. 2, pp. 307–319, 2002.
- [43] S. Piao, A. Mohammat, J. Fang, Q. Cai, and J. Feng, "NDVI-based increase in growth of temperate grasslands and its responses to climate changes in China," *Global Environmental Change*, vol. 16, no. 4, pp. 340–348, 2006.
- [44] M.-E. Ren and Y.-L. Shi, "Sediment discharge of the Yellow River (China) and its effect on the sedimentation of the Bohai and the Yellow Sea," *Continental Shelf Research*, vol. 6, no. 6, pp. 785–810, 1986.
- [45] X. Mu, L. Zhang, T. R. McVicar, B. Chille, and P. Gau, "Analysis of the impact of conservation measures on stream flow regime in catchments of the Loess Plateau, China," *Hydrological Processes*, vol. 21, no. 16, pp. 2124–2134, 2007.
- [46] Q. Tang, Y. Xu, and Y. Liu, "Spatial difference of land use change in Loess Plateau region," *Journal of Arid Land Resources and Environment*, vol. 24, no. 8, pp. 15–21, 2010.
- [47] Z. Xin, J. Xu, and W. Zheng, "The impacts of climate variability and human activities on the change of vegetation coverage on the Loess Plateau," *Science China Earth Sciences*, vol. 37, no. 11, pp. 1504–1514, 2007.

Research Article

Contribution of River Mouth Reach to Sediment Load of the Yangtze River

C. Wang,^{1,2} S. B. Dai,² L. S. Ran,³ L. Jiang,² and W. T. Li²

¹State Key Laboratory of Soil Erosion and Dry Land Farming on the Loess Plateau, Institute of Water and Soil Conservation, Chinese Academy of Sciences and Ministry of Water Resources, Yangling, Shaanxi 712100, China

²Anhui Center for Collaborative Innovation in Geographical Information Integration and Application, Chuzhou University, Fengle Road 1528, Chuzhou, Anhui 239012, China

³Department of Geography, National University of Singapore, 10 Kent Ridge Crescent, Singapore 119260

Correspondence should be addressed to S. B. Dai; shibaodai@163.com

Received 4 February 2015; Revised 9 April 2015; Accepted 21 April 2015

Academic Editor: Steffen Mischke

Copyright © 2015 C. Wang et al. This is an open access article distributed under the Creative Commons Attribution License, which permits unrestricted use, distribution, and reproduction in any medium, provided the original work is properly cited.

This paper examined the sediment gain and loss in the river mouth reach of the Yangtze River by considering sediment load from the local tributaries, erosion/accretion of the river course, impacts of sand mining, and water extraction. A quantitative estimation of the contribution of the river mouth reach to the sediment load of the Yangtze River was conducted before and after impoundment of the Three Gorges Dam (TGD) in 2003. The results showed that a net sediment load loss of 1.78 million ton/yr (Mt/yr) occurred from 1965 to 2002 in the study area. The contribution of this reach to the sediment discharge into the sea is not as high as what was expected before the TGD. With impoundment of the TGD, channel deposition (29.90 Mt/yr) and a net sediment loss of 30.89 Mt/yr occurred in the river mouth reach from 2003 to 2012. The river mouth reach has acted as a sink but not a source of sediment since impoundment of the TGD, which has exacerbated the decrease in sediment load. Technologies should be advanced to measure changes in river channel morphology, as well as in water and sediment discharges at the river mouth reach.

1. Introduction

Over the past several decades, riverine sediment issues have received a great deal of attention worldwide because of the importance of sediment transport in fluvial systems [1, 2], as well as increasing anthropogenic impacts, such as construction of the Three Gorges Dam (TGD) in the Yangtze River (or Changjiang in Chinese) basin [3]. Many rivers have experienced decreasing sediment loads, triggering bank collapses and channel erosion in their deltas [4, 5]. Sediment load in the Yangtze River has decreased sharply since the 1950s, due largely to dam construction [2, 6, 7]. This has led to serious river management problems, such as channel erosion and delta retreat [2, 6, 8]. Additionally, undercutting of the river channel has reduced the water level and depleted water resources in the dry season [9]. Delta erosion has hampered expansion of the shoreline and government land exploitation projects in Shanghai, the largest city in China. The world's largest dam (the TGD) was put into operation on the river in

2003. Since then, more than 70% of the sediment [6, 10] that previously passed through the dam site has been sequestered. Sediment starvation of the downstream waters has had serious impacts, including undercutting of the river channel bed and bank failures. Because of the large-scale human activities within the watershed, the Yangtze River provides a valuable opportunity to evaluate the responses of a river system to natural and anthropogenic impacts.

Though many studies have been conducted to investigate sediment in the Yangtze River, little attention has been given to the lower reaches, especially below Datong station. Sediment load at Datong station (located at the tidal limit, 624 km upstream of the river mouth) is generally taken as the sediment flux that is discharged into the ocean from the Yangtze River [6, 10] since there is no gauging station on the river trunk below. Sediment export in the river mouth reach (from Datong station to the estuary) remains largely unknown to researchers, partly because of the complex impacts of tides. Previous studies have shown that the main channel and

connected lakes have great potential to regulate sediment transport processes of the Yangtze River [11]. Hence, the river mouth reach might also play an important role in its sediment budget in the context of sediment deficiency after closure of the TGD. This is for several reasons; namely, (a) the river mouth reach extends 624 km from Datong station to the sea, comprising one-tenth of the total length of the Yangtze River. The channel width in this reach varies from 1 to 10 km, which provides the potential to regulate sediment discharge from the upper reaches [11]; (b) the local drainage area in this reach is about $0.1 \times 10^6 \text{ km}^2$ ($\approx 6\%$ of the total drainage area of the Yangtze River basin); accordingly, sediment supply from this area cannot be neglected; (c) the Huaihe River (a large river located in the northern part of the Yangtze River basin) joins the Yangtze River in this reach. Accordingly, sediment supply from the Huaihe River might play an important role in mitigating the sediment deficiency of the Yangtze River; (d) finally, intensified anthropogenic activities, such as sand mining and water diversion, may have substantial impacts on the sediment processes.

Taking the above factors into account, sediment discharge into the sea from the Yangtze River would be quite different from that gauged at Datong station. Since less sediment has been discharged into the river mouth in recent years, sediment supply from this local reach might play an increasingly important role in maintenance of sediment balance in this reach and coastal areas. An exact evaluation of the quantity of sediment discharged into the sea will be beneficial to both scientific research and government engineering projection. Furthermore, since many of the lowest gauging stations on rivers worldwide are located at a distance from the river mouths, investigation of the buffering function of the river mouth reaches is essential for proper determination of variations in riverine sediment flux to the sea and understanding the land-sea interaction. Accordingly, the results presented herein will be useful to studies of other similar rivers.

In this study, a quantitative evaluation of sediment discharge into the sea was conducted using the sediment budget method. The specific goals of the study were to (a) evaluate sediment supply from local tributaries and the Huaihe River in the river mouth reach, (b) examine the erosion/accretion of the river course, including the impacts of sand mining, (c) evaluate sediment losses because of water extraction, and (d) establish a sediment budget for this reach and evaluate how much sediment is discharged into the sea, especially after closure of the TGD.

2. Physical Setting

The Yangtze River originates from the Qinghai-Tibetan Plateau at an elevation of 5100 m and runs east for 6300 km to the East China Sea (Figure 1). The main source of sediment in the Yangtze River is the lower section of the upper reach, which ends at Yichang (where the TGD is located). Significant sediment deposition occurred in the middle reaches, from Yichang to Hankou [10, 11], before 2003. However, the deposition reach shifted to the upper Yichang following impoundment of the TGD. The channel in the lower reach (from Hankou to Datong) has remained largely in balance in the

last few decades, and Datong station is free of tidal influences. Given the difficulty quantifying the effects of tidal impacts on sediment transport, estimating sediment load below Datong is very challenging. Therefore, the observed sediment flux at Datong station is generally regarded as the sediment load into the ocean. The river course below Datong station mainly drains through Anhui and Jiangsu Provinces, and Datong station is located in the middle of Anhui Province. The channel length below Datong station in Anhui Province is 199 km, which is half the total channel length at Anhui Province. The total length from the boundary of Anhui to Jiangyin, which is located at the tidal flow limit in the low flow seasons in Jiangsu Province, is 218 km. Shanghai is located at the mouth of the river. The entire subbasin of the river mouth reach is in the most prosperous area in China, and intensified human impacts of projects such as sand mining and water diversion are widespread.

Several tributaries join the Yangtze River below Datong station, namely, the Yuxi, Qingyijiang, Shuiyangjiang, Chuhe, and Qinhuaihe rivers, and the Lake Taihu system. These tributaries originate from the low hilly areas alongside the trunk river and then drain through the alluvial plain along the Yangtze River (Figure 1). The annual precipitation is 1000–1100 mm in this local drainage area. The specific soil erosion rate is less than that of the above reaches of the Yangtze River because of the lower relief and better vegetation cover.

The Huaihe River is one of the seven largest rivers in China, with a drainage area of 0.27 million km^2 . Historically, the Huaihe River was an independent river system that discharged into the Yellow Sea. However, after 1128, the majority of its runoff and sediment load (80%) was discharged into the Yangtze River through a connective waterway because of the diversion of the Huanghe River [18]. Annually, $22.6 \times 10^9 \text{ m}^3$ and 3.73 million tons (Mt/yr) of water and sediment were discharged into the Yangtze River from the Huaihe River, respectively, from 1965 to 2005. Thus, the actual water and sediment load discharged into the river mouth reach is not only from the upper reaches, although runoff and sediment from the Huaihe River are commonly neglected. In the present study, sediment discharge from the Huaihe River was taken into account.

3. Data and Methods

The sediment budget method is widely used to examine the sediment transport process in river systems [19]. In this study, a sediment budget was established in the river mouth reach to evaluate its contribution to sediment discharge from the Yangtze River and determine how much sediment is discharged into the sea. Consider

$$Q_{s,\text{out}} = Q_{s,\text{upper reach}} + Q_{s,\text{local reach}} + Q_{s,\text{erosion}} - Q_{s,\text{deposition}} - Q_{s,\text{water extraction}}, \quad (1)$$

where $Q_{s,\text{out}}$ is the sediment discharged out of the river course and into the sea, $Q_{s,\text{upper reach}}$ refers to the sediment load from the upper reach, $Q_{s,\text{local reach}}$ is sediment load from the local tributaries in the river mouth reach (including the Huaihe

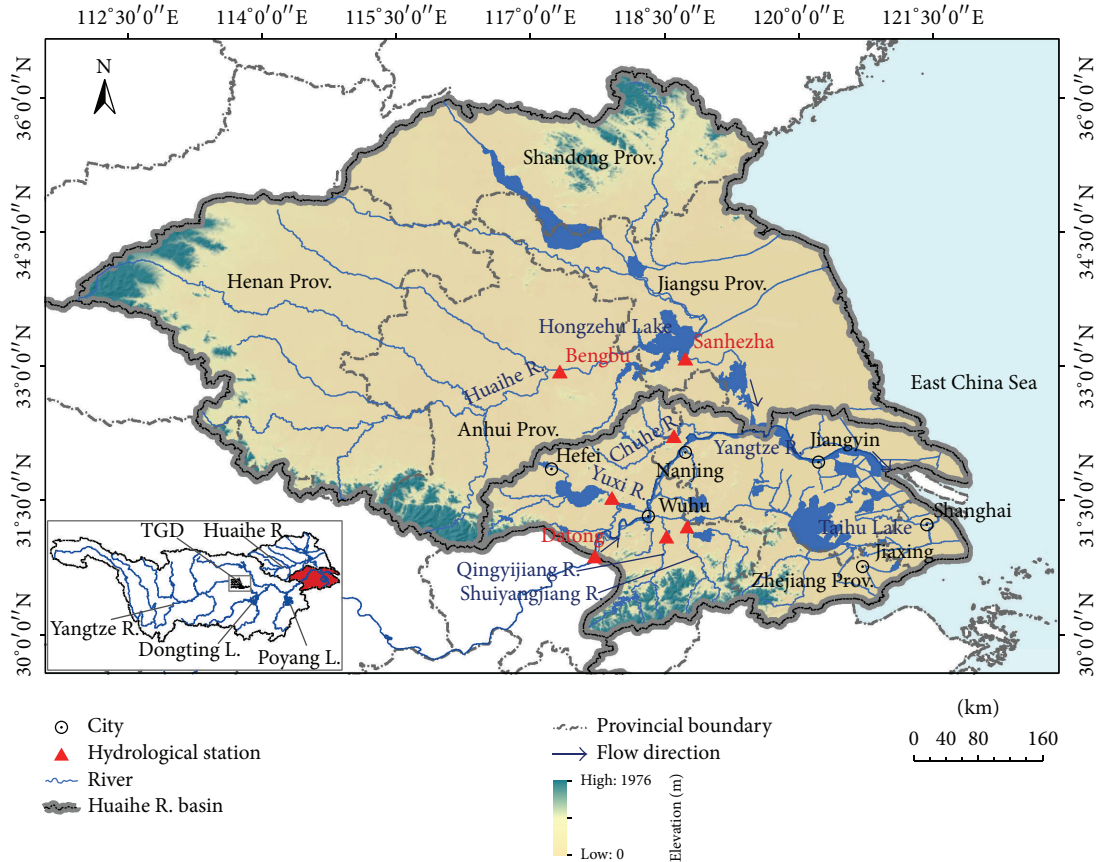


FIGURE 1: Map of the study area.

River), $Q_{s,water\ extraction}$ refers to sediment losses because of the water extraction, and $Q_{s,erosion}$ and $Q_{s,deposition}$ refer to the sediment eroded from or deposited in the river channel, respectively.

A variety of data sources were collected to build this budget. The annual sediment load at Datong station and some tributaries (such as the Yuxi River, Qingyijiang River, Shuiyangjiang River, and the Chuhe River) from 1965 to 2005 was obtained from the Hydrology Bureau of Anhui Province, which is an affiliate of the Ministry of Water Resources of China (MWRC). The data describing the Huaihe River [13, 14] and Taihu Lake system [12] are from previously published material. Channel erosion/accretion data were obtained from Wang et al. [16], Liu [15], and Qu [17], who conducted studies based on relief maps. The data sources of Wang et al. [16] and Qu [17] are maps published by the Navigation Guarantee Department of Chinese Navy Headquarters, while Liu [15] used data provided by the Bureau of Changjiang River Management of Anhui Province.

The total drainage area of the river mouth reach is 0.1 million km^2 , while the total drainage area of the Yuxi, Qingyijiang, Shuiyangjiang, and Chuhe rivers is 24,568 km^2 , and the total drainage area of the Lake Taihu system is 36,895 km^2 . Thus, there is still an area of about 38,537 km^2 that is not gauged or for which gauged data is not available (hereafter referred to as ungauged area). To establish the sediment

budget, it is necessary to evaluate sediment yield from this area. Owing to the similarity of the natural conditions of the ungauged area to the Yuxi, Qingyijiang, Shuiyangjiang, and Chuhe rivers, the average specific sediment yield of these four rivers was assigned to the ungauged area.

4. Results

4.1. Sediment Supply from the Local Tributaries. The local drainage area of the river mouth reach could be divided into three parts, the area that the four gauged rivers (the Yuxi, Qingyijiang, Shuiyangjiang, and Chuhe rivers) drain through, the area composed of regions that are not gauged or for which gauging data is not available, and the Lake Taihu drainage system. The average sediment load from each area is shown in Table 1, and the temporal variations of the four rivers are shown in Figure 2. The combined sediment from the four rivers was 1.45 Mt/yr during 1965–2002. The ungauged area was 1.56-fold larger than that of the four rivers. Sediment load from this area was 2.26 Mt/yr, assuming that it has the same specific sediment yield as the basins of the four rivers. The sediment load of the Lake Taihu system was obtained from a study by Wu [12], who reported that 0.1 Mt/yr of sediment was discharged from the system in 1954. This was a high flow year in Lake Taihu, and 0.1 Mt/yr may be among the highest discharges that occurred from 1965 to 2012.

TABLE 1: Sediment load of the tributaries of the river mouth reach of the Yangtze River.

River	Station	Drainage area (km ²)	Sediment load (Mt/yr)		Data source
			1965–2002	1996–2005	
Qingyijiang	Xihe	5796	0.36	0.23	MWRC*
Shuiyangjiang	Xuancheng	3410	0.53	0.27	MWRC*
Yuxihe	Chaohezha	9258	0.38	0.18	MWRC*
Chuhe	Chaheji	6104	0.18	0.08	MWRC*
Total rivers		24,568	1.45		
Taihu Lake		36,895	0.10	0.10	[12]
Ungauged area		38,537	2.38	1.14	Estimation in this study
Sum		100,000	3.81	2	
Huaihe	Sanhezha	270,000	3.73	2.64	[13, 14]
Total			7.54	4.65	

*MWRC, Ministry of Water Resources of China.

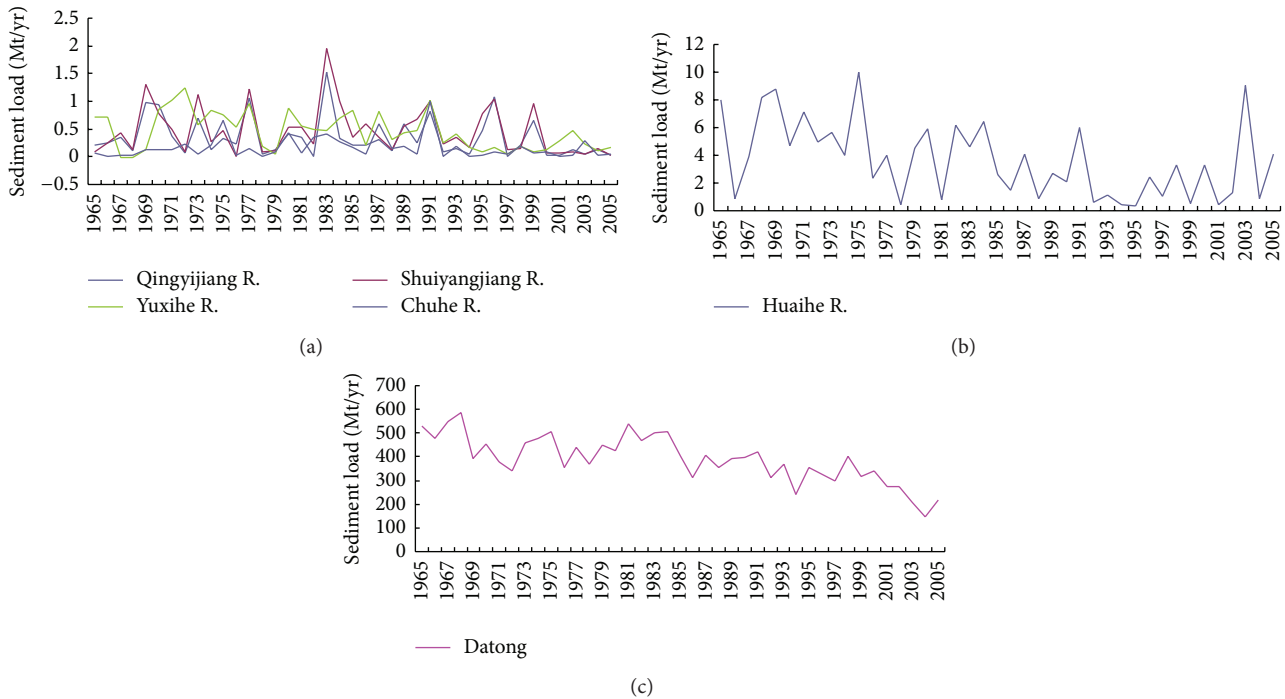


FIGURE 2: Variations in sediment load of local tributaries in the river mouth reach, Huaihe River, and Datong station.

Because this was the only data available for the Lake Taihu system, we selected 0.1 Mt/yr as the sediment load of the Lake Taihu system from 1965 to 2012, even though it was likely an overestimation.

The total sediment load of the local tributaries is 3.81 Mt/yr. As indicated above, the majority of runoff and sediment load (80%) of the Huaihe River is discharged into the Yangtze River through a connective waterway. In this study, the sediment discharge from the Huaihe River was taken into account. Although the Huaihe River has a drainage basin of 270,000 km², its average specific sediment yield is much less than that of the Yangtze River. Additionally, attenuation by Lake Hongzehu, which is located in the middle of the Huaihe River, results in only 49.9% of the sediment being discharged from the lake. Of this sediment, 80%

(3.73 Mt/yr) is discharged into the Yangtze River [14]. When combined with that from the local tributaries and the Huaihe River, 7.54 Mt/yr sediments are discharged into the river mouth reach of the Yangtze River. The average sediment load from the upper reach of the Yangtze River was 400.15 Mt/yr in 1965–2002; therefore, sediment load from the local tributaries together with the Huaihe River comprises only 1.9% of that from the upper reach of the Yangtze River. Yang [20] investigated the contribution of water and sediment fluxes to the sea from the subcatchment below Datong station in the Yangtze River (excluding the Huaihe River) based on several estimations. Assuming that the specific sediment yield of the river mouth reach is similar to that of Poyang Lake (above the river mouth reach), Yang [20] estimated that the sediment yield of the river mouth reach would be 11 Mt/yr in 1956–2010, which

TABLE 2: Erosion/accretion of the river mouth reach (unit: Mt/yr)*.

Anhui section [15]		Jiangsu section [16]		Whole section [17]	
Time	Erosion/accretion	Time	Erosion/accretion	Time	Erosion/accretion
1966–1987	–30.67	1970–1985	104.66		
1987–2002	–29.12	1985–1992	–196.34		
1966–2002	–30.02	1992–2003	–78.30	1969–2003	–1.55
2002–2007	5.34	1970–2003	9.01		
2007–2012	5.95				
2002–2012	5.66			2003–2008	124.33

*The original units of the referenced data were $10^6 \text{ m}^3/\text{yr}$, but these were changed to Mt/yr for convenience under the assumption that the dry bulk density of the sediments was $1.3 \times 10^3 \text{ kg/m}^3$ [6].

was 2.9% of the sediment load of Datong station in the same time interval. Yang [20] suggested that the actual specific sediment yield of the river mouth reach might be higher than that of the Poyang Lake river system due to the better vegetation and large dam interception in the Poyang Lake river system and lower than that of the middle and lower reaches owing to the higher relief and steeper river gradient. Hence, he estimated that the proportion of sediment flux from the river mouth reach to that of the entire basin would be greater than 2.9%, but lower than that of its proportion of water yield (6.3%). Specifically, he suggested that the proportion would be 3% to 4% [20]. This value was almost double that of the present study. Based on the gauged data, we compared the sediment load of the tributaries in the Poyang Lake river system and local tributaries of the river mouth reach and found that the former was much higher than the later. Accordingly, the results reported by Yang [20] are likely higher than the actual value.

4.2. Erosion/Accretion of the River Channel. Several studies have investigated the erosion/accretion of the river channel below Datong station (Table 2). Liu [15] studied the channel evolution of the Anhui section. They found that the river channel in this section eroded at an average rate of -30.02 Mt/yr from 1966 to 2002, while a slight (5.66 Mt/yr) accretion occurred from 2002 to 2012 (after impoundment of the TGD). Wang et al. [16] studied changes in the channel of Jiangsu Province (from the boundary of Anhui to Jiangyin, hereafter referred to as Jiangsu reach) and found that sediment was deposited at an average rate of 104.66 Mt/yr from 1970 to 1985, but that severe erosion occurred from 1985 to 2003. On average, slight deposition (9.01 Mt/yr) occurred from 1970 to 2003 in Jiangsu reach. When combined with the results reported by Liu (2013) and Wang et al. [16], the evolution of the river channel from Datong to Jiangyin before impoundment of the TGD in 2003 can be determined, even though the time scale of the two studies does not match exactly. We found that the river channel below Datong underwent moderate (-21.01 Mt/yr) erosion from 1966 to 2002. Qu [17] investigated the evolution of the entire reach between Datong and Jiangyin and found that the river channel experienced slight erosion (-1.55 Mt/yr) in 1969–2003.

Previous studies indicated that the river channel of the lower reach of the Yangtze River was almost in balance in previous decades [21–23]. Examination of the results of studies

conducted by Wang et al. [16], Liu [15], and Qu [17] revealed that, although differences exist, these studies are generally consistent with the results of previous studies of the river channel (slight erosion/accretion) above Datong station before 2003. Since there is no way to tell which results were most likely, we arbitrarily selected the average of the results reported by Liu [15] and Wang et al. (2007) [16] (-21.01 Mt/yr) and Qu [17] (-1.55 Mt/yr) as the actual erosion/accretion results before 2003. Hence, we obtained a slight erosion of -11.28 Mt/yr for the river channel from Datong to Jiangyin before 2003. The distance from Datong to Jiangyin is 417 km and the channel width is 1–10 km. Thus, this erosion (-11.28 Mt/yr) is very small when the entire river course is considered.

After impoundment of the TGD in 2003, sediment transport processes below the dam were quite different from the pre-TGD period. An investigation by Liu indicated that deposition of 5.66 Mt/yr occurred in the Anhui section in 2002–2012. The Bulletin of River Sediment of China 2008 [24] reported a deposition of 5.79 Mt/yr from 2001 to 2006 in the Nanjing section (92.3 km). If the deposition rate at the Nanjing section in 2001–2006 was selected as the deposition rate of the entire Jiangsu section (218 km) in 2003–2012, then the total deposition would be 13.67 Mt/yr . Then the deposition in the whole river mouth reach would be 19.33 Mt/yr .

It should be noted that Qu [17] indicated that a significant deposition (124.33 Mt/yr , 80.9% of the sediment load at Datong station at the same time) occurred from 2003 to 2008. If these results are accurate, significant deposition would occur in the river channel and a sharp decrease in sediment load would occur in the river mouth reach. However, no studies have reported these issues; therefore, the results reported by Qu should be verified.

4.3. Sediment Losses because of Water Extraction and Sand Mining

4.3.1. Water Extraction. Because there is little data available regarding water extraction, its effects on sediment flux in the Yangtze River are still not fully understood. Zhang and Chen [25] reported that, in a typical dry year of 1978, the total water extraction below Datong station was $32.1 \times 10^9 \text{ m}^3/\text{yr}$. In 1995, about $20.4 \times 10^9 \text{ m}^3/\text{yr}$ water was extracted from the Yangtze River in Jiangsu Province alone. Because water extraction increased greatly from the 1970s, they estimated that the total

water extraction below Datong station would reach $800 \text{ m}^3/\text{s}$, or 2.8% of the average water discharge at Datong ($896.4 \times 10^9 \text{ m}^3/\text{yr}$), in 1950–2010. In the present study, we assumed that the water extraction before 2000 was half that after 2000, and the suspended sediment concentration of the extracted water was the same as that of the Datong station. Accordingly, 1.4% and 2.8% of the sediment load at Datong, which was 5.6 Mt/yr and 4.41 Mt/yr, respectively, were lost because of water extraction before and after 2000.

4.3.2. Sand Mining. Sand mining is frequently mentioned when addressing the factors that impact sediment load [6, 10, 26]. Although some researchers have suggested that sand extraction may have had a significant impact on sediment load [26], an in situ study indicated that the infilling of an excavation pit was mainly the result of erosion from nearby sites [27, 28], but not from the settlement of the suspended load. The previous experimental study implied that sand mining [27, 28] could effectively shape the river channel, but would have limited direct impact on the suspended sediment load [29, 30].

Since sand mining could substantially shape the river channel, its impacts on changes in morphology calculated by the relief maps (as conducted by Wang et al. [16], Liu [15], and Qu [17]) would be significant. Relief maps in different stages can directly indicate the evolution of the river channel, and consequently the sediment load change. When considering the contribution of sand mining, the actual sediment load change calculated by the relief maps should be subtracted from the volume of the sand mined.

To date, no overall investigation of sand mining in the Yangtze River basin has been conducted. It has been reported that, in Anhui Province, sand extraction from the stem channel of the Yangtze River increased from 7 Mt/yr at the beginning of the 1990s to 15 Mt/yr at the end of the 1990s [15]. Since the total length of the river channel at Anhui Province (400 km) is almost equal to that of the study area (417 km), we assumed that the amount of sand extracted from the study area was equal to that removed from Anhui Province (15 Mt/yr) before 2003.

To reduce and legalize sand mining activities in the Yangtze River, the government issued the “Regulations of management of sand mining in the Yangtze River” in 2001. Under these regulations, the authorized quantity of sand mining in the Anhui Province section for 2004–2010 was 15.54 Mt/yr [15], while it was 5.6 Mt/yr in the Jiangsu Province section. Considering that the river length of the studied area of the present paper (417 km) is 53% of that of the total length of the river channel in Anhui and Jiangsu Provinces (780 km), sand extraction from the study area will be 10.57 Mt/yr in 2004–2010, excluding illegal mining. Herein, the authorized quantity of sand mining (10.57 Mt/yr) in 2004–2010 was taken as the actual volume of sand mining after 2003.

4.4. Sediment Discharge into the Sea by the Yangtze River before and after Impoundment of the TGD

4.4.1. Preimpoundment Sediment Budget. The quantity of sediment load released out of the river mouth reach was

determined by the gains and losses of the sediment in the river channel. The gains included sediment from the upper reach, local reach, and erosion of the river bed. The losses included sediment deposition and water extraction (for uses such as agriculture, industrial use, and domestic consumption). As discussed above, sand mining could substantially shape the river channel and have impacts on the changes in morphology calculated by the relief maps. When constructing the sediment budget, the contribution of the erosion/accretion calculated by the relief maps should subtract the volume of sand mined. We estimated that the sand extracted from the study area before 2002 was 15 Mt/yr; hence, the $Q_{s,\text{deposition}}$ should be 3.72 Mt/yr ($15 \text{ Mt/yr} - 11.28 \text{ Mt/yr}$). These findings indicate that the erosion calculated by the relief maps is lower than that of the volume of sand mining, implying that slight deposition must have occurred (3.72 Mt/yr).

Based on the discussion above, we established the sediment budget in the river mouth reach for the pre- and post-TGD periods, respectively. The sediment budget in 1965–2002 was as follows (units, Mt/yr):

$$\begin{aligned} Q_{s,\text{out}} (398.37) &= Q_{s,\text{upper reach}} (400.15) \\ &+ Q_{s,\text{local reach}} (7.54) \\ &- Q_{s,\text{deposition}} (3.72) \\ &- Q_{s,\text{water extraction}} (5.6). \end{aligned} \quad (2)$$

The combined sediment load loss was 9.32 Mt/yr, while the sediment gain was 7.54 in the river mouth reach, indicating that there was a net loss of 1.78 Mt/yr before impoundment. The sediment loss (1.78 Mt/yr) was only 0.44% of the sediment load at Datong at the same time (400.15 Mt/yr). Therefore, the contribution of the river mouth reach to the total sediment discharge into the sea was minimal before 2003.

4.4.2. Sediment Budget after 2003. To match the time scale (2002–2012) of the present study, it was necessary to estimate the sediment load of the local tributaries and the Huaihe River over the same time period because only the times series data before 2005 was available for these rivers. Evaluation of the annual sediment load of the local tributaries and the Huaihe River from 1965–2005 revealed that sediment load of these rivers showed a decreasing trend during this time interval. In the present study, we took the average sediment load of the local tributaries and the Huaihe River from the time period of 1996–2005 (3.42 Mt/yr) as the sediment load during 2002–2012.

As indicated above, the total deposition in the study area was 19.33 Mt/yr in 2003–2012, while the amount of sand mining was 10.57 Mt/yr during the same period. When sand mining was considered, the actual sediment deposition (loss) was 29.90 Mt/yr. Additionally, water extraction was responsible for 2.8% (4.41 Mt/yr) of the sediment load at Datong station

(145.06 Mt/yr) in 2003–2012. We used these data to construct the sediment budget for 2003–2012 (unit: Mt/yr). Consider

$$\begin{aligned}
 Q_{s_out} (114.17) &= Q_{s_upper\ reach} (145.06) \\
 &+ Q_{s_local\ reach} (3.42) \\
 &- Q_{s_deposition} (29.90) \\
 &- Q_{s_water\ extraction} (4.41).
 \end{aligned} \tag{3}$$

The combined sediment loss was 34.31 Mt/yr, while the sediment gain was 3.42 Mt/yr in the river mouth reach, indicating that a net loss of 30.89 Mt/yr occurred after the TGD. The sediment loss (30.89 Mt/yr) was about 21.3% of the sediment load at Datong during the same period (145.06 Mt/yr).

Examination of the sediment budget for the two periods revealed that sediment load decreased sharply in the river mouth reach from 398.37 Mt/yr in 1965–2002 to 114.17 Mt/yr in 2003–2012 after impoundment of the TGD. In both periods, deposition occurred in the river mouth reach, especially after impoundment of the TGD, which indicated that downstream sediment recovery was limited to the middle and lower reaches.

5. Discussion

5.1. Regulation Effects of the River Mouth Reach on Sediment Load. It has been suggested that the buffering function of river mouth reaches plays an important role in regulation of the sediment processes. In the present study, we examined the sediment gain and loss based on gauged data together with estimated values and found that the river mouth reach did not strongly influence sediment discharge into the sea from the Yangtze River before the impoundment of the TGD. Evaluation of the role that each impact factor could play in regulation of the sediment budget in the river mouth reach revealed the following: (a) The sediment yield in the river mouth reach is very low relative to that of the middle and upper reaches. The proportion of the drainage area of the river mouth reach to the entire basin is comparatively small. Accordingly, the contribution of the sediment yield from the drainage basin to the sediment load of the trunk river is limited. (b) Although a large quantity of water was extracted from the river mouth reach in recent years, relative to the huge water flow of the mainstream of the river ($896.4 \times 10^9 \text{ m}^3/\text{yr}$ in 1950–2010), the volume of water extracted comprises only a small proportion of the total and therefore has a minimal impact on sediment load. (c) Sand mining appeared to play a more important role in shaping the river course than reduction of the sediment load. Overall, the regulatory effect of the river mouth reach is very limited. These results indicate that this large river has great potential to accommodate disturbances of the river mouth reach from the local drainage basins.

5.2. Impacts of the TGD. Previous studies demonstrated that the TGD has significant impacts on the hydrological regime of the middle and lower reaches. However, its effects on

the river mouth reach have not been fully addressed. In the present study, we found that the TGD also had significant impacts on the sediment process in the river mouth reach. Before impoundment of the TGD, the average deposition rate in the study area was 3.07 Mt/yr; however, the deposition increased to 29.90 Mt/yr after impoundment. Since there were no significant changes in the physical conditions of the river channel and the local drainage basin, this change was mainly due to the impacts of the TGD. It is believed that this increasing deposition was due to the coarsening of the suspended load caused by erosion in the middle reaches of the Yangtze River [31].

Erosion will generally occur below a dam. In the Yangtze River, the severity of erosion increases with proximity to the TGD [10]. The study area is located 1149 km away from the TGD, and erosion does not appear to have extended to the study area during the first ten years of operation (2003–2012). Accordingly, more time may be needed for the impacts of the TGD to fully manifest. The responses of the river channel of the river mouth reach might be very complicated because of the length and the large body of the river channel.

5.3. Limitations of the Results of the Present Study. A large dataset was compiled to facilitate the investigation; however, these data originate from a variety of sources and have different reliabilities, which might lead to the uncertainty associated with the results presented herein. Nevertheless, the hydrological data used in this study were obtained from the Ministry of the Water Resources of China and underwent strict examinations before being released [32]. In the present study, only suspended load was applied in the discussion. A previous study showed that the bed load comprised a very small proportion of the total load in the Yangtze River [32]. Accordingly, the error associated with these data as well as the estimations based on these data is likely minimal.

The main uncertainties in the present study are likely related to errors in results calculated based on the relief maps and the estimated volume of sand mining, which both may have had significant impacts on studies of changes in the river channel.

In this study, we reviewed the findings of Wang et al. [16], Liu [15], and Qu [17] and applied their results to build a sediment budget for the river mouth reach. However, it is important to note that the results of these studies are quite different. We thought that these differences could be attributed to errors associated with the process used for depth measurement and digital elevation model (DEM) building (Figure 3). Errors could exist in each step in the above processes, and consequently bring uncertainty to the results. Specifically, for determination of the depth, the error might exist in the precision of the bathymetric point in different measurement times, the accuracy of the depth measurement, and the density of the bathymetric point. For DEM building, the error might exist in the methodologies, or the control points and boundary conditions. The studies conducted by Wang et al. [16], Liu [15], and Qu [17] are all based on relief maps of the river channel that were generated by government agencies. However, these relief maps were developed for navigation and

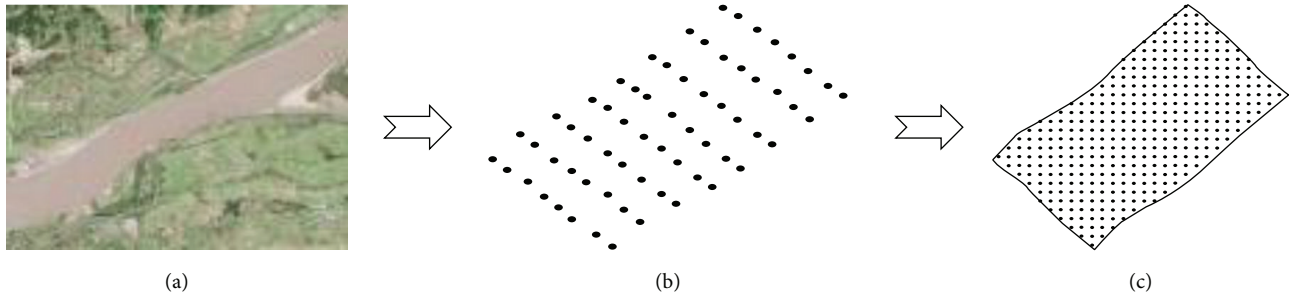


FIGURE 3: The processes of depth measurement and DEM building of the river channel. (a) River course; (b) cross section measurement (dots are bathymetric points); (c) grid DEM data.

their applicability to river channel mapping has not yet been addressed. In view of this uncertainty, we thought that the differences of the studies of Wang et al. [16], Liu [15], and Qu [17] might be attributed to the careless applications of the relief maps. Further studies are needed to address these issues.

6. Conclusions

This study investigated sediment issues at the river mouth reach of the Yangtze River. The results presented herein enable quantitative estimation of the contribution of the river mouth reach to the sediment load of the Yangtze River. From 1965 to 2002, sediment discharge into the river mouth reach of the Yangtze River was 7.54 Mt/yr from the local tributaries and the adjacent Huaihe River, which is much lower than its proportion in terms of its length and drainage area. When the impacts of sand mining and water extraction were considered, a total loss of 1.78 Mt/yr occurred during this period. This sediment loss was very low relative to the large body of the studied river course (417 km in length and 1–10 km in width) and was below our expectations.

After impoundment of the TGD, downstream sediment recovery below the TGD was limited to the middle and lower reaches. In the river mouth reach, deposition occurred after impoundment (29.90 Mt/yr, including the impact of sand mining). When combined with the sediment from local tributaries and the Huaihe River, as well as sediment loss because of water extraction, a net loss of 30.89 Mt/yr (about 21.3% of the sediment load at Datong at the same time) of sediment load occurs in the river mouth reach. The river mouth reach has acted as a sink, but not a source, since impoundment, which exacerbates the decrease of sediment discharge into the sea.

We also found that uncertainties exist in examination of the sediment processes due to insufficient datasets, as well as defects in the methodologies used to calculate changes in the channel. Additional studies should be conducted to improve measurements of changes in both river channel morphology and water and sediment discharges at the river mouth reach.

Conflict of Interests

The authors declare that there is no conflict of interests regarding the publication of this paper.

Acknowledgments

This study was supported by the Natural Science Foundation of China (41001301, 412014015), Anhui Provincial Natural Science Foundation of China (1408085MD77), Foundation of State Key Laboratory of Soil Erosion and Dry land Farming on the Loess Plateau (K318009902-1319, 10501-1217), and the Natural Science Foundation of Education Bureau of Anhui Province (KJ2013Z246). Two anonymous reviewers are thanked for their valuable comments and suggestions.

References

- [1] D. E. Walling and D. Fang, "Recent trends in the suspended sediment loads of the world's rivers," *Global and Planetary Change*, vol. 39, no. 1-2, pp. 111–126, 2003.
- [2] S. B. Dai and X. X. Lu, "Sediment load change in the Yangtze River (Changjiang): a review," *Geomorphology*, vol. 215, pp. 60–73, 2014.
- [3] C. Nilsson, C. A. Reidy, M. Dynesius, and C. Revenga, "Fragmentation and flow regulation of the world's large river systems," *Science*, vol. 308, no. 5720, pp. 405–408, 2005.
- [4] O. E. Frihy, K. M. Dewidar, and M. M. El Banna, "Natural and human impact on the northeastern Nile delta coast of Egypt," *Journal of Coastal Research*, vol. 14, no. 3, pp. 1109–1118, 1998.
- [5] J. P. M. Syvitski, C. J. Vörösmarty, A. J. Kettner, and P. Green, "Sinking deltas due to human activities," *Nature Geoscience*, vol. 2, pp. 681–686, 2009.
- [6] S. L. Yang, J. D. Milliman, P. Li, and K. Xu, "50,000 dams later: erosion of the Yangtze River and its delta," *Global and Planetary Change*, vol. 75, no. 1-2, pp. 14–20, 2011.
- [7] X. K. Yang and X. X. Lu, "Estimate of cumulative sediment trapping by multiple reservoirs in large river basins: an example of the Yangtze River basin," *Geomorphology*, no. 227, pp. 49–59, 2014.
- [8] X. Li, Y. X. Zhou, L. P. Zhang, and R. Y. Kuang, "Shoreline change of Chongming Dongtan and response to river sediment load: a remote sensing assessment," *Journal of Hydrology*, vol. 511, pp. 432–442, 2014.
- [9] X. Lai, J. Jiang, G. Yang, and X. X. Lu, "Should the Three Gorges Dam be blamed for the extremely low water levels in the middle-lower Yangtze River?" *Hydrological Processes*, vol. 28, no. 1, pp. 150–160, 2014.
- [10] Z. J. Dai and J. T. Liu, "Impacts of large dams on downstream fluvial sedimentation: an example of the Three Gorges Dam (TGD)

- on the Changjiang (Yangtze River)," *Journal of Hydrology*, vol. 480, pp. 10–18, 2013.
- [11] S. L. Yang, J. Zhang, S. B. Dai, M. Li, and X. J. Xu, "Effect of deposition and erosion within the main river channel and large lakes on sediment delivery to the estuary of the Yangtze River," *Journal of Geophysical Research F: Earth Surface*, vol. 112, no. 2, Article ID F02005, 2007.
- [12] X. G. Wu, "The sediments and evolution of Taihu Lake," *Journal of Lake Sciences*, vol. 4, no. 3, pp. 54–60, 1992 (Chinese).
- [13] G. X. Hong and G. M. Han, "An analysis on the sediment load discharging into and out of the Hongzehu Lake," *Water Conservancy Science and Technology and Economy*, vol. 13, no. 4, pp. 240–241, 2007 (Chinese).
- [14] B.-Y. Yu and Y.-S. Yu, "Sediment deposition in Hongze Lake," *Journal of Sediment Research*, no. 6, pp. 36–41, 2010 (Chinese).
- [15] D. F. Liu, "An analysis on the erosion and deposition of the channel of the Yangtze River in Anhui section," *Jianghuai Water Resources Science and Technology*, no. 6, pp. 26–28, 2013 (Chinese).
- [16] J. Wang, P. Liu, Z. R. Gao, S. B. Bao, G. J. Cao, and G. X. Qu, "Temporal-spatial variation of the channel in Jiansu reach of the Yangtze River during the last 44 years," *Acta Geographica Sinica*, vol. 62, no. 11, pp. 1185–1193, 2007 (Chinese).
- [17] G. X. Qu, *The Characteristics and Explanations of Channel Change in the Datong-Jiangyin Reach of the Lower Yangtze River: 1959–2008*, Nanjing Normal University, Nanjing, China, 2014.
- [18] Q. Wang and J. Y. Chen, "Formation and evolution of hongze lake and the huaihe river mouth along the lake," *Journal of Lake Science*, vol. 11, no. 3, pp. 237–244, 1999 (Chinese).
- [19] D. E. Walling and A. L. Collins, "The catchment sediment budget as a management tool," *Environmental Science and Policy*, vol. 11, no. 2, pp. 136–143, 2008.
- [20] S. L. Yang, "Discussion on contribution of water and sediment fluxes to sea from sub-catchment below Datong Station of Yangtze River," *Journal of Yangtze River Scientific Research Institute*, vol. 3, no. 44, pp. 13–15, 2013.
- [21] H. F. Yin, G. J. Chen, and C. A. Li, "Sediment deposition issues of the middle Yangtze River," *Science of China: Series D*, vol. 34, no. 3, pp. 195–209, 2004.
- [22] S.-B. Dai, S.-L. Yang, J. Zhu, A. Gao, and P. Li, "The role of Lake Dongting in regulating the sediment budget of the Yangtze River," *Hydrology and Earth System Sciences*, vol. 9, no. 6, pp. 692–698, 2005.
- [23] S. L. Yang, J. D. Milliman, K. H. Xu, B. Deng, X. Y. Zhang, and X. X. Luo, "Downstream sedimentary and geomorphic impacts of the Three Gorges Dam on the Yangtze River," *Earth-Science Reviews*, vol. 138, pp. 469–486, 2014.
- [24] MWR, *Bulletin of China River Sediment*, Press of Ministry of Water Resources of the People's Republic of China, 2008, <http://www.cjh.com.cn/>.
- [25] E. F. Zhang and X. Q. Chen, "Changes of water discharge between Datong and the Changjiang Estuary during the dry season," *Acta Geographica Sinica*, vol. 58, no. 2, pp. 231–238, 2003.
- [26] C. Xiqing, Z. Erfeng, M. Hongqiang, and Y. Zong, "A preliminary analysis of human impacts on sediment discharges from the Yangtze, China, into the sea," *Journal of Coastal Research*, vol. 21, no. 3, pp. 515–521, 2005.
- [27] J.-Q. Mao, "Numerical simulation study of flow field around the sandpit with complicate shape in riverbed," *Advances in Water Science*, vol. 15, no. 1, pp. 6–10, 2004 (Chinese).
- [28] Y. Mao and C. A. Huang, "Experimental study on effect of sand mining on riverbed deformation," *Shuili Xuebao*, no. 5, pp. 64–69, 2005 (Chinese).
- [29] S. B. Dai and S. L. Yang, "The impacts of sand mining on the sediment load of the Yangtze River," *Shanghai Geology*, no. 1, pp. 17–20, 2004 (Chinese).
- [30] S. B. Dai, X. X. Lu, S. L. Yang, and A. M. Cai, "A preliminary estimate of human and natural contribution to the sediment decline from the Yangtze River to the East China Sea," *Quaternary International*, vol. 186, pp. 43–54, 2008.
- [31] X. X. Luo, S. L. Yang, and J. Zhang, "The impact of the Three Gorges Dam on the downstream distribution and texture of sediments along the middle and lower Yangtze River (Changjiang) and its estuary, and subsequent sediment dispersal in the East China Sea," *Geomorphology*, vol. 179, pp. 126–140, 2012.
- [32] Z. Y. Wang, Y. Li, and Y. He, "Sediment budget of the Yangtze River," *Water Resource Research*, vol. 43, Article ID W04401, 2007.

Research Article

Millennial-Scale Asian Monsoon Influenced Longjie Lake Evolution during Marine Isotope Stage 3, Upper Stream of Changjiang (Yangtze) River, China

Chaozhu Li,¹ Jianli Fu,¹ Liang Yi,² Xin Zhou,³ Shubing Wang,¹ and Fuchu Jiang¹

¹*Institute of Geomechanics, Chinese Academy of Geological Sciences, Beijing 10081, China*

²*MSG Group, Sanya Institute of Deep-Sea Science and Engineering, Chinese Academy of Sciences, Sanya 572000, China*

³*School of Earth and Space Sciences, University of Science and Technology of China, Hefei 230026, China*

Correspondence should be addressed to Chaozhu Li; lichzh@163.com

Received 6 February 2015; Revised 20 April 2015; Accepted 20 April 2015

Academic Editor: Steffen Mischke

Copyright © 2015 Chaozhu Li et al. This is an open access article distributed under the Creative Commons Attribution License, which permits unrestricted use, distribution, and reproduction in any medium, provided the original work is properly cited.

Millennial-scale climate change in Asian monsoon region during MIS 3 has been studied using stalagmite, loess, and peat sediments. However, records from more materials are essential to further illustrate dynamics of these events. In the present study, a time-series of grain size covering 60–30 ka was reconstructed from lake sediments in the Yunnan Province, southwestern China. The time-series contains 14 obvious millennial-scale events during the period. On millennial-scale, the grain size record is generally consistent with mean stalagmite $\delta^{18}\text{O}$ from Hulu Cave, grain size of Gulang loess sequence, Chinese Loess Plateau, and Greenland ice core $\delta^{18}\text{O}$. The results show that the millennial-scale variation was well compared with the Dansgaard-Oeschger (DO) events, indicating that those global events were well documented in lake sediments in the Asian monsoon region. Because the grain size can be used as a proxy for water discharge, we suggest that signal of the DO events might be transmitted to lake evolution by Asian monsoon.

1. Introduction

Marine Isotope Stage 3 (MIS 3), with relatively warm and wet climate and high sea level, is a particular period during the last glacial [1, 2]. The more attractive character during this period is the typical millennial-scale climate oscillations, which was named as Dansgaard-Oeschger (DO) events [3, 4], and has been extensively studied [5, 6]. To date, studies on MIS 3 in China were mainly focused on how warm or/and wet the period was, especially on whether megalakes existed in northwestern China during this period [7–9].

Due to the lack of suitable materials, few records have been reconstructed to study millennial-scale climate events during the MIS 3 in China. Earlier studies [10, 11] have characterized these events using magnetic susceptibility, grain size of quartz, and weathering indices in Chinese Loess Plateau. Recently, Sun et al. reconstructed two high-resolution and precisely dated winter monsoon records by loess sequences with high sedimentary rates, and attributed these abrupt events to variations in Atlantic meridional overturning circulation [12]. Because stalagmite can be precisely dated, more

researches [13–15] used stalagmite to study millennial climate events during the MIS 3, since Yuan et al. published high-resolution stalagmite $\delta^{18}\text{O}$ records and compared them with Greenland ice core $\delta^{18}\text{O}$ [13]. More recently, peat sediment has also been used to investigate millennial-scale climate changes [16]. However, lack of enough records limited the comparison of the events between different regions and studies on the forcing of the events during the MIS 3.

Yunnan Province is located in northwestern China and is thus sensitive to Asian monsoon changes. In the present study, we reconstructed climate change at a study site in Yunnan Province during the MIS 3, focusing on millennial-scale events and the transmitting mechanisms of the DO signal to lake evolution.

2. Study Area, Materials, and Methods

2.1. Longjie Silt Layers. Longjie Silt Layers [17] were located in the lower stream of the Jinshajiang River, which belongs to the upper stream of the Changjiang (Yangtze) River, where the

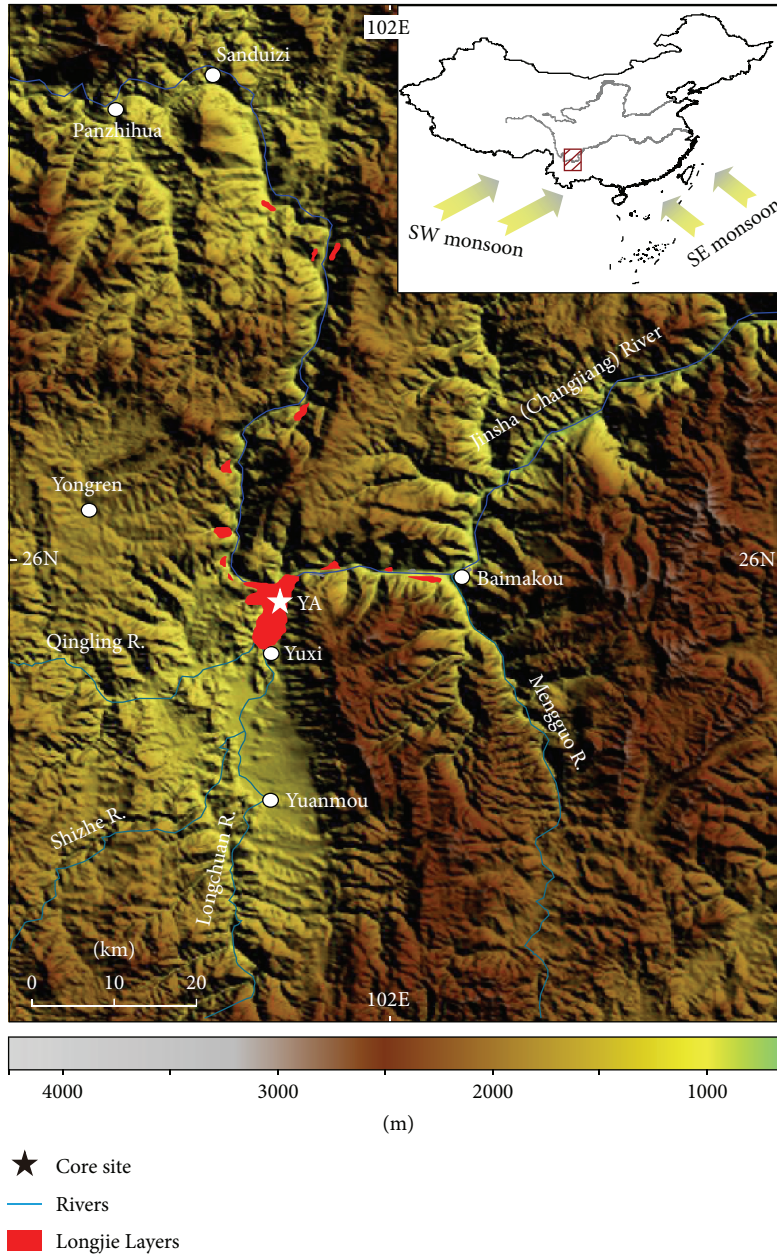


FIGURE 1: Study area, distribution of Longjie Silt Layers, and YA core site. The base map was generated using the open and free software DIVA-GIS 7.5 (<http://www.diva-gis.org/>).

climate is significantly influenced by the Asian monsoon with an annual precipitation of 800–1600 mm. The Longjie Silt Layers are composed of grey white-grey, yellow-grey silt, clay silt, and clay, distributing along the Jinshajiang River between the Sanduizi and the Baimakou (Figure 1). Its thickness is commonly 40–50 m, and the depositional environment is supposed to be shallow lake [18]. However, the formation, mechanism, and controlling factors of this lacustrine layer are still unclear [19–22].

2.2. YA Core. The YA core was located on the southern side of the modern Jinshajiang River, 57 m higher relative to

present river level ($101^{\circ}52'56''\text{E}$, $25^{\circ}57'34''\text{N}$; elevation 979 m, Figure 1). The length of core obtained from the drill site was 91.9 m and the recovery rate was >95%. An exceptional section of the record, raised from 11.0 to 30.0 m below the core top, was selected here for study, because of being well constrained by luminescence dating. This sediment interval is composed of yellow-grey fine to coarse silt, namely, the Longjie Silt Layers, which is similar in composition to the modern sediment in the Jinshajiang River (upper stream of Changjiang River). This unit is interpreted as a lacustrine environment, and the vertical variation of these sedimentary facies is depicted in Figure 2.

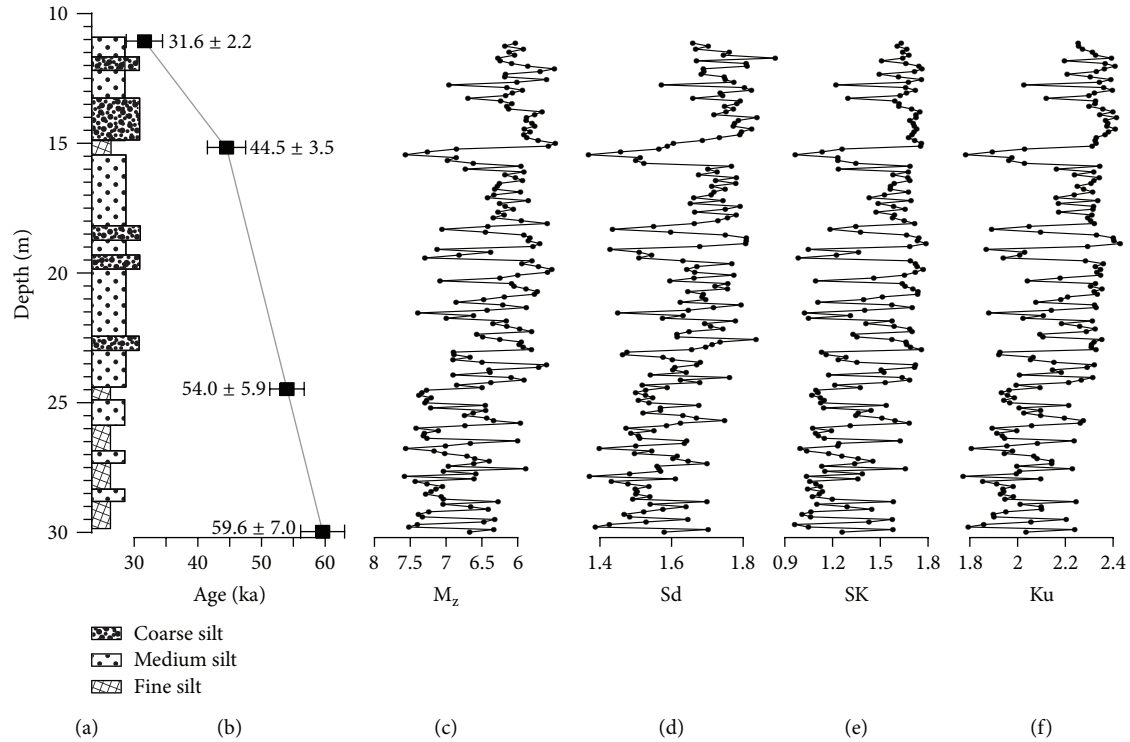


FIGURE 2: Profile (a), OSL ages (b), and grain size variation (c–f) of YA core.

2.3. Luminescence Dating. Four samples (Figure 2) were collected for optically stimulated luminescence (OSL) dating by hammering metal cylinders of 2.5 cm (diameter) \times 6 cm (length) horizontally into cores. Sample preparation was conducted under subdued red light. The light-exposed sediment was removed from both ends of the cylinders. All samples were pretreated with 10% HCl and 30% H_2O_2 to remove carbonates and organics, respectively. To remove feldspars, the quartz fraction of fine silty grains (4–11 μm) was then treated with silica saturated fluorosilicic acid (H_2SiF_6) for about two weeks [23, 24]. The purity of the prepared quartz was tested by routine IR stimulation. Any sample with detectable decaying IRSL signal above the background was reetched with H_2SiF_6 to avoid the age underestimation that may originate from the contamination of feldspars [25]. For equivalent dose determination, we followed the sensitivity-corrected multiple aliquot regenerative-dose protocol given by Lu et al. [26], performing on a Daybreak 2200 automated OSL reader in the OSL laboratory, Institute of Hydrogeology and Environmental Geology, Chinese Academy of Geological Sciences.

The concentrations of uranium (U), thorium (Th), and potassium (K), involved in dose rate calculations, were measured by neutron activation analysis in the China Institute of Atomic Energy in Beijing. The cosmic-ray dose rate was estimated according to Prescott and Hutton [27]. The dose rate of each sample was then calculated following the method of Aitken [28].

2.4. Sediment Grain Size. A total of 183 grain size samples were measured at a 10 cm sampling interval. The grain size samples were pretreated with 10–20 mL of 30% H_2O_2 to

remove organic matter, washed with 10% HCl to remove carbonates, rinsed with deionized water, and then placed in an ultrasonic bath for several minutes to facilitate dispersion. The grain size spectra of the remaining terrigenous material were measured using a Malvern Mastersizer 2000 laser-particle size analyzer at East China Normal University. One hundred grain size classes between 0.2 and 200 μm were exported for further analysis.

Sediment grain size is a powerful proxy for paleoenvironmental reconstruction because depositional interpretation varies with sedimentary grain size and composition. Because grain size spectra represent mixtures of sediment delivered by multiple processes, to identify the processes controlling grain size variation, varimax-rotated, principle component analysis (VPCA) is often employed. This method partitions the variance in the grain size data set into sediment input components that can be interpreted in terms of processes [29, 30].

3. Results

3.1. Chronology of YA Core. Parts (a–d) of Figure 3 show OSL decay curves of the natural dose (N) and a regeneration dose. Their OSL signals decrease very quickly during the first ten seconds of stimulation, indicating that the OSL signal is dominated by the fast component. Parts (e–h) of Figure 3 show the growth curves. For all samples, the growth curves can be well fitted using the exponential form.

The water contents decrease stratigraphically with depth probably due to the lower part of the core being closer to the level of groundwater because of regional uplift. In contrary, the OSL ages from the YA core increase stratigraphically

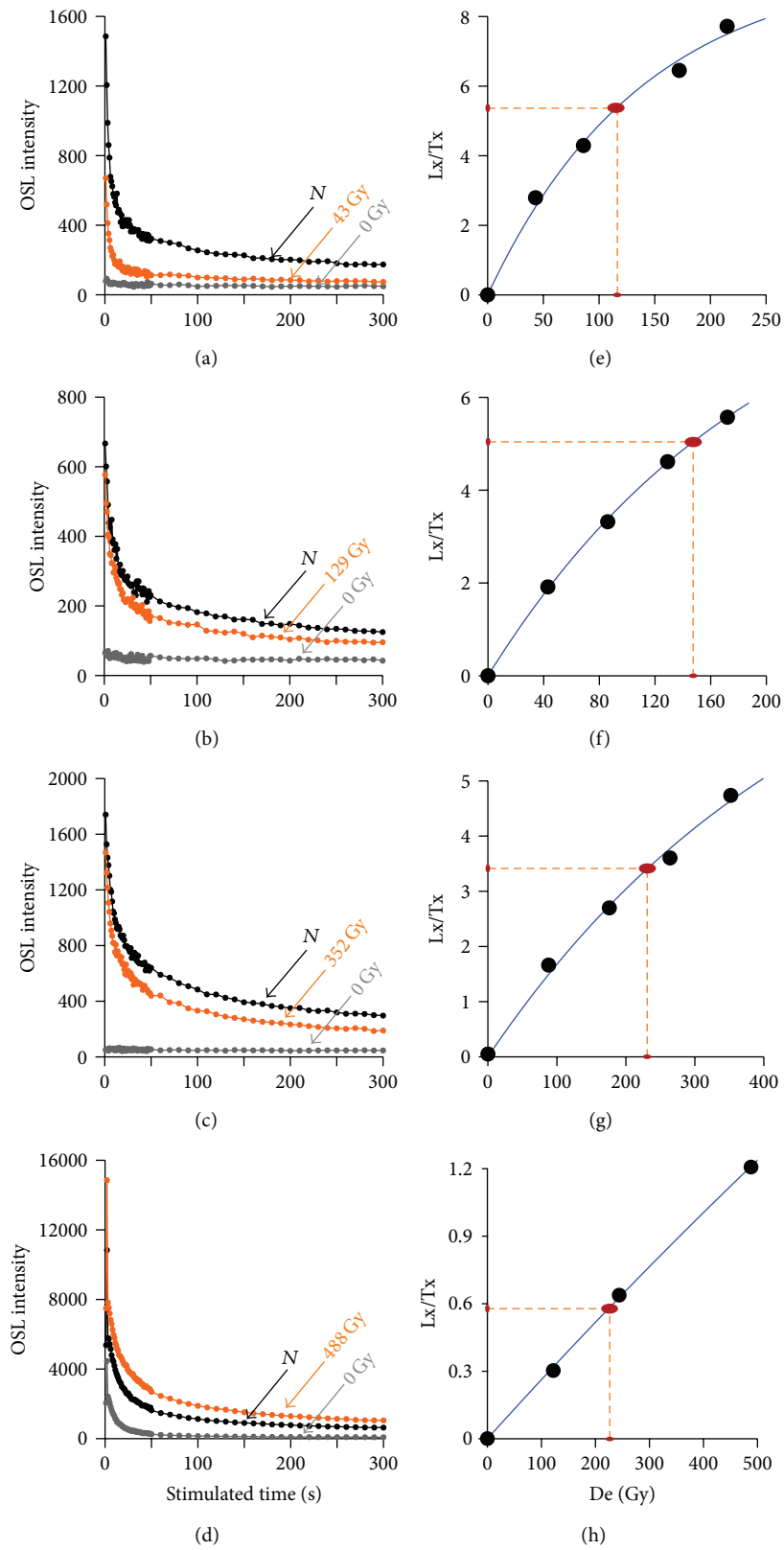


FIGURE 3: Luminescence decay (left panel) and growth (right panel) curves of Y-1 (a, e), Y-2 (b, f), Y-6 (c, g), and Y-8 (d, h), respectively.

TABLE 1: Optically stimulated luminescence dating results of the YA core.

Longjie YA core	Depth (m)	U (ppm)	Th (ppm)	K (%)	De (Gy)	Dr (Gy/ka)	Water (%)	Age (ka)
Y-1	11.1	2.66 ± 0.015	12.60 ± 0.2	1.58 ± 0.05	116.21 ± 5.55	3.68 ± 0.38	12.45 ± 5	31.6 ± 2.2
Y-2	15.2	2.70 ± 0.015	11.50 ± 0.2	1.48 ± 0.05	147.86 ± 3.30	3.32 ± 0.20	20.91 ± 5	44.5 ± 3.5
Y-6	24.5	3.06 ± 0.015	15.60 ± 0.2	2.23 ± 0.05	227.31 ± 1.21	4.21 ± 0.17	30.15 ± 5	54.0 ± 5.9
Y-8	30.0	2.36 ± 0.015	13.40 ± 0.2	2.05 ± 0.05	220.57 ± 5.90	3.70 ± 0.15	27.14 ± 5	59.6 ± 7.0

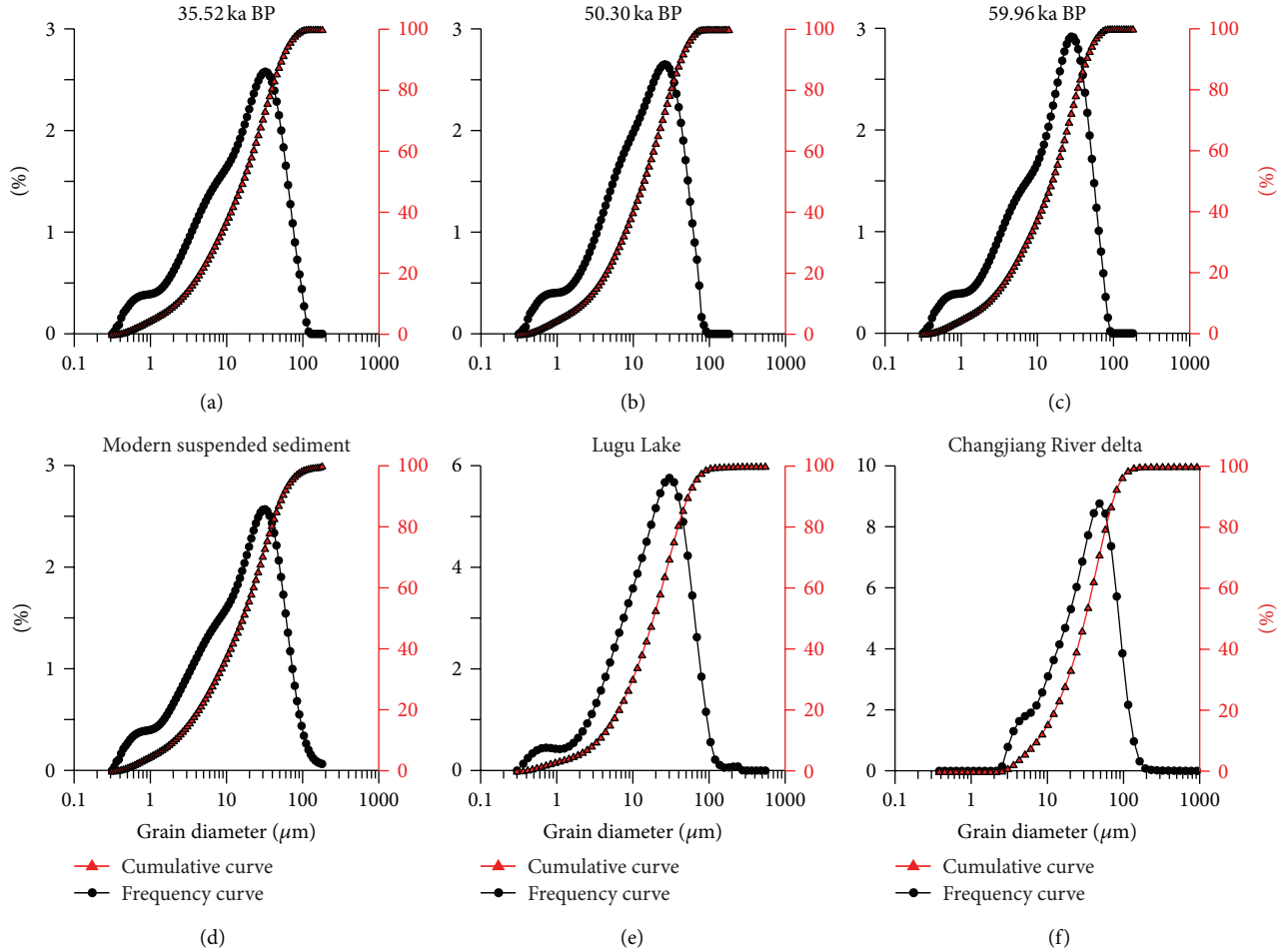


FIGURE 4: Grain size distribution of three samples from the Longjie Section (a–c) and three samples of modern suspended sediment (d), Lugu Lake ((e) Wang et al., 2014), and Changjiang River delta (f).

with depth (Table 1), indicating that, within the chronological resolution of the depth-age pairs, the sediment accumulation rate follows a clear relationship. To establish a depth-age transfer model, we apply a simply linear interpolation strategy to provide geochronological information for each grain size sample.

3.2. Grain Size Variation. Frequency and cumulative curves of grain size of three typical samples in Longjie Section show a similar distribution pattern (Figure 4), indicating that they were deposited under similar sedimentary environment. Furthermore, we found that these frequency and cumulative curves are similar to those of modern suspended sediment

of the Jinshajiang River (this study) and Lugu Lake near the study area [31] but different from the modern sediment of Changjiang River delta [32] and loess deposits.

Variation in the clay, sand, and silt fractions is subtle in the younger sedimentary unit but more pronounced in the older stratigraphic unit (Figure 5). The grain size VPCA results of the individual data sets (Figure 6) indicate that the leading components, grain size component GSC-1 and GSC-2, account for roughly 78% of the variance in the down core sediment samples, while the minor components (GSC-3 and GSC-4) only account for less than 10% of the total variance.

To evaluate the environmental information included in these stable components for further analyses, we calculate the weighted average of the two leading components to form

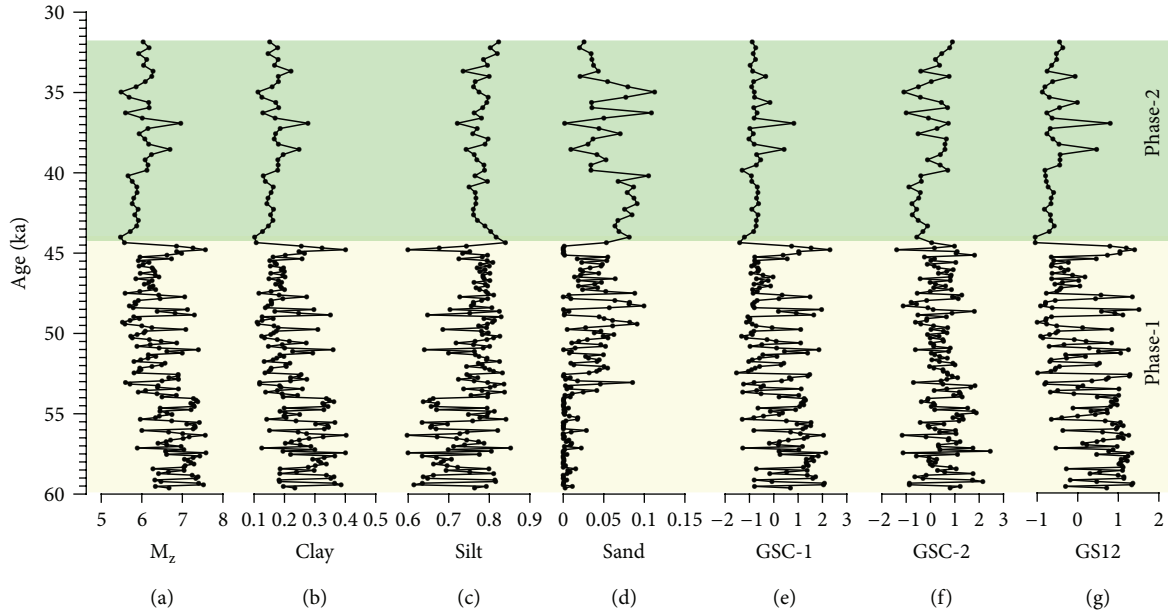


FIGURE 5: Sediment grain size (a-d) and its variation (e-g) derived from varimax-rotated, principle component analysis (VPCA).

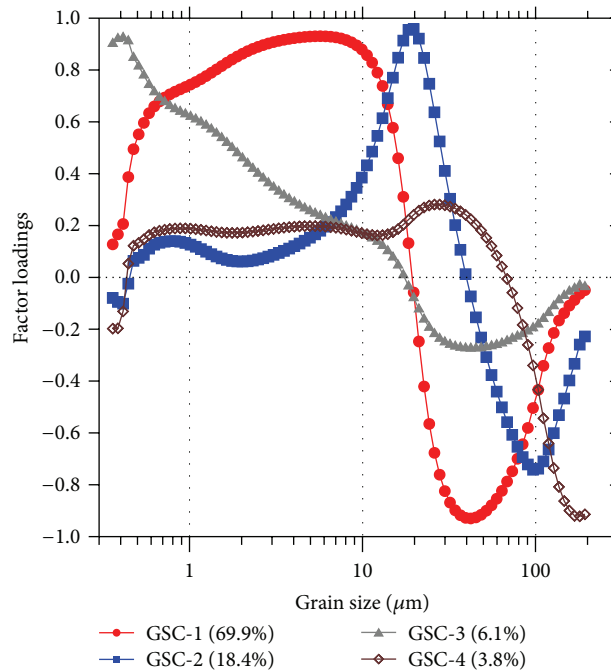


FIGURE 6: VPCA results from YA sediment and the percentage of each component.

a new series, GS12, which captures 78.3% of the overall grain size variability:

$$GS12 = (69.9 \times GSC-1 + 18.4 \times GSC-2) \div 78.3. \quad (1)$$

The weighting coefficients are simply the percentage of variance associated with each component. This approach filters out the minor constituents from the grain size spectra using the data adaptive filters defined by the first and second components [30, 33].

4. Discussion

4.1. Interpretation of Sediment Grain Size. The sediment of the Longjie Silt Layers was supposed to be formed in fluvial or lake environments [20, 34], and this hypothesis was verified [22] by field investigation and grain size comparison between Longjie sediment and Daihai [35] and Lugu Lake sediments [31]. Frequency and accumulative curves of grain size of most samples in the YA core share a common pattern, demonstrating a similar sedimentary environment through the MIS 3.

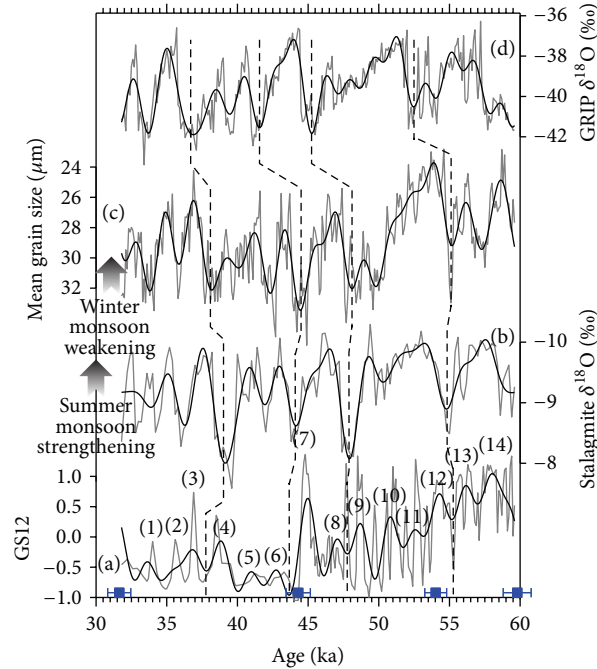


FIGURE 7: Comparison of grain size in Longjie Section (a) with stalagmite $\delta^{18}\text{O}$ in Hulu Cave [36–39] (b), mean grain size of the Gulang loess sequence, Chinese Loess Plateau [12] (c), and Greenland ice core $\delta^{18}\text{O}$ [40] (d). Thin lines represent original data, and bold lines were filtered from 1.5 ka low-frequency pass process. Numbers labeled in (a) represent possible warm-wet events regarding Dansgaard-Oeschger (DO) events.

Furthermore, we found that the VPCA factor loadings of YA core are similar to those of shallow water sediments but different from those of the loess and river sand (see Figure 4 in [30]). Therefore, it is inferred that the sediment of YA core from the Longjie Silt Layers was deposited in a shallow-lake environment (Longjie Lake).

Because the Longjie Silt Layers distribute at the cross-point of the Jinshajiang River and Longchuan River, there were two possible sources of the sediment in the Longjie Lake: (1) suspended from the Jinshajiang River and (2) trapped from the Longchuan River. As a branch, the runoff of the Longchuan River is only 1/60 of the runoff of the Jinshajiang River, and its sediment loads are also much smaller. In this context, it is supposed that fine grains might be mainly from suspended materials of the Jinshajiang River, somewhat similar as a flood plain of the Jinshajiang River, but the coarse grains were possibly from the Longchuan River due to gravitational differentiation. Thus, integrating positively from fine particles and negatively from coarse particles (Figure 6), the GSI2 series can be an indicator of runoff variation of the Jinshajiang and Longchuan Rivers.

4.2. Lake Evolution within MIS 3 and Its Driving Forces. In general, GSI2 variation can be grouped into two phases: great variability before 44 ka and low variability after (Figure 5). From 60 to 44 ka, GSI2 is characterized by high variation with distinct changes. During the early MIS 3, GSI2 has an average value of 0.23 with a much larger value of standard deviation, 0.73. This zone of high variability can be partitioned into dozens of substages and all of the transitions between each

substage are abrupt. In contrast, from 44 to 30 ka, GSI2 exhibits lower variation, with an average value of -0.40 and a moderate standard deviation of 0.60. Subsequently, we divided lake evolution within the MIS 3 period into two stages: the first one was from 60 to 44 ka; frequent fluctuation of the GSI2 series indicates a subperiod with high-frequency variation of water discharge and lake-level changes and the other was from 44 to 30 ka, and it is supposed to be a subperiod with relatively stable water discharge and lake level.

Because the YA core site is located within valleys of Jinshajiang catchments, rainfall and ice melting should be two major factors affecting river runoff. When precipitation increased, GSI2 value will increase, while melting of ice and snow can be positively related to GSI2 series. Thus, it is inferred that GSI2 variation was mainly controlled by both monsoon precipitation and temperature on Tibetan Plateau.

Stalagmite $\delta^{18}\text{O}$ has always been used to indicate Asian monsoon intensity [13, 36–39], although its indicative significance is still in debate [41–45]. Herein, we compared the GSI2 with that of the stalagmite $\delta^{18}\text{O}$ in Asian monsoon region. The results show that trends of the two time-series are roughly consistent on millennial-scale (Figure 7(b)). The consistence further confirms that stalagmite $\delta^{18}\text{O}$ can be used as proxy of monsoon precipitation during MIS 3, and that summer monsoon signals recorded in different materials are comparable during the period.

To study the forcing mechanism and transmitting process of the millennial events during MIS 3, we then compared our GSI2 with grain size variation of the Gulang loess sequence, Chinese Loess Plateau, considering the uncertainty

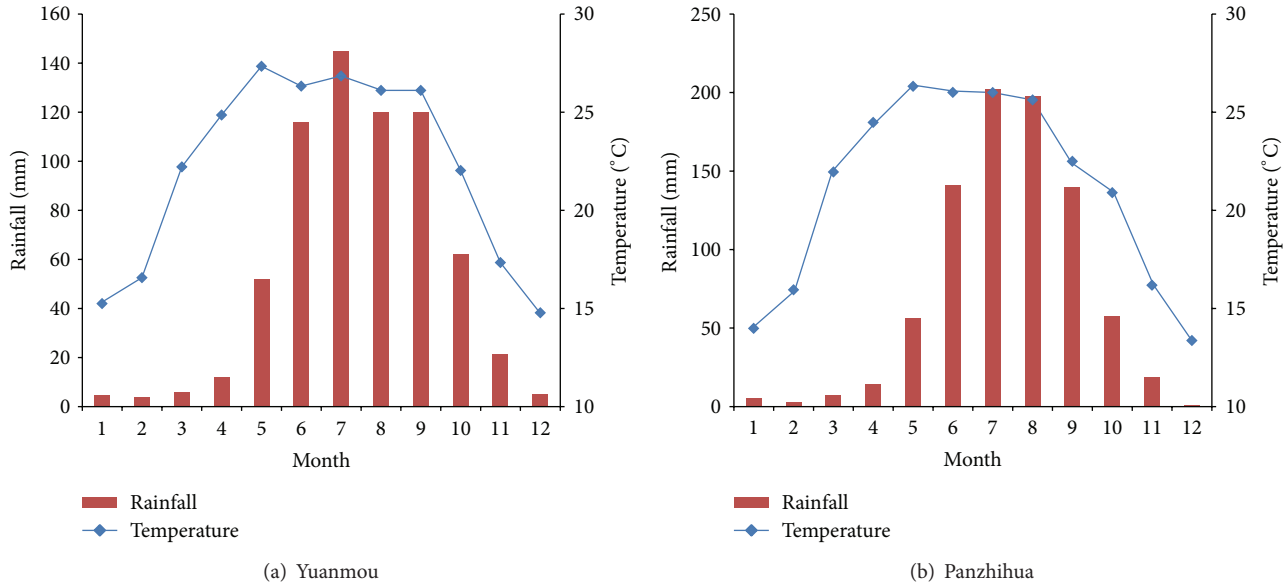


FIGURE 8: Monthly distributions of the precipitation and temperature of the Yuanmou (a) and Panzhihua (b) meteorological stations for 1951–2004 AD period.

of OSL dating (Figure 7(c)). These variations are comparable between two records on millennial-scale, indicating the common forcing of Asian monsoon, as indicated by Sun et al. [12]. Additionally, we also found consistence with Greenland ice core $\delta^{18}\text{O}$ series (Figure 7(d)).

Because the summer and winter monsoon are mainly considered as low- and high-latitude factors, respectively, the common forcing of the two signals should be linked to both low- and high-latitude processes. Generally, changes in summer and winter monsoon strength were attributed to shift of Intertropical Convergence Zone (ITCZ) and strength of the Siberia High, respectively. The northern westerly, located in the mid- to high-latitude, can influence both the ITCZ and the Siberia High. As indicated by earlier studies [12], slowdown of the Atlantic meridional overturning circulation would cause decreasing of temperature in the northern hemisphere and strengthen the northern westerly circulation. Then the winter monsoon would be strengthened during the cold periods, and the ITCZ would shift southward, causing the weakening of the Asian summer monsoon.

We therefore summarized the linkage between lake evolution recorded in the Longjie Silt Layers and commonly climatic forces as follows: when the winter monsoon strengthened and the summer monsoon weakened, winter snowfall increased but summer rainfall significantly decreased. Although melting snow would increase, because the summer rainfall accounts for >80% of annual quantity (Figure 8), regional water discharge significantly decreased. Due to weakened hydrodynamics, lake sediment would become finer. However, possibly due to incised river channels and/or tectonic uplift, this paleolake turned far away or higher than the river base level, causing influences from climatic change and grain size variability significantly decreased from 60–44 ka to 44–30 ka. More evidence and further studies will be

necessary to test the interaction between tectonic activity and climate change in the future.

5. Conclusions

In summary, a time-series for Longjie Silt Layers during the MIS 3 was reconstructed by grain size of lake sediments. The record contains a series of millennial-scale events, which are comparable with DO events in other Asian monsoon records. The consistence of these events in both summer and winter monsoon records indicated common forcing of summer and winter monsoon strength on millennial-scale during the period. The signal was suggested to be transmitted into lake evolution through physical relationship between climatic changes and regional water discharges and sediment transport.

Conflict of Interests

The authors declare that there is no conflict of interests regarding the publication of this paper.

Acknowledgments

The research was financially supported by National Natural Science Foundation of China (Project no. 40772211). And thanks for the help are due to Professor Hua Zhao, Institute of Hydrogeology and Environmental Geology, Chinese Academy of Geological Sciences.

References

- [1] A. H. L. Voelker and Workshop participants, “Global distribution of centennial-scale records for Marine Isotope Stage (MIS)

- 3: a database," *Quaternary Science Reviews*, vol. 21, no. 10, pp. 1185–1212, 2002.
- [2] M. Siddall, E. J. Rohling, W. G. Thompson, and C. Waellbroeck, "Marine isotope stage 3 sea level fluctuations: data synthesis and new outlook," *Reviews of Geophysics*, vol. 46, no. 4, Article ID RG4003, 2008.
- [3] W. Dansgaard, S. Johnsen, H. B. Clausen et al., "North Atlantic climatic oscillations revealed by deep Greenland ice cores," in *Climate Processes and Climate Sensitivity*, J. E. Hansen and T. Takahashi, Eds., pp. 288–298, American Geophysical Union, Washington, DC, USA, 1984.
- [4] K. K. Andersen, N. Azuma, J.-M. Barnola et al., "High-resolution record of Northern Hemisphere climate extending into the last interglacial period," *Nature*, vol. 431, no. 7005, pp. 147–151, 2004.
- [5] L. A. Hinnov, M. Schulz, and P. Yiou, "Interhemispheric space-time attributes of the Dansgaard-Oeschger," *Quaternary Science Reviews*, vol. 21, pp. 1213–1228, 2002.
- [6] S. V. Petersen, D. P. Schrag, and P. U. Clark, "A new mechanism for Dansgaard-Oeschger cycles," *Paleoceanography*, vol. 28, no. 1, pp. 24–30, 2013.
- [7] B.-Y. Li, "The last greatest lakes on the Xizang (Tibetan) plateau," *Acta Geographica Sinica*, vol. 55, no. 2, pp. 174–182, 2000.
- [8] Y. Shi, Y. Jia, G. Yu et al., "Features, impacts and causes of the high temperature and large precipitation event in the Tibetan Plateau and its adjacent area during 40–30 ka BP," *Journal of Lake Sciences*, vol. 14, pp. 1–11, 2002.
- [9] J. Wang, "Glacial advance in the Qinghai-Tibet Plateau and peripheral mountains during the mid-MIS 3," *Quaternary Sciences*, vol. 30, no. 5, pp. 1055–1065, 2010.
- [10] S. C. Porter and A. Zhisheng, "Correlation between climate events in the North Atlantic and China during the last glaciation," *Nature*, vol. 375, no. 6529, pp. 305–308, 1995.
- [11] Z. Guo, S. Peng, L. Wei, and T. Liu, "Weathering signals of millennial-scale oscillations of the East-Asian summer monsoon over the last 220 ka," *Chinese Science Bulletin*, vol. 44, pp. 20–25, 1999.
- [12] Y. Sun, S. C. Clemens, C. Morrill, X. Lin, X. Wang, and Z. An, "Influence of Atlantic meridional overturning circulation on the East Asian winter monsoon," *Nature Geoscience*, vol. 5, no. 1, pp. 46–49, 2012.
- [13] D. Yuan, H. Cheng, R. L. Edwards et al., "Timing, duration, and transitions of the last Interglacial Asian monsoon," *Science*, vol. 304, no. 5670, pp. 575–578, 2004.
- [14] K. Zhao, X. Kong, H. Cheng, and Y. Wang, "Intensity and timing of D-O events of East Asian monsoon during the late episode of MIS 3," *Quaternary Sciences*, vol. 28, no. 1, pp. 177–183, 2008.
- [15] D. Liu, Y. Wang, S. Chen, H. Cheng, and R. L. Edwards, "Sub-Dansgaard-Oeschger events of East Asian monsoon and their global significance," *Quaternary Sciences*, vol. 28, pp. 169–176, 2008.
- [16] Y. Zhu, Z. Zhao, Y. Chen, M. Zhang, and G. Lei, "Record of environmental and millennial-scale climatic changes during MIS 3 by peat at Shennongjia," *Quaternary Sciences*, vol. 33, pp. 155–166, 2013.
- [17] M. Bian, "Yuanmou Basin geology, Yunnan Province, China," *Geological Society of China*, vol. 20, pp. 23–33, 1940.
- [18] C. Li, F. Jiang, J. Fu, and S. Wang, "The formation time of the Longjie silt layer in the Yuanmou Area, Yunnan Province," *Quaternary Sciences*, vol. 31, no. 5, pp. 933–934, 2011.
- [19] W. Huang, J. Wang, Z. Que, and S. Zheng, "Geochronological comparison between Yuanmou, Longjie and Zigeda formations," *Proceedings of Stratigraphy and Paleontology*, vol. 7, pp. 30–39, 1978.
- [20] L. Min, Z. Yin, and J. Zhang, "The formation time and paleoenvironment of the Longjie silt bed," *Quaternary Science*, vol. 10, pp. 354–362, 1990.
- [21] F. Jiang, X. Wu, and F. Qiang, "Silt bed of Longjie Area, Yuanmou Basin, Yunnan Province, China," in *Loess, Quaternary Geology, Global Changes*, pp. 99–106, Science Press of China, Beijing, China, 1996.
- [22] Y.-Y. Chen, C.-Z. Li, S.-B. Wang, J.-L. Fu, Z.-S. Zhang, and F.-C. Jiang, "Grain-size characteristics and origin of Longjie silt layer in the Yuanmou area, Yunnan, China," *Geological Bulletin of China*, vol. 28, no. 5, pp. 578–584, 2009.
- [23] G. W. Berger, P. J. Mulhern, and D. J. Huntley, "Isolation of silt-sized quartz grains from sediments," *Ancient TL*, vol. 11, pp. 8–9, 1980.
- [24] H. M. Roberts, D. R. Muhs, A. G. Wintle, G. A. T. Duller, and E. A. Bettis III, "Unprecedented last-glacial mass accumulation rates determined by luminescence dating of loess from western Nebraska," *Quaternary Research*, vol. 59, no. 3, pp. 411–419, 2003.
- [25] Z. Lai and H. Brückner, "Effects of feldspar contamination on equivalent dose and the shape of growth curve for osl of silt-sized quartz extracted from Chinese loess," *Geochronometria*, vol. 30, no. 1, pp. 49–53, 2008.
- [26] Y. C. Lu, X. L. Wang, and A. G. Wintle, "A new OSL chronology for dust accumulation in the last 130,000 yr for the Chinese Loess Plateau," *Quaternary Research*, vol. 67, no. 1, pp. 152–160, 2007.
- [27] J. R. Prescott and J. T. Hutton, "Cosmic ray contributions to dose rates for luminescence and ESR dating: large depths and long-term time variations," *Radiation Measurements*, vol. 23, no. 2–3, pp. 497–500, 1994.
- [28] M. J. Aitken, *An Introduction to Optical Dating*, Oxford University Press, Oxford, UK, 2nd edition, 1998.
- [29] D. A. Darby, J. Ortiz, L. Polyak, S. Lund, M. Jakobsson, and R. A. Woodgate, "The role of currents and sea ice in both slowly deposited central Arctic and rapidly deposited Chukchi-Alaskan margin sediments," *Global and Planetary Change*, vol. 68, no. 1–2, pp. 58–72, 2009.
- [30] L. Yi, H.-J. Yu, J. D. Ortiz et al., "Late Quaternary linkage of sedimentary records to three astronomical rhythms and the Asian monsoon, inferred from a coastal borehole in the south Bohai Sea, China," *Palaeogeography, Palaeoclimatology, Palaeoecology*, vol. 329–330, pp. 101–117, 2012.
- [31] Q. Wang, X. Yang, N. J. Anderson, E. Zhang, and Y. Li, "Diatom response to climate forcing of a deep, alpine lake (Lugu Hu, Yunnan, SW China) during the Last Glacial Maximum and its implications for understanding regional monsoon variability," *Quaternary Science Reviews*, vol. 86, pp. 1–12, 2014.
- [32] L. Yi, X. Ye, J. Chen et al., "Magnetostatigraphy and luminescence dating on a sedimentary sequence from northern East China Sea: constraints on evolutionary history of eastern marginal seas of China since the Early Pleistocene," *Quaternary International*, vol. 349, pp. 316–326, 2014.
- [33] J. D. Ortiz, "Application of visible/near infrared derivative spectroscopy to arctic paleoceanography," *IOP Conference Series: Earth and Environmental Science*, vol. 14, no. 1, Article ID 012011, 2011.

- [34] N. Jiang, R. Sun, and Q. Liang, "Late-Cenozoic deposits and mammalian faunas of Yuanmou Basin, Yunnan," *Yunnan Geology*, supplement 1, pp. 63–71, 1989.
- [35] D. Sun, J. Bloemendal, D. K. Rea et al., "Grain-size distribution function of polymodal sediments in hydraulic and aeolian environments, and numerical partitioning of the sedimentary components," *Sedimentary Geology*, vol. 152, no. 3-4, pp. 263–277, 2002.
- [36] H. Cheng, R. L. Edwards, W. S. Broecker et al., "Ice age terminations," *Science*, vol. 326, no. 5950, pp. 248–252, 2009.
- [37] Y. Wang, H. Cheng, R. L. Edwards et al., "The holocene Asian monsoon: links to solar changes and North Atlantic climate," *Science*, vol. 308, no. 5723, pp. 854–857, 2005.
- [38] Y. Wang, H. Cheng, R. L. Edwards et al., "Millennial- and orbital-scale changes in the East Asian monsoon over the past 224,000 years," *Nature*, vol. 451, no. 7182, pp. 1090–1093, 2008.
- [39] Y. J. Wang, H. Cheng, R. L. Edwards et al., "A high-resolution absolute-dated late pleistocene monsoon record from Hulu Cave, China," *Science*, vol. 294, no. 5550, pp. 2345–2348, 2001.
- [40] P. M. Grootes, M. Stulver, J. W. C. White, S. Johnsen, and J. Jouzel, "Comparison of oxygen isotope records from the GISP2 and GRIP Greenland ice cores," *Nature*, vol. 366, no. 6455, pp. 552–554, 1993.
- [41] A. N. LeGrande and G. A. Schmidt, "Sources of Holocene variability of oxygen isotopes in paleoclimate archives," *Climate of the Past*, vol. 5, no. 3, pp. 441–455, 2009.
- [42] S. C. Clemens, W. L. Prell, and Y. Sun, "Orbital-scale timing and mechanisms driving late pleistocene Indo-Asian summer monsoons: reinterpreting cave speleothem $\delta^{18}\text{O}$," *Paleoceanography*, vol. 25, no. 4, Article ID PA4207, 2010.
- [43] F. S. R. Pausata, D. S. Battisti, K. H. Nisancioglu, and C. M. Bitz, "Chinese stalagmite $\delta^{18}\text{O}$ controlled by changes in the indian monsoon during a simulated heinrich event," *Nature Geoscience*, vol. 4, no. 7, pp. 474–480, 2011.
- [44] B. A. Maher and R. Thompson, "Oxygen isotopes from chinese caves: records not of monsoon rainfall but of circulation regime," *Journal of Quaternary Science*, vol. 27, no. 6, pp. 615–624, 2012.
- [45] M. Tan, "Circulation effect: response of precipitation $\delta^{18}\text{O}$ to the ENSO cycle in monsoon regions of China," *Climate Dynamics*, vol. 42, no. 3-4, pp. 1067–1077, 2014.

Research Article

Impacts of Climate Change and Human Activities on Runoff and Sediment Load of the Xiliugou Basin in the Upper Yellow River

Haifang Yao,^{1,2} Changxing Shi,¹ Wenwei Shao,^{1,2} Jianbin Bai,^{1,2} and Hui Yang^{1,2}

¹*Institute of Geographic Sciences and Natural Resources Research, Key Laboratory of Water Cycle and Related Land Surface Processes, Chinese Academy of Science, Beijing 100101, China*

²*University of Chinese Academy of Sciences, Beijing 100049, China*

Correspondence should be addressed to Changxing Shi; shicx@igsnr.ac.cn

Received 27 January 2015; Accepted 11 April 2015

Academic Editor: Steffen Mischke

Copyright © 2015 Haifang Yao et al. This is an open access article distributed under the Creative Commons Attribution License, which permits unrestricted use, distribution, and reproduction in any medium, provided the original work is properly cited.

Using data of temperature, wind, precipitation, water discharge, and sediment load, the changes in runoff and sediment load of the Xiliugou basin in the upper Yellow River were investigated and the contributions of climate change and human activities to these changes were quantitatively estimated. Results show that the runoff and sediment load of the stream declined gradually in 1960–2012. According to the abrupt change point detected, the runoff and sediment series were divided into two periods: 1960–1998 and 1999–2012. The reductions of runoff and sediment load in 1999–2012 were found to be related to climate change and human activities, and the latter played a dominant role with a contribution of about 68% and 75%, respectively. The effects of rainfall intensity should be considered to avoid overestimating or underestimating the contributions of rainfall changes to the variations of runoff and sediment load in the semiarid region. An inspection of changes in water discharge and sediment regime indicated that the frequency of discharge between 0 and 5 m³/s increased while that between 5 and 1000 m³/s decreased in 2006–2012. This phenomenon can be attributed principally to the soil and water conservation practices.

1. Introduction

Warming of the climate system is unequivocal. According to the IPCC [1], the average global surface temperature increased by 0.85°C over the period 1880–2012. With global warming and temperature increasing, the rainfall will be affected, hence river flows [2]. Water discharge and sediment flux, which are the two most important elements of the hydrologic cycle, not only reflect the characteristics of river systems themselves but also reflect the changing of the catchment environment [3, 4]. Therefore, the impacts of climate change on the streamflow [2–13] and sediment [3, 4, 9–15] have been well studied in the literature.

Aside from climate change, recently, human activities (such as land use/land cover change [16–24], dam construction and operation of large reservoirs [10, 12, 25, 26], and soil and water conservations [4, 12, 27]) have played a crucial role in the changes of water discharge and sediment flux. The study by Walling [28] analyzed the changes of sediment yield of the Black Sea over the past 20,000 years, revealing that

climate change was more important than human impact in driving changes in sediment yield in the long time scale. The same study summarized the trends of runoff and sediment loads for the Yellow River in China, Chao Phraya River in Thailand, and the Kolyma River in Eastern Siberia and concluded that human activities were primary drivers causing changes in the sediment loads of the world's rivers in the short time scale. For the runoff variation, Miao et al. [29] suggested that climate change usually impacts it periodically and lastingly, whereas human activities impact it suddenly and directionally.

Climate change often interacts with anthropogenic impacts in causing runoff and sediment load changes, and defining their contributions is of significance for managing rivers. Some recent studies have come to quantify the relative effects of climate change and human activities on streamflow and sediment load. Naik and Jay [10] analyzed climate change and human influences (water withdrawal for irrigation, reservoir manipulation, mining, and deforestation) on the Columbia River's runoff and sediment load. They identified

that human influences contributed 8-9% to the decrease of runoff, and climate change contributed 7-8%. Ahn and Merwade [30] quantified the role of climate change and human impacts on the streamflow of four states in USA, including Arizona, Georgia, Indiana, and New York, suggesting that the streamflow change of the four states caused by human activities accounted for 74%, 55.5%, 71.4%, and 85.7%, respectively. In China, Gao et al. [31] reported that 12.2% of the decrease in the sediment load of the middle Yellow River could be attributed to the changes in precipitation and the remaining 87.8% to human activities. For the decrease of sediment load of the Pearl River, 90% was caused by dam construction and 10% was due to climate change [26]. As a whole, the effects of human activities and climate change on runoff and sediment load vary from place to place and need to be investigated at a local scale based on watershed properties and regional environment characteristics.

As the second longest river in China, the Yellow River is noted for its relatively low water discharge as compared with its huge sediment load. Since the 1970s, the sediment discharge of the Yellow River has changed significantly, and many studies were devoted to the analysis of runoff and sediment changes in the river. The ten small tributaries, including Maobula, Buersetaigou, Heilaigou, Xiliugou, Hantaichuan, Haoqinghe, Hashenlachuan, Muhaerhe, Dongliugou, and Husitaihe, are a principal sediment source in the upper Yellow River and are adjacent to the middle Yellow River basin which is one of the regions with the most severe soil erosion in the world [32]. These tributaries originate from the Ordos Plateau, flow through the Hobq Desert, and finally enter the Yellow River [33]. The upstream of these tributaries is a loess hilly and gully region, the midstream is a desert area, and the downstream is an alluvial plain. The huge sediment output from the ten small tributaries has caused heavy sedimentation in the Inner-Mongolia reach [34–36]. So far, numerous studies have examined the characteristics of runoff and sediment load in this region [36–39], but the anthropogenic and climatic impacts on the changes of runoff and sediment load in the ten small tributaries have received less attention. Hence, we take one of the ten small tributaries, the Xiliugou basin, as a case to study the effects of climate change and human activities on the variations in the runoff and sediment load.

The objectives of this paper are as follows: (1) to analyze the variation tendency of runoff and sediment yield in the Xiliugou basin based on the hydrological records during 1960–2012 and (2) to quantify the relative effects of climate change and human activities on the streamflow and sediment load of the tributary. Better understanding of the response of the river to climate change and anthropogenic interferences might provide a theoretical basis for improving policy and plans of water and soil conservation in this sediment source area of the upper Yellow River and also give a reference for studying the same issues in other rivers.

2. Study Area and Data

2.1. Study Area. The Xiliugou basin is located between $109^{\circ}24' \sim 110^{\circ}00' E$ and $39^{\circ}47' \sim 40^{\circ}30' N$ and in the middle

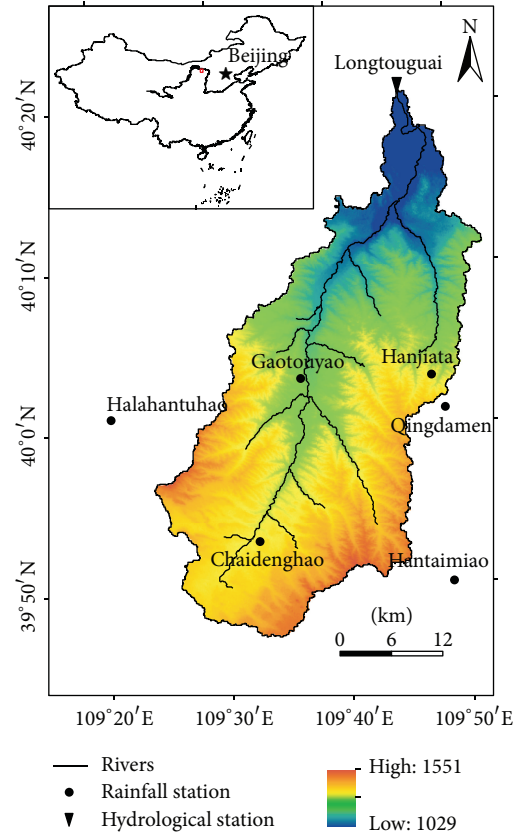


FIGURE 1: Location of the Xiliugou basin.

of the ten small tributaries (Figure 1). It has a drainage area of 1180 km^2 and a fall from 1551 to 1029 m. The watershed belongs to semiarid climate zones. It has a long and cold winter and a short and torrid summer. From November to next April, it is windy. The mean annual temperature was $6.8^{\circ}C$ and the average annual precipitation was 289.6 mm in the period from 1960 to 2012. The distribution of monthly precipitation, runoff, and sediment load was extremely uneven and was mainly concentrated in the flood season (from June to September). Precipitation in the flood season accounted for 79.8% of the total precipitation in a year, producing 55.7% of the yearly runoff, which carried 87% of the yearly sediment load.

2.2. Data Collection. Data used in this paper include the annual runoff and sediment load (1960–2012), daily discharge and sediment concentration (1964–2012, excluding 1991–2005) in the flood season at Longtougouai hydrological station of the Xiliugou basin, and daily meteorological data at 17 rainfall stations and 10 weather stations from 1960 to 2012. The runoff and sediment data at Longtougouai hydrological station and precipitation data at 17 rainfall stations were collected from the Yellow River Conservancy Commission (YRCC). The meteorological data from 10 weather stations were provided by the National Climate Centre (NCC) of China Meteorological Administration (CMA). Using the IDW method in the tools of ArcGIS, the mean daily rainfall and temperature

of the Xiliugou basin were extracted from the daily records at rainfall and weather stations. The Dongsheng weather station, which is nearest to the Xiliugou basin, was selected to obtain the wind speeds and sand-dust storms data. The sand-dust storms data supplied by the NCC of CMA cover the period from 1960 to 2007. In addition, the vegetation coverage of the Xiliugou basin was calculated from 8 km AVHRR (1981–2006) and 250 m MODIS (2000–2010) NDVI products, which were downloaded from the website of Geospatial Data Cloud (<http://www.gscloud.cn/>).

3. Methods

3.1. Trend Analysis. The Mann-Kendall (MK) test [40, 41] is one of the popular nonparametric methods for analyzing trends in hydrologic variables [30, 42]. For a given time series $X(x_1, x_2, \dots, x_n)$, the statistic S is defined as

$$S = \sum_{i=1}^n \sum_{j=i+1}^{n-1} \text{sgn}(x_j - x_i), \quad (1)$$

where

$$\text{sgn}(x_j - x_i) = \begin{cases} 1, & x_j > x_i, \\ 0, & x_j = x_i, \\ -1, & x_j < x_i; \end{cases} \quad (2)$$

n is the sample size. Once n is greater than 8, S values will follow an approximate normal distribution [30, 43]. Its variance is calculated as

$$\text{Var}(S) = \frac{n(n-1)(2n+S)}{18}. \quad (3)$$

Then, the Mann-Kendall Z is given by

$$Z = \begin{cases} \frac{(S-1)}{\sqrt{\text{Var}(S)}}, & S > 0, \\ 0, & S = 0, \\ \frac{(S+1)}{\sqrt{\text{Var}(S)}}, & S < 0. \end{cases} \quad (4)$$

A positive value of Z indicates an increasing trend, and vice versa. The null hypothesis of no trend is rejected if $|Z| > 1.96$ at the 5% significance level.

3.2. Breakpoint Detection

3.2.1. Pettitt. The Pettitt test [44] is a nonparametric method widely applied to detect the abrupt changes of water discharge and sediment load [42, 45]. For a given time series $X(x_1, x_2, \dots, x_N)$, divided into two samples x_1, x_2, \dots, x_t and $x_{t+1}, x_{t+2}, \dots, x_N$, the Pettitt test uses a version of the Mann-Whitney statistic $U_{t,N}$ calculated as

$$U_{t,N} = U_{t-1,N} + \sum_{j=1}^N \text{sgn}(x_t - x_j), \quad t = 2, 3, \dots, N, \quad (5)$$

where

$$\text{sgn}(x_t - x_j) = \begin{cases} 1, & x_t > x_j, \\ 0, & x_t = x_j, \\ -1, & x_t < x_j. \end{cases} \quad (6)$$

The breakpoint is defined to be where $|U_{t,N}|$ reaches its maximum value:

$$K_N = \text{Max}|U_{t,N}|, \quad (1 \leq t \leq N). \quad (7)$$

The significance level associated with K_N is determined approximately by

$$p \cong 2 \exp \left[\frac{-6(K_N)^2}{(N^3 + N^2)} \right]. \quad (8)$$

If $p < 0.05$, a significant change point exists.

3.2.2. Sequential Cluster. The sequential cluster method can be used to estimate the optimal dividing point of hydrological series [46, 47]. For a given time series $X(x_1, x_2, \dots, x_n)$, divided into two samples x_1, x_2, \dots, x_τ and $x_{\tau+1}, x_{\tau+2}, \dots, x_n$, the sum of the squared deviation before τ and after τ is defined as follows:

$$V_\tau = \sum_{i=1}^{\tau} (x_i - \bar{x}_\tau)^2, \quad (9)$$

$$V_{n-\tau} = \sum_{i=\tau+1}^n (x_i - \bar{x}_{n-\tau})^2,$$

where

$$\bar{x}_\tau = \frac{1}{\tau} \sum_{i=1}^{\tau} x_i, \quad (10)$$

$$\bar{x}_{n-\tau} = \frac{1}{n-\tau} \sum_{i=\tau+1}^n x_i;$$

\bar{x}_τ is the average of the hydrological sequence before τ and $\bar{x}_{n-\tau}$ is the average of the hydrological sequence after τ . Then, $S_n(\tau)$ is given by

$$S_n(\tau) = V_\tau + V_{n-\tau}; \quad (11)$$

when $S_n(\tau)$ reaches its minimum value, τ is the optimal breakpoint.

The rank-sum test is usually used to determine the significance of the abrupt change point [48, 49]. For a given abrupt point τ , the statistic of U is calculated as

$$U = \frac{W - n_1(n_1 + n_2 + 1)/2}{\sqrt{n_1 n_2 (n_1 + n_2 + 1)/12}}, \quad (12)$$

where n_1 is the subsample size with fewer samples and n_2 is the subsample size with more samples. W is the sum of the rank in subsample with fewer samples.

If $|U| \geq 1.96$, the abrupt change point is significant.

TABLE 1: Changes of annual precipitation, temperature, wind, runoff, and sediment load of the Xiliugou basin.

Periods	Precipitation (mm)	Average temperature (°C)	Days of strong wind (days)	Days of sand-dust storms (days)	Runoff (10 ⁴ m ³)	Sediment load (10 ⁴ t)
1960–1969	297.3	6.2	74.3	18.3	3450.5	614.9
1970–1979	263.0	6.2	66.5	17.2	3476.6	438.3
1980–1989	248.6	6.3	29.7	2.5	2597.8	673.5
1990–1999	351.4	7.3	27.3	1.2	3259.8	409.6
2000–2012	288.0	7.6	12.5	0.4	1803.2	101.5
Max	502.5	8.5	104.0	45.0	9659.0	4749.0
Min	109.0	5.0	3.0	0.0	736.2	0.01
Average	289.6	6.8	40.4	7.5	2854.5	428.0
C_v	0.3	0.1	0.7	1.3	0.7	1.9

3.3. *Separating the Impacts of Climate Change and Human Activities on Streamflow and Sediment Load.* By the abrupt changes identified, the runoff and sediment load series are divided into two periods. The first period is regarded as the natural period or reference period and the second period is regarded as the measure period or impact period. Following previous studies [50], we separated the effects of human activities and climate change on runoff and sediment load in the second period by comparing with runoff and sediment load in the reference period. The separation approach can be described by the following equations:

$$\begin{aligned}
 W_T &= W_I - W_N, \\
 W_C &= W_S - W_N, \\
 W_H &= W_T - W_C, \\
 \eta_H &= \frac{W_H}{W_T} \times 100\%, \\
 \eta_C &= \frac{W_C}{W_T} \times 100\%,
 \end{aligned} \tag{13}$$

where W_T is the total runoff or sediment load variation and W_I and W_N are the average observed runoff or sediment load in the impact period and natural period, respectively. W_C is the runoff or sediment load variation caused by climate impact, W_S is the simulated virgin runoff or sediment load from the basin with the same land cover as that in the reference period by the rainfall in the impact period, W_H is the runoff or sediment load variation caused by human activities, and η_H and η_C measure the relative impacts of human activities and climate change on runoff or sediment load, respectively.

The double mass curves between annual precipitation and runoff/sediment load can reflect the impacts of human activities [15, 31]. Here, we use the regression equations established from the double mass curves of precipitation versus runoff and precipitation versus sediment load in the natural period to calculate the annual runoff and sediment load in the impact period (W_S).

4. Results

4.1. *Changes in Precipitation, Temperature, Wind, Runoff, and Sediment Load.* Figure 2 shows trends of runoff, sediment load, and meteorological indices, estimated by the MK test. Overall, the runoff, sediment discharge, and annual days of strong wind (daily wind speed ≥ 5 m/s) and sand-dust storms decreased significantly at the 99% confidence level with the Z value at -2.65 , -2.57 , -7.93 , and -6.67 , respectively, while the mean annual temperature increased significantly at the 99% confidence level with a Z value of 5.1. For the precipitation series, no significant trend was detected.

For investigating the decadal changes of the six variables, the mean of each variable in each decade was calculated (Table 1). The results indicate that the runoff, sediment discharge, precipitation, temperature, and annual days of strong wind and sand-dust storms of the Xiliugou basin changed obviously during the period 1960–2012, especially for sediment discharge which fluctuated in the range of 0.01–4749 t/a with an average of 428 t/a and a coefficient of variance (C_v) as high as 1.9. Moreover, regarding the sediment discharge during 1960–1969 as the reference value, except the 1980s, the sediment discharge during the 1970s, 1990s, and 2000–2012 decreased by 28.7%, 33.4%, and 83.5%, respectively. For the annual runoff, a considerable reduction up to 47.7% occurred in the period 2000–2012. The annual days of strong wind and sand-dust storms decreased continuously during the last four decades (from the year 1970 to 2012). The maximum change of the annual days of strong wind and sand-dust storms occurred in the period 2000–2012, in which the annual days of strong wind and sand-dust storms decreased by 83.1% and 97.9%, respectively. By contrast, the mean annual temperature increased gradually during the last three decades, especially in the 1990s and 2000–2012. The decadal means of annual precipitation ranged from 248.6 to 351.4 mm with no noticeable trend.

4.2. *Abrupt Change Analysis.* The abrupt changes in runoff and sediment load recorded at Longtougai hydrological station during 1960–2012 were examined using Pettitt test. Figure 3 shows the changes of K statistic of Pettitt test during the period 1960–2012. Obviously, abrupt changes appeared

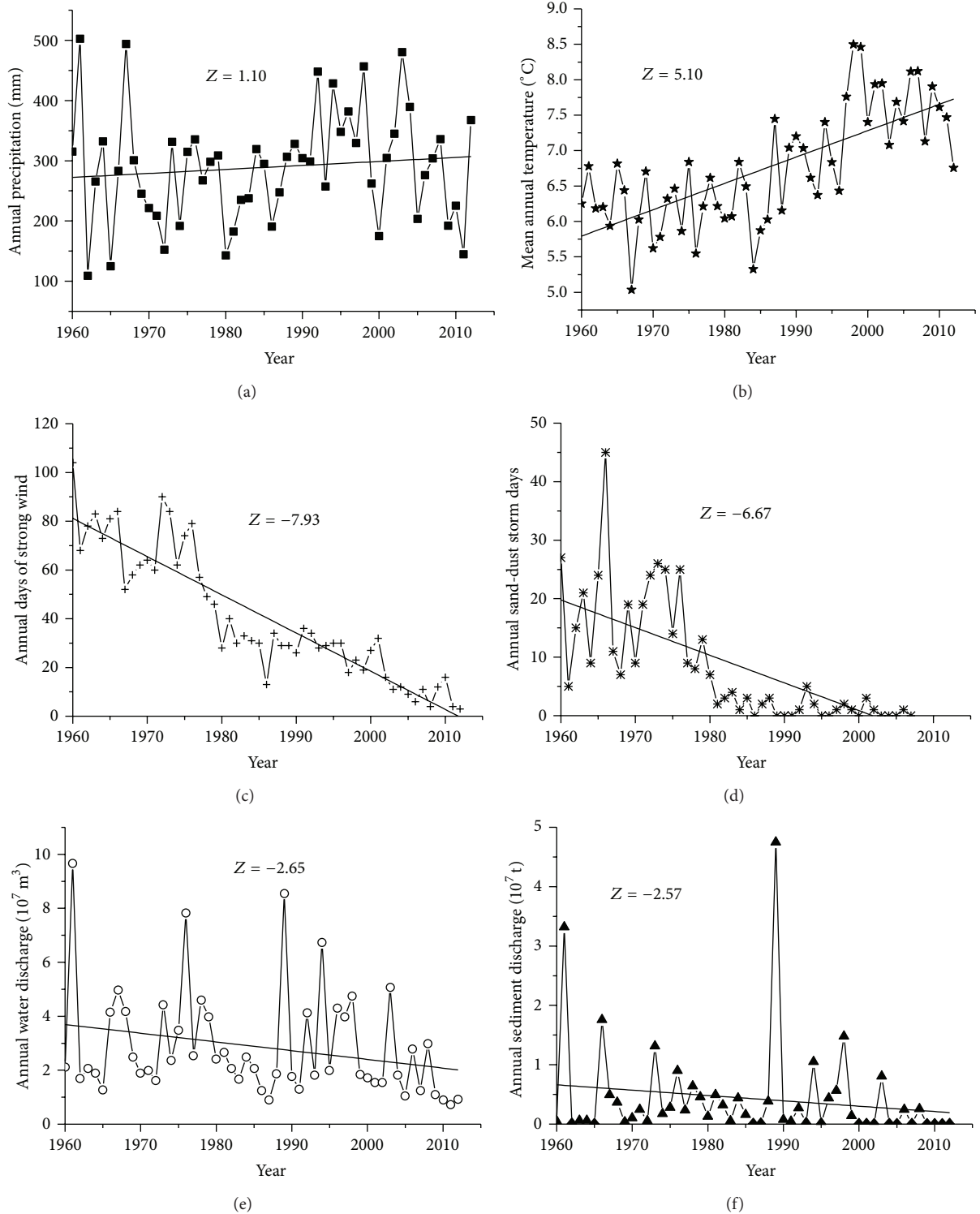


FIGURE 2: Trends of precipitation, temperature, wind, runoff, and sediment load ($|Z| \geq 1.96, p < 0.05$; $|Z| \geq 2.576, p < 0.01$).

in 1998 in both the runoff and sediment load series. The abrupt change in the sediment load series is statistically significant with a p value of 0.007, but that in the runoff series has a p value of 0.052. In this case, the sequential cluster method was adopted to further detect the abrupt change

points in the runoff series. Figure 4 shows the changes in $S_n(\tau)$ during the period 1960–2012. Again, the point in 1998 is the lowest. By applying the rank-sum test to the abrupt change point in 1998, it is proved that the abrupt change point is statistically significant with a U value of -3.12 . According to

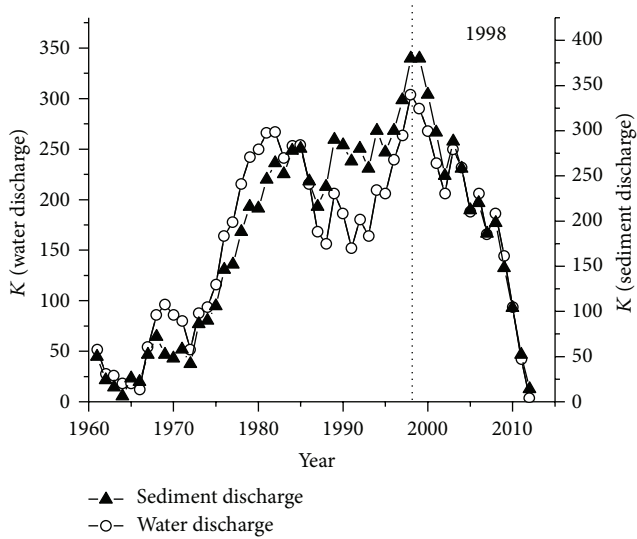


FIGURE 3: Abrupt changes in annual runoff and sediment load in 1960–2012 (by Pettitt test).

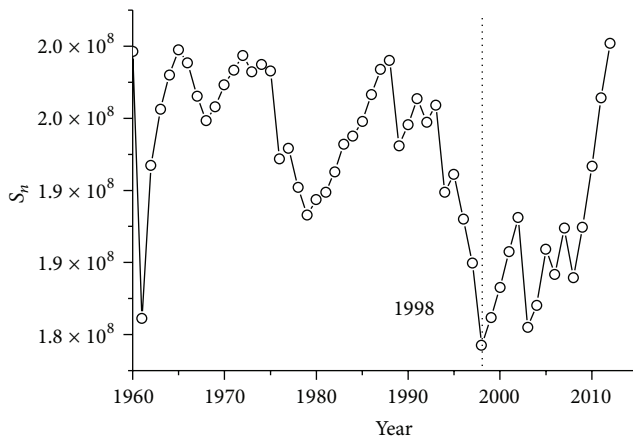


FIGURE 4: Abrupt changes in annual runoff in 1960–2012 (by sequential cluster test).

these breakpoints, the study period for runoff and sediment load and all influencing variables in the Xiliugou catchment was divided into the natural period (1960–1998) and the impact period (1999–2012).

4.3. Separating Climatic and Anthropogenic Impacts on Annual Water Discharge and Sediment Load. The Xiliugou basin belongs to the region where wind-water two-phase coupling processes prevail. Therefore, hydroclimatic variables including precipitation, temperature, and annual days of strong wind and sand-dust storms were considered to analyze the effects of climate change on runoff and sediment load variations. The correlation coefficients between runoff, sediment load, and meteorological indices were calculated by SPSS19 software (Table 2). The statistics demonstrate that precipitation is the key factor affecting runoff and sediment load.

To define a better relationship between precipitation and runoff and that between precipitation and sediment discharge, we investigated the performance of six categories of annual precipitation, which are the sums of different daily rainfall (≥ 0 mm, ≥ 5 mm, ≥ 10 mm, ≥ 15 mm, ≥ 20 mm, and ≥ 30 mm). Table 3 shows the statistics of the runoff, sediment load, and six categories of annual precipitation by SPSS19. The correlation coefficients between runoff and the six categories of annual precipitation are 0.60, 0.64, 0.69, 0.74, 0.77, and 0.75, respectively, and the correlation coefficients between sediment load and the six categories of annual precipitation are 0.39, 0.43, 0.48, 0.51, 0.53, and 0.54, respectively. All the correlation coefficients are significant at the 0.01 level. The runoff is best correlated with the fifth category, which is the annual sum of daily rainfall ≥ 20 mm, and the sediment load is best correlated with the sixth category, which is the annual sum of daily rainfall ≥ 30 mm. Considering that the correlation coefficients between the annual sediment load and the fifth category and between the annual sediment load and the sixth category are nearly the same, the annual rainfall series with daily rainfall ≥ 20 mm was selected to analyze the effects of climate change on both the runoff and sediment load.

Using the annual precipitation of daily rainfall ≥ 20 mm, double mass curves of rainfall versus runoff and rainfall versus sediment load for the reference period of 1960–1998 were plotted in Figure 5. Linear regression relations of the double mass curves were also shown in Figure 5 and could be represented by

$$\begin{aligned}\Sigma Q &= 27.862\Sigma P - 1079.9, \\ \Sigma S &= 4.3707\Sigma P + 343.09,\end{aligned}\quad (14)$$

where ΣQ is the cumulative runoff discharge, ΣP is the cumulative precipitation, and ΣS is the cumulative sediment discharge.

Based on (14), the annual virgin streamflow and sediment discharge under the rainfall in the period 1999–2012 were calculated. Then, the effects of climate change and human activities on runoff and sediment load in the impact period 1999–2012 were separated using (13). The results are shown in Tables 4 and 5. Comparing with the natural period (1960–1998), the mean annual runoff and sediment load in the impact period decreased by 44.1% and 80.9%, respectively. Clearly, the rate of sediment load reduction is much greater than that of runoff reduction. For the runoff reduction, human activities made a contribution of 68% and the remaining 32% was associated with climate change. In contrast, the anthropogenic impacts contributed 75% to the sediment load reduction, and the climate change was responsible for the remaining 25%. Thus, human activities had been the dominant influence factor for both the runoff and sediment load reductions in the Xiliugou basin.

5. Discussion

5.1. Impacts of Climate Change. As disclosed in Table 2, both the runoff and sediment load are more closely related with precipitation in the Xiliugou basin. Thus, when there was

TABLE 2: Correlation coefficients between annual runoff, sediment load, and meteorological indices.

	Annual precipitation	Mean annual temperature	Annual days of strong wind	Annual days of sand-dust storms
Runoff	0.61**	-0.14	0.13	0.22
Sediment	0.40**	0.01	0.08	0.12

**Significant at the 0.01 level.

TABLE 3: Correlation coefficients between annual runoff, sediment load, and precipitation with different daily precipitation thresholds.

	Categories of rainfall (mm)					
	Daily rainfall ≥ 0	Daily rainfall ≥ 5	Daily rainfall ≥ 10	Daily rainfall ≥ 15	Daily rainfall ≥ 20	Daily rainfall ≥ 30
Runoff	0.60**	0.64**	0.69**	0.74**	0.77**	0.75**
Sediment	0.39**	0.43**	0.48**	0.51**	0.53**	0.54**

**Significant at the 0.01 level.

TABLE 4: Contributions of precipitation variation and human activities to changes in runoff.

Period	Precipitation (mm)	Observed runoff W_I (10^4 m ³)	Simulated virgin runoff W_S (10^4 m ³)	Effect of precipitation		Effect of human activities	
				W_C (10^4 m ³)	η_C (%)	W_H (10^4 m ³)	η_H (%)
1960–1998	119.45	3231.05	—	—	—	—	—
1999–2012	99.34	1805.58	2767.78	-463.27	32%	-962.20	68%

TABLE 5: Contributions of precipitation variation and human activities to changes in sediment load.

Period	Precipitation (mm)	Observed sediment load W_I (10^4 t)	Simulated virgin sediment load W_S (10^4 t)	Effect of precipitation		Effect of human activities	
				W_C (10^4 t)	η_C (%)	W_H (10^4 t)	η_H (%)
1960–1998	119.45	544.21	—	—	—	—	—
1999–2012	99.34	104.13	434.18	-110.02	25%	-330.05	75%

TABLE 6: Differences of precipitation, runoff, and sediment load of the Xiliugou basin between natural period and impact period.

	Annual runoff	Annual sediment load	Daily rainfall ≥ 0	Daily rainfall ≥ 5	Daily rainfall ≥ 10	Daily rainfall ≥ 15	Daily rainfall ≥ 20	Daily rainfall ≥ 30
	(10^4 m ³)	(10^4 t)	(mm)	(mm)	(mm)	(mm)	(mm)	(mm)
1960–1998	3231.1	544.2	290.8	239.5	184.1	146.4	119.5	92.2
1999–2012	1805.6	104.1	286.1	230.0	172.2	128.7	99.3	75.0
Percentage of change	-44.1%	-80.9%	-1.6%	-4.0%	-6.5%	-12.1%	-16.8%	-18.6%

a reduction in rainfall in the period from 1999 to 2012, it was expected that a fall occurred in runoff and sediment load. The runoff and sediment load of the basin decreased by 44.1% and 80.9%, respectively (Table 6). To the total reductions of runoff and sediment load, as mentioned above, the contributions of climate change were estimated to be 32% and 25%, respectively. This means that the rainfall decrease in the years from 1999 to 2012 induced a reduction of 14.1% in runoff and a reduction of 20.2% in sediment load in the basin. Nevertheless, it is not the changes of all sizes of rainfall strength that are responsible for the reduction of runoff or sediment load. Table 3 shows that the annual runoff and sediment load are more closely related with the annual precipitation of the higher daily rainfall. In other words, the runoff and sediment load in the Xiliugou basin are sensitive to rainfall intensity. Hence, it is the reduction of storm and

heavy storm rainfalls that induces the reduction of the runoff and sediment load. The annual precipitation of the daily rainfall ≥ 20 mm, used in this study for deriving the effect of climate change, decreases by 16.8% (Table 6). Thus, a decrease of effective rainfalls tends to cause a bit lower percentage (14.1%, as given above) of runoff reduction and a slightly higher portion (20.2%) of sediment load reduction in the Xiliugou basin.

Many previous studies used the total annual rainfall to investigate the contributions of precipitation change to runoff and sediment variations [11, 15, 29, 31, 50–53]. However, in arid and semiarid regions, the rainfall intensity is important for runoff generation and soil erosion [21]. As stated above, we choose the annual rainfall series with daily rainfall ≥ 20 mm to estimate the effects of precipitation change on runoff and sediment load based on the correlation coefficients between

TABLE 7: Contributions of precipitation variation and human activities to changes in runoff and sediment load with different daily precipitation thresholds.

Categories of rainfall (mm)	Runoff		Sediment load	
	Effect of precipitation	Effect of human activities	Effect of precipitation	Effect of human activities
Daily rainfall ≥ 0	2.9%	97.1%	9.4%	90.6%
Daily rainfall ≥ 5	7.4%	92.6%	11.8%	88.2%
Daily rainfall ≥ 10	10.6%	89.4%	13.6%	86.4%
Daily rainfall ≥ 15	21.1%	78.9%	19.1%	80.9%
Daily rainfall ≥ 20	32.5%	67.5%	25.0%	75.0%
Daily rainfall ≥ 30	19.7%	80.3%	27.9%	72.1%

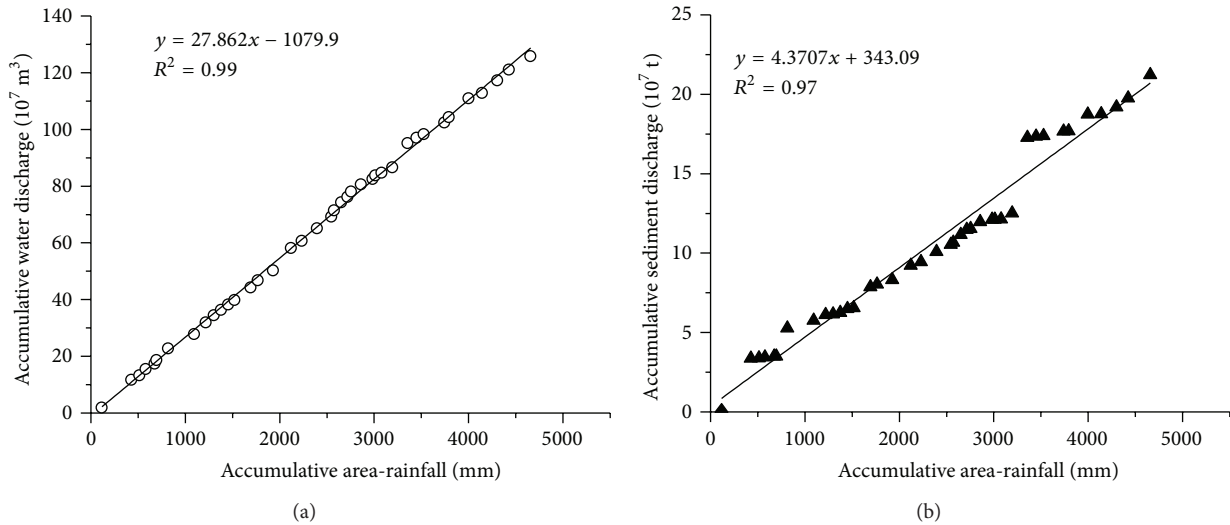


FIGURE 5: Regression relations of cumulative precipitation (daily precipitation ≥ 20 mm) with cumulative runoff and sediment load in 1960–1998.

the six categories of annual precipitation and runoff/sediment load. Here, to illustrate the importance of selecting a proper category of annual rainfall, we made an investigation about the effects of adopting annual rainfall with different intensities on the estimated contributions of rainfall changes to runoff and sediment variations. As shown in Table 7, the effects of precipitation change on the deviations of runoff and sediment load vary with different categories of annual precipitation. For runoff, except the sixth category, the contribution rate by rainfall changes increased gradually while that by human activities declined correspondingly. Comparing the percentage of change of the rainfall in Table 6 with the contribution rates of different annual precipitation categories in Table 7, we can find that the contribution rates by precipitation variation increase with the percentage of change of annual rainfall in different categories between natural period and the impact period. We think that the lower contribution rates derived from the first four annual precipitation categories underestimate the effects of climate change. The reasons are that the rainfall with a low intensity may not generate runoff in this semiarid basin. When the amount of rainfall with a low intensity does not change noticeably from the first to the second period as illustrated by the lower differences of the first four annual precipitation

categories between the two periods, the lower difference of the total of both low and high rainfall between the two periods will dampen the true effects of changes in high runoff-generating rainfall on runoff variations. As to the exception in the case of the sixth category, it might be the result of excluding some rainfall which can generate runoff. For the sediment load, the contribution rates by rainfall changes also increase gradually with rainfall intensity. Again, the lower contribution rates derived from the first four annual precipitation categories underestimate the effects of climate change for the same reasons. Therefore, when we calculate the contributions of precipitation and human activities to the changes in runoff and sediment load, we should consider the influences of rainfall intensity to avoid overestimating or underestimating the contribution by rainfall variation.

5.2. Impacts of Human Activities. In this paper, the anthropogenic contributions to runoff and sediment load reductions in one of the ten small tributaries were found to be 68% and 75%, respectively, during 1999–2012. These estimates are consistent with those given in previous studies for watersheds in the middle Yellow River, which is located on the south of the ten small tributaries. Since the late 1970s, the streamflow and sediment load in the Yellow River basin have decreased

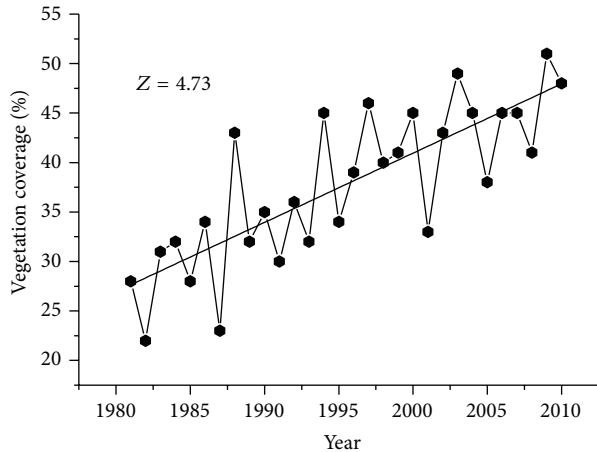


FIGURE 6: Changes of vegetation coverage in the Xiliugou basin.

greatly owing to anthropogenic impacts such as building dams and soil-water conservations [4, 27, 31]. The study by Gao et al. [31] suggested that human activities were responsible for 72% and 87.8% of the runoff and sediment load decreases in the middle Yellow River basin. For the Wuding River, which is one of the large tributaries in the middle Yellow River, it was estimated that the human activities accounted for 70% of the runoff reduction [47] and 88.9% of the sediment decrease [51]. Liang et al. [52] addressed that human activities contributed 60% to the streamflow decrease in the Kuye River basin in the north part of the middle Yellow River. In another tributary of the middle Yellow River, the Huangfuchuan River basin, 70% of the runoff decline was related to human activities [53]. All these studies indicated that human activities had become the dominant influence factor for the reductions of runoff and sediment load in the middle Yellow River in recent decades and this study finds the same phenomenon in the upper reaches of the Yellow River.

Soil and water conservation measures were implemented in the Yellow River basin as early as the 1950s and intensified in the late 1970s [27]. In contrast, the soil and water conservation measures were applied to the Xiliugou basin in a later period [54]. By the end of 2007, 26,020 ha of forests and 976 ha of grass had been planted, 2,100 ha of enclosure had been built, and the number of check dams reached 47 [55]. The total conservation area accounted for approximately 37.80% of the total basin area. Based on the AVHRR-NDVI and MODIS-NDVI data, the vegetation coverage in the Xiliugou watershed in the period from 1981 to 2010 was calculated by using the dimidiate pixel model [56]. Clearly, the vegetation coverage in the Xiliugou basin increased significantly from 1981 to 2010 (Figure 6). The mean vegetation coverage in the period of 1999–2010 reached 44%, increased by 10% compared with the period of 1981–1998. As shown in Figure 2 and Table 6, there was not a significant increasing trend in precipitation in the Xiliugou basin but a noticeable reduction in the years of 1999–2012. Considering that water availability is the control element for vegetation growth in this semiarid region, the rise of vegetation coverage in the basin could be attributed principally to the implementation of conservation

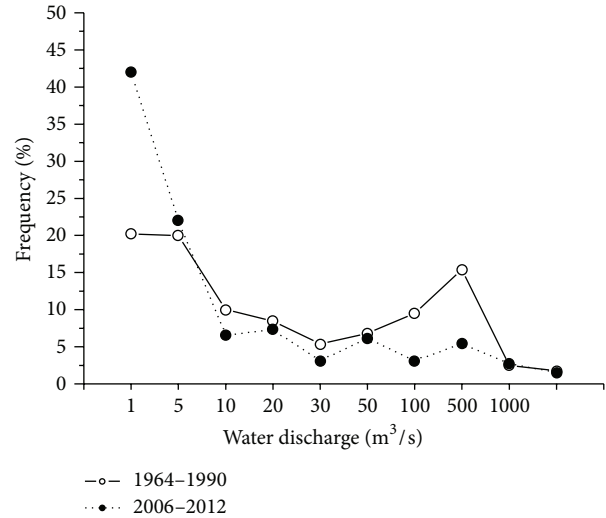


FIGURE 7: Frequency distribution of discharge.

measures including afforestation, grass-planting, and enclosure. Thus, it is soil and water conservation measures that have played an important role in the reduction of the runoff and sediment yield in the Xiliugou basin.

5.3. Changes of Water-Sediment Relation and Flow Frequency Distribution and Some Implications. A reduction of runoff in the impact period in the Xiliugou basin has been revealed above. Nevertheless, this is not applicable to the full water discharge spectrum. Figure 7 shows the frequency distribution of different categories of water discharge in both the reference and impact periods. It is demonstrated that, during the impact period, the frequency of discharge between 0 and 5 m³/s increased and that between 5 and 1000 m³/s decreased. For the water discharge larger than 1000 m³/s, the frequency changed little. This discrepancy in the changes of flows in different size intervals can also be attributed to the implementation of soil and water conservation measures. As mentioned above, the vegetation coverage in Xiliugou basin increased significantly from 1981 to 2010 owing to the soil and water conservation practices (Figure 6). By intercepting precipitation, enhancing evaporation, and increasing infiltration, vegetation can reduce the total runoff but may elevate the runoff of low flows. This should be the main reason for the increase of water discharge in the range of 0–5 m³/s and the decrease of flows within 5–1000 m³/s.

Clearly, in the Xiliugou basin, it is reasonable to reach the fact that the reduction of sediment load mainly results from the decrease of moderate flows, which are the events, as stated by Wolman and Miller [57], that tend to carry the largest portion of sediment in most rivers. Consequently, with the reduction of moderate flows and the increase of low flows, a higher portion of sediment load than that for runoff was reduced during the impact period.

Besides the discrepancy of runoff changes for different flows, the higher percentage of sediment load reduction than runoff (indicated by 80.9% versus 44.1%) in the impact

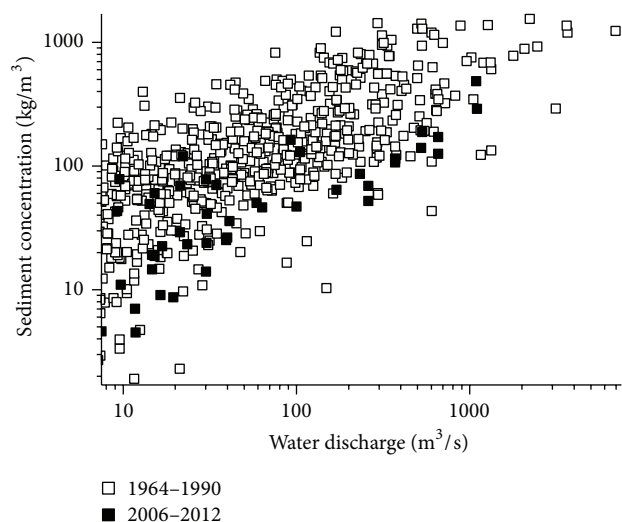


FIGURE 8: The relationship of discharge and sediment concentration.

period must be also partly associated with the changes in the relation between water discharge and sediment concentration (the water-sediment relation). The scatter plot between daily discharge and sediment concentration in the flood season is shown in Figure 8. It can be seen that the sediment concentration in the impact period was much lower than that in the natural period at the same water discharge in the range 300–1100 m³/s. This means that the reduced flows in the impact period carried a much lower sediment load. The reduction in sediment concentration for the same water discharge should be the result of reduced sediment yield on the slopes under the same climate, which have been applied with soil and water conservation measures. Therefore, the implementation of soil and water conservation measures in the basin has been the principal cause for a higher portion of sediment load reduction and a higher contribution of human activities to the reduction than those for the runoff in the Xiliugou basin in the period of 1999–2012.

6. Conclusions

In this study, we analyzed the patterns of change in the runoff and sediment load in the Xiliugou basin from 1960 to 2012 and separated the effects of climate change and human activities on the reductions of runoff and sediment load in 1999–2012. Our conclusions are as follows.

- (1) The annual runoff and sediment load of this basin decreased significantly at the 99% confidence level during the period 1960–2012, while no significant trend was detected in the annual precipitation. According to the abrupt changes in 1998 identified in the runoff and sediment series, the years from 1960 to 2012 were divided into two periods: 1960–1998 and 1999–2012. Comparing with the period 1960–1998, the runoff and sediment load over 1999–2012 reduced by 44.1% and 80.9%, respectively.

- (2) Human activities were the major drivers of the runoff and sediment load variations in the Xiliugou basin recently. They induced 68% and 75%, respectively, of the reductions of runoff and sediment load during 1999–2012, while climate change was responsible for the remaining reductions.
- (3) Different contribution rates of rainfall changes to the deviations of runoff and sediment load could be produced by using different categories of annual precipitation, so we should pay attention to the effects of rainfall intensity to avoid overestimating or underestimating the contributions of rainfall changes to the variations of runoff and sediment load.
- (4) A further inspection on the changes in flow frequency distribution and the water-sediment relation indicated that the implementation of soil and water conservation measures should be the main reason for the phenomenon that the frequency of flows between 0 and 5 m³/s increased and that between 5 and 1000 m³/s decreased during the impact period and also for the sediment load reduction and the contribution of human activities to the reduction being much higher than those for the runoff.

Conflict of Interests

The authors declare that there is no conflict of interests regarding the publication of this paper.

Acknowledgments

This work was supported by the National Natural Science Foundation of China (Grant no. 41371036), the National Major Basic Research Program of China (Grant no. 2011CB403305), and the Ministry of Science and Technology of China (Grant no. 2013 DFA91700). The authors thank Dr. Mischke and the anonymous reviewer for the precious and helpful comments.

References

- [1] D. Qin, G. K. Plattner, M. Tignor et al., *Climate Change 2013: The Physical Science Basis*, Cambridge University Press, Cambridge, UK, 2014.
- [2] N. W. Arnell and N. S. Reynard, “The effects of climate change due to global warming on river flows in Great Britain,” *Journal of Hydrology*, vol. 183, no. 3–4, pp. 397–424, 1996.
- [3] S. Zhang, X. X. Lu, D. L. Higgitt, C.-T. A. Chen, J. Han, and H. Sun, “Recent changes of water discharge and sediment load in the Zhujiang (Pearl River) Basin, China,” *Global and Planetary Change*, vol. 60, no. 3–4, pp. 365–380, 2008.
- [4] C. Miao, J. Ni, and A. G. L. Borthwick, “Recent changes of water discharge and sediment load in the Yellow River basin, China,” *Progress in Physical Geography*, vol. 34, no. 4, pp. 541–561, 2010.
- [5] J. Nèmec and J. Schaake, “Sensitivity of water resource systems to climate variation,” *Hydrological Sciences Journal*, vol. 27, no. 3, pp. 327–343, 1982.

- [6] N. W. Arnell, "Climate change and global water resources: SRES emissions and socio-economic scenarios," *Global Environmental Change*, vol. 14, no. 1, pp. 31–52, 2004.
- [7] P. C. D. Milly, K. A. Dunne, and A. V. Vecchia, "Global pattern of trends in streamflow and water availability in a changing climate," *Nature*, vol. 438, no. 7066, pp. 347–350, 2005.
- [8] I.-W. Jung and H. Chang, "Assessment of future runoff trends under multiple climate change scenarios in the Willamette River Basin, Oregon, USA," *Hydrological Processes*, vol. 25, no. 2, pp. 258–277, 2011.
- [9] U. Scherer, K. Gerlinger, and E. Zehe, "Modeling climate change impact on surface runoff, erosion and sediment yield in agriculturally used catchments," in *Proceedings of the EGU General Assembly Conference Abstracts*, vol. 12, p. 5864, Vienna, Austria, May 2010.
- [10] P. K. Naik and D. A. Jay, "Distinguishing human and climate influences on the Columbia River: changes in mean flow and sediment transport," *Journal of Hydrology*, vol. 404, no. 3–4, pp. 259–277, 2011.
- [11] P. Gao, V. Geissen, C. J. Ritsema, X. Mu, and F. Wang, "Impact of climate change and anthropogenic activities on stream flow and sediment discharge in the Wei River basin, China," *Hydrology and Earth System Sciences*, vol. 17, no. 3, pp. 961–972, 2013.
- [12] G. Zhao, X. Mu, A. Strehmel, and P. Tian, "Temporal variation of streamflow, sediment load and their relationship in the Yellow River Basin, China," *PLoS ONE*, vol. 9, no. 3, Article ID e91048, 2014.
- [13] Z. Ye, Y. Chen, and X. Zhang, "Dynamics of runoff, river sediments and climate change in the upper reaches of the Tarim River, China," *Quaternary International*, vol. 336, pp. 13–19, 2014.
- [14] X. Mu, X. Zhang, H. Shao et al., "Dynamic changes of sediment discharge and the influencing factors in the Yellow River, China, for the recent 90 years," *CLEAN—Soil, Air, Water*, vol. 40, no. 3, pp. 303–309, 2012.
- [15] X. X. Lu, L. S. Ran, S. Liu, T. Jiang, S. R. Zhang, and J. J. Wang, "Sediment loads response to climate change: a preliminary study of eight large Chinese rivers," *International Journal of Sediment Research*, vol. 28, no. 1, pp. 1–14, 2013.
- [16] A. Vacca, S. Loddò, G. Ollesch et al., "Measurement of runoff and soil erosion in three areas under different land use in Sardinia (Italy)," *Catena*, vol. 40, no. 1, pp. 69–92, 2000.
- [17] N. Fohrer, S. Haverkamp, K. Eckhardt, and H.-G. Frede, "Hydrologic response to land use changes on the catchment scale," *Physics and Chemistry of the Earth, Part B: Hydrology, Oceans and Atmosphere*, vol. 26, no. 7–8, pp. 577–582, 2001.
- [18] W. D. Erskine, A. Mahmoudzadeh, and C. Myers, "Land use effects on sediment yields and soil loss rates in small basins of Triassic sandstone near Sydney, NSW, Australia," *Catena*, vol. 49, no. 4, pp. 271–287, 2002.
- [19] A. Lufafa, M. M. Tenywa, M. Isabiry, M. J. G. Majaliwa, and P. L. Woomer, "Prediction of soil erosion in a Lake Victoria basin catchment using a GIS-based Universal Soil Loss model," *Agricultural Systems*, vol. 76, no. 3, pp. 883–894, 2003.
- [20] F. H. Hao, L. Q. Chen, C. M. Liu et al., "Impact of land use change on runoff and sediment yield," *Journal of Soil and Water Conservation*, vol. 18, no. 3, pp. 5–8, 2004.
- [21] W. Wei, L. Chen, B. Fu, Z. Huang, D. Wu, and L. Gui, "The effect of land uses and rainfall regimes on runoff and soil erosion in the semi-arid loess hilly area, China," *Journal of Hydrology*, vol. 335, no. 3–4, pp. 247–258, 2007.
- [22] T. Homdee, K. Pongput, and S. Kanae, "Impacts of land cover changes on hydrologic responses: a case study of Chi River Basin, Thailand," *Journal of Japan Society of Civil Engineers Series B1 (Hydraulic Engineering)*, vol. 55, pp. S31–S36, 2011.
- [23] Z. H. Shi, X. D. Huang, L. Ai, N. Fang, and G. Wu, "Quantitative analysis of factors controlling sediment yield in mountainous watersheds," *Geomorphology*, vol. 226, pp. 193–201, 2014.
- [24] W. Sun, Q. Shao, J. Liu, and J. Zhai, "Assessing the effects of land use and topography on soil erosion on the Loess Plateau in China," *Catena*, vol. 121, pp. 151–163, 2014.
- [25] J. P. M. Syvitski, C. J. Vörösmarty, A. J. Kettner, and P. Green, "Impact of humans on the flux of terrestrial sediment to the global coastal ocean," *Science*, vol. 308, no. 5720, pp. 376–380, 2005.
- [26] C. S. Wu, S. L. Yang, and Y.-P. Lei, "Quantifying the anthropogenic and climatic impacts on water discharge and sediment load in the Pearl River (Zhujiang), China (1954–2009)," *Journal of Hydrology*, vol. 452–453, pp. 190–204, 2012.
- [27] C. Shi, Y. Zhou, X. Fan, and W. Shao, "A study on the annual runoff change and its relationship with water and soil conservation practices and climate change in the middle Yellow River basin," *Catena*, vol. 100, pp. 31–41, 2013.
- [28] D. E. Walling, *The Impact of Global Change on Erosion and Sediment Transport by Rivers: Current Progress and Future Challenges*, UNESCO, 2009.
- [29] C. Miao, L. Yang, B. Liu, Y. Gao, and S. Li, "Streamflow changes and its influencing factors in the mainstream of the Songhua River Basin, Northeast China over the past 50 years," *Environmental Earth Sciences*, vol. 63, no. 3, pp. 489–499, 2011.
- [30] K.-H. Ahn and V. Merwade, "Quantifying the relative impact of climate and human activities on streamflow," *Journal of Hydrology*, vol. 515, pp. 257–266, 2014.
- [31] P. Gao, X.-M. Mu, F. Wang, and R. Li, "Changes in streamflow and sediment discharge and the response to human activities in the middle reaches of the Yellow River," *Hydrology and Earth System Sciences*, vol. 15, no. 1, pp. 1–10, 2011.
- [32] J. X. Xu, "The wind-water two-phase erosion and sediment-producing processes in the middle Yellow River basin, China," *Science in China, Series D: Earth Sciences*, vol. 43, no. 2, pp. 176–186, 2000.
- [33] Y. Zhang, P. Wang, B. Wu, and S. Hou, "An experimental study of fluvial processes at asymmetrical river confluences with hyperconcentrated tributary flows," *Geomorphology*, vol. 230, pp. 26–36, 2015.
- [34] X.-Y. Liu, S.-Z. Hou, and W.-H. Chang, "Cause of main channel shrinkage occurred to the Inner-Mongolia reaches of Yellow River," *Journal of Hydraulic Engineering*, vol. 40, no. 9, pp. 1048–1054, 2009.
- [35] Y. Qin, X. F. Zhang, F. L. Wang, H. Yan, and H. Han, "Scour and silting evolution and its influencing factors in Inner Mongolia reach," *Acta Geographica Sinica*, vol. 66, no. 3, pp. 324–330, 2011.
- [36] J. X. Xu, "Erosion and sediment yield of 10 small tributaries joining Inner-Mongolia reach of upper Yellow River in relation with coupled wind-water processes and hyperconcentrated flows," *Journal of Sediment Research*, no. 6, pp. 28–37, 2013.
- [37] T. Liu, S. F. Zhang, and S. X. Liu, "Primary analysis of the relationship between storm runoff and sediment yield in Ten-watershed—a case study in Xiliu Brook," *Journal of Water Resources & Water Engineering*, vol. 18, no. 3, pp. 18–21, 2007.
- [38] P. Wang, Y. Tian, S. Z. Hou, and Y.-F. Zhang, "Analysis on characteristics of flow and sediment of the hyperconcentration

- tributaries of Inner Mongolia reach of the Yellow River," *Yellow River*, vol. 34, no. 11, pp. 39–42, 2012.
- [39] P. Wang, S. Z. Hou, Y. F. Zhang et al., "Scouring and silting characteristics of hyperconcentrated floods of ten tributaries of upper Yellow River," *Journal of Sediment Research*, vol. 1, pp. 67–73, 2013.
- [40] H. B. Mann, "Nonparametric tests against trend," *Econometrica*, vol. 13, no. 3, pp. 245–259, 1945.
- [41] M. G. Kendall, *Rank Correlation Measures*, Charles Griffin, London, UK, 1975.
- [42] C. Rougé, Y. Ge, and X. Cai, "Detecting gradual and abrupt changes in hydrological records," *Advances in Water Resources*, vol. 53, pp. 33–44, 2013.
- [43] Q. Zhang, J. Li, Y. D. Chen, and X. Chen, "Observed changes of temperature extremes during 1960–2005 in China: natural or human-induced variations?" *Theoretical and Applied Climatology*, vol. 106, no. 3–4, pp. 417–431, 2011.
- [44] A. N. Pettitt, "A non-parametric approach to the change-point problem," *Journal of the Royal Statistical Society C: Applied Statistics*, vol. 28, no. 2, pp. 126–135, 1979.
- [45] X. Fan, C. Shi, Y. Zhou, and W. Shao, "Sediment rating curves in the Ningxia-Inner Mongolia reaches of the upper Yellow River and their implications," *Quaternary International*, vol. 282, pp. 152–162, 2012.
- [46] J. Ding, "Statistical detection for transition point in flood time sequences," *Journal of Wuhan University of Hydraulic and Electric Engineering*, vol. 5, pp. 35–37, 1986.
- [47] Y. Zhou, C. Shi, J. Du, and X. Fan, "Characteristics and causes of changes in annual runoff of the Wuding River in 1956–2009," *Environmental Earth Sciences*, vol. 69, no. 1, pp. 225–234, 2013.
- [48] W. S. Wang, J. Ding, and J. L. Jin, *Statistical Hydrology*, China WaterPower Press, Beijing, China, 2008.
- [49] H. L. Shi, C. H. Hu, Y. G. Wang et al., "Analysis on variation trends of runoff and sediment of the Yellow River Basin and reasons discussion," *Yellow River*, vol. 36, no. 4, pp. 1–5, 2014.
- [50] W. Dong, B. Cui, Z. Liu, and K. Zhang, "Relative effects of human activities and climate change on the river runoff in an arid basin in northwest China," *Hydrological Processes*, vol. 28, no. 18, pp. 4854–4864, 2013.
- [51] P. Gao, *Streamflow and Sediment Discharge Change Trend and Its Response to Human Activities in the Middle Reaches of the Yellow River*, University of Chinese Academy of Sciences (Research Centre of Soil and Water Conservation & Eco-Environment), Yangling, China, 2010.
- [52] K. Liang, C. Liu, X. Liu, and X. Song, "Impacts of climate variability and human activity on streamflow decrease in a sediment concentrated region in the Middle Yellow River," *Stochastic Environmental Research and Risk Assessment*, vol. 27, no. 7, pp. 1741–1749, 2013.
- [53] S. Wang, Y. Yan, M. Yan, and X. Zhao, "Contributions of precipitation and human activities to the runoff change of the Huangfuchuan drainage basin: application of comparative method of the slope changing ratio of cumulative quantity," *Acta Geographica Sinica*, vol. 67, no. 3, pp. 388–397, 2012.
- [54] X. J. Xu, "Temporal and spatial variation in erosion and sediment yield and the cause in the Ten small tributaries to the Inner Mongolia reaches of the Yellow River," *Journal of Desert Research*, vol. 34, no. 6, pp. 1–9, 2014.
- [55] H. W. Chen, Q. S. Ren, and Y. M. Cao, "Analysis on the dam system construction and sediment reduction benefit of loess hilly and gully region in the Xiliugou basin to the Inner Mongolia," *Inner Mongolia Water Resources*, no. 4, pp. 69–70, 2008.
- [56] M. M. Li, B. F. Wu, C. Z. Yan et al., "Estimation of vegetation fraction in the upper basin of Miyun Reservoir by remote sensing," *Resources Science*, vol. 26, no. 4, pp. 153–159, 2004.
- [57] M. G. Wolman and J. P. Miller, "Magnitude and frequency of forces in geomorphic processes," *The Journal of Geology*, vol. 68, no. 1, pp. 54–74, 1960.